Universidad de Cantabria
Departamento de Física Moderna

CSIC - Universidad de Cantabria
Instituto de Física de Cantabria

Propiedades Multifrecuencia de Galaxias Hiperluminosas en el Infrarrojo

Memoria presentada por el Licenciado

Ángel Ruiz Camuñas

para optar al título de Doctor en Física y Ciencias de la Tierra

2010

Declaración de Autoría

Francisco Jesús Carrera Troyano, Doctor en Ciencias Físicas y Profesor Titular de la Universidad de Cantabria,

y

Francesca Panessa, Doctora en Astronomía e Investigadora en el Istituto di Astrofisica Spaziale e Fisica Cosmica,

CERTIFICAN que la presente memoria

Propiedades Multifrecuencia de Galaxias Hiperluminosas en el Infrarrojo

ha sido realizada por **Ángel Ruiz Camuñas** bajo nuestra dirección.
Consideramos que esta memoria contiene aportaciones suficientes para construir la tesis Doctoral del interesado.

En Santander, a 11 de Junio de 2010

Francisco Jesús Carrera Troyano | Francesca Panessa

A mi familia y amigos...

Agradecimientos

Recuerdo la primera vez que le dije a alguien que quería ser astrofísico. Estaba en casa de un amigo y sus padres hicieron la típica pregunta a unos chavales que acaban de empezar el instituto: ¿qué carrera quieres estudiar? También fue la primera vez que escuche “La Pregunta”, esa que todos los que decidimos dedicarnos a la ciencia básica escuchamos tan a menudo: ¿y eso para qué vale? Desde entonces he respondido a ambas preguntas en multitud de ocasiones, pero la respuesta a la primera siempre ha sido la misma (obstinado que es uno). En todos estos años han sido muchas las personas que me han ayudado a alcanzar ese sueño: profesores, amigos, familia... A todos ellos, muchas gracias por apoyarme siempre en este empeño, por extraño o inútil que les pareciera a algunos de ellos.

Podría dejar los agradecimientos aquí, pero entonces la mayoría de los lectores se sentirían defraudados (seamos sinceros, ¿cuantos pensáis leer la tesis entera?). Bromas aparte, no puedo dejar de mencionar a algunas de las personas que, de un modo u otro, me han ayudado a llegar hasta aquí.

Para empezar, nunca podría haber realizado este trabajo sin mis directores de tesis, Francisco Carrera y Francesca Panessa. Los consejos que me han dado a lo largo de estos años y la paciencia que han tenido conmigo son impagables. Espero que mi trabajo haya estado a la misma altura que el suyo. Me gustaría extender este agradecimiento a Giovanni Miniutti y a Guido Risaliti. Poder trabajar durante unos meses con astrónomos como ellos fue una experiencia increíble. Además gracias a ellos he vivido en dos ciudades como Cambridge y en Florencia, ¡que más se puede pedir! No puedo olvidar tampoco a Laura Cayón, la primera persona que me ofreció una oportunidad para colarme en el mundo de la investigación.

Mi agradecimiento también a toda la gente del grupo de Astronomía de Rayos X del IFCA, por hacerme sentir como en casa desde el primer día. En especial gracias a Xavier Barcons (es el jefe, así que sin él nunca hubiera podido trabajar ahí); a la SUSI, Maite Ceballos (espero no haberle dado demasiado trabajo) y a mis compañeros becarios Jacobo y Amalia (los congresos no hubieran sido iguales sin ellos). Y gracias en general a toda la gente del IFCA por crear un ambiente de trabajo tan sano y, en ocasiones, lleno de *frikismo* (como echo de menos las partidas de Diplomacia... aunque al final siempre ganara Marcos). Ha sido un verdadero placer pasar estos años allí. Toda la gente que he conocido y los lugares que he podido visitar durante mi doctorado han hecho de este mucho más que una mera experiencia académica.

Por otro lado, he de agradecer todo el apoyo que me han dado mis padres (curiosamente ellos nunca me hicieron “La Pregunta”). Sin ellos nunca hubiera podido dedicarme a esto. Seguramente sin las revistas “Muy Interesante” y los libros que mi padre traía a casa nunca se me hubiera despertado el gusanillo de la ciencia (la verdad es que tenía que ser gracioso ver a un *moco* de cinco años hojeando “Cosmos”). Me gustaría también dedicarle un recuerdo a mi abuelo Basilio, que ya no está con nosotros. Aunque él siempre me dijo que tenía que ser cura o torero, estoy seguro de que le haría mucha ilusión verme convertido en un doctor.

Mención especial merecen mis amigos Juan, Fonso, Javi, Montse, Borja, Jorge, Krys, Iván, Esther, Selaya, Mikel, Susana, Zabala, Escubi... Son lo mejor que tengo y con ellos cualquier cosa que me proponga hacer en esta vida resulta mucho más sencilla (y tremendamente más divertida). Aunque a veces tienen que aguantar mis divagaciones sobre gravitones o agujeros negros, espero que les compense. Quiero agradecerle en especial a Adolfo nuestras conversaciones compartiendo unas copas, que me han permitido ampliar mi visión de la ciencia y la filosofía de un modo muy original. Por último, un gran beso a Ruth. A pesar de la distancia y el poco tiempo que podemos pasar juntos, sigue conmigo... ¡Increíble!

Finalmente, quiero dar las gracias a los compañeros del Osservatorio di Brera en Milán por permitirme dedicar parte de mi tiempo a terminar esta tesis. Siento que se haya alargado más de lo previsto, pero ahora sí, ya está terminada.

Abrazos a todos.

Resumen de la tesis en castellano

Objetivos de la Investigación

El observatorio *IRAS* (*Infrared Astronomical Satellite*) fue puesto en órbita en 1983 con la misión de explorar el cielo completo en distintas longitudes de onda dentro del rango infrarrojo (IR). Una de sus aportaciones más importantes fue el descubrimiento de una nueva población de galaxias con una intensa luminosidad en el IR ($L_{\rm IR} > 10^{11}\ L_{\odot}$) que además domina completamente respecto a la emisión en otros rangos de energía. Se las denominó Galaxias Luminosas en el IR (*Luminous Infrared Galaxies* – LIRG).

Dentro de las LIRG se descubrieron nuevas galaxias con una luminosidad en el IR aún mayor: las Galaxias Ultraluminosas en el Infrarrojo (*Ultraluminous Infrared Galaxies* – ULIRG) si su luminosidad IR excedía de $10^{12}\ L_{\odot}$, y las Galaxias Hiperluminosas en el Infrarrojo (*Hyperluminous Infrared Galaxies* – HLIRG) si su luminosidad IR excedía de $10^{13}\ L_{\odot}$.

La elevada luminosidad de estas galaxias solo podía explicarse o bien mediante episodios de violenta formación estelar (*starburst* - SB), o bien por la acreción sobre un agujero negro supermasivo (supemassive black holes - SMBH) central de grandes masas de gas y polvo (Núcleo activo de galaxia – AGN). Cuál de estos fenómenos es el verdadero motor de la emisión IR de estas galaxias ha sido un tema muy debatido por la comunidad astronómica desde el descubrimiento de las ULIRG y las HLIRG.

Finalmente, los nuevos telescopios terrestres y espaciales disponibles durante la última década han permitido elaborar un paradigma consistente para las ULIRG. Actualmente se acepta que éstas son el resultado de fusiones y/o interacciones entre galaxias ricas en gas. Dichas colisiones conducen grandes cantidades de gas y polvo al núcleo de las galaxias, parte del cual es consumido en episodios de formación estelar muy intensos y otra parte cae en el SMBH, encendiendo un AGN. El debate actual sobre estos objetos se centra en como interaccionan ambos fenómenos (SB y AGN) entre sí y su posible influencia en la evolución posterior de la galaxia.

Este paradigma sin embargo no parece ser completamente correcto en el caso de las HLIRG. Si bien se acepta que, como en las ULIRG, la luminosidad IR es provocada por alguna combinación de SB y AGN, observaciones realizadas con el telescopio espacial Hubble demuestran que sólo un tercio de estas galaxias muestran señales de colisiones o interacciones. Son necesarias pues investigaciones más detalladas para comprender la naturaleza de las HLIRG y su relación con las ULIRG.

Por otro lado, si los fenómenos de formación estelar y acreción sobre SMBH son tan extremos como estudios anteriores sugieren, las HLIRG resultan un laboratorio excelente para estudiar las interacciones y procesos de retroalimentación entre AGN y SB, así como con la galaxia que los hospeda. Lograr una comprensión detallada de estas interacciones resulta imprescindible dentro del paradigma de coevolución de los AGN y las galaxias. Un número cada vez mayor de observaciones señalan claramente que la formación de las galaxias se encuentra de algún modo relacionada con el crecimiento de los SMBH que albergan en su centro. El estudio de las HLIRG es por tanto crucial dentro de dicho paradigma.

El principal objetivo de esta tesis es presentar un marco global y coherente de las HLIRG en el cual poder explicar las propiedades de estos objetos derivadas de observaciones multifrecuencia. Necesitamos pues estimar la contribución relativa de AGN y SB a la emisión bolométrica total de las HLIRG. ¿Los procesos de acreción son dominantes respecto a la formación estelar? ¿O más bien sucede lo contrario? ¿Cómo es la emisión de estos objetos a lo largo del espectro electromagnético? Puede explicarse su enorme luminosidad IR simplemente por la emisión de un AGN o de un SB, ¿o son ambos fenómenos necesarios? ¿Cuál es el rango de energías más adecuado para estudiar y poder separar la emisión del AGN de la formación estelar en estos objetos?

Podemos resumir los objetivos de esta tesis en los siguientes puntos:

1. Caracterizar las propiedades de las HLIRG en distintos rangos de energía e interpretarlas desde un punto de vista amplio y consistente.

2. Separar la emisión originada en los AGN y los SB presentes en las HLIRG mediante diferentes técnicas complementarias y estimar la contribución relativa de cada una de esas componentes a la emisión total.

3. Comprobar si las luminosidades de los AGN y de los SB están de algún modo relacionados en distintas épocas del Universo.

4. Estimar las tasas de formación estelar de estas galaxias utilizando diferentes métodos y comprobar si dichas tasas son tan extremas como han encontrado estudios anteriores.

5. Estudiar la densidad del gas y la fracción de cielo cubierto por polvo en las HLIRG.

6. Reproducir la emisión global de las HLIRG mediante la combinación de modelos sencillos de AGN y SB, así como estudiar cualquier dependencia de esta emisión con otras propiedades de las HLIRG como el oscurecimiento o la luminosidad bolométrica.

7. Comprobar si las HLIRG forman una única población bien definida o pueden separarse en distintas “familias” y, en ese caso, intentar explicar los orígenes físicos de éstas.

Planteamiento y metodología

Los AGN y los procesos de formación estelar se producen habitualmente en entornos muy oscurecidos por grandes cantidades de gas y polvo. La observación en rayos X y en el IR permiten penetrar en esta clase de entornos y estudiar dichos fenómenos. Mientras que los rayos X proporcionan una visión clara de la emisión primaria de los AGN, observaciones en el IR ofrecen información detallada acerca de los niveles de polvo y la formación estelar que se produce en las cercanías del AGN.

Las observaciones en el IR y rayos X resultan pues esenciales para comprender de un modo detallado la formación estelar y los AGN. Afortunadamente hoy en día disponemos de potentes observatorios en estos rangos de energía, como *Chandra*, XMM-*Newton*, *Suzaku*, *Spitzer*, o AKARI. Pueden emplearse diferentes estrategias para aprovechar la sinergia entre rayos X e IR, por ejemplo mediante exploraciones del cielo multifrecuencia como los proyectos GOODS, AEGIS o COSMOS, mediante observaciones puntuales en el IR de objetos con propiedades peculiares en rayos X (como los cuásares absorbidos en rayos X), o mediante observaciones en rayos X de fuentes que emiten fuertemente en el IR, como las ULIRG o las HLIRG.

Gracias a las excepcionales características de los nuevos observatorios antes mencionados podemos estudiar las propiedades de las HLIRG en distintas longitudes de onda con un detalle muy elevado. Para desarrollar esta investigación seleccionamos una muestra de HLIRG compuesta por fuentes que habían sido observadas por los observatorios espaciales XMM-*Newton* (rayos X) y *Spitzer* (IR). La tesis que aquí se presenta está dividida en tres partes: el estudio de los espectros X de las HLIRG, el estudio de sus espectros en el IR medio (MIR) y el estudio de sus distribuciones espectrales de energía (*Spectral Energy Distribution* – SED).

La comparación entre HLIRG y ULIRG de sus propiedades X e infrarrojas, así como de sus SED, nos permiten determinar hasta que punto estos objetos forman dos poblaciones bien diferenciadas. Aún más, mediante el análisis de una muestra amplia y representativa de HLIRG podremos concretar si todos las HLIRG comparten características similares o pueden ser divididos en distintas familias.

Podemos aplicar también distintos métodos para detectar las señales típicas de la emisión de AGN y SB en distintas longitudes de onda, así como estimar la contribución de cada uno de estos procesos a la emisión bolométrica de las HLIRG. Nuestro enfoque multifrecuencia puede proporcionas pruebas más concluyentes acerca de cuál es el mecanismo dominante en las HLIRG comparado con anteriores estudios restringidos a un único rango de energía.

Gracias a la capacidad penetrante de las observaciones en rayos X y en el IR, podemos detectar la emisión AGN incluso en entornos altamente oscurecidos. Aplicando las correcciones bolométricas estándar es posible estimar la luminosidad total del AGN y su contribución relativa a la emisión total de cada HLIRG. Además a través del estudio de sus SED podemos comprobar si estas correcciones bolométricas son adecuadas para estos objetos de luminosidad tan elevada.

Los rayos X y el IR también ofrecen una ventana excelente para el estudio de los procesos de formación estelar que se pueden dar en las HLIRG. Es posible estimar las luminosidades de la emisión SB y las tasas de formación estelar que se dan en las HLIRG, así como comprobar si éstas se encuentran de algún modo relacionadas con las propiedades del AGN, lo que señalaría hacia un origen físico común.

Aportaciones originales

La investigación presentada en esta tesis ha contribuido significativamente al conocimiento de las HLIRG. Anteriores trabajos se limitan a un solo rango de energía y, generalmente, a un pequeño número de fuentes. Solo dos trabajos anteriores han estudiado una muestra significativa de HLIRG (Rowan-Robinson 2000; Farrah et al. 2002a), pero ambos están restringidos al rango IR y utilizan las mismas técnicas para su estudio. Nuestro trabajo es el primero que ha estudiado una muestra moderadamente grande de HLIRG en distintos rangos de energía, permitiendo obtener una visión consistente capaz de explicar la elevada luminosidad de estos objetos.

Nuestras investigaciones de los espectros X y MIR de las HLIRG han sido los primeros estudios sistemáticos de estos objetos realizados en dichos rangos de energía. Del mismo modo, nuestro trabajo sobre las SED de las HLIRG es también pionero en estudiar la emisión global de estas fuentes más allá de la banda infrarroja. Estos resultados han sido presentados en varios congresos y revistas internacionales (Ruiz et al. 2006, 2007, 2010a,b,c).

Conclusiones

Esta investigación ha permitido caracterizar las propiedades de las HLIRG en rayos X y en el MIR, así como explicar su emisión global a través de la construcción de sus distribuciones espectrales de energía, desde la banda de radio hasta los rayos X. Nuestro enfoque multifrecuencia nos ha permitido presentar pruebas sólidas de que todas las fuentes que hemos estudiado albergan un AGN. En la mayoría de estas fuentes es necesaria la existencia de un SB para explicar completamente todas sus propiedades. Hemos podido determinar también que aquellas fuentes sin formación estelar significativa son en realidad cuásares muy luminosos, con lo que no deben considerarse auténticas HLIRG ya que su emisión bolométrica no está dominada completamente por la emisión IR. Así pues, los fenómenos de AGN y SB resultan ambos cruciales para entender la luminosidad extrema de las HLIRG.

Hemos encontrado indicios significativos de que las HLIRG no forman una población homogénea. Por un lado hemos encontrado HLIRG muy oscurecidas en rayos X y el MIR, señalando la existencia de grandes cantidades de gas y polvo que envuelven casi completamente el núcleo galáctico. Los AGN y SB presentes en esta clase fuentes parecen encontrarse fuertemente interconectados y los estudios morfológicos de algunas de estas galaxias indican que se encuentran sometidas a fenómenos de interacción y/o fusión entre galaxias. Todas estas propiedades son comunes a las ULIRG, con lo que podemos concluir que este tipo de HLIRG son el extremo de mayor luminosidad dentro de la población de ULIRG.

Por otro lado encontramos HLIRG poco oscurecidas en rayos X y el MIR, con lo que las cantidades de polvo y gas presentes son significativamente menores a las encontradas en el anterior grupo. Los procesos de retroalimentación entre los AGN y los SB en estas fuentes parecen ser también menos importantes. Los SB de la mayoría de estas fuentes pueden ser reproducidos mediante modelos de SB jóvenes. Los estudios morfológicos señalan que son fuentes aisladas, no encontrando evidencias de que hayan sufrido interacciones o fusiones recientes con otras galaxias. Si bien se necesitan estudios más detallados para comprender la naturaleza de estas HLIRG, podrían ser galaxias jóvenes que están sufriendo su primer proceso importante de formación estelar. Parte del gas necesario para esta formación estelar cae en su SMBH central, encendiendo un AGN.

Podemos concluir por tanto que las fuentes estudiadas en esta tesis pertenecen a una de estas tres poblaciones:

1. Cuásares muy luminosos sin formación estelar significativa.

2. Galaxias activas aisladas y jóvenes sometidas a su primer episodio importante de formación estelar, sin ninguna relación con interacciones o fusiones galácticas recientes.

3. Galaxias sometidas a interacciones recientes con otras galaxias, lo cual atrae a su centro grandes cantidades de gas y polvo. Estos eventos disparan episodios violentos de formación estelar y enciende el AGN en un entorno altamente oscurecido. Estos objetos pueden clasificarse como la versión de alta luminosidad de las ULIRG.

Futuras líneas de investigación

Los resultados presentados en esta tesis pueden mejorarse significativamente mediante las siguientes líneas de actuación:

1. **Incrementar la muestra de HLIRG.** En este trabajo se ha estudiado un número moderado de fuentes, alrededor de unas veinte HLIRG. Este número era una fracción importante del total de

HLIRG conocidas (cerca de cincuenta) cuando se comenzó esta tesis. Sin embargo las exploraciones de gran área realizadas por los nuevos telescopios infrarrojos lanzados en los últimos años como *Spitzer* y AKARI, junto con los futuros resultados de WISE o *Herschel*, están incrementando espectacularmente el número de HLIRG conocidas. Todos estos nuevos datos nos permitirán construir muestras de HLIRG con un número mucho mayor de fuentes, seleccionadas de una manera más homogénea. Esto hará posible obtener conclusiones acerca de la población global de HLIRG mucho más sólidas.

2. **Comparación con otras poblaciones de fuentes astronómicas.** Esta tesis se ha limitado al estudio de HLIRG a *redshift* moderado, pero los nuevos observatorios infrarrojos han descubierto un número cada vez mayor de HLIRG a alto *redshift*. La comparación entre las propiedades de las poblaciones de las ULIRG y HLIRG a bajo y alto *redshift* es crucial para comprender la evolución de estos objetos a lo largo del tiempo. Resulta también importante estudiar la posible relación entre HLIRG y otras fuentes de alta luminosidad como las galaxias sub-milimétricas o los QSO con absorción en rayos X. Estas investigaciones son necesarias para obtener una visión global acerca de la relación entre los AGN y la formación galáctica.

3. A largo plazo, la **nueva generación de observatorios X.** La misión conjunta de NASA, ESA y JAXA para desarrollar el nuevo observatorio internacional de rayos X (IXO) proporcionará una herramienta excelente para el estudio de las HLIRG. El notable aumento de sensibilidad y la ampliación del rango de energía en el que presumiblemente funcionará IXO permitirán la observación directa de la emisión nuclear de las fuentes más oscurecidas. También permitirá la detección de la emisión X originada por procesos de formación estelar incluso en aquellas HLIRG dominadas por la emisión del AGN.

Universidad de Cantabria
Departamento de Física Moderna

CSIC - Universidad de Cantabria
Instituto de Física de Cantabria

Multiwavelength Properties of Hyperluminous Infrared Galaxies

A dissertation submitted in partial fulfillment of the requirements
for the degree of Doctor of Philosophy in Physics

by

Ángel Ruiz Camuñas

“They both savoured the strange warm glow of being much more ignorant than ordinary people, who were only ignorant of ordinary things.”

Discworld scientist at work
(Terry Pratchett, Equal Rites)

“In order to make an apple pie from scratch, you must first create the Universe.”

Carl Sagan

Summary

One of the most challenging results brought by the Infrared Astronomical Satellite (IRAS) is the discovery of a new population of extragalactic objects, the Ultraluminous Infrared Galaxies (ULIRG). These sources showed a luminosity comparable to quasars ($L_{\mathrm{IR}} \gtrsim 10^{12}\ L_{\odot}$), but their bolometric output was completely dominated by the infrared (IR) emission.

The origin of their extreme IR luminosities has been in discussion for decades, but in the last few years a consensual picture has emerged, brought by multi-wavelength observations. Now is broadly accepted that ULIRG are dusty galaxies where fierce star formation processes have been triggered by mergers or interactions between rich-gas galaxies. Only half of them show Active Galactic Nuclei (AGN), which usually are minor contributors to the total IR emission, but the fraction of ULIRG harbouring an AGN and its relative contribution to the bolometric output increases with luminosity.

Hyperluminous Infrared Galaxies (HLIRG) are defined as those LIRG with $L_{\mathrm{IR}} > 10^{13}\ L_{\odot}$. However the ULIRG paradigm described above is not so well-grounded for HLIRG. Most of these objects seem to be composite sources, i.e. AGN and SB phenomena are both needed to fully explain their IR emission and only about a third of them has been found in interacting systems. Further investigations are needed to fully understand the nature of HLIRG and its connection with ULIRG. Moreover, as HLIRG could represent the most vigorous stage of galaxy formation they are unique laboratories to investigate extremely high stellar formation, and its connection to super-massive black hole (SMBH) growth. HLIRG could be key objects to understand the co-evolution between SMBH and galaxies.

AGN and star formation processes occur in environments enshrouded by large amounts of gas and dust. X-ray and IR observations offer the needed penetrating power to study these phenomena. While X-rays provide a largely uncontaminated view of the primary AGN emission, measures of infrared emission yield detailed information about the levels of dust and on-going star-formation surrounding AGN.

Infrared and X-ray observations are therefore essential to understand the AGN and SB phenomena ongoing in HLIRG. The main objective of this thesis is to draw a comprehensive and consistent picture on HLIRG derived from multi-wavelength observations. Thanks to the unprecedented capabilities of

state-of-the-art observatories we are able to characterize the properties of HLIRG in several wavelength ranges.

We selected a moderate size sample of HLIRG observed by XMM-*Newton* and/or *Spitzer*, which allows performing our study in two complementary energy bands, X-ray and MIR, and we have also studied their broadband SED from radio to X-rays. We have applied different techniques to detect the signatures of AGN and SB emission at several wavelengths and estimate the contribution of these processes to the bolometric output. Our multi-wavelength approach provides more conclusive evidence on which is the dominant mechanism with respect to any other previous study restricted to a particular energy range.

We found that all the studied sources harbour an AGN. MIR and X-ray observations have allowed its detection even in heavily enshrouded environments. Most of these sources posses a strong SB, with star forming rates up to $\sim 1000\ M_{\odot}\ \mathrm{yr}^{-1}$. Moreover, we found that those sources with no SB contribution are in fact luminous quasars and hence they are not "bona fide" HLIRG, since their bolometric emission is not dominated by the IR output. We can confirm that both AGN and SB phenomena are indispensable to understand the extreme luminosity of HLIRG.

However, the "bona fide" HLIRG do not seem to be an homogeneous population. On one hand there are sources with large amounts of gas and dust enshrouding the nucleus as it is suggested by the strong absorption shown in X-rays and MIR and by the shape of their SED. Their large dust covering factors are also consistent with a nucleus almost completely enshrouded by dust. The gas and dust fuel powerful AGN activity and strong star formation, that could be triggered by galaxy interactions and/or mergers, as suggested by the study of the morphology and environment of some of these HLIRG. The analysis of their SED also hints toward a strong feedback between both phenomena. These are common properties of ULIRG and hence we can consider these HLIRG as the objects occupying the high luminosity tail of the ULIRG population distribution.

On the other hand there are HLIRG with minor MIR/optical/X-ray obscuration, suggesting lower quantities of gas and dust than in the "ULIRG-like" population. However the strong SB observed in these sources need large amounts of gas to fuel the star formation. The SB emission in these HLIRG can be modelled with young SB models. They seem to be isolated galaxies, with no signs of interactions or ongoing mergers. Further studies are needed to explain the nature of these HLIRG, but they could be young active galaxies undergoing their first major episode of star formation.

Therefore, the sources studied in this thesis likely belong to three different populations:

1. Very luminous QSO with minor star formation activity.

2. Young, isolated active galaxies undergoing their first episode of major star formation with little connection with a recent major merger.

3. Galaxies which have recently experienced a merger/disturbance that brought lots of gas and dust into the inner regions. This event triggered both the star formation and the AGN activity in a heavily obscured environment. These objects are good candidates to be the high luminosity tail of the ULIRG population distribution.

Contents

Declaración de Autoría **iii**

Agradecimientos **vii**

Resumen en castellano **ix**

Summary **xix**

List of Figures **xxvii**

List of Tables **xxix**

1 Introduction **1**

1.1 Active galactic nuclei . . . 1

1.1.1 Emission mechanisms . . . 3

1.1.2 Spectral Energy Distribution . . . 4

1.1.3 The Unified Model . . . 7

1.2 Starburst galaxies . . . 9

1.2.1 Spectral Energy Distribution . . . 9

1.2.2 Starburst models . . . 11

1.3 Infrared Galaxies . . . 12

1.3.1 Ultraluminous Infrared Galaxies . . . 13

1.3.2 Hyperluminous Infrared Galaxies . . . 16

1.4 Co-evolution of galaxy formation and SMBH growth . . . 17

1.5 Aims of this thesis . . . 20

2 HLIRG samples **23**

2.1 Rowan-Robinson's HLIRG Sample . . . 23

2.2 Farrah's HLIRG Sample . . . 24

2.2.1 IRAS 13279+3401 . . . 25

2.3 HLIRG samples assembled for this thesis . . . 26

2.3.1 XMM-*Newton* HLIRG Sample . . . 26

2.3.2 *Spitzer* HLIRG Sample . . . 27

2.4 Description of the sources . . . 27

3 An XMM-*Newton* Study of HLIRG **33**
3.1 Motivation . . . 33
3.2 The XMM-*Newton* X-ray observatory . . . 34
3.3 X-ray data reduction and analysis . . . 36
3.3.1 Data reduction . . . 36
3.3.2 Non-detected sources . . . 36
3.3.3 Cluster emission subtraction . . . 36
3.3.4 Spectral analysis . . . 37
3.3.5 Source by source analysis . . . 39
3.4 Discussion . . . 49
3.4.1 Comparison with IR emission . . . 50
3.4.2 Origin of the IR “excess” . . . 52
3.4.3 Soft X-ray excess . . . 55
3.4.4 Cosmic evolution . . . 56
3.5 Conclusions . . . 57

4 Analysis of *Spitzer*-IRS spectra of HLIRG **59**
4.1 Motivation . . . 59
4.2 The *Spitzer* Space Telescope . . . 60
4.2.1 Infrared Array Camera . . . 60
4.2.2 Infrared Spectrograph . . . 61
4.2.3 Multiband Imaging Photometer for Spitzer . . . 61
4.3 Data reduction . . . 61
4.4 SB/AGN spectral decomposition . . . 62
4.4.1 Notes on particular sources . . . 64
4.5 Results . . . 68
4.5.1 Star formation rate from PAH emission . . . 68
4.5.2 AGN contribution to the IR luminosity . . . 70
4.5.3 Covering Factor . . . 72
4.6 Conclusions . . . 76

5 Spectral energy distributions of HLIRG **77**
5.1 Motivation . . . 77
5.2 Data compilation . . . 78
5.2.1 Radio . . . 78
5.2.2 Infrared . . . 79
5.2.3 Optical and UV . . . 79
5.2.4 X-ray . . . 79
5.2.5 Overall description of the SED . . . 79
5.3 SED fitting . . . 81
5.3.1 Templates . . . 82
5.4 Results . . . 85
5.4.1 Class A HLIRG . . . 86
5.4.2 Class B HLIRG . . . 86
5.4.3 Fitting without X-ray data . . . 87
5.4.4 Notes on particular sources . . . 89
5.5 Comparison with previous results . . . 91

5.5.1 X-ray emission 91
5.5.2 IR SED: comparison with previous works 92
5.6 Discussion and conclusions 94

6 Conclusions and future work **101**
6.1 Conclusions 101
6.2 Future work 105

A Tables of SED data **107**

References **115**

List of Figures

1.1 AGN Spectral Energy Distribution. 5
1.2 AGN X-ray spectrum. 6
1.3 AGN Unified model. 7
1.4 SB Spectral Energy Distribution. 10
1.5 Accretion rate and star formation evolution. 18

2.1 Optical and MIR spectra of IRAS 13279+3401. 25

3.1 XMM-*Newton* spectra of HLIRG. 41
3.2 2-10 keV versus FIR luminosities. 51
3.3 AGN contribution to the IR luminosity. 53
3.4 X-ray soft excess versus 2-10 keV AGN luminosities. 54
3.5 X-ray soft excess versus FIR luminosities. 56
3.6 Evolution in redshift of SFR and X-ray-to-FIR luminosities ratio. 57

4.1 MIR templates. 63
4.2 *Spitzer* spectra and best fit models. 66
4.3 Comparison of star formation rates. 69
4.4 Star formation rates versus IR luminosities. 70
4.5 6 μm-to-bolometric flux ratio (R) versus AGN emission at 6 μm. 71
4.6 AGN contribution to the IR luminosity. 72
4.7 Covering factor. 74

5.1 Rest-frame spectral energy distributions. 80
5.2 Flux ratios distributions. 80
5.3 AGN SED templates. 83
5.4 Starburst and composite SED templates. 83
5.5 AGN bolometric luminosity versus AGN X-ray luminosity. 91
5.6 Comparison of IR luminosities and AGN fraction. 93
5.7 Rest-frame SED and best-fit models of class A HLIRG. 96
5.8 Rest-frame SED and best-fit models of class B HLIRG. 98

List of Tables

2.1 Farrah's HLIRG Sample . . . 24
2.2 HLIRG Samples . . . 28

3.1 Description of the XMM-*Newton* observations. . . . 35
3.2 *Chandra* observations description. . . . 37
3.3 Results of the XMM-*Newton* spectral analysis. . . . 40
3.4 Infrared fluxes and luminosities of the sample. . . . 46

4.1 Description of the *Spitzer* observations. . . . 62
4.2 Results of the *Spitzer* spectral analysis. . . . 65
4.3 Covering factor. . . . 73

5.1 SED templates. . . . 84
5.2 Best fit models for the HLIRG's SED. . . . 88
5.3 IR and X-ray luminosities. . . . 90

A.1 IRAS 00182-7112. . . . 107
A.2 IRAS F00235+1024. . . . 107
A.3 IRAS 07380-2342. . . . 108
A.4 IRAS 09104+4109. . . . 108
A.5 PG 1206+459. . . . 109
A.6 PG 1247+267. . . . 109
A.7 IRAS F12509+3122. . . . 110
A.8 IRAS 12514+1027. . . . 110
A.9 IRAS 14026+4341. . . . 111
A.10 IRAS F14218+3845. . . . 111
A.11 IRAS F15307+3252. . . . 112
A.12 IRAS 16347+7037. . . . 112
A.13 IRAS 18216+6418. . . . 113

Chapter 1

Introduction

The “extreme” has been always a fascination for human beings. Our history is in some way a reflect of our ambition to go higher, to get deeper, to reach the farthest, to be the best. And science is not immune to our desire to search for the Universe’s own brand of the biggest and the brightest. But the curiosity of science for extreme objects and conditions is not only a matter of this particular quality of the human behaviour.

Strange and extreme environments allow scientist to test theories beyond the “normal” conditions where they were established and to learn better how is their nature. Special relativity tells us how objects behave at the highest velocities, general relativity describes how gravity works in extreme conditions and how the Universe evolves in the largest scales, quantum mechanics was developed to understand the tiniest scales of the Universe.

Astronomy, in particular, is a science of extremes. Most situations studied by astronomers are far beyond our daily experience, but we still are interested in the extremes. We search for the biggest and brightest sources in the Universe, we call them ultra-this or hyper-that, and all of them teach us about the most extreme conditions in the Universe. This work is dedicated to one family of these extreme astronomical objects, the Hyperluminous Infrared Galaxies. And behind these objects we found two of the most powerful astronomical phenomena: active galactic nuclei and starburst episodes.

1.1 Active galactic nuclei

The term ’Active Galactic Nuclei’ (AGN) refers to the existence of energetic phenomena in the nuclei, or central regions, of galaxies which cannot be attributed clearly and directly to stars. The luminosity of the centre can range from tens to thousands of times that of the underlying host galaxy, which is completely outshined, appearing in the optical images as a bright point source when the AGN is distant. These objects are among the most luminous persistent sources known in the Universe (gamma ray bursts can be brighter by a few orders of magnitude but they only last a few seconds) and about 10% of all known galaxies harbour an AGN. Their bolometric luminosities span a broad range of values, from 10^{42} to 10^{48} erg s^{-1} for the most luminous AGN. A fundamental characteristic of most AGN is the strong time-variability observed in their optical/UV/X-ray emission, implying that the spatial scale of the main engine of AGN is within the order of light days: a nucleus comparable to the size of the Solar System is emitting hundreds of times as much energy as an entire galaxy.

There is an enormous number of AGN ’flavours’ based on their observational properties. Here we list some of the most relevant classifications:

- Based on their luminosity, we differentiate between Seyfert (Sy) galaxies and quasars[1] (or quasi-stellar objects - QSO). Seyfert galaxies are those AGN with absolute magnitude in B band $M_B > -21.5 + 5 \log H_0$. An alternative criterion, based on the X-ray luminosity, defines as QSO those objects with $L_X > 10^{44}$ erg s^{-1}. There is also a family of AGN whose emission does not dominate over the host galaxy, the low-luminosity AGN (LLAGN, Ho 1999; Panessa et al. 2007).

- According to their optical/UV spectrum, ’Type 1’ and ’Type 2’ sources are distinguished. Type 1 AGN show broad (widths[2] up to several thousands kilometres per second) permitted lines and narrow (widths of a few hundreds of kilometres per second) permitted and forbidden[3] lines in the spectrum, while Type 2 objects show only narrow lines. Type 1s and 2s do not form two completely separate groups. There is a continuum of objects in between where the broad line components are increasingly difficult to observe and may vary quite considerably.

- Based on their radio emission, AGN are classified in ’Radio-loud’ (RL) and ’Radio-quiet’ (RQ). This classification is based on the radio-loudness of the source, the ratio between the radio flux at 5 GHz and the optical flux in the B band (centred at 4400 Å): $R_L = \log \frac{F_{5\ \mathrm{GHz}}}{F_\mathrm{B}}$. Those objects with $R_L \geq 10$ are labelled as RL AGN whereas the rest are RQ AGN. Roughly 10% of AGN are RL.

The ’taxonomy’ of AGN include several other types of objects, like radio galaxies, low-ionization nuclear emission-line regions (LINERS), blazars, optically violent variables (OVV) AGN, etc.. See Peterson (1997) for a complete review.

[1]In the beginning the term ’quasar’ (acronym of ’quasi-stellar radio source’) was applied only to objects with significant radio emission, but nowadays is often used to refers all high-luminosity AGN.

[2]The widths of AGN emission lines are usually expressed in velocity units since the broadening is due to the Doppler effect.

[3]The term ’forbidden lines’ refers to spectral lines not observed in laboratory spectra. The low pressure and temperature conditions of some astronomical environments, not reproducible in Earth laboratories, allow the existence of these lines.

1.1.1 Emission mechanisms

The principal physical mechanisms responsible of the observed emission in AGN at different wavelengths can be summarized as follows:

1. **Black body emission:** a black body (BB) is a body in thermal equilibrium with the surrounding radiation field, i.e. it is a perfect emitter and absorber (no radiation is reflected). The emission spectrum of a BB depends only on its temperature. Although no real object is a perfect BB, it is a fair approximation in many cases. The optical/UV continuum observed in AGN is described as BB emission originated in an accretion disk: the gas and dust surrounding a super-massive black hole (SMBH) is attracted forming a disk due to the conservation of angular momentum. The material in the disk is heated due to the viscous friction, radiating energy and loosing angular momentum until it finally falls into the black hole. AGN accretion disks are relatively cool ($\sim 10^5 - 10^6$ K) producing blue spectra in the optical/UV energy range. A fraction of this continuum is absorbed by the dust around the SMBH (the dusty torus and/or the interstellar medium of the host galaxy) and then re-emitted in the MIR and FIR. A BB (or a combination of BBs at different temperatures) is also a good description of this reprocessed emission due to heated dust.

2. **Inverse Compton scattering:** "normal" Compton scattering is the process where a photon of wavelength λ interacts with an electron bound to an atom resulting a new photon of $\lambda' > \lambda$, i.e. the original photon imparts a fraction of its energy to the electron. If free, relativistic electrons are present, the inverse effect can occur: the photon is kicked up to higher energies (i.e. shorter wavelengths) by the electron. This process is known as Inverse Compton scattering. The spectrum of the scattered radiation depends on the electron energy distribution. The broad X-ray continuum observed in AGN is usually explained through this effect. A corona of high energy electrons, coming from the ionized material in the accretion disk, is believed to surround the inner regions close to the SMBH event horizon . The optical/UV photons emitted in the disk are transformed into X-ray photons due to Inverse Compton scattering.

3. **Synchrotron radiation:** electromagnetic radiation produced by charged particles moving at relativistic velocities (near the speed of light) in external magnetic fields is named synchrotron radiation. The emission spectrum depends on the velocity distribution of the particles. Assuming a power law (non-thermal) distribution of the particles, the emitted spectrum is a power law with an energy index α ($F_\nu \propto \nu^{-\alpha}$). It is believed that synchrotron radiation from a population of relativistic electrons located in jets is responsible for the radio emission in radio-loud AGN. However, it is very unlikely that synchrotron radiation is an important contributor to the high energy spectra of AGN, excepting the small fraction of radio-loud AGN.

4. **Free-free emission:** a free charged particle subject to decelerated movement (e.g. due to the interaction with particles of opposite charge) emits electromagnetic radiation. Since the energy of

free particles spans a broad range, the emission has a thermal continuum distribution. This emission is named free-free radiation or bremsstrahlung ('braking radiation' in German). It is related to emission produced in hot dense ionized plasma (the electrons lose energy due trough interactions with ionized atoms). If there are metals in the plasma, intense emission lines superimposed to the continuum can be produced.

1.1.2 Spectral Energy Distribution

The broadband emission of AGN is very different from that of normal galaxies. They emit over the entire electromagnetic spectrum from radio to gamma rays (Risaliti and Elvis 2004). In particular, from hard X-rays to FIR, an AGN releases energy with almost equal power per decade of frequency (see Fig. 1.1). The main features observed in the AGN spectral energy distributions (SED) include:

- **Radio continuum:** the radio emission is only a small fraction of the total AGN output, 5-6 orders of magnitude lower than the optical continuum. Only $\sim$ 10% of AGN are strong radio emitters (RL sources). The radio emitting regions of RL AGN are powerful relativistic jets and extended lobes with kiloparsecs and even megaparsecs scales, while RQ sources show parsec-scale central radio cores. The radio spectrum is well described with a power law, indicating a non-thermal origin. The radio emission of jets is usually steeper (i.e. higher values of the power law index) than that observed in the radio cores.

- **Infrared:** AGN continua show a broad IR bump. The IR emission starts increasing at $\sim$ 1 μm (the 'NIR inflection'), peaking at $\sim$ 60 μm and rapidly decreasing at lower energies (the 'sub-millimetre break') until reaching the radio continuum. In RL sources the emission drops only $\sim$ 2 decades, while for RQ sources it is usually $\sim 5-6$ decades. The IR continuum is consistent with thermal emission of dust and molecular gas (the obscuring torus, see Sect. 1.1.3) heated by the optical/UV/X-ray radiation of the central engine (Efstathiou and Rowan-Robinson 1995; Granato et al. 2004). However the origin of the FIR/sub-millimetre (sub-mm) emission is still debated, with several authors proposing that a significant fraction of this emission could be originated in circumnuclear starburst (Elitzur et al. 2004; Schweitzer et al. 2006).

  High-resolution spectra of AGN show high-ionization forbidden emission lines (e.g. [Ne V], [O IV], [S III]) superimposed on the IR continuum (Sturm et al. 2002; Dudik et al. 2007; Dasyra et al. 2008), originated in the narrow line region (see Sect. 1.1.3).

- **Optical/UV:** a significant amount of energy is emitted in a strong, broad feature that dominates the SED at wavelengths shortward of $\sim$ 4000 Å (the 'big blue bump' - BBB) and peaks around $\sim$ 1000 Å. This feature is attributed to some kind of thermal emission in the range around $10^4 - 10^6$ K, usually the emission of a heated accretion disk surrounding a SMBH (see

Sect. 1.1.3). Superposed on the continuum the optical spectrum of AGN shows strong broad permitted emission lines and narrow forbidden and permitted emission lines.

- **X-rays:** a fundamental signature of AGN is the strong X-ray emission exhibited by these objects.

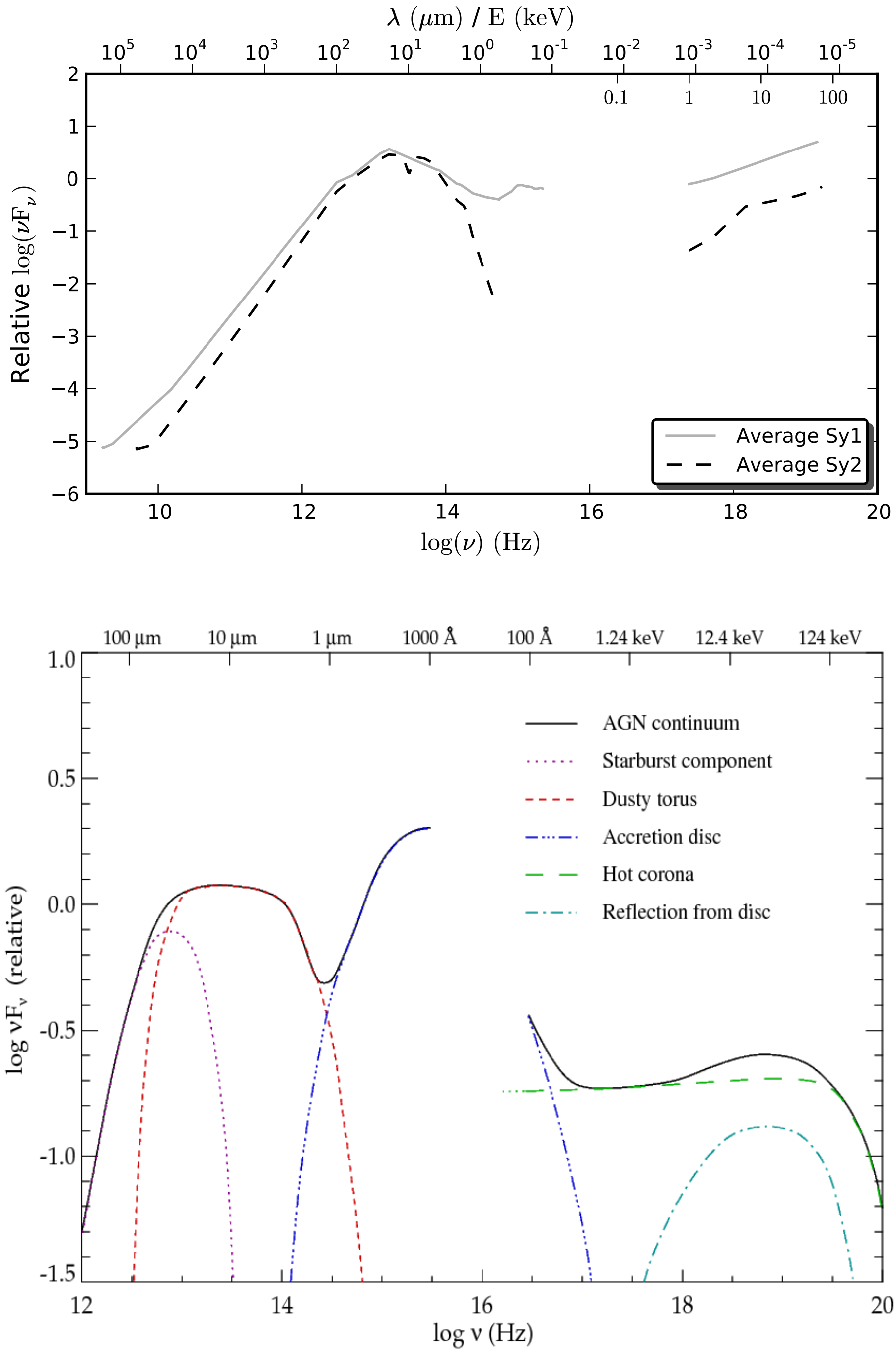

FIGURE 1.1: **Top:** Average SED of Seyfert 1 and Seyfert 2 galaxies (from Prieto et al. 2010). **Bottom:** Schematic representation of the AGN SED including a possible source for each emission components (from Manners Ph.D. thesis).

The X-ray continuum can be broadly described as a power law with a typical slope of $\sim$ 1.9 (Mateos et al. 2005a) from energies of $\sim$ 1 keV up to an eventual cut-off somewhere beyond 100 keV (see Fig. 1.2). Other significant features shown in AGN X-ray spectra are:

1. Photoelectric absorption due to neutral Hydrogen (Galactic, from material surrounding the central engine and from the host galaxy). If the hydrogen column density ($N_{\rm H}$) reaches 10^{24} cm^{-2}, all the direct X-ray emission below 10 keV is absorbed and only reflected emission from the AGN can be observed (Matt et al. 2000). Those sources showing column densities greater than that limit are named "Compton-thick" (CT), while AGN showing absorption below that limit are named "Compton-thin".
2. Soft emission (below $\sim$ 2 keV), peaking in the extreme UV, superimposed to the power law continuum (the 'soft excess') is found in $\sim$ 30% of AGN. It has been usually explained as thermal emission associated to the accretion disk, i.e. the tail of the BBB, but the origin of the soft excess is still unclear (see Chapter 3 for a more detailed discussion of this topic).
3. Emission lines at $\sim$ 6.4 – 6.7 keV are usually observed in AGN X-ray spectra with enough signal-to-noise ratio (Mushotzky et al. 1995; Nandra et al. 2007). This feature is explained as the fluorescent emission of iron (the direct X-ray emission is reflected by excitation of the inner electronic layer - Kα - of iron atoms) in the accretion disk (George and Fabian 1991; Fabian et al. 2000) and/or in the absorbing torus (Ghisellini et al. 1994).

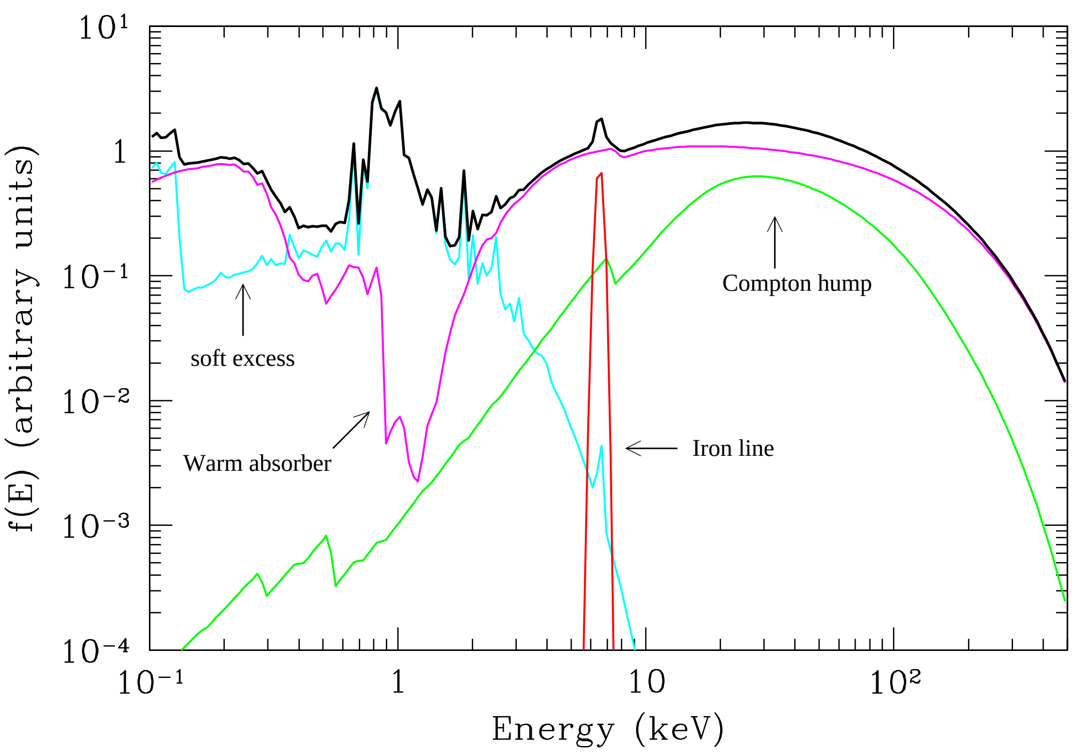

FIGURE 1.2: Schematic X-ray spectrum of an unabsorbed AGN (black solid line) along with the most relevant spectral components (from Risaliti and Elvis 2004).

4. A broad bump above the power law continuum is observed in many AGN within $\sim 7 - 60$ keV, peaking at ~ 30 keV (the 'Compton reflection hump'). This spectral feature is often explained as reflection of the direct X-ray continuum in the accretion disk or the molecular torus (Turner and Miller 2009).

1.1.3 The Unified Model

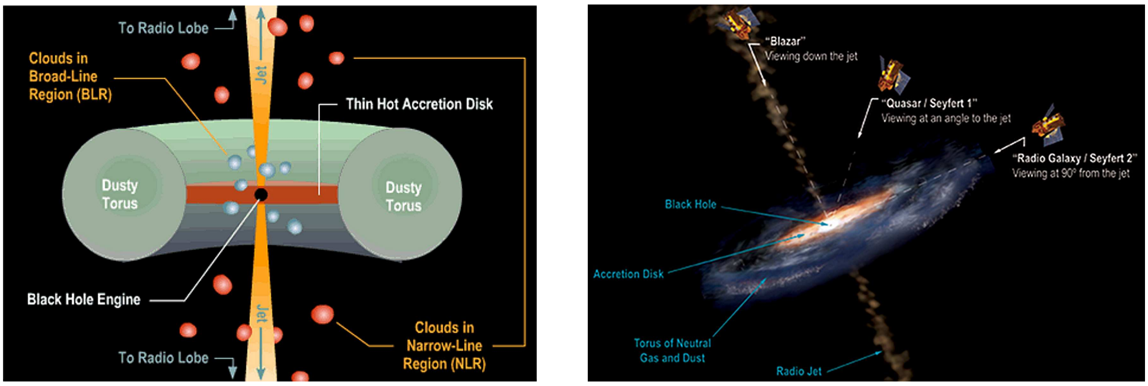

(a) Image credit: Brooks/Cole Thomson Learning.

(b) Image credit: Aurore Simonnet/Sonoma State University.

FIGURE 1.3: Conceptual schemes for unification of AGN. Left: AGN structure proposed by the unified model. Right: dependence of the AGN classification with the angle of view of the observer.

It was early pointed out that the most plausible physical process able to explain the large luminosities within such small regions observed in AGN should be the accretion of matter due to the intense gravity of a super-massive object (or objects), like black holes or neutron stars[4] It is broadly accepted that the main engine of AGN activity is the matter accretion into a SMBH with masses of $10^6 - 10^{10}\ M_\odot$.

To explain the enormous diversity of AGN, each with particular properties, Antonucci and Miller (1985) proposed the Unified Model for AGN. These authors suggested that the different characteristics observed in AGN are just dependent on the angle of view of the observer. They proposed an structure for AGN as showed in Fig. 1.3(a), with the following components:

- **Black Hole and Accretion disk:** The material surrounding the SMBH cannot fall into it radially due to its large angular momentum, thus forming an optically thick, geometrically thin accretion disk. Gravitational potential energy is converted into radiation via viscous dissipation and/or magnetic processes (Shakura and Sunyaev 1973).

- **Broad Line Region:** the broad emission lines observed in the optical/UV spectrum of some AGN (type 1) have typical widths of $\sim 5000\ \mathrm{km\,s^{-1}}$, reaching in some objects widths of $\sim$

[4]Theoretical estimates suggest that no cluster of neutrons stars or low-mass BH is stable within the small space regions and time scales where the AGN activity occurs (Miller 2006).

30 000 $\mathrm{km\,s^{-1}}$. These lines are emitted by clouds of high density gas ($\rho \gtrsim 10^9\,\mathrm{cm^{-3}}$, needed by the observed ratio between forbidden and permitted emission lines) moving at high velocity in keplerian orbits close to the SMBH (within 0.01-0.1 pc), which explain the large Doppler broadening observed.

- **Narrow Line Region:** the narrow lines observed in the optical/UV spectrum of AGN have much smaller widths, typically $\sim 100\ \mathrm{km\,s^{-1}}$. They can be explained by the emission of low-velocity gas clouds further away from the central engine (as far as $\sim$ 100 pc). These clouds have lower densities ($\rho \sim 10^3 - 10^6\,\mathrm{cm^{-3}}$) than the BLR clouds. Both BLR and NLR clouds are excited by the ionizing radiation of the accretion disk.

- **Obscuring torus:** outside the BLR, at distance scales of few parsecs, there is a region of cold gas and dust with a toroidal geometry in a similar plane as the accretion disk. The details of its structure and formation, as its dependence on other physical properties of the AGN (e.g. luminosity) are still uncertain. The torus absorbs and scatters the nuclear radiation and partially covers the central engine, blocking the BLR and the accretion disk to certain lines of sight. The dust heated by the nuclear emission is believed the responsible for the MIR/FIR continuum observed in AGN.

- **Radio Jet:** this component arises from the sub-parsec scales of the AGN and it is probably related to magnetic processes within the inner accretion disk, although a complete mechanism able to explain the formation of jets is still a challenge in modern astronomy (Narayan et al. 2010). The radio emission is due to synchrotron emission of relativistic electrons.

The dusty torus is the essential piece to explain the inclination-dependent of the observed properties. According to this model there is intrinsically only one type of AGN (type 1), but in some cases we observe the nuclear regions through an attenuating medium that hides the central engine and the BLR, and the AGN is seen as a type 2 object (see Fig. 1.3(b)). The existence of a jet of relativistic charged particles (e.g. electrons) has been proposed to take into account the bi-modality of RQ and RL AGN (Urry and Padovani 1995): those AGN with a jet emitting synchrotron radiation would be RL objects, while those with no jet would be RQ.

The Unified Model is well established for local Seyfert galaxies. A fundamental prediction of the unified models is the existence of broad emission lines behind the obscuring material, which have been detected through several techniques: spectropolarimetry observations of Sy2 AGN have revealed hidden polarized broad lines (Antonucci and Miller 1985; Tran 2001) scattered by free electrons in a “mirror” of ionized gas located just outside the opening of the torus; broad emission lines have also been observed in the NIR unpolarized spectra of optically type 2 sources (Rix et al. 1990; Ruiz et al. 1994; Goodrich et al. 1994), since the absorption is less effective in the NIR than in the optical range. X-ray observations of Seyfert 2 galaxies have shown heavy photoelectric absorption due to cold gas, likely associated with the dusty torus (Matt et al. 2003). The dust torus itself, or a similar structure, has been observed in nearby AGN (Gallimore et al. 1997; Jaffe et al. 2004; Capetti et al. 2005).

This unification scheme offers a simple explanation for the diversity observed in AGN. Over the years detailed observations have suggested indeed a more sophisticated structure for the innermost regions of AGN which account for all the AGN types seen in the sky and at different wavelengths. There are however a growing number of observational results hardly explained by these models (Lutz et al. 2004; Mateos et al. 2005a,b), suggesting a more complex extension of the Unified model (Elitzur and Shlosman 2006), or even a change of paradigm (Elvis 2000).

1.2 Starburst galaxies

A significant fraction of galaxies shows the signatures of intense ongoing star formation activity, i.e. an starburst (SB) episode. The most general definition of a SB galaxy is one whose luminosity is dominated by an episode of star formation which cannot be sustained over its life-time, i.e. continued star formation with the current star formation rate (SFR) would exhaust the available gas reservoir in much less than the dynamical time-scale of the galaxy (perhaps one rotation period in a disk type galaxy). See Moorwood (1996) for a complete review on starburst galaxies.

Bursts of massive star formation were first invoked in the mid 1970s to explain the unexpected discovery of galaxies whose IR luminosities and optical-to-IR ratios appeared too high to be sustained over their life-times (Harwit and Pacini 1975; Rieke and Low 1975; Rieke and Lebofsky 1979). There are several astronomical sources where violent, episodic star formation has been observed, like the blue compact dwarf galaxies (Zwicky 1965; Binggeli and Cameron 1991; Hunter et al. 2010), the Wolf-Rayet galaxies (Conti 1991; López-Sánchez and Esteban 2008, 2009) or the luminous and ultraluminous infrared galaxies (see Sect. 1.3).

1.2.1 Spectral Energy Distribution

Figure 1.4(a) shows the average SED of SB galaxies dominated by young and old stellar populations (Schmitt et al. 1997). The emission of SB galaxies is primarily characterized by a prominent IR bump peaking around 60-100 μm. The optical/UV/X-ray emission is much lower than that observed in type 1 AGN (see Fig. 1.1), although the difference between SB and type 2 AGN emission is relatively small.

- **Radio:** radio emission is only a small part of the bolometric output from SB galaxies. It is explained as a combination of free-free continuum from HII regions (i.e. regions of atomic hydrogen ionized by the UV radiation field emitted by hot young stars) and synchrotron radiation from supernova generated electrons interacting with the interstellar magnetic field. Only young

SB in HII regions like dwarf galaxies are dominated by free-free emission. In spiral galaxies the radio emission is modelled as a power law with index ~ -0.7.

- **Infrared:** the broad IR bump is reprocessed emission from dust heated mainly by hot massive stars formed in the SB. Characteristic temperatures are around 45 K, but the bump is broader than a single black-body due to the presence of different components including cold dust associated

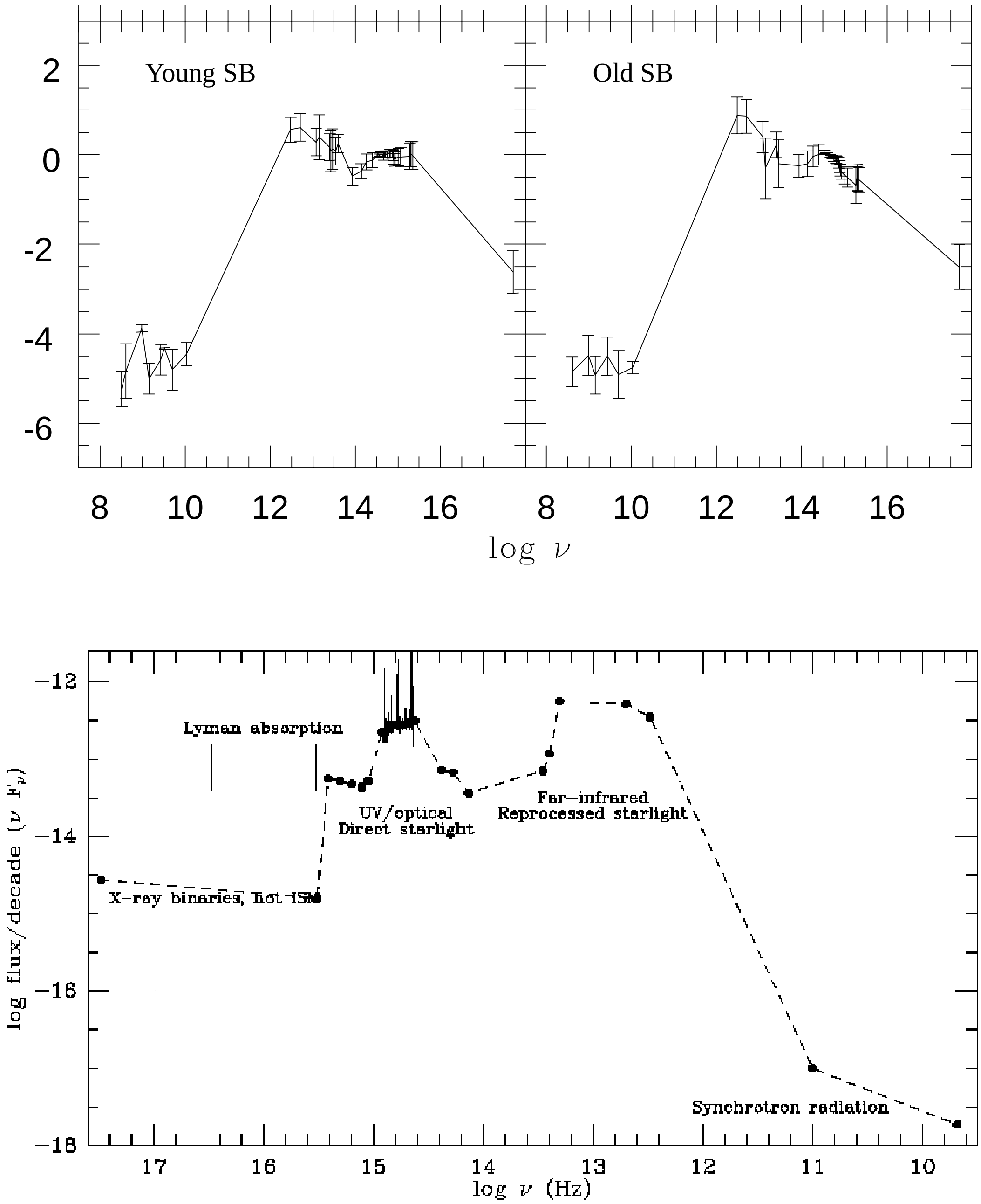

FIGURE 1.4: **Top:** Average SB SED dominated by old (right panel) and young (left panel) stellar population (from Schmitt et al. 1997). **Bottom:** SED of NGC 7714, a typical young SB, including a possible source for each emission components (data from NED).

with molecular clouds, dust heated by the interstellar radiation field and dust in and around HII regions heated by stellar UV photons. SB IR spectra show broad dust (silicates and polycyclic aromatic hydrocarbons - PAH) absorption and emission features, along with strong emission lines (Laurent et al. 2000).

- **Optical/UV:** The optical emission is dominated by starlight of the host galaxy, while the UV radiation is emitted by young hot stars formed in the burst. Most of the UV emission is absorbed by the large amounts of dust and gas in the star-forming regions and re-emitted in the IR range. Superimposed to this continuum, the optical/UV spectrum of SB galaxies show narrow strong forbidden and permitted emission lines emitted by excited gas in HII regions. Optical line ratios diagrams, e.g. [OIII]5007Å/H_β versus [NII]6583Å/H_α are the most common tool to distinguish between SB and AGN (Osterbrock 1989).

- **X-rays:** The high energy emission of SB exhibits a rough power law spectrum with a mean photon index of $\sim$ 1.5 between $\sim$ 0.5 – 100 keV. It contains contribution from massive X-ray binaries, supernova remnants, starburst-driven winds and inverse Compton scattering of FIR photons by relativistic electrons. The soft X-ray spectrum can be modelled as thermal (black-body) emission with temperature $\sim$ 0.5 keV (Rephaeli et al. 1995; Persic and Rephaeli 2002; Persic et al. 2004).

It has been established, as a first approach, that the overall properties of star-forming galaxies are dependent on two parameters: age and luminosity. Thus, the SED can be modelled with templates that vary primarily with luminosity (Devriendt et al. 1999; Chary and Elbaz 2001; Dale and Helou 2002), and stellar population synthesis models demonstrate how the characteristics of the galaxy evolve with the age of the dominant star-forming episode (Engelbracht et al. 1998; Kewley et al. 2001; Asari et al. 2007). With the improvements in sensitivity and sophistication of MIR and FIR instrumentation it has become apparent that metallicity constitutes a third critical parameter influencing the overall properties of SB galaxies (Asari et al. 2007; Engelbracht et al. 2008).

1.2.2 Starburst models

A pre-requisite for star formation is the existence of giant molecular clouds which may form from the agglomeration of small clouds or through magnetic, thermal or gravitational instabilities. Stars form in such clouds, either spontaneously due to further gravitational instabilities and/or via a collapse induced by cloud-cloud collisions, supernova explosions or radiation and wind pressure from pre-existing star clusters (cf. McKee and Ostriker 2007 for a complete review about the current theory of star formation).

In 'normal' spiral galaxies the star formation is induced in the spiral arms through density waves which compress the interstellar matter passing through them (Vogel et al. 1988; Kim et al. 2008). However this mechanism is slow at converting gas into stars (few Gigayears, i.e. several rotation periods in an spiral galaxy) and inefficient: the ionizing radiation and supernovae destroy the molecular clouds thus providing a negative feedback to the process (Larson 1987; Williams and McKee 1997; Krumholz et al. 2006; Price and Bate 2009). In contrast, SB in central regions convert gas more efficiently into star and are of transient nature. They are associated with large concentrations of gas with high critical densities for star formation and hence high star formation rates. It seems that in most occasions this gas is generally captured during interactions and mergers (Whitmore et al. 1999; Lambas et al. 2003; Woods et al. 2006; Overzier et al. 2008), although merger-driven starburst seem to be less important at high redshift (Daddi et al. 2007; Shapiro et al. 2008), favouring other mechanisms like the fragmentation of gas-rich disks, or the presence of large gas reservoirs (Daddi et al. 2008).

In circumnuclear SB the gas driven in should form a disk in the central kpc region (Barnes 2002) whose mass could be a significant fraction of the dynamical mass. This large amount of gas ($\gtrsim 10^9$ $M_\odot$) can collapse further due to gravitational instability, cloud-cloud collisions and dynamical friction (Shlosman et al. 1990; Immeli et al. 2004). Clouds are supported by turbulent motions and shrink as the turbulence dissipates. Star formation begins once a critical density is reached and turbulent energy can be replenished by supernovae explosions. The resulting gas densities are higher than those in the galactic disk by factors of $\sim$ 1000 due to the large tidal and Coriolis forces. When star formation starts, therefore, it does so rapidly and with SFR $\sim 10^6$ times larger and gas consumptions times $\sim$ 100 times shorter than in the disk (Elmegreen 1994; Mihos and Hernquist 1996; Elmegreen 2004).

The later evolution of the burst depends on a number of parameters (Mihos and Hernquist 1996; Di Matteo et al. 2008) including the structure of the progenitor galaxies, the ratio of dissipation time to massive star lifetime and the gravitational potential. A low gravitational potential may result in repetitive SB or expulsion of gas from the core. A high gravitational potential leads to a continually increasing density and the formation of compact objects in which stellar collisions may result in a super-massive star cluster or in stars which finally collapse into black holes (Loose et al. 1982; Barnes and Hernquist 1991).

1.3 Infrared Galaxies

In 1983 the Infrared Astronomical Satellite (*IRAS*) was launched, the first space telescope to perform a survey of the entire sky in the infrared waveband. One of the most important results from the mid- and far-infrared all sky surveys carried out by this mission was the detection of a new class of galaxy where the bulk of the bolometric emission lies in the infrared range (Soifer et al. 1984). This population, named ”Luminous Infrared Galaxies” (LIRG), becomes the dominant extragalactic population at IR luminosities above $10^{11} L_\odot$, with a space density higher than all other classes of galaxies of comparable bolometric luminosity (see Sanders and Mirabel 1996, for a complete review of these objects). At the brightest end of this population distribution lie ultraluminous and hyperluminous infrared galaxies.

1.3.1 Ultraluminous Infrared Galaxies

Ultraluminous Infrared Galaxies (ULIRG) are a class of galaxies with IR luminosity $L_{\rm IR} \geq 10^{12}\ L_{\odot}$, dominated by the emission in the infrared (IR) waveband. They are, together with optical quasars, the most luminous objects in the local Universe. See Lonsdale et al. (2006a) for a complete review of these objects.

A few luminous galaxies with IR emission comparable to their optical output were discovered by the pioneers of IR astronomy (Low and Kleinmann 1968; Kleinmann and Low 1970; Rieke and Low 1972; Rieke and Lebofsky 1979), but it was thanks to the *IRAS* surveys that the first ULIRG came to light: nine *IRAS* sources invisible or extremely faint on the Palomar Sky Survey plates, and exhibiting IR-to-optical luminosity ratios ratios over 50 (Houck et al. 1985).

Since then, larger samples of ULIRG have been discovered. The Revised Bright Galaxy Sample (RBGS; 625 IRAS galaxies brighter than 5.24 mJy at 60 μm- Sanders et al. 2003) contains 20 ULIRG, and the complete flux-limited IRAS 1 Jy sample (Kim and Sanders 1998) contains 118 ULIRG drawn from the IRAS Faint Source Catalog (FSC, Moshir et al. 1990). See Sanders and Mirabel (1996) for a complete review of the IRAS legacy on ULIRG. The new generation of IR observatories like *Spitzer* and AKARI have dramatically increased the number of known ULIRG (Serjeant et al. 2004; Matsuhara et al. 2006).

The mechanism which powers these objects has been discussed since their discovery. All the diagnostic studies concerning ULIRG have to deal with the great opacity of their nuclear regions, that precludes a straight identification of the hidden power source. The compactness of the IR-emitting regions in luminous IR galaxies (cf. Condon et al. 1991) suggests two possible origins for the observed high ULIRG luminosities: compact nuclear SB (see Sect. 1.2) and/or highly obscured AGN activity (see Sect. 1.1). Over the last decade comprehensive observations from X-rays through radio band have produced a consistent paradigm for local ULIRG, showing that they are mergers between gas rich dusty galaxies, where the interaction triggers a sort of combination of dust-enshrouded SB and AGN. The emphasis has now shifted to the determination of the dominant radiative mechanism and to the understanding of the relationship between co-existing AGN and SB emission, being whether evolutionary (one evolves into the other) or causal (one triggers the other somehow) or coincidental (a third element triggers both phenomena).

The early, ground-based, optical/NIR imaging studies of ULIRG revealed that $\sim 70\% - 90\%$ were interacting systems, with morphologies expected from the collision of two disk galaxies (Armus et al. 1987; Leech et al. 1994; Clements et al. 1996; Murphy et al. 1996). Observations from the Hubble Space Telescope (HST) offered enhanced angular resolution and sensitivity. All studies carried-out with this telescope are consistent with all local ULIRG showing signs of interactions and mergers (Surace et al. 1998; Farrah et al. 2001; Bushouse et al. 2002). The largest imaging study of ULIRG

(Veilleux et al. 2002), based on ground observations of the IRAS 1 Jy sample, is also consistent with these results.

Mergers provide a plausible trigger to the huge IR luminosities of ULIRG. These events provide the large amount of gas and dust needed to fuel and enshroud the power sources in ULIRG (irrespective of whether they are SB, AGN, or both), and it is channelled into a small volume, most plausibly sited in the nucleus of the resulting host galaxy.

The global view offered by multi-wavelength observations of local ULIRG obtained in the last decades suggest that, at lower luminosities at least, they are dominated by SB emission. The majority of ULIRG have optical and NIR spectra reminiscent of SB (Veilleux et al. 1999), but with a systematic increase of Seyfert (1 or 2) optical spectra with increasing IR luminosity, reaching $\sim$ 50% at $L_{\rm IR} > 10^{12.3}\ L_\odot$ (Veilleux et al. 2002). However most ULIRG with Seyfert spectra also show evidence for ongoing or recent star formation.

The modelling of the IR spectral energy distributions (SED) of ULIRG offers a consistent view. The study of a sample of 41 local ULIRG (where only $\sim$ 10% have $L_{\rm IR} > 10^{12.3}\ L_\odot$) showed that all of them seem to contain a luminous SB, whereas approximately half contain a luminous AGN. The mean SB fraction is $\sim$ 80%, and in $\sim$ 90% the SB produces more than half of the total IR emission. The fraction of purely AGN-powered ULIRG in the local Universe is less than 2% (Farrah et al. 2003).

The analysis through emission lines diagnostic techniques (Sturm et al. 2002) of high resolution mid-infrared (MIR) spectra shows again that the infrared emission from most ULIRG is powered mostly by star formation, with only $\sim$ 20% of ULIRG hosting an AGN with an IR luminosity greater than that of the SB, but in $\sim$ 40% of ULIRG the AGN contribution in the MIR is significant (Farrah et al. 2007).

When a larger number of luminous ULIRG (those with $L_{\rm IR} > 10^{12.3}\ L_\odot$) are present in the analysed samples, and more sensitive techniques to AGN emission are applied, the fraction of ULIRG harbouring an AGN rises. The study of the continuum of low resolution MIR spectra of larger samples of ULIRG (where more than half ULIRG have $L_{\rm IR} > 10^{12.3}\ L_\odot$) found signatures of AGN activity in $\sim$ 70% of ULIRG, but the main fraction of ULIRG luminosity is confirmed to arise from star formation events (Nardini et al. 2008, 2009). The average AGN contribution to the total IR luminosity is non-negligible ($\sim$ 20 – 30%) and again is shown to increase with luminosity (Nardini et al. 2009, 2010).

Radio observations of neutral molecular gas, principally through CO (Downes and Solomon 1998; Bryant and Scoville 1999), HCN (Gao and Solomon 2004) and OH masers (Baan et al. 1989; Darling and Giovanelli 2002) emission demonstrated that ULIRG exhibit compact nuclear reservoirs of high-density gas, with mass estimates of order $10^9 - 10^{10}\ M_\odot$ in HI and H_2. These results are consistent with the interpretation that star formation accounts for a substantial fraction of the FIR luminosity in Luminous IR Galaxies.

X-ray observations are also important not only because of the diagnostic ability of the X-ray to discriminate between AGN and SB emission (Rieke 1988), but also because models of the X-ray background (XRB) require substantial populations of highly-obscured AGN at redshifts $\sim 0.5 - 1.5$, to reproduce the observed XRB spectrum (Ueda et al. 2003; Gilli 2004; Gilli et al. 2007).

ULIRG are generally under-luminous in X-rays compared to classical AGN (Rieke 1988; Boller et al. 1998), requiring sensitive, high energy, observations to detect them. Recent ULIRG X-Ray surveys with XMM-*Newton* (Franceschini et al. 2003), *Chandra* (Ptak et al. 2003; Teng et al. 2005) and Suzaku (Teng et al. 2009) obtained X-ray luminosities typically of $L_{2-10\ \mathrm{keV}} < 10^{42} - 10^{43}$ erg s^{-1}. These luminosities represent $< 1\%$ of the IR luminosities in these systems, confirming that ULIRG are much less luminous in X-rays than classical AGN. The soft X-ray emission from all systems is dominated by extended, thermal emission with $kT \sim 0.7$ keV associated with a SB origin, while the hard X-ray emission is consistent with heavily absorbed AGN emission (Franceschini et al. 2003; Teng et al. 2009). The observed high X-ray obscuring columns could explain the observed low flux levels. X-ray data seem to be consistent with the vision of ULIRG as composite sources where the SB activity is dominant.

LIRG and ULIRG are rare in the local Universe (Soifer et al. 1987). They account only for $\sim 6\%$ to the total IR luminous energy density, and about $\sim 3\%$ of the total bolometric energy density (Soifer and Neugebauer 1991). However large numbers of ULIRG are detected in deep-IR surveys, and are a fundamental constituent of the high redshift galaxy population (Smail et al. 1997; Genzel and Cesarsky 2000; Franceschini et al. 2001). It has been proposed that ULIRG at high redshift could be at the origin of present day massive elliptical and S0 galaxies (Franceschini et al. 1994; Lilly et al. 1999; Genzel and Cesarsky 2000). A large fraction of stars in present day galaxies would have been formed during these evolutionary phases.

As mentioned above, the debate about ULIRG is now more focused on the connection between AGN and SB. Evolutionary schemes of all kinds and implications have been proposed, and extensive studies comparing AGN and SB population have been carried out. We outline here only a few key points.

One popular scenario is an evolutionary sequence in which a major gas-rich galaxy merger first results in a massive cool SB-dominated ULIRG, followed by a warm ULIRG phase as a QSO turns on inside the dust cocoon and heats the surrounding dust, and then finally the QSO emerges in an optically bright phase when it blows away the surrounding dust cocoon, and the resulting stellar system resembles a spheroid (Sanders et al. 1988; Kormendy and Sanders 1992; Joseph 1999; Fabian and Iwasawa 1999; Lípari et al. 2003).

The evolutionary scenarios have received a boost from several works performing high resolution hydrodynamic simulations of major gas-rich mergers (Di Matteo et al. 2005; Hopkins et al. 2005; Springel and Hernquist 2005) motivated by linking the growth of spheroid masses and SMBH masses in order to explain the observed correlations between SMBH mass and bulge mass or velocity dispersion of local spheroids (see Sect. 1.4). Accretion rates are predicted to be highest at late merger stages, when the SMBH grows exponentially, followed by the most luminous optically-visible QSO phase when the active QSO essentially explosively drives out all remaining material in the system (Hopkins et al. 2005). The period of high obscuration during the high accretion rate phase would correspond to an obscured QSO phase, i.e. an AGN-powered ULIRG. Starburst events occur earlier in the lifetime of the merger when gas is still plentiful, and a SB-ULIRG phase could occur when the gas is centrally concentrated into a dense compact region at relatively late stages.

There are several works lending support to this evolutionary sequence (Canalizo and Stockton 2001; Masegosa and Márquez 2003; Stevens et al. 2005; Schweitzer et al. 2006; Netzer et al. 2007), but further studies are needed to obtain a full understanding of the interplay between AGN and SB and how it affects the co-evolution of SMBH and galaxy formation (see Sect. 1.4). The study of objects at higher luminosities than ULIRG may add new insights on this subject.

1.3.2 Hyperluminous Infrared Galaxies

Hyperluminous Infrared Galaxies (HLIRG, Rowan-Robinson 2000) are defined as those infrared galaxies with $L_{\rm IR} \geq 10^{13}\ L_{\odot}$. The first object of this family was discovered by Kleinmann et al. (1988) when the IR source IRAS 09104+4109 was identified with a z = 0.44 galaxy, implying a total far infrared (FIR) luminosity of $1.5 \times 10^{13}\ L_{\odot}$, a factor 3 higher than any other ultraluminous galaxy seen to that date.

The programme carried out to identify IRAS FSC sources (Rowan-Robinson et al. 1991) lead to the discovery of seven new objects with IR luminosities comparable to that observed in IRAS 09104+4109 (McMahon et al. 1999). This discovery brought to our knowledge an entirely new class of infrared galaxies. Subsequent IR surveys and follow-up programs increased the number of known HLIRG (Cutri et al. 1994; Dey and van Breugel 1995; Wilman et al. 1998; Irwin et al. 1998).

As in the case of ULIRG, the dichotomy between AGN and SB has been claimed to explain the emission mechanism of these objects. However the ULIRG paradigm described above is not so well-grounded for these more luminous objects. Only a third of these sources has been found in interacting systems (Farrah et al. 2002b), therefore in most HLIRG mergers cannot be the trigger of the powerful AGN and star formation activity needed to explain the observed luminosities. Rowan-Robinson (2000) suggested that HLIRG could be, instead of a high-luminosity version of ULIRG, primeval or very young galaxies. He argues that if the rest-frame FIR and sub-mm emission from HLIRG is due to star formation, then the star formation rates would be the highest for any objects in the Universe. This would strongly suggest that these galaxies are going through their maximal star formation periods, implying that they are galaxies in the first stages of formation. An alternative possibility is that the IR emission arises via some other mechanism (e.g. a transient IR luminous phase in QSO evolution not triggered by interactions), HLIRG would then be an entirely different class of objects.

The relative contribution of both components (AGN and SB) to the bolometric luminosity of HLIRG is still in debate. Previous studies of small samples of HLIRG showed contradictory results, with some authors suggesting that their IR emission arises predominantly from a SB (Frayer et al. 1998, 1999) with SFR of the order 1000 $M_{\odot}\mathrm{yr}^{-1}$, while other authors suggested that HLIRG are powered by dusty AGN (Granato et al. 1996; Evans et al. 1998; Yun and Scoville 1998). The analysis of the IR SED of large samples of HLIRG reveals that about half of these sources are AGN dominated (Rowan-Robinson 2000; Verma et al. 2002). These results were however based on samples biased toward AGN.

Farrah et al. (2002a) built a sample of HLIRG unbiased toward AGN and they obtained sub-mm data of these objects, introducing tight constraints on SB luminosity contribution in the IR SED analysis. They found most HLIRG being AGN dominated, but with a significant contribution due to star formation in all objects ($\gtrsim$ 20%).

Observations of individual HLIRG with *Chandra* and XMM-*Newton* show that the IR emission of these objects could be powered by buried quasars through dust re-radiation. The nuclear source is heavily obscured, reaching the CT limit (Iwasawa et al. 2001; Wilman et al. 2003; Iwasawa et al. 2005). It has also been suggested that a galaxy merger in an over-density region may be a necessary condition for the formation of this class of sources (Iwasawa et al. 2005). However this suggestion is in contradiction with the significant fraction of isolated HLIRG found by Farrah et al. (2002b).

Both SB and AGN activity seem to be therefore important to understand the properties of these objects. Moreover, as HLIRG could represent the most vigorous stage of galaxy formation, with SFR $>$ 1000 $M_{\odot}\mathrm{yr}^{-1}$ in several objects, they are unique laboratories to investigate extremely high stellar formation, and its connection to SMBH growth. Like ULIRG, HLIRG could be key objects to understand the co-evolution between SMBH and galaxies.

1.4 Co-evolution of galaxy formation and SMBH growth

During the last decade a growing number of observations have revealed tight links and feedback loops between the evolution of galaxies and the growth of SMBHs at their centres. In the local Universe, most galaxy bulges host a SMBH (Magorrian et al. 1998; Kormendy and Gebhardt 2001; Ferrarese and Ford 2005), and studies of their dynamical influence on the surrounding stars and gas have led to the discovery of tight correlations between the SMBH mass and the bulge mass and stellar velocity dispersion (Gebhardt et al. 2000; McLure and Dunlop 2002; Häring and Rix 2004).

Extensive programs of optical and NIR follow-up observations of X-ray selected AGN in the *Chandra* and XMM-*Newton* era put on solid ground the evolution of the AGN luminosity function (Ueda et al. 2003; Hasinger et al. 2005; Ebrero et al. 2009), which traces the growth of SMBHs during active accretion phases, over a significant fraction of cosmic time. This evolution matches the mass function of SMBHs in the local Universe (Yu and Tremaine 2002; Shankar et al. 2004; Marconi et al. 2006),

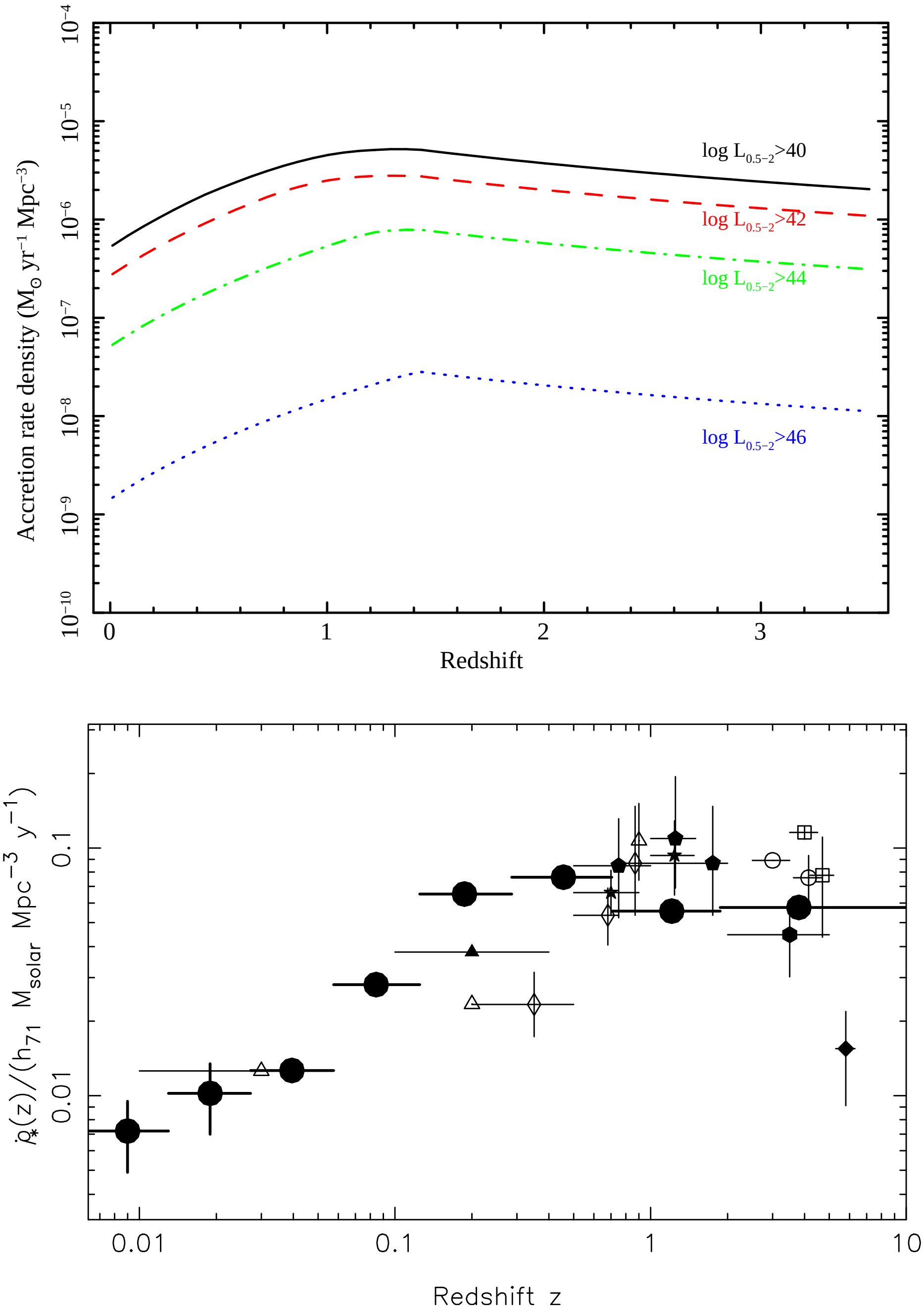

FIGURE 1.5: **Top:** Accretion rate density of AGN calculated through the X-ray luminosity function (from Ebrero et al. 2009). **Bottom:** Star formation history (from Heavens et al. 2004). SFR estimates from: SDSS (large filled circles), Hα (open triangles), UV from Subaru (open squares), GOODS (filled diamond), HST (open circles), CFRS (open diamonds), HDF (filled pentagons), galaxies (stars), galaxies (filled triangle), sub-mm galaxies (filled galaxies).

suggesting that most galaxies in the Universe went through an AGN phase. Furthermore, lower luminosity/lower mass AGN peak at a lower redshift than luminous QSO. Such an “anti-hierarchical” behaviour is analogous to that observed for star formation (Calzetti 1997; Connolly et al. 1997; Dickinson et al. 2003b; Heavens et al. 2004), usually referred to as "cosmic downsizing". The peak activity of luminous QSO occurs at $z \sim 2$, where large galaxies were also forming most of their stars (see Fig. 1.5), while moderately luminous AGN are more common at the current epoch, where stars are forming in smaller galaxies, lending further support to the idea that the formation and evolution of SMBHs and their host galaxies might be closely related.

While the SMBH/galaxy co-evolution is now an accepted scenario, the details of this joint evolution are not yet fully understood. In particular, the downsizing behaviour is in contradiction with the cosmological models based on a Universe dominated by dark energy and cold dark matter (Λ-CDM models). The latter models are in good agreement with state-of-the-art observations of Type Ia supernovae, the cosmic microwave background and cluster of galaxies evolution (Spergel et al. 2003; Komatsu et al. 2009). However they predict a "hierarchical" formation of galaxies, where low-mass objects are formed first (Springel et al. 2005). This contradiction could be because feedback mechanisms due to star formation and accretion onto SMBH and their interplay, are not yet properly treated in these models (Fontanot et al. 2009).

The study of objects where violent episodic star formation (starburst) and AGN activity are both present (e.g. ULIRG and HLIRG, see Sect. 1.3) offers an excellent opportunity to obtain a better understanding of these processes. AGN and star formation processes occurs in environments enshrouded by large amounts of gas and dust (see Sects. 1.1 and 1.2). X-ray and IR observations offer the needed penetrating power to study these phenomena. While X-rays provide a largely uncontaminated view of the primary AGN emission, measures of infrared emission yield detailed information about the levels of dust and on-going star-formation surrounding AGN.

Infrared and X-ray observations are therefore essential to understand the phenomena of star formation and AGN. Fortunately, nowadays powerful tools are available to observe the Universe in both energy ranges, i.e. *Chandra*, XMM-*Newton*, *Spitzer*, AKARI or *Suzaku*. Different strategies can be employed to investigate the IR/X-ray synergy on the study of the AGN-galaxy co-evolution, e.g. by multi-wavelength surveys like GOODS, AEGIS or COSMOS (Dickinson et al. 2003a; Davis et al. 2007; Scoville et al. 2007), or by targeted MIR observations of peculiar X-ray sources like X-ray absorbed broad line QSO (Stevens et al. 2005; Page et al. 2007), by targeted X-ray observations of MIR/FIR-emitting objects like ULIRG (Franceschini et al. 2003; Teng et al. 2005) and HLIRG (Wilman et al. 1998).

The *Wilkinson Microwave Anisotropy Probe* (*WMAP*) concordance cosmology has been adopted to calculate luminosities throughout this thesis: $H_0 = 70\,\mathrm{km\,s^{-1}\,Mpc^{-1}}, \Omega_m = 0.27, \Omega_\Lambda = 0.73$ (Komatsu et al. 2009).

1.5 Aims of this thesis

As discussed above, the nature of HLIRG is a highly debated subject. In particular, the emission mechanisms active in these sources and their trigger are still unclear, together with the understanding of the AGN and SB contribution to the overall emission, as well as their interplay.

The main objective of this thesis is to draw a comprehensive and consistent picture on HLIRG derived from multi-wavelength observations. Thanks to the unprecedented capabilities of state-of-the-art observatories we are able to characterize the properties of HLIRG in several wavelength ranges. We will perform our HLIRG study in two complementary energy bands, X-ray and MIR, and we will also study their broadband SED from radio to X-rays.

The comparison of X-ray and IR properties of HLIRG and ULIRG, as well as their broadband SED, allows determining if these objects are truly two different populations. Moreover, through the study of a large sample of HLIRG we can also ascertain whether all HLIRG share common properties or they could be divided in different “flavours”.

In addition, we can apply different techniques to detect the signatures of AGN and SB emission at several wavelengths and estimate the contribution of these processes to the bolometric output. Our multi-wavelength approach can provide more conclusive evidence on which is the dominant mechanism with respect to any other previous study restricted to a particular energy range.

Thanks to the penetrating power of X-ray and MIR observations, AGN activity can be detected even in heavily enshrouded environments. Applying standard bolometric corrections is possible to estimate the AGN bolometric luminosity and its relative contribution to the total output. Furthermore, by constructing the individual SED, we can test if the bolometric corrections hold in these extremely luminous sources.

X-rays and IR observations offer also a good window to study the star-formation processes going on in these objects. We can estimate SB luminosities and SFR and check to what extent they are correlated with the AGN activity, pointing or not toward a common physical link.

Summarizing, along this work we will tackle the following issues:

1. Characterize the properties of HLIRG in several energy ranges and study them from a global, coherent point of view.
2. Disentangle the AGN and SB emission in HLIRG using different, complementary techniques and estimate the relative contribution of each component to the total output.
3. Test if AGN and SB luminosities are in some way related along cosmic time.
4. Estimate the SFR of these objects through different proxies, checking if it is as extreme as has been found by previous studies.

5. Study the column density of neutral Hydrogen and the dust covering factor (the fraction of sky covered by dust as seen from the nucleus) of HLIRG, which can offer some clues on the gas and dust distribution of these objects.

6. Reproduce the broadband emission of HLIRG combining simple models of AGN and SB and study any dependence of this emission with several properties of HLIRG like obscuration or bolometric luminosity.

7. Check if HLIRG are a unique population or can be separated in several groups and, in that case, explain the physical origin of that division.

Chapter 2

HLIRG samples

Throughout this chapter we describe different samples of known HLIRG (Sects. 2.1 and 2.2). Section 2.3 explain the selection criteria we have applied to assemble the HLIRG samples that have been analysed for this thesis. In Sect. 2.4 we give a brief description of each source.

2.1 Rowan-Robinson's HLIRG Sample

The largest sample of known HLIRG was presented in Rowan-Robinson 2000, hereafter RR00. The author define as HLIRG those galaxies with rest-frame infrared (1-1000 μm) luminosities in excess of $10^{13.0} h_{65}^{-2}\ L_{\odot}$ ($10^{13.22} h_{50}^{-2}\ L_{\odot}$). Forty-five sources selected from different catalogs are included in the RR00 sample, which can be divided, accordingly to the original selection criteria, in four sub-samples:

1. Objects found from direct optical follow-up of unbiased surveys at far infrared or sub-mm wavelengths, such as the IRAS point source catalogue survey (Saunders et al. 1995), the 850 μm SCUBA surveys or the follow-up of IRAS faint source survey (McMahon et al. 1999). A total of thirteen HLIRG were identified through these methods.

2. Sources found from cross-correlation of known quasar (PG quasars, Sanders et al. 1989) and radio galaxy (Texas radio survey, Dey and van Breugel 1995) lists with 60 μm catalogues, or using warm IR colour selection (Cutri et al. 1994; Wilman et al. 1998). Twelve objects were classified as HLIRG using this technique.

3. Sources selected ad-hoc from sub-mm observations of very high redshift quasars and radio-galaxies (Omont et al. 1997; Hughes et al. 1997; McMahon et al. 1999). Fourteen HLIRG were identified through this selection.

4. Known luminous IR galaxies with $L_{\mathrm{IR}} < 10^{13.0} h_{65}^{-2}\ L_{\odot}$, but satisfying $L_{\mathrm{IR}} > 10^{13} h_{50}^{-2}\ L_{\odot}$. Six sources are included in this sub-sample.

The sub-sample 1 is a flux-limited sample, unbiased towards AGN; the sources in the sub-samples 2 and 3 have been selected in order to host an AGN, and therefore the sub-samples suffer from selection effects. Since the RR00's criterion to define a source as HLIRG is based only on its IR luminosity, we expect a certain level of "contamination" from sources having a large IR luminosity which however does not dominate the bolometric luminosity (e.g. very luminous QSO). Through the analysis of the broadband SED we will be able to distinguish "bona fide" HLIRG from other classes of sources (see Chapter 5).

From the surveys collected in sub-sample 1 the estimated number of HLIRG per square degree brighter than 200 mJy at 60 μm is 0.0027-0.0043, which would imply that there are 100-200 hyperluminous IRAS galaxies over the whole sky brighter than 200 mJy at 60 μm (RR00).

2.2 Farrah's HLIRG Sample

Farrah et al. 2002a, hereafter F02, assembled a sample of 11 HLIRG as targets for sub-mm observations with SCUBA. These objects were chosen from the RR00 sub-sample 1 described above and were selected in a manner independent of obscuration, inclination or AGN content. Given the statistical homogeneity and completeness of the parent samples, the F02 sample is therefore entirely free from AGN bias and suitable for drawing global conclusions about the HLIRG population. Table 2.1 shows the sources included in this sample.

TABLE 2.1: HLIRG in F02's sample.

Name	RA[a]	Dec[a]	z[a]	Type[b]
IRAS F00235+1024	00 26 06.7	10 41 27.6	0.58	NL
IRAS 07380-2342	07 40 09.8	-23 49 57.9	0.29	NL
IRAS F10026+4949	10 05 52.5	49 34 47.8	1.12	Sy1
IRAS F12509+3122	12 53 17.6	31 05 50.5	0.78	QSO
IRAS 13279+3401[c]	13 30 15.3	33 46 28.7	0.36	QSO
IRAS 14026+4341	14 04 38.8	43 27 07.2	0.32	Sy1
IRAS F14218+3845	14 23 55.5	38 31 51.3	1.21	QSO
IRAS F16124+3241	16 14 22.1	32 34 03.7	0.71	NL
ELAISP90 J164010+410502	16 40 10.2	41 05 22.1	1.10	QSO
IRAS 18216+6418	18 21 57.3	64 20 36.4	0.30	Sy1
IRAS F23569-0341	23 59 33.6	-03 25 12.8	0.59	NL

[a] Positions and redshifts are taken from the NASA Extragalactic Database.
[b] Spectral Type, taken from RR00 and NED. NL: Narrow Line object, Sy1: Seyfert 1 galaxy.
[c] New optical and MIR observations reject this source as HLIRG. See Sect. 2.2.1 below for details.

2.2.1 IRAS 13279+3401

The galaxy IRAS 13279+3401, included in RR00 and F02 samples, has been previously classified as a QSO (RR00), and the IR luminosity estimated through the redshift presented in the literature ($z = 0.36$, RR00) identified it as an HLIRG. However, we have now strong evidence showing that this source is a much closer galaxy.

Figure 2.1(a) shows the optical spectrum of IRAS 13279+3401 obtained by the 2.5m Isaac Newton Telescope with the Intermediate Dispersion Spectrograph instrument.[1] We did not detect any type I feature, indeed a QSO with $z = 0.36$ should present a broad H_β emission line at $\sim$ 6600 Å. We estimated a redshift $z = 0.023$ for this source with a standard galaxy template. The template was redshifted matching its stellar absorption features with those of the observed spectrum.

The MIR spectrum of this source (see Fig. 2.1(b)), obtained by the *Spitzer Space Telescope*,[2] was also analysed. We estimated the redshift of the source using a SB template from Nardini et al. (2008). We redshifted the template matching the most important spectral features and the estimate obtained is $z \sim 0.02$, which is consistent with our estimate from the optical spectrum. The IR luminosity derived with this redshift is $\sim 3 \times 10^{10}$ $L_\odot$, well below the HLIRG limit and even below LIRG luminosity.

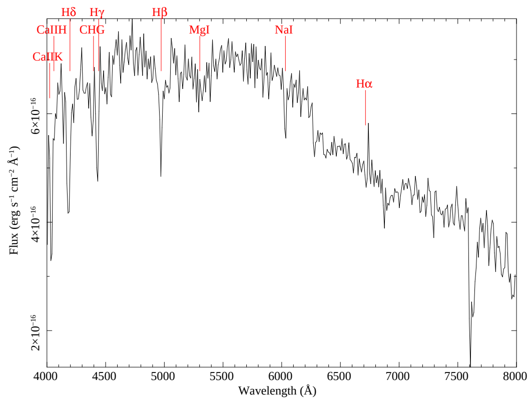

(a) Optical spectrum (2.5m INT).

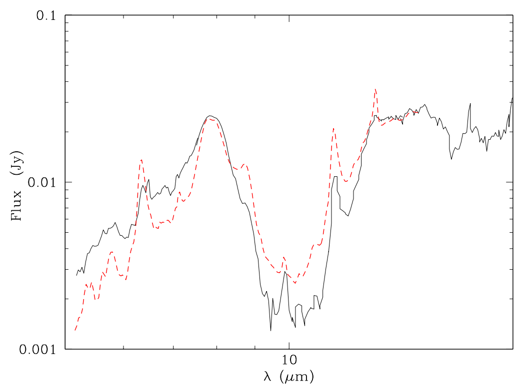

(b) MIR spectrum (*Spitzer*-IRS).

FIGURE 2.1: Optical (a) and MIR (b) spectra of IRAS 13279+3401 in the observer frame. The red slashed line in the right panel is an SB template from Nardini et al. (2008).

[1]Observation performed on 2008-03-30 during service time. The 2.5m Isaac Newton Telescope and its service programme are operated on the island of La Palma by the Isaac Newton Group in the Spanish Observatorio del Roque de los Muchachos of the Instituto de Astrofísica de Canarias.

[2]Observation performed on 2005-02-07 for programme 3746, P.I. A. Verma.

2.3 HLIRG samples assembled for this thesis

This section presents the HLIRG samples studied throughout this thesis. Each sample is composed of sources extracted from the RR00 and F02's samples and was selected fundamentally on the basis of the availability of XMM-*Newton* (Sect. 2.3.1) and *Spitzer* (Sect. 2.3.2) data.

2.3.1 XMM-*Newton* HLIRG Sample

We built this sample selecting those HLIRG from the RR00 sample with public data available in the XMM-*Newton* Science Archive (XSA), as of December 2004. We also included observations of five sources from OBS-ID 030536 by our group (see next Chapter, Table 3.1). We then constrained the resulting sample to those sources with redshift less than ~2, to prevent strong biases due to the presence of high-*z* QSO.

A total of thirteen objects compose this X-ray selected sample (see Table 2.2). There are seven sources which are included in the first RR00's sub-sample (six of them also included in the F02's sample), four sources are in the second sub-sample, one source is in the third and one is in the fourth one. Most of our sources are therefore selected from sub-samples which are in principle not biased in favour of AGN. However, selecting the sample by using the availability of XMM-*Newton* data probably introduces a selection effect in favour of the presence of bright sources in X-rays and, hence towards AGN. Moreover, estimating the completeness level of this sample is difficult, since it is not flux limited. As stated above, the estimated number of HLIRG brighter than 200 mJy at 60 μm over the whole sky is 100-200. Thirteen of them are included in this sample, which is the largest sample of HLIRG studied in X-rays.

Table 2.2 describes our sample. Column 3 shows the optical spectral classification as derived from the literature: eleven sources in our sample present AGN characteristics. Seven of them are classified as 'type 1', and four of them as 'type 2'. We have classified as QSO (instead of Seyfert) those objects with intrinsic 2-10 keV luminosity $> 10^{44}$ erg s^{-1} (see next Chapter, Table 3.3). A couple of sources have been classified from the literature as "Narrow line" (NL) sources, i.e. sources showing narrow forbidden emission lines with line flux ratios associated to HII (star-forming) regions. Previous observations suggest that all 'type 2' and one NL galaxy could present CT absorption in X-rays.

Several authors have analysed the IR SED of these HLIRG (RR00, F02, Verma et al. 2002) using radiative transfer models (RTM) to reproduce their IR emission, e.g. the standard M82-like SB model and the Arp220-like high optical depth SB model from Efstathiou et al. (2000) and the AGN dust torus model from Rowan-Robinson (1995). These studies revealed that the IR SED can be modelled by a combination of an AGN and an SB component. In Table 2.2, column 5 we report the relative contribution of the AGN and SB component to the IR luminosity needed to fit the IR SED with these models. Nine objects show an AGN-dominated IR SED (i.e. the AGN contribution is greater than 50%) and three are SB-dominated (i.e. the SB contribution is greater than 50%).

2.3.2 *Spitzer* HLIRG Sample

Nine out of ten sources in F02 sample have been observed with the Infrared Spectrograph (IRS) on board the *Spitzer Space Telescope* and the data were publicly available in the *Spitzer* Archive. However, only five sources had complementary XMM-*Newton* data and just two of these five HLIRG were detected (see Chapter 3). In order to study the relation between the X-ray and MIR emission for this kind of sources, we included four sources from the XMM-*Newton* sample that have also public IRS data.

Thirteen sources compose the *Spitzer* HLIRG sample (see Table 2.2). Accordingly to their optical spectra, six are type 1 AGN (Seyfert 1 or QSO), four are type 2 AGN (Seyfert 2 or QSO2) and three are NL objects. As presented above, the IR SED of these sources have been studied using RTM to reproduce the AGN and SB emission (RR00, F02, Verma et al. 2002). Both components (AGN and SB) are needed to model the IR emission of these HLIRG, being the AGN output dominant for most sources (see Table 2.2, column 5).

Concerning to the objects in F02's sample, six are type 1 AGN and three are optically classified as narrow-line objects. Six out of nine show an AGN-dominated IR SED, accordingly to the analysis using RTM.

2.4 Description of the sources

In this section we briefly describe the most relevant characteristics of each source included in the samples presented above, based on the observations and analyses performed previously to this thesis.

IRAS 00182-7112

Using the optical emission lines ratios from Armus et al. (1989), and the diagnostic diagram from Osterbrock (1989, chap. 12), we classified this source as a type 2 AGN. IR data from *IRAS* suggest the presence of both AGN and SB components, the former being responsible for $\sim$ 35% of the IR luminosity (RR00). New observations with *Spitzer* set this value up to $\sim$ 70%, based on the strength of the 11.2 μm PAH feature (Spoon et al. 2004a). Both *ISO* and *Spitzer* data suggest the presence of a deeply obscured nuclear power source (Tran et al. 2001; Spoon et al. 2004a). This result along with X-ray observations (Nandra and Iwasawa 2007) points towards this source as a CT source.

Table 2.2: HLIRG studied in this thesis.

Source	Sample [a]			Type [b]	CT	IR-Model [c]		RA	DEC	z	$\log L_{\mathrm{FIR}}$ [d]
	X	S	F			AGN / SB					[erg s^{-1} cm^{-2}]
IRAS 00182-7112	✓	✓	-	QSO 2	✓	0.35 / **0.65**	RR00	00 20 34.7	-70 55 27	0.327	46.49
IRAS F00235+1024	✓*	✓	✓	NL	✓	0.5 / 0.5	F02	00 26 06.5	+10 41 32	0.575	<46.76
IRAS 07380-2342	✓*	✓	✓	NL	-	**0.6** / 0.4	F02	07 40 09.8	-23 49 58	0.292	46.56
IRAS 09104+4109[e]	✓	✓	-	QSO 2	✓	**1** / 0	RR00	09 13 45.4	+40 56 28	0.442	<46.42
IRAS F10026+4949	-	✓	✓	Sy1	-	**0.8** / 0.2	F02	10 05 52.9	+49 34 42	1.120	<47.07
PG 1206+459	✓	-	-	QSO	-	**1** / 0	RR00	12 08 58.0	+45 40 36	1.158	47.20
PG 1247+267	✓	-	-	QSO	-	**1** / 0	RR00	12 50 05.7	+26 31 08	2.038	47.70
IRAS F12509+3122	✓	✓	✓	QSO	-	**0.6** / 0.4	F02	12 53 17.6	+31 05 50	0.780	<46.86
IRAS 12514+1027	✓	✓	-	Sy2	✓	0.4 / **0.6**	RR00	12 54 00.8	+10 11 12	0.3	46.18
IRAS 14026+4341	✓*	✓	✓	QSO 1.5[f]	-	**0.6** / 0.4	F02	14 04 38.8	+43 27 07	0.323	46.26
IRAS F14218+3845	✓	-	✓	QSO	-	0.2 / **0.8**	F02	14 23 55.0	+38 32 14	1.21	47.80
IRAS F15307+3252	✓	✓	-	QSO 2	✓	**0.7** / 0.3	V02	15 32 44.0	+32 42 47	0.926	<47.07
IRAS F16124+3241	-	✓	✓	NL	-	0.4 / **0.6**	F02	16 14 22.1	+32 34 04	0.71	<46.46
IRAS 16347+7037	✓	-	-	QSO	-	**0.8** / 0.2	F02b	16 34 28.9	+70 31 33	1.334	47.42
ELAISP90 J164010+410502	-	✓	✓	QSO[f]	-	**0.7** / 0.3	F02	16 40 10.1	+41 05 22	1.099	<46.67
IRAS 18216+6418[e]	✓	✓	✓	QSO 1.2	-	**0.6** / 0.4	F02	18 21 57.3	+64 20 36	0.297	46.49
IRAS F23569-0341	-	✓	✓	NL	-	0.05 / **0.95**	RR00	23 59 33.6	-03 25 13	0.59	<45.79

[a] X: sources from the XMM-*Newton* sample. Asterisk marks those sources observed but not detected with XMM-*Newton*; S: sources from the *Spitzer* sample; F: sources from the F02's sample;

[b] NL: narrow-line objects; Sy2: Seyfert 2 galaxy. Compton-thick candidates are labelled as CT. Spectral classification from Rowan-Robinson (2000), except IRAS F00235+1024 (Verma et al. 2002), IRAS 14026+4321 (Wang et al. 2006) and IRAS 18216+6418 (Véron-Cetty and Véron 2006). IRAS 00182-7112 has been classified as type 2 source using the optical emission lines from Armus et al. (1989) and the diagnostic diagrams from Osterbrock (1989, chap. 12).

[c] Fraction of the IR emission originating in AGN and/or SB. Data from: (RR00) Rowan-Robinson 2000, (F02) Farrah et al. 2002a, (V02) Verma et al. 2002, (F02b) Farrah et al. 2002b.

[d] FIR luminosity calculated through IRAS fluxes as in Sanders and Mirabel (1996).

[e] Source in cluster.

[f] Not detected in X-rays. We use the optical data to classify this source as QSO.

IRAS F00235+1024

This galaxy is optically classified as a NL galaxy (Verma et al. 2002). HST images reveal an object that is clearly strongly interacting (Farrah et al. 2002b). Its IR emission cannot be modelled solely by a pure SB or a pure AGN model (Verma et al. 2002). Sub-mm observations with SCUBA suggest a comparable contribution ($\sim$ 50%) of the AGN and SB components to the bolometric luminosity. The modelling of its IR emission suggested strong obscuration which could arise from viewing an AGN dust torus almost edge-on, through intervening absorption by cooler dust (F02). Moreover, XMM-*Newton* observations suggest CT absorption for this object (Wilman et al. 2003).

IRAS 07380-2342

This galaxy is a NL object. Its IR emission can be reproduced by a combination of SB and AGN models, with the AGN component providing $\sim$ 60% of the total IR luminosity. The SB component is dominant at wavelengths > 45 μm (F02).

IRAS 09104+4109

This galaxy lies in a rich cluster of galaxies (Kleinmann et al. 1988) and is radio-loud with a radio jet (Norman et al. 2002). It is considered a dust-enshrouded type 2 QSO (Tran et al. 2000; Franceschini et al. 2000) and optical spectropolarimetry has revealed hidden broad emission lines (Hines et al. 1999). There is no evidence of a SB component in its IR SED (RR00), which is consistent with the non detection of CO (Evans et al. 1998) and the absence of cold dust (Deane and Trentham 2001) in this source.

There is a controversy on the X-ray absorption levels shown by this object, which has been usually classified as a CT AGN on the basis of BeppoSAX and *Chandra* observations (Franceschini et al. 2000; Iwasawa et al. 2001). However Piconcelli et al. (2007), using XMM-*Newton* data, states that its X-ray spectrum is consistent either with a transmission model (i.e. Compton-thin absorption) or a pure reflection model (i.e. CT absorption). The estimates by Piconcelli et al. (2007) of the equivalent width of the observed Fe Kα emission line ($<$ 1 keV) seem to favour the former interpretation, although some CT AGN with equivalent widths below 1 keV have been observed before (Ueda et al. 2007, Severgnini et al. 2010, in preparation). On the other hand, the strong emission above 10 keV detected by *Beppo*SAX (Franceschini et al. 2000) favour the CT model. Piconcelli et al. (2007) argues that the *Beppo*SAX data, given its low angular resolution ($\sim$1°), could be contaminated by other hard X-ray sources or, alternatively, that this source could be a "changing-look" quasar, i.e. the gas column density changed from CT to Compton-thin level during the five years between *Beppo*SAX and XMM-*Newton* observations.

IRAS F10026+4949

This object has been optically classified as a Sy1 galaxy (RR00). HST observations show moderate morphological disturbance and multiple very close companions suggesting that the object is in ongoing interactions. Its IR emission can be reproduced with an AGN model, providing ~ 80% of the total IR luminosity, plus an SB component.

PG 1206+459

This source has been classified as a QSO through its optical spectrum, without evidence of optical obscuration. The *IRAS* 12-60 μm data and the *ISO* 12-200 μm data for this galaxy are well reproduced by an AGN model (Haas et al. 1998), and there is no evidence of SB emission (RR00).

PG 1247+267

The *ISO* data of this QSO (Haas et al. 2000) can be reproduced with an AGN dust torus model, and there is no evidence for a SB component (RR00).

IRAS F12509+3122

In this QSO the AGN and SB components are both needed to properly model the IR emission. The majority (~ 60%) of the emission is provided by the AGN, but the SB dominates at wavelengths $> 50\ \mu$m (F02). The HST image of this galaxy shows no signs of interaction (Farrah et al. 2002b).

IRAS 12514+1027

This object has been classified as a Seyfert 2 galaxy, based on its optical spectrum. It has been observed in the IR by *IRAS* and in X-rays by *ROSAT* and XMM-*Newton*. The IR data suggest a ~ 40% AGN contribution and a ~ 60% SB contribution to the bolometric luminosity (RR00). XMM-*Newton* observations suggest that its X-ray emission is absorbed by CT material (Wilman et al. 2003).

IRAS 14026+4341

The optical spectrum of this source was classified as a broad absorption line (BAL) QSO by Low et al. (1989). However, new observations classify it as a type 1.5 object (Wang et al. 2006). Optical spectropolarimetry shows that the observed polarization is due to dust scattering (Hines et al. 2001).

Its IR emission is reproduced using a composite model, with the AGN providing ~ 60% of the total IR output (F02).

IRAS F14218+3845

This source presents a type 1 QSO optical spectrum. HST observations suggest that this galaxy is not involved in ongoing interactions. The IR data suggest that its IR luminosity is dominated by SB emission (Farrah et al. 2002b). An AGN is also needed to completely reproduced its IR emission, contributing ~ 20% to the total luminosity, and dominating the emission at rest-frame wavelengths $< 30\ \mu$m (Verma et al. 2002, F02).

IRAS F15307+3252

This source presents a type 2 UV/optical spectrum (Cutri et al. 1994), and optical spectropolarimetry indicates the presence of a dust-enshrouded quasar (Hines et al. 1995). This result along with previous X-ray observations (Fabian et al. 1996; Ogasaka et al. 1997; Iwasawa et al. 2005) classified it as CT candidate. The HST image of this object shows an interacting system (Farrah et al. 2002b). The IR emission of IRAS F15307+3252 can be reproduced by a composite model, where the AGN emission is dominant (~ 70%), though a strong SB is needed (~ 30%), in order to explain its FIR emission (Verma et al. 2002).

IRAS F16124+3241

This NL galaxy show no detectable polarized broad lines in its optical spectrum, suggesting that the IR emission may be powered by a young SB rather than a dust obscured AGN (Tran et al. 1999). However to reproduce completely its IR SED both AGN and SB components are needed (F02).

IRAS 16347+7037

This galaxy presents a near-IR spectrum consistent with a type 1 QSO (Evans et al. 1998). The IR data from *IRAS* and *ISO* could be reproduced with an AGN model (Haas et al. 1998; Farrah et al. 2002b), rejecting any significant SB contribution. The non-detection of CO is also consistent with the absence of star formation activity (Evans et al. 1998). HST observations show no signs of interaction in this galaxy.

EJ1640+41

This radio-quiet QSO was discovered (Morel et al. 2001) as part of the European Large Area ISO Survey (ELAIS, Oliver et al. 2000). The IR emission of this galaxy can be reproduced with a composite model, with the AGN providing $\sim 70\%$ of the total IR luminosity. Its soft X-ray emission, detected by *ROSAT*, is consistent with an unabsorbed AGN (Morel et al. 2001).

IRAS 18216+6418

IRAS 18216+6418, a giant elliptical (cD) galaxy in the center of a rich (Abell 2) cluster, is a type 1 QSO, one of the most luminous at low redshift. Its IR SED is reproduced with a mixed model, with an AGN component, providing $\sim 60\%$ of the IR emission, and a SB component (RR00; F02).

IRAS F23569-0341

This NL galaxy (Clements et al. 1999) was detected at 60 μm by *IRAS*, but ulterior observations of *ISO* (Verma et al. 2002) and SCUBA (F02) could not confirm this detection. RR00 reproduced the IR SED of this source with a pure SB model.

Chapter 3

An XMM-*Newton* Study of HLIRG

3.1 Motivation

X-ray studies are an essential tool to study star formation and AGN phenomena ocurring in HLIRG (see Chapter 1, Sect. 1.4) and hence useful to unravel the relative contribution of SB and AGN emission to the bolometric luminosity in this kind of sources. Observations in the X-ray range can give us a first clue on which is the dominant process and allow to study the possible interplay between SB and AGN, as well as how their relative contribution varies with cosmic time.

In this chapter we present an X-ray study of HLIRG, for which we have considered the X-ray selected HLIRG sample, made of thirteen sources observed by the X-ray observatory XMM-*Newton* (see Chapter 2, Sect. 2.3.1).). In order to compare the X-ray properties of HLIRG with other similar classes of objects, we have included two samples in our study. On one hand, we chose a sample of ten ULIRG studied in X-rays by XMM-*Newton* (Franceschini et al. 2003). This sample is flux-limited at 60 μm and complete to $S_{60\ \mu m} \geq 5.4$ Jy. On the other hand, we have selected all the HLIRG (six) from the Stevens et al. (2005) sample of high redshift X-ray Compton-thin absorbed QSO. These sources have been observed in X-rays by *ROSAT* (Page et al. 2001) and by XMM-*Newton* (Page et al. 2010, submited), and by SCUBA in the sub-mm band (Stevens et al. 2010).

This chapter is structured as follows: Sect. 3.2 describes the XMM-*Newton* observatory; data reduction and spectral analysis of each source are described in Sect. 3.3; results are discussed in Sect. 3.4 and Sect. 3.5 summarizes the conclusions we obtained from this study. This study has been published in an international journal as Ruiz et al. (2007).

3.2 The XMM-*Newton* X-ray observatory

The XMM-*Newton* observatory is the second cornerstone of the Horizon 2000 science programme of the European Space Agency (ESA) and was launched on the 10th of December of 1999. The satellite is in a 48-hour elliptical orbit allowing continuous monitoring of selected targets up to about 40 hours.

XMM-*Newton* carries six science instruments. The three co-aligned X-ray telescopes onboard XMM-*Newton* have the largest effective area achieved so far, 0.15 m^2 at 1 keV and 0.05 m^2 at 5 keV. Each telescope has its own Point Spread Function (PSF, the distribution of light of a point-like source in the focal plane), which has a minor energy dependence but a strong dependence with the off-axis position.

On the focal plane of each telescope there is an European Photon Imaging Camera (EPIC) instrument. XMM-Newton carries two different technologies of CCD detectors: Metal-Oxide Semiconductor (MOS) and p-n junction (pn), which was specially developed for XMM-*Newton*. There are two cameras (MOS1, MOS2) constituded each one by 7 individual MOS CCD arrays (600 × 600 pixel each, Turner et al. 2001) and one camera (pn) containing 12 pn CCDs (64 × 200 pixel each, Strüder et al. 2001).

The EPIC cameras can perform imaging over a 30 arcmin diameter field of view, and are sensitive to photons with energies from 0.1 to 15 keV providing moderate energy resolution (resolving power $E/\Delta E \sim 20-50$). The angular resolution is determined by the PSF of their mirror modules (the pixel size of the EPIC cameras is much smaller than the PSF). The FWHM of the PSF is 6 arcsec, allowing to obtain X-ray source positions with accuracies of $\sim 1-3$ arcsec.

The EPIC cameras can be operated in different observing modes (Kendziorra et al. 1997, 1999; Kuster et al. 1999). Each camera is equipped with three aluminized filters with different thicknesses (named thick, medium and thin filters) to block IR, visible and UV radiation and reduce the contamination of the observations (the EPIC CCDs are also sensitive to those energies).

The telescopes with MOS cameras in their focal planes have a grating assembly (RGA) that split about 40% of the incoming X-rays to a Reflection Grating Spectrometer (RGS, den Herder et al. 2001). About 44% of the incoming light reaches the MOS cameras, while the remaining ∼ 16% is absorbed by the supporting structures of the RGA. The RGS instruments perform high resolution dispersive spectroscopy ($E/\Delta E \sim 200-800$) of bright sources in the soft energy band.

XMM-*Newton* also carries aboard the Optical Monitor (OM, Mason et al. 2001), a 30 cm Ritchey-Chretien telescope feeding a compact image-intensified photon-counting detector. The detector operates in the UV and the blue region of the optical spectrum (170 to 550 nm). The OM is co-aligned with the X-ray telescopes to allow simultaneous UV/optical/X-ray observations.

TABLE 3.1: Description of the XMM-*Newton* observations.

Source	Net. exp. time [ks]			Ext.radius [arcsec]			Source counts[a]			Obs. date	Filter
	pn	MOS1	MOS2	pn	MOS1	MOS2	pn	MOS1	MOS2		
IRAS 00182-7112	9.1	-	-	19	-	-	134 ± 15	-	-	2003-04-17	Thin
IRAS F00235+1024	14.4	-	-	35	-	-	< 30	-	-	2001-01-10	Thin
IRAS 07380-2342	4.7	11.4	11.6	30	40	40	< 45	-	-	2005-10-13[c]	Medium
IRAS 09104+4109[b]	9.2	12.6	12.5	20	20	20	5544 ± 75	2245 ± 47	2332 ± 48	2003-04-27	Medium
PG 1206+459	5.9	6.9	6.9	26	32	29	731 ± 32	188 ± 16	193 ± 16	2002-05-11	Thin
PG 1247+267	19.4	25.5	26.6	35	35	35	5132 ± 74	1646 ± 42	1694 ± 43	2003-06-18	Medium
IRAS F12509+3122	11.9	14.6	14.1	25	25	25	508 ± 24	156 ± 13	139 ± 13	2005-12-11[c]	Thin
IRAS 12514+1027	16.7	20.0	18.2	22	40	40	105 ± 22	28 ± 13	7 ± 12	2001-12-28	Thin
IRAS 14026+4341	-	6.6	5.6	-	35	35	-	< 30	< 27	2005-11-26[c]	Thin
IRAS F14218+3845	11.5	15.2	15.1	30	34	31	550 ± 29	185 ± 17	176 ± 16	2003-08-01	Medium
	2.3	7.3	7.0	30	30	30	91 ± 14	109 ± 20	79 ± 18	2005-06-07[c]	Medium
IRAS F15307+3252	9.4	11.5	12.0	22	40	40	97 ± 21	30 ± 12	42 ± 13	2002-07-30	Medium
IRAS 16347+7037	12.9	15.6	15.8	30	56	48	11172 ± 106	3546 ± 67	3785 ± 66	2002-11-23	Medium
IRAS 18216+6418[b]	0.5	2.9	3.3	20	20	20	-	7402 ± 86	8481 ± 92	2002-10-16	Thin

[a] Total source counts in the 0.2-10 keV band.
[b] *Chandra* data are also used in the study of this source. See Sect. 3.3.3 for details.
[c] Data from OBS-ID 030536.

3.3 X-ray data reduction and analysis

3.3.1 Data reduction

Table 3.1 presents the most relevant information about the XMM-*Newton* observations. The data have been processed using the Science Analysis System (SAS) version 6.1.0, and have been analyzed using the standard software packages (FTOOLS and XSPEC) included in HEAsoft 5.3.1.

We reprocessed the EPIC pn and MOS Observation Data Files (ODFs) to obtain new calibrated and concatenated event lists, using the SAS tasks `EMPROC` and `EPPROC`, including the latest calibration files at the time of reprocessing.

The new event files were filtered to avoid intervals of flaring particle background, and only events corresponding to pattern 0-12 for MOS and 0-4 for pn were used (Ehle et al. 2005). The events with energy above 12 keV and below 0.2 keV were also filtered out. The source spectra were extracted from circular regions, whose radii were chosen in each case to optimize the signal-to-noise ratio (S/N), and to avoid the CCD gaps. The background spectra were taken in circular source-free regions near the object, also avoiding CCD gaps. We generated our own redistribution matrices and ancillary files (correction for the effective area) using the SAS tasks `RMFGEN` and `ARFGEN`.

XMM-*Newton* detected ten out of thirteen sources ($\sim 80\%$) with different S/N quality. In cases where the S/N ratio was poor, the MOS and pn spectra were co-added (Page et al. 2003). All spectra were rebinned to have $\geq$ 25 counts per energy channel, except IRAS 00182-7112 ($\geq$ 15 counts) and PG 1206+459 ($\geq$ 20 counts). The resulting EPIC spectra (see Fig. 3.1) reveal heterogeneous spectral properties for these objects (see Table 3.3 and Sect. 3.3.5).

3.3.2 Non-detected sources

We have estimated upper limits to the luminosity of those sources not detected by XMM-*Newton*. We estimated the count rate which would correspond to 3σ fluctuations of the background in a circular region of the pn-EPIC images, centered in the source coordinates. To convert between count rate and physical units a simple model was chosen: a power law[1] with photon index $\Gamma = 2$ and Galactic absorption.

3.3.3 Cluster emission subtraction

Two sources of our sample, IRAS 09104+4109 and IRAS 18216+6418, reside in clusters. They present soft extended emission from the intra-cluster medium (ICM). To take into account this residual foreground in the subsequent spectral analysis, we added an XSPEC thermal component to the spectral

[1] $\frac{dN}{d\varepsilon dt} \propto \varepsilon^{-\Gamma}$, where N are the number of photons and ε is the energy of the photons.

Table 3.2: *Chandra* observations description.

Source	Instrument	Grating	Exp. time. [ks]	Obs. date
IRAS 09104+4109	ACIS-S	None	9.17	1999-11-03
IRAS 18216+6418	ACIS-S	LETG	171.82	2001-01-18

model (`zbremss` or, if emission lines are significant, `mekal`). Two parameters characterize this model: temperature and normalization.

We estimated the temperature of the cluster by extracting an X-ray spectrum in an annular region around the source and fitting it with a thermal bremsstrahlung model. The normalization was obtained re-normalizing the flux from the annulus to that from the source circular region. If we assume $N_R \propto S_R$, where N_R is the normalization of the X-ray spectrum in region R and S_R is the surface brightness of the region R, we have

$$N_C = N_A \times \frac{S_C}{S_A}, \tag{3.1}$$

where A is the annular region and C is the source circular region. Therefore we can use the X-ray surface brightness profile of the cluster, integrating it over both regions to obtain the normalization [2].

We determined the brightness profile using public *Chandra* data (see Table 3.2). The angular resolution of *Chandra* is higher than of XMM-*Newton* ($\sim$ 0.6 arcsec compared to $\sim$ 6 arcsec of XMM-*Newton*), allowing to extract a better profile. Assuming an isothermal ICM, the radial profile of a cluster can be well-fitted using a β-model[3] (Sarazin 1986; Mushotzky 2004). This profile was then convolved with the XMM-*Newton* PSF, before integrating it over the regions of interest.

3.3.4 Spectral analysis

Our aim is to estimate the AGN and SB contribution to the total X-ray emission. As described in Chapter 1, Sect. 1.1, the X-ray spectrum emitted by an AGN can be typically modelled with four components: an underlying absorbed power law, a reflection component, an iron K_α emission line and a soft excess above the power law at energies below $\sim$ 1 keV.

The power law component is associated with the direct X-ray emission of the central engine of the AGN, where the optical/UV photons emitted by the accretion disk are converted in X-ray photons by high energy electrons surrounding the disk through inverse Compton scattering (see Chapter 1). Several observational results show that the typical photon index of this power law in unobscured AGN is $\Gamma \simeq 1.5-2$ (Nandra and Pounds 1994; Reeves and Turner 2000; Mateos et al. 2005a, 2010).

[2] The background spectrum of the annular region was extracted in a circular region free of sources away from the cluster emission. We used the XMM-*Newton* "blank fields" (Read and Ponman 2003) to extract the background spectrum of the source.

[3] $S(r) = S_0(1 + (r/r_0)^2)^{-3\beta+0.5}$

The soft excess component, common in type 1 AGN (Reeves and Turner 2000; Piconcelli et al. 2005), can be reproduced with a thermal model, with an expected temperature remarkably constant around 0.1-0.3 keV (Piconcelli et al. 2005; Gierliński and Done 2006) and the ratio between its 0.5-2 keV luminosity and the luminosity of the power law component in the same band is found in the range $\sim 0.15 - 1.45$ (Piconcelli et al. 2005). Several alternative models have been proposed for the origin of this soft excess, such as a relativistically blurred photoionized disk reflection (Ross and Fabian 1993; Crummy et al. 2006) or ionized absorption in a wind from the inner disc (Gierliński and Done 2004, 2006). It has also been shown that the analysis of the high resolution XMM-*Newton* RGS spectra is important to understand the nature of the soft excess emission (Bianchi et al. 2006). We have only used thermal models in this work for simplicity, since more detailed models are not warranted by the quality and low spectral resolution of the data.

The SB emission can be modeled with a power law with a typical photon index $\Gamma \simeq 1.0 - 1.4$ (White et al. 1983; Dahlem et al. 1998; Persic and Rephaeli 2002), or with a thermal model with temperature $0.5 - 1.0$ keV (Iwasawa 1999; Franceschini et al. 2003). The soft X-ray-to-bolometric luminosity ratio for an SB is $\sim 10^{-4}$, as found by Iwasawa (1999) for a sample of four prototype powerful FIR SB galaxies. This factor can be used to estimate the bolometric luminosity of the SB component of the sources.

All sources were analyzed using the following scheme. First we fitted the data with a power law model plus Galactic absorption[4] (see Table 3.3, column 3). We added intrinsic absorption (XSPEC `zpha` model) where it was statistically significant[5].

We compared this model with a power law reflected from neutral material (modeled with the XSPEC `pexrav`[6], Magdziarz and Zdziarski 1995). When two models had the same number of parameters (and hence the F-test is not useful), the fit with the lowest χ^2 was taken as our baseline model. However, when the χ^2 from two models were comparable, we adopted as our baseline fit the one with less uncertainty in the determination of the model parameters.

We then checked for any significant additional component: iron emission line (modeled with `zgauss` at ~ 6.4 keV) and/or soft excess. We fitted the latter with different thermal models (blackbody: `zbbody`; bremsstrahlung: `zbremss`, Kellogg et al. 1975; bremsstrahlung with emission lines: `mekal`, Mewe et al. 1985; Kaastra and Mewe 1993). We introduced the thermal component to parameterize the starburst emission and/or the AGN soft excess emission.

In those cases where Γ was out of the range expected for AGN or SB, this parameter was fixed to 2, and we tried to fit again the spectrum with two alternative models: an absorbed power law and a reflection

[4]All models referred to in this Chapter implicitly include a multiplicative Galactic absorption component fixed at the Galactic $N_{\rm H}$ value from Dickey and Lockman (1990).

[5]To this end we used the F-test, accepting additional spectral components only when they improved the fit with a significance $\geq 3\sigma$.

[6]We kept fixed all the parameters of the `pexrav` model to the standard values except the photon index of the incident power law, the reflection scaling factor and the normalization.

model (`pexrav`). In both cases, additional intrinsic absorption and thermal emission models were also added (if needed) to improve the fit.

The best fit model for each source is given in Table 3.3. We calculated the luminosity for each component in the hard and soft X-ray bands, corrected by Galactic and intrinsic absorption. A more detailed description of the analysis and the results for each source is presented in Sect. 3.3.5.

We estimated upper limits on the luminosity (see Table 3.3, column 11) for a thermal component in the X-ray spectra of those sources where it was not significant. To this end, we fixed all parameters to their best fit values. We added a thermal component (`zbremss`) with a fixed temperature, $kT = 0.6$ keV (the mean temperature of the ULIRG thermal component from Franceschini et al. 2003), and we calculated the 2σ confidence interval for the normalization parameter, which was then used to estimate the upper limit of the luminosity.

3.3.5 Source by source analysis

IRAS 00182-7112

This type 2 QSO was detected by the EPIC-pn camera only. We modeled its spectrum with a reflection component, using the `pexrav` model (Magdziarz and Zdziarski 1995). The photon index is fixed to 2 and a pure reflection component is assumed. This implies a lower limit to the column density of the absorber material ($N_{\rm H} > 10^{25}$ cm^{-2}). We marginally detect a narrow emission line at $6.75^{+0.08}_{-0.11}$ keV (significance within $2-3\sigma$), consistent with He-like Fe line (this energy is also consistent at 2σ level with neutral Fe 6.4 keV line).

ISO and *Spitzer* IR data suggest the presence of a deeply obscured nuclear power source (Tran et al. 2001; Spoon et al. 2004a). This is qualitatively consistent with our X-ray analysis results. The X-rays detected by XMM-*Newton* are consistent with the reflected emission from the AGN, with an iron K_α fluorescent emission from the reflecting material. The equivalent width of this line, 0.8 ± 0.6 keV, is consistent with the CT hypothesis, but the poor quality of the spectrum prevents us from reaching any stronger conclusion. Assuming that the direct X-ray emission is completely absorbed by CT material, we estimate that the intrinsic 2-10 keV luminosity of the AGN responsible for the reflection component is $6.3 \times 10^{44}(2\pi/\Omega_{refl})$ erg s^{-1}, where $\Omega_{refl} < 2\pi$ is the solid angle subtended by the reflector at the illuminating source.

Our X-ray analysis of this source points towards an AGN with CT obscuration. The analysis of the broadband SED of this source which we perform in Chapter 5 is also consistent with the presence of a highly obscured AGN in this galaxy and its MIR spectrum (see Chapter 4) shows signatures of strong obscuration.

TABLE 3.3: XMM-*Newton* spectral analysis results. Fluxes and luminosities in CGS units. All errors are quoted at 90% confidence level for one parameter of interest (i.e. $\Delta\chi^2 = 2.71$) throughout this chapter.

Source	Model [a]	$N_{\rm H}$ [b]	Γ	kT (keV)	EW (keV)	χ^2/ν	$\Delta\chi^2$	$\log S_X$ [c]	$\log L$ [d]			
									$L^{\rm SX}_{\rm PL}$	$L^{\rm SX}_{\rm TH}$	$L^{\rm HX}_{\rm PL}$	$L^{\rm HX}_{\rm TH}$
IRAS 00182-7112	D + E	4.24	$2, E_c = 9^{+21}_{-4}$	-	0.8 ± 0.6	5.0/9	10.7	-12.8	44.9	<41.9	44.8	<40.7
IRAS F00235+1024	-	5.07	2	-	-	-	-	<-14.5	<42.2	-	<42.4	-
IRAS 07380-2342	-	64.3	2		-	-	-	<-13.7	<41.7	-	<42.5	-
IRAS 09104+4109	(B)[e] + A + E	1.82	1.62 ± 0.07	-	$0.38^{+0.10}_{-0.11}$	374/324	42	-11.7	44.2	<43.0	44.5	<41.8
+*Beppo*SAX:	(B)[e] + B + D + E	″	$1.2^{+0.3}_{-0.2}$	$3.1^{+0.4}_{-0.3}$	$0.2^{+3.4}_{-0.1}$	330/326	53	″	44.7	44.2	45.3	44.2
PG 1206+459	A	1.31	1.7 ± 0.9	-	-	72/67	-	-12.5	45.8	<44.0	45.1	<42.8
PG 1247+267	A + C	0.90	$1.98^{+0.05}_{-0.07}$	$0.49^{+0.23}_{-0.17}$	-	235/281	30	-12.3	45.9	45.5	45.9	44.0
IRAS F12509+3122	A + B	1.24	$1.38^{+0.11}_{-0.12}$	0.21 ± 0.03	-	38/30	80	-12.9	43.8	43.8	44.3	40.2
IRAS 12514+1027	B + F × A[f]	1.67	2	$0.35^{+0.17}_{-0.07}$	-	5/15	15	-14.2	43.2	42.2	43.3	39.7
IRAS 14026+4341	-	1.19	2	-	-	-	-	<-13.7	<42.5	-	<42.6	-
IRAS F14218+3845	A	0.93	2.24 ± 0.12	-	-	70/75	-	-13.1	44.7	<43.8	44.6	<42.5
IRAS F15307+3252	A	2.03	2.1 ± 0.4	-	-	16/22	-	-13.6	45.4[g]	<43.1	45.5[g]	<41.9
IRAS 16347+7037	C + A	4.48	1.77 ± 0.13	1.53 ± 0.18	-	561/547	26	-11.7	45.8	45.7	46.0	45.4
IRAS 18216+6418	(C)[e] + C + A	4.04	$1.57^{+0.10}_{-0.12}$	$0.49^{+0.09}_{-0.08}$	-	329/332	151	-10.7	45.2	45.1	45.6	43.6

[a] XSPEC models: A: `power law`, B: `mekal`, C: `zbremss`, D: `pexrav`, E: `zgauss` (emission line), F: `zpha` (intrinsic absorption).
[b] Galactic neutral hydrogen column density (in units of 10^{20} atoms cm^{-2}), from Dickey and Lockman (1990).
[c] Observed frame 0.5-10 keV flux.
[d] Logarithm of the rest-frame intrinsic X-ray luminosity: SX: Soft X-ray (0.5-2 keV) band; HX: Hard X-ray (2-10 keV) band; PL: Power law component; TH: Thermal (soft excess) component.
[e] This component models the cluster contribution.
[f] Intrinsic $N_{\rm H} = 4^{+20}_{-3} \times 10^{23}$ cm^{-2}.
[g] Luminosity corrected assuming Panessa et al. (2006) results. See Sect. 3.3.5 for details.

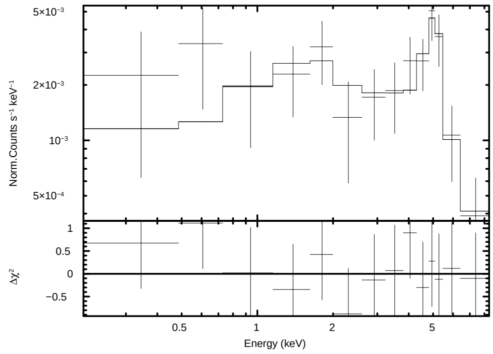

(a) IRAS 00182-7112: pn

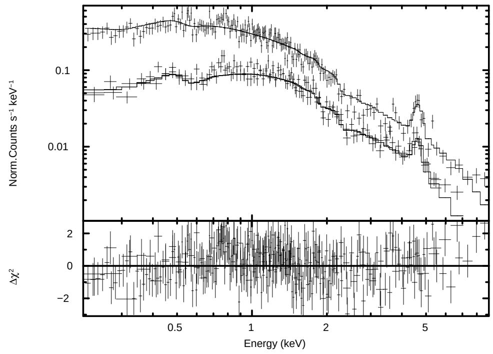

(b) IRAS 09104+4109: pn, MOS1, MOS2

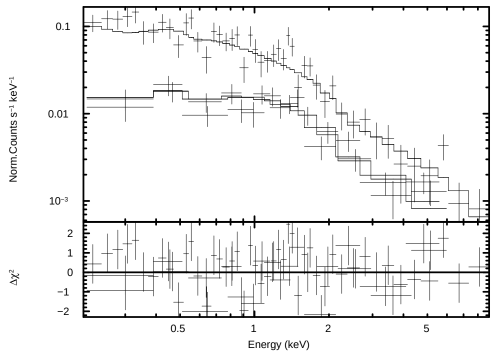

(c) PG 1206+459: pn, MOS1, MOS2

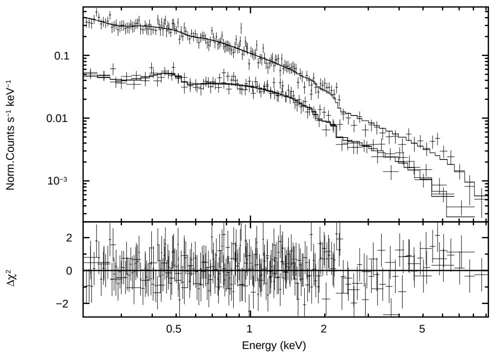

(d) PG 1247+267: pn, MOS1, MOS2

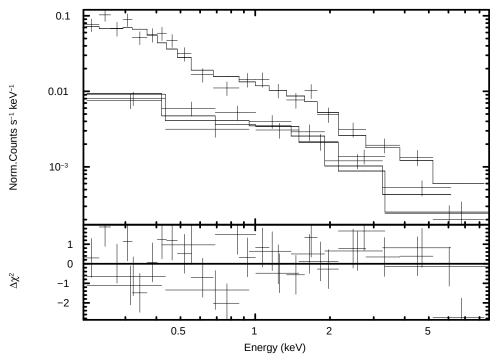

(e) IRAS F12509+3122: pn, MOS1, MOS2

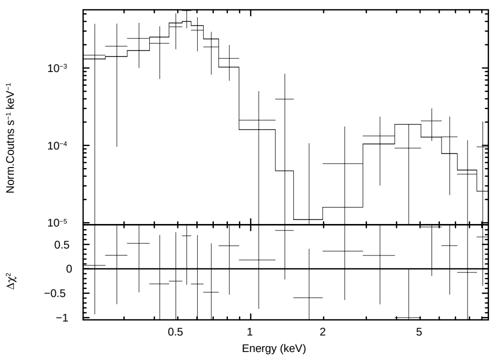

(f) IRAS 12514+1027: pn+MOS1+MOS2

FIGURE 3.1: XMM-*Newton* X-ray spectra and residuals of the detected sources from the HLIRG sample. The solid line is the best fit model. Continues in the next figure.

IRAS F00235+1024

XMM-*Newton* observed this NL SB galaxy for 26 ks, but it was not detected by the EPIC cameras. Wilman et al. (2003), assuming a thermal `mekal` model ($kT = 0.5$ keV), estimate an upper limit to the

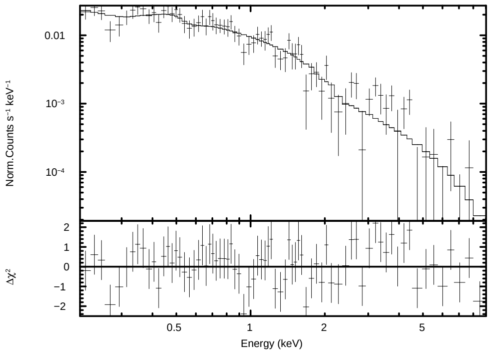

(g) IRAS F14218+3845: pn+MOS1+MOS2 (two observations)

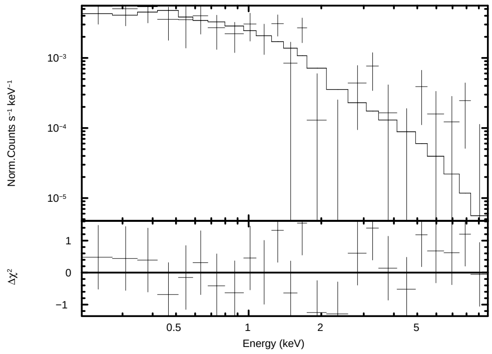

(h) IRAS F15307+3252: pn+MOS1+MOS2

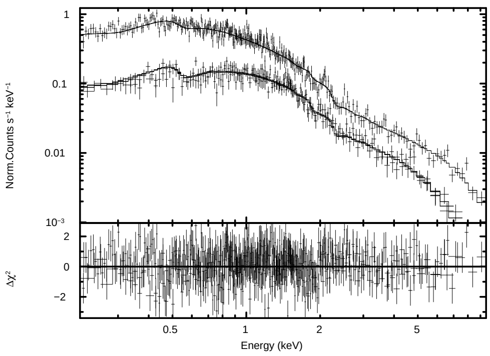

(i) IRAS 16347+7037: pn, MOS1, MOS2

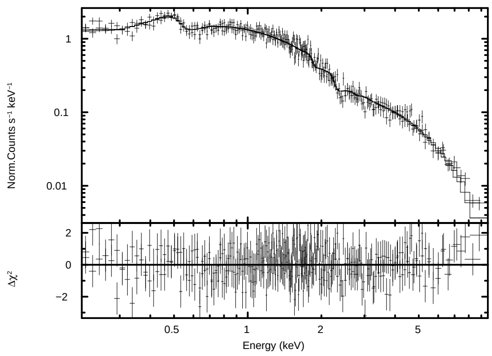

(j) IRAS 18216+6418: MOS1, MOS2

FIGURE 3.1: Continued.

0.5-2 keV luminosity of 2.8×10^{42} erg s^{-1}, consistent with our result in this band. The reported upper limit to the hard X-ray luminosity ($\sim 1.9 \times 10^{44}$ erg s^{-1}) is also consistent with our estimate.

The model able to reproduce the IR SED of this source suggest that roughly half of its bolometric luminosity is originated in an AGN (F02). The analysis of its MIR spectrum (Chapter 4) and broadband SED (Chapter 5) also suggest that a dust-enshrouded AGN resides in this galaxy. CT absorption could then explain the low X-ray emission of this source.

IRAS 07380-2342

This NL object was not detected by XMM-*Newton* and we estimated upper limits as described in Sect. 3.3.2. Its MIR spectrum (Chapter 4) and broadband SED (Chapter 5) suggest that the non-detection is probably due to strong absorption.

IRAS 09104+4109

The type 2 QSO IRAS 09104+4109 resides in a rich cluster (Kleinmann et al. 1988). The X-ray soft extended emission from the ICM was already detected by *ROSAT* (Fabian and Crawford 1995). We subtracted this foreground as explained in Sect. 3.3.3.

The source spectra were extracted from circular regions of 20″ radii for all detectors, and the cluster spectra from an annular region between 20″ and 90″ (constrained to the CCD where the source is located). The cluster emission was fitted with a `mekal` model. The temperature is $kT = 5.5 \pm 0.4$ keV, and the metal abundance is 0.30 ± 0.12 $Z_{\odot}$, which is consistent with the mean Fe abundance for clusters with a temperature greater than 5 keV (Baumgartner et al. 2001). We obtained the radial brightness profile using *Chandra* data: a β-model with a core radius $r_0 = 4''.6 \pm 0''.6$ and $\beta = 0''.576^{+0''.018}_{-0''.016}$. The cluster emission represents 62% of the total 0.5-10 keV luminosity.

The spectrum of the source was fitted with a power law with a Fe Kα broad ($\sigma = 0.27 \pm 0.09$ keV) emission line at $6.61^{+0.08}_{-0.10}$ keV. This broad line could be explained as a complex of neutral and ionized narrow lines merged due to the low resolution of the detector.

Although IRAS 09104+4109 is classified as a type 2 QSO, the XMM-*Newton* data did not reveal any intrinsic absorption feature. However, the *Chandra* observation of this source suggested a column density of 3×10^{23} cm^{-2} (Iwasawa et al. 2001). Also, *Beppo*SAX detected this object at energies greater than 10 keV, pointing to non-thermal quasar emission emerging from a thick absorbing torus (Franceschini et al. 2000), with $N_{\rm H} \sim 7 \times 10^{24}$ cm^{-2}. On the other hand, Piconcelli et al. (2007) found that the XMM-*Newton* spectrum of this source is consistent either with a transmission model (i.e Compton-thin absorption) or a pure reflection model (i.e. CT absorption), although the low equivalent width of the iron emission line they found seem to favour the Compton-thin hypothesis (see Chapter 2, Sect. 2.4). However CT sources showing iron lines with equivalent width below 1 keV have been observed (Ueda et al. 2007).

Our combined analysis of the *Beppo*SAX and XMM-*Newton* data sets (which will be taken as the best fit for this source in what follows) shows that a reflection-only model is needed to explain the complete spectrum in the 0.2 to 50 keV range. This implies a lower limit $N_H > 10^{25}$ cm^{-2} to the column density of the absorber, which it is consistent with Iwasawa et al. (2001), where a similar analysis of this source is done with *Beppo*SAX and *Chandra* observations. Assuming $\Gamma = 1.4$, which is in the flatter side of the photon index distribution of quasars (Reeves and Turner 2000), they found that a cold reflection model without transmitted component fits well the complete data. This model gives an intrinsic hard X-ray luminosity of $2 \times 10^{45}(2\pi/\Omega_{refl})$ erg s^{-1} for the AGN. The estimated bolometric luminosity of this source is then $\sim 3.5 \times 10^{13}$ $L_{\odot}$.

We have also found in our combined analysis a new thermal component, but its temperature ($kT \sim$ 3 keV) is too high to be associated with SB or AGN emission. Since there is no evidence of an

SB component in the IR SED of this source (RR00), this thermal component is probably due to an incomplete subtraction of the cluster emission. Previous results indicate that a strong cooling flow of the ICM is taking place in the core of the cluster (Fabian and Crawford 1995; Allen and Fabian 1998; Ettori and Fabian 1999; Iwasawa et al. 2001), so the isothermal ICM hypothesis we have assumed could underestimate the cluster luminosity in the central region.

We confirm that IRAS 09104+4109 is affected by CT absorption, and that the X-ray emission detected below 10 keV by XMM-*Newton* is only due to a reflection continuum from cold matter. Its broadband SED (see Chapter 5) is also consistent with an obscured AGN. The MIR spectrum of this object is dominated by synchrotron emission and hence does not show any absorption features (see Chapter 4).

PG 1206+459

The XMM-*Newton* observation of this QSO is contaminated by background flares at the beginning and at the end of the observation. The final effective exposure is $\sim$ 7 ks. The spectra continuum has been modelled with a power law. We have not detected significant intrinsic absorption or soft excess. The lack of absorption in the X-ray spectra is consistent with the optical and IR evidence (Haas et al. 1998, RR00). The X-ray spectrum of this object is therefore consistent with having a pure AGN origin. Tha analysis of the broadband SED of this galaxy is also consistent with a pure AGN with no SB contribution (see Chapter 5).

PG 1247+267

The X-ray spectrum of this QSO has been modelled with a power law and a thermal component. A `pexrav` model is formally the best fit ($\chi^2/\nu = 224/282$) of these data. However, the photon index obtained ($\Gamma \sim 2.3$) with this model is slightly larger than that expected for an AGN. Moreover, the reflection scaling factor (~ 4) is sensibly larger than that typically expected for type 1 sources (within 0 and 1). No other reflection features have been found in the X-ray spectrum. Therefore, we have adopted the power law plus thermal component as our best fit.

The temperature of the thermal component ($kT = 0.48^{+0.23}_{-0.17}$ keV) is consistent with the typical temperature of an SB galaxy. However, the bolometric luminosity that we can estimate through the soft X-ray emission for this SB is $\sim 10^{49}$ erg s^{-1}, much higher than the RR00 estimate ($< 5.2 \times 10^{46}$ erg s^{-1}). Therefore, the soft excess component is too luminous to have a pure SB origin. Furthermore, its soft excess-to-power law soft X-ray luminosity ratio is ~ 0.4, which is typical for soft excess observed in AGN.

We can conclude that the X-ray spectrum of this source is consistent with being dominated by an AGN. The analysis of the broadband SED of this galaxy agrees with this result (see Chapter 5).

IRAS F12509+3122

A significant fraction ($\sim$ 50%) of the observation time of this QSO is affected by high background. The pn and MOS spectra can be fitted by a power law model and a thermal component with $kT = 0.21 \pm 0.03$ keV, at a lower energy than that expected for a standard SB, but consistent with soft excess originating in an AGN. The thermal-to-power law luminosity ratio is ~ 1.2, in the range of AGN soft excess. All these evidences clearly suggest that this X-ray spectrum is AGN-dominated. The study of the full SED of this source also reveals that the SB contribution to the total X-ray emission is negligible (Chapter 5).

IRAS 12514+1027

This Seyfert 2 galaxy was also observed by *ROSAT* (Wilman et al. 1998), but only XMM-*Newton* has been able to detect its X-ray emission. Wilman et al. (2003) considered only the pn spectrum, modelled with a reflection component (`pexrav`, with fixed $\Gamma = 2$) and a thermal component (`mekal`, $kT = 0.31^{+0.13}_{-0.05}$ keV) corrected by intrinsic absorption ($N_{\rm H} = 1.3^{+0.9}_{-0.7} \times 10^{21}$ cm^{-2}). The resulting χ^2/ν is 8.5/12.

In our analysis, the three EPIC spectra were co-added (see Sect. 3.3.1). We modelled the spectrum with an absorbed power law with a photon index fixed to 2, and a thermal component.

The temperature of the thermal component is $kT = 0.35^{+0.17}_{-0.07}$ keV, consistent with that usually observed in SB galaxies. The soft component-to-power law luminosity ratio is slightly lower than that associated with an AGN. The 0.5-2.0 keV luminosity of this soft component is 1.5×10^{42} erg s^{-1}, which implies a bolometric luminosity for the SB of $\sim 1.5 \times 10^{46}$ erg s^{-1}. The IR luminosity of the SB estimated from the analysis of the IR SED of the source is $\sim 5 \times 10^{46}$ erg s^{-1} (RR00). This thermal component seems to have an SB origin.

The optical, IR and X-ray data point to a CT AGN and an SB of comparable bolometric luminosities. Our study of the MIR spectrum and broadband SED of this HLIRG is consistent with this result (see Chapters 4 and 5).

IRAS 14026+4341

The XMM-*Newton* observation of this QSO 1.5 is heavily contaminated by background flares. All the pn data are affected by a count rate background greater than 15 counts per second. The MOS data have a brief interval free of flares, but the source was not detected. We estimated upper limits as described in Sect. 3.3.2.

TABLE 3.4: Infrared fluxes and luminosities of the sample.

Source	R[b]	Flux density (Jy)[a]				IR	log L (erg s^{-1})				
		12μm	25μm	60μm	100μm	Model[c]	L_{FIR}[d]	L_{IR}[d]	$L_{IR,RR}$	$L_{IR,RR}^{AGN}$	$L_{IR,RR}^{SB}$
IRAS 00182-7112	17.738	<0.06025	0.133±0.010	1.20±0.08	1.19±0.12	S+A	46.49	<46.72	<46.93	<46.48	46.74
IRAS F00235+1024	>21.5	<0.173	<0.193	0.43±0.06	<0.94	S+A	<46.76	<47.27	46.74	46.44	46.45
IRAS 07380-2342	16.869	0.48±0.03	0.80±0.08	1.17±0.09	3.5±0.3	A+S	46.56	47.08	46.97	46.79	46.48
IRAS 09104+4109	17.819	0.13±0.03	0.334±0.013	0.53±0.04	<0.44	A	<46.42	<46.99	<46.92	46.84	<46.15
PG 1206+459 [e]	15.135	0.21±0.04	<0.113	0.26±0.05	0.35±0.07	A	47.20	<47.94	<47.80	47.78	<46.57
PG 1247+267 [e]	14.621	<0.126	<0.113	0.24±0.05	0.17±0.03	A	47.70	<48.39	<47.94	47.91	<46.76
IRAS F12509+3122	16.590	<0.106	0.10±0.03	0.22±0.04	<0.675	A+S	<46.86	<47.37	47.00	46.76	46.62
IRAS 12514+1027	17.654	<0.0632	0.190±0.016	0.71±0.06	0.76±0.15	S+A	46.18	<46.51	46.63	46.27	46.39
IRAS 14026+4341	15.651	0.12±0.03	0.285±0.014	0.62±0.06	0.99±0.24	A+S	46.26	46.70	46.54	46.34	46.11
IRAS F14218+3845	>21.5	<0.0969	<0.075	0.57±0.06	2.10±0.17	S+A	47.80	<48.06	46.86	46.15	46.76
IRAS F15307+3252	19.131	<0.065	0.071±0.019	0.23±0.04	<0.71	A+S	<47.07	<47.46	47.22	47.05	46.73
IRAS 16347+7037 [e]	13.979	0.059±0.010	0.122±0.004	0.27±0.05	0.35±0.07	A+S	47.42	47.86	47.81	47.73	47.04
IRAS 18216+6418	13.403	<0.238	0.445±0.012	1.24±0.05	2.13±0.17	A+S	46.49	<46.89	46.78	46.54	46.37

[a] Observed by *IRAS* (from NED).
[b] UK-R magnitude (SuperCOSMOS Sky Survey).
[c] AGN (A) and/or starburst (S) components needed to fit the IR SED (as in Table 2.2, col. 5). First letter indicates the dominant component.
[d] Infrared luminosities in the 40 – 500 μm (FIR) and 1 – 1000 μm (IR) bands, computed using *IRAS* fluxes (Sanders and Mirabel 1996).
[e] 60 and 100 μm fluxes are *ISO* data from Haas et al. (2000).

IRAS F14218+3845

The QSO IRAS F14218+3845 was observed by XMM-*Newton* in two occasions. The second observation was heavily affected by high radiation background. We checked that no significant variability was present in the flux state of the source between the two observations so we could co-add the six spectra of the different observations to increase the S/N ratio. The spectrum was modeled with a power law. No significant soft excess or intrinsic absorption was found.

The IR data suggest that this HLIRG is an SB dominated source (Verma et al. 2002; Farrah et al. 2002a), but our analysis of its XMM-*Newton* X-ray spectrum did not reveal any SB features. Using the upper limit estimated (see Table 3.3) for a thermal component, the total SB luminosity is less than 6×10^{47} erg s^{-1}, which is consistent with the SB luminosity estimated by Farrah et al. (2002a) through IR and sub-mm data (6×10^{46} erg s^{-1}). Although an SB component cannot be excluded, the data point to an AGN-dominated X-ray emission. The analysis of its full SED (see Chapter 5) shows that an SB component is needed to reproduce the IR emission of this HLIRG, but the SB contribution to the total X-ray emission is negligible.

IRAS F15307+3252

Previous observations with *ROSAT* and *ASCA* detected no X-ray emission from this QSO 2 (Fabian et al. 1996; Ogasaka et al. 1997). We detected a faint X-ray emission in the XMM-*Newton* public data. The observation of this source is affected by high background flares. The three EPIC extracted spectra were coadded to increase the S/N ratio. We fitted this spectrum using a power law. We were not able to find any absorption feature or thermal emission.

XMM-*Newton* has observed IRAS F15307+3252 on two more occasions, but the data were still private when we carried out this analysis. Iwasawa et al. (2005), using the complete data set, found a prominent Fe Kα line at $\sim$ 6.5 keV, indicating the presence of a CT AGN. This is in agreement with optical spectropolarimetry data indicating the presence of a dust-enshrouded quasar (Hines et al. 1995). The estimate of the AGN bolometric luminosity using the observed emission line luminosity is also consistent with previous results (Yun and Scoville 1998; Aussel et al. 1998; Verma et al. 2002; Peeters et al. 2004). The hard X-ray emission detected by us is probably reflected radiation, because of CT obscuration. Panessa et al. (2006) found that the ratio between the intrinsic and the observed X-ray luminosity in CT Seyfert galaxies is $\sim$ 60. We have corrected our estimate X-ray luminosity by this factor. The resulting hard X-ray luminosity ($\sim 3.2 \times 10^{45}$ erg s^{-1}) is consistent with the estimate given by Iwasawa et al. (2005) ($L_{\mathrm{X}} > 1 \times 10^{45}$ erg s^{-1}), using the luminosity of the iron emission line.

Iwasawa et al. (2005) also found extended soft emission, with $kT = 2.1^{+0.6}_{-0.4}$ keV. They identify this extended emission with hot gas associated with a relatively poor cluster around this object. Although no galaxy cluster has been found associated with this source, *HST* observations show a moderate galaxy over-density (Farrah et al. 2002b). Moreover, its bolometric luminosity to temperature relation would be similar to that typical of poor clusters (Fukazawa et al. 2004).

In summary, the X-ray spectrum of this source is consistent with the emission originating in a CT AGN. The presence of an obscured AGN is also pointed out by its MIR spectrum (see Chapter 4) and its broadband SED (see Chapter 5).

IRAS 16347+7037

The spectrum of the QSO IRAS 16347+7037 was modelled with a power law and a thermal component. No intrinsic absorption was detected.

The XMM-*Newton* spectrum is consistent with a type 1 AGN spectrum, as the optical (Evans et al. 1998) and IR (Haas et al. 1998; Farrah et al. 2002b) observations suggest. Previous X-ray data from *ASCA* were also consistent with the XMM-*Newton* data, and there was no evidence of iron Kα emission feature or any absorption edge (Nandra et al. 1995).

The soft excess has $L(0.5-2.0 \text{ keV}) = 5.6\times10^{45}$ erg s^{-1}. This would imply an SB bolometric luminosity three orders of magnitude greater than the SB luminosity calculated with the IR data (Farrah et al. 2002b, see Table 3.4). Therefore this component is unlikely to be associated with an SB. Moreover, its thermal-to-power law luminosity ratio is consistent with a soft excess from the AGN.

Our analysis points towards a pure AGN origin for the X-ray emission, which is also in agreement with the broadband SED analysis of this galaxy, where no SB emission is found (see Chapter 5).

IRAS 18216+6418

The pn data of this QSO 1.2 were heavily affected by pile-up, so we used only the MOS data. The source spectra were extracted from a 20$''$ radius circular region in both MOS detectors. This QSO is located in a rich cluster, and *ROSAT* detected the ICM thermal emission (Saxton et al. 1997; Hall et al. 1997). We subtracted the soft X-ray emission from the cluster, as explained in Sect. 3.3.3.

The MOS cameras operated in small-window mode, so we considered the pn image to model the cluster (the pile-up only affects the central region of the source). We extracted a spectrum from an annular region between 20$''$ and 80$''$ (constrained to the CCD where the source is located). The resulting temperature of the `zbremss` model was $kT = 2.3^{+1.0}_{-0.6}$ keV. We also used the *Chandra* radial X-ray brightness profile published by Fang et al. (2002), (core radius of $17''.6 \pm 0''.17$, $\beta = 0''.74^{+0''.05}_{-0''.03}$), to renormalize the cluster model (see Sect. 3.3.3). The cluster X-ray emission is 32% of the total 0.5-10 keV luminosity.

The source spectrum best fit is a power law ($\Gamma = 1.57^{+0.10}_{-0.11}$) with a soft thermal component. A `pexrav` model is formally the best fit ($\chi^2/\nu = 321/333$) of this spectrum. As discussed for PG 1247+267, the steeper photon index ($\Gamma \sim 2.3$) and the extremely large reflection scaling factor $\gg 1$ ($R \sim 15$) led us to adopt the former model as our best fit.

The photon index of the power law is not consistent with previous X-ray observations with *ASCA* ($\Gamma = 1.75 \pm 0.03$, Yamashita et al. 1997) and *Chandra* ($\Gamma = 1.761^{+0.047}_{-0.052}$, Fang et al. 2002).

In Fig.3.1(j) a systematic effect in the $\Delta\chi^2$ spectrum can be seen above 5 keV. This may be due to a bad extraction of the cluster emission or to the use of the blank-field background. Ignoring data above 4.5 keV we obtain a steeper photon index ($\Gamma = 1.68 \pm 0.11$), compatible with previous X-ray observations.

A thermal component is also detected, with a temperature of $0.49^{+0.09}_{-0.08}$ keV, consistent with SB emission. However, if this emission were to be associated with the SB, the bolometric luminosity of the SB would be three orders of magnitude higher than the luminosity calculated using the IR data (Farrah et al. 2002a). The soft component-to-power law luminosity ratio is in the range of that typically observed in AGN.

Ginga (Kii et al. 1991), *ASCA* (Yamashita et al. 1997) and *Chandra* (Fang et al. 2002; Yaqoob and Serlemitsos 2005) detected iron emission features in this HLIRG. Jiménez-Bailón et al. (2007) detected a Fe-K emission line with a complex structure in the XMM-*Newton* pn spectrum of this source. We also detected an emission line in the 6-7 keV rest frame band, but the significance of the detection ($< 2\sigma$) was below our adopted threshold, and therefore we have not considered it further. We estimated a 3σ flux upper limit to a broad ($\sigma = 0.1$ keV) line component at 6.4 keV of $< 3 \times 10^{-5}$ photons cm^{-2} s^{-1}, consistent with the value $\sim (3 \pm 1) \times 10^{-5}$ photons cm^{-2} s^{-1} obtained with *Chandra* data (Fang et al. 2002).

The X-ray spectrum of this object is therefore consistent with a pure AGN origin. The study of the full SED of this source detect an SB component needed to reproduce its FIR emission, but the SB emission in the X-ray range is negligible compared to the AGN (see Chapter 5).

3.4 Discussion

Franceschini et al. (2003), studying the X-ray emission of ULIRG, define that the X-ray emission of a ULIRG is AGN-dominated if it presents either: a) a high X-ray luminosity, $L(2-10\text{ keV}) > 10^{42}$ erg s^{-1}; b) a heavily obscured hard X-ray component with $N_H > 10^{22}$ cm^{-2} (very flat or inverted hard X-ray spectra); or c) a Fe-K emission complex at $\sim$ 6.4 keV with equivalent width $\gtrsim$ 1 keV (iron fluorescent emission from material illuminated by the AGN). The ten detected HLIRG from our sample present at least one of the three characteristics above, thus showing an AGN-dominated X-ray spectrum.

This result is in agreement with the trend noted by Veilleux et al. (2002) for ULIRG: the fraction of sources with Seyfert characteristics increase with L_{IR} (from $\sim$ 25% among ULIRG with $L_{IR} < 10^{12.3}$ $L_\odot$ to $\sim$ 50% among those with $L_{IR} > 10^{12.3}$ $L_\odot$). However, we must keep in mind that our sample is not complete, and could be slightly biased towards the presence of an AGN. Taking into account only those sources that belong to the RR00 sub-sample 1, which is not biased in favour of AGN (see Chapter 2, Sect. 2.1), we found that five out of seven objects ($\sim$ 70%) harbour an AGN. The other two sources were not detected by XMM-*Newton*.

Five objects from our full sample (four type 2 objects and one NL object) are probably CT, as reported in the literature. Our analysis of the XMM-*Newton* data of two of them (IRAS 00182-7112, IRAS 12514+1027) is consistent with the CT hypothesis, as well as our combined analysis of *Beppo*SAX and XMM-*Newton* data for IRAS 09104+4109. A heavily obscured environment could also explain the non-detection of a fourth one (IRAS F00235+1024). We have found no absorption features in the last one (IRAS F15307+3252), but as explained in Sect. 3.3.5, ulterior XMM-*Newton* observations suggest the presence of a CT obscured AGN (Iwasawa et al. 2005).

3.4.1 Comparison with IR emission

We calculated the FIR (40-500 μm) luminosities ($L_{\rm FIR}$) of these HLIRG using the *IRAS* fluxes (see Table 3.4) as in Sanders and Mirabel (1996). In Fig. 3.2 we plotted the 2-10 keV luminosities of their power law component versus their FIR luminosities. We included the ULIRG sample from Franceschini et al. (2003) and the high-z QSO from Stevens et al. (2005) for comparison. No significant correlation between the 2-10 keV and the FIR luminosity is found in HLIRG, although it must be kept in mind that this sample is not complete in any sense.

We estimated the expected X-ray luminosity for a standard AGN, given its FIR luminosity. To this end, we calculated the 2-10 keV-to-FIR luminosity ratio typical of nearby bright QSO, using their average SED. Since the original Elvis et al. (1994) sample was biased towards bright sources in X-rays, we employed the Risaliti and Elvis (2004) new data on QSO SED. Using this corrected SED, the ratio of the 2-10 keV band to bolometric luminosity changes significantly by a factor 2, from $\sim$ 0.03 to $\sim$ 0.015. The X-ray luminosity derived from the IR luminosity using the latter ratio is plotted in Fig. 3.2 with a thick solid line. The top area between thin lines ("AGN zone") is the dispersion of the SED, calculated with the 90 percentile distribution (Elvis et al. 1994).

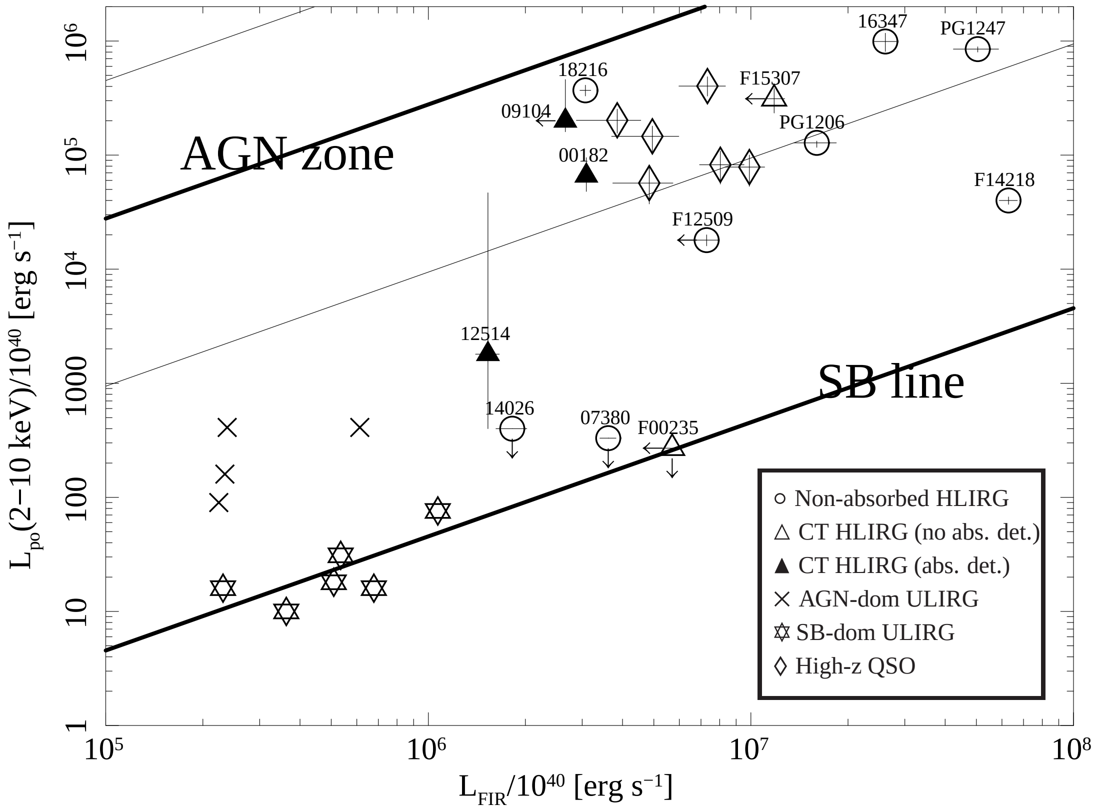

FIGURE 3.2: 2-10 keV X-ray luminosity of the power law component versus FIR luminosity. Filled symbols represent sources where we have detected X-ray absorption (models D or F in Table 3.3). The top thick solid line and area between the thin solid lines ("AGN-zone") indicate the X-ray luminosity expected for an AGN of a given FIR luminosity (90% dispersion, Elvis et al. 1994; Risaliti and Elvis 2004). The bottom thick solid line ("SB-line") indicates the X-ray luminosity expected for an SB of a given FIR luminosity (Persic et al. 2004; Kennicutt 1998). See Sect. 3.4 for details.

We can also calculate a relationship between FIR and X-ray luminosity for SB galaxies. The SFR of an SB can be estimated by its FIR luminosity (Kennicutt 1998) through

$$\mathrm{SFR_{FIR}} \sim \frac{L_{\mathrm{FIR}}\ (\mathrm{erg\ s^{-1}})}{2.2\times 10^{43}}\ M_{\odot}\ \mathrm{yr}^{-1}, \tag{3.2}$$

and by its 2-10 keV X-ray luminosity (Persic et al. 2004) by

$$\mathrm{SFR_{X}} \sim \frac{L_{2-10\ \mathrm{keV}}\ (\mathrm{erg\ s^{-1}})}{10^{39}}\ M_{\odot}\ \mathrm{yr}^{-1}. \tag{3.3}$$

Assuming equal SFR, the 2-10 keV to FIR luminosity ratio is

$$\frac{L_{2-10\ \mathrm{keV}}}{L_{\mathrm{FIR}}} \sim 4.5\times 10^{-5}. \tag{3.4}$$

This relation is shown in Fig. 3.2 as the lower solid line ("SB line").

Most HLIRG and all high-z QSO are in the "AGN-zone", but all towards higher IR-to-X-rays flux ratios (see Sect. 3.4.2), while only the AGN-dominated ULIRG and two HLIRG (IRAS 12514+1027 and

IRAS F14218+3845) seem to be composite sources: their X-ray luminosity is too high to be produced only by an SB (above the "SB-line"), and their FIR luminosity is too high to be produced only by an AGN (to the right of the "AGN-zone"). The SB-dominated ULIRG are, as expected, concentrated near the "SB-line". The upper limits for the X-ray-undetected HLIRG (IRAS F00235+1024, IRAS 07380-2342 and IRAS 14026+4341) seem to indicate that their hard X-ray emission should come only from SB activity, but a heavy obscured environment could also explain the low X-ray luminosities of these sources. In fact, the analysis of their MIR spectra reveals that all of them harbour an AGN (see Chapter 4), so its X-ray emission could be depressed by heavy absorption. However, one of them (IRAS 14026+4341) is an optical QSO, where little or no absorption is expected. Nevertheless, optical QSO from Stevens et al. (2005) show significant absorption in X-rays ($21 < \log N_{\rm H} < 22$ cm^{-2}). XMM-*Newton* observations of these high-z HLIRG suggest highly ionized winds with $22.5 < \log N_{\rm H} <$ 23.5 cm^{-2} (Page et al. 2007, Page et al. 2010, submited) to explain this absorption. Further sensitive data on isotropic indicators (such as FIR or MIR or high energy emission beyond 10 keV) are needed to investigate the seemingly contradictory nature of this HLIRG (see Chapters 4 and 5).

Note that if the Elvis et al. (1994) X-ray-to-FIR ratio is used instead of the Risaliti and Elvis (2004) ratio, only three HLIRG (IRAS 09104+4109, IRAS 16347+7037 and IRAS 18216+6418) would lie on the "AGN-zone", and the rest would be considered as composite AGN/SB sources. This confirms the relevance of the Risaliti and Elvis (2004) correction.

3.4.2 Origin of the IR "excess"

Figure 3.2 shows that the HLIRG FIR emission is systematically above the Risaliti and Elvis (2004) estimate for a standard local QSO of the same X-ray luminosity (i.e., the sources are located to the right of the thick upper line in the plot). This FIR excess could be associated with the SB activity in HLIRG. Alternatively, this could also hint to a possible difference between the SEDs of standard QSO and AGN in HLIRG. In this line, it has been shown that the shape of the QSO SED is probably related to the luminosity (Marconi et al. 2004; Hopkins et al. 2007).

We attempted to unravel the origin of this FIR excess. We estimated the AGN contribution to the total IR luminosity of the HLIRG in two independent ways, in order to know if the excess comes from SB activity, or from an intrinsic difference in the AGN SED.

On one hand, RR00 modeled the IR SED of all sources in this sample with RTM and estimated the contribution of the AGN dust torus ($L_{\rm IR,RR}^{\rm AGN}$) and of the SB to the total IR luminosity (1-1000 μm, $L_{\rm IR,RR}$) (Table 3.4, columns 9 and 10 respectively). For the sources IRAS F00235+1024, IRAS 07380-2342, IRAS F12509+3122, IRAS 12514+1027, IRAS 13279+3401, IRAS 14026+4341, IRAS F14218+3845, IRAS F15307+3252 and IRAS 16347+7037, instead of using the AGN relative contributions estimated by RR00, we included the results of F02; Verma et al. (2002); Farrah et al. (2002b), where new IR and sub-mm data were used (see Table 2.2).

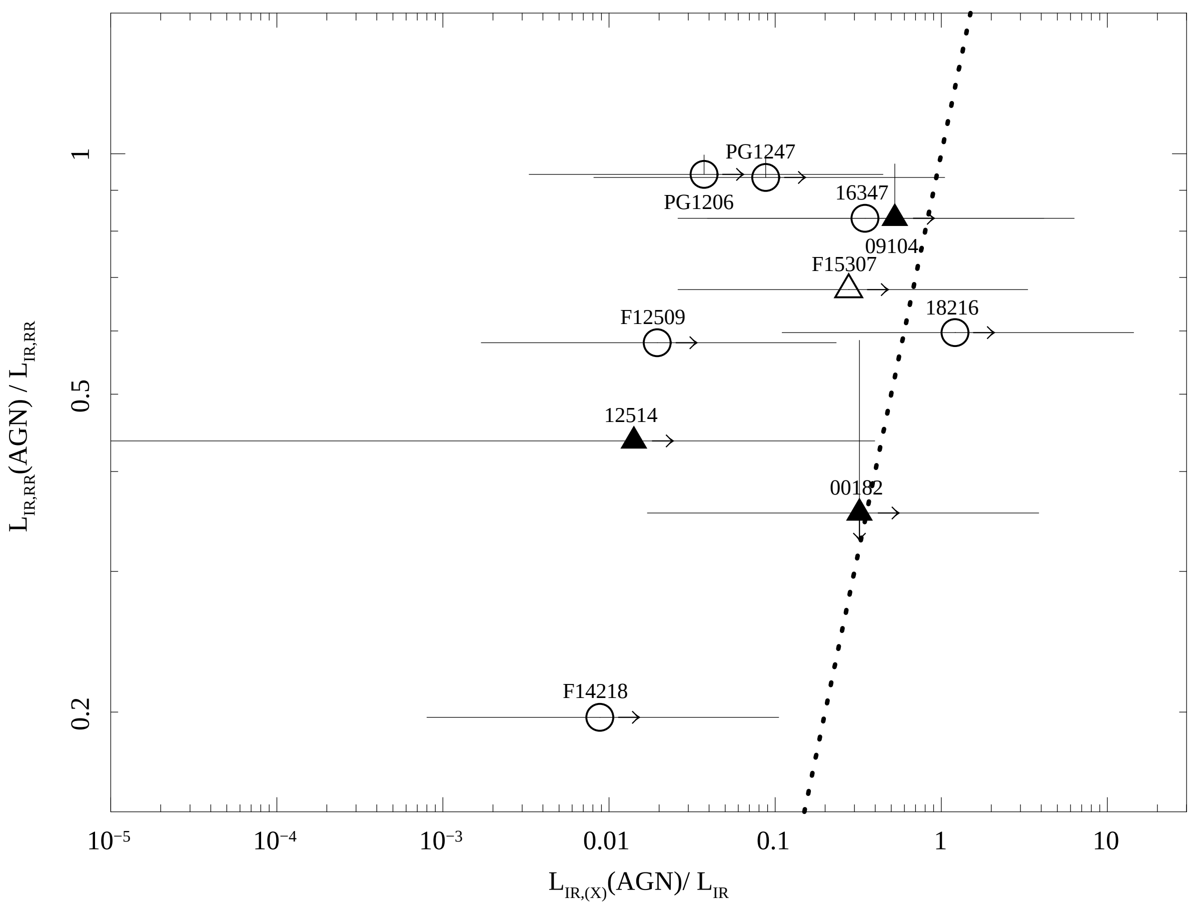

FIGURE 3.3: AGN to total-IR luminosity ratio, calculated by RR00, versus AGN (estimated through our X-ray data) to total (computed with the *IRAS* fluxes) IR luminosity ratio. The dotted line means equal values for the ratios. In the case of upper limits we plot as error bars the dispersion of X-ray-to-IR luminosity ratio from Elvis et al. (1994). IR estimates for IRAS F00235+1024, IRAS 07380-2342, IRAS F12509+3122, IRAS 12514+1027, IRAS 14026+4341 and IRAS F14218+33845 were taken from F02; for IRAS F15307+3252, from Verma et al. (2002) results; for IRAS 16347+7037 they were from Farrah et al. (2002b). Symbols as in Fig. 3.2.

On the other hand, assuming that the power law X-ray luminosity is associated with an AGN with a standard SED (Risaliti and Elvis 2004) we can apply the IR-to-2-10 keV luminosity ratio, similarly to that shown in Fig. 3.2 and obtain an independent estimate of the expected IR luminosity of the AGN ($L_{\mathrm{IR,(X)}}^{\mathrm{AGN}}$). We can also obtain an independent estimate of the total IR luminosity, L_{IR}, for each source through their IRAS fluxes as in Sanders and Mirabel (1996).

Figure 3.3 compares the relative contribution of the AGN to the total IR luminosity calculated through RTM, to our estimate obtained from X-ray data (we included only the X-ray detected sources). The dotted line corresponds to the 1:1 relation, i.e. an agreement between the two estimates. Most of the sources have lower limits on the abscissae because their 12 and 25 μm *IRAS* fluxes are upper limits (see Table 3.4).

Our estimates of the AGN relative contribution for all sources are formally consistent with those of RR00. However, there seems to be a systematic overestimate of the IR AGN component from RR00

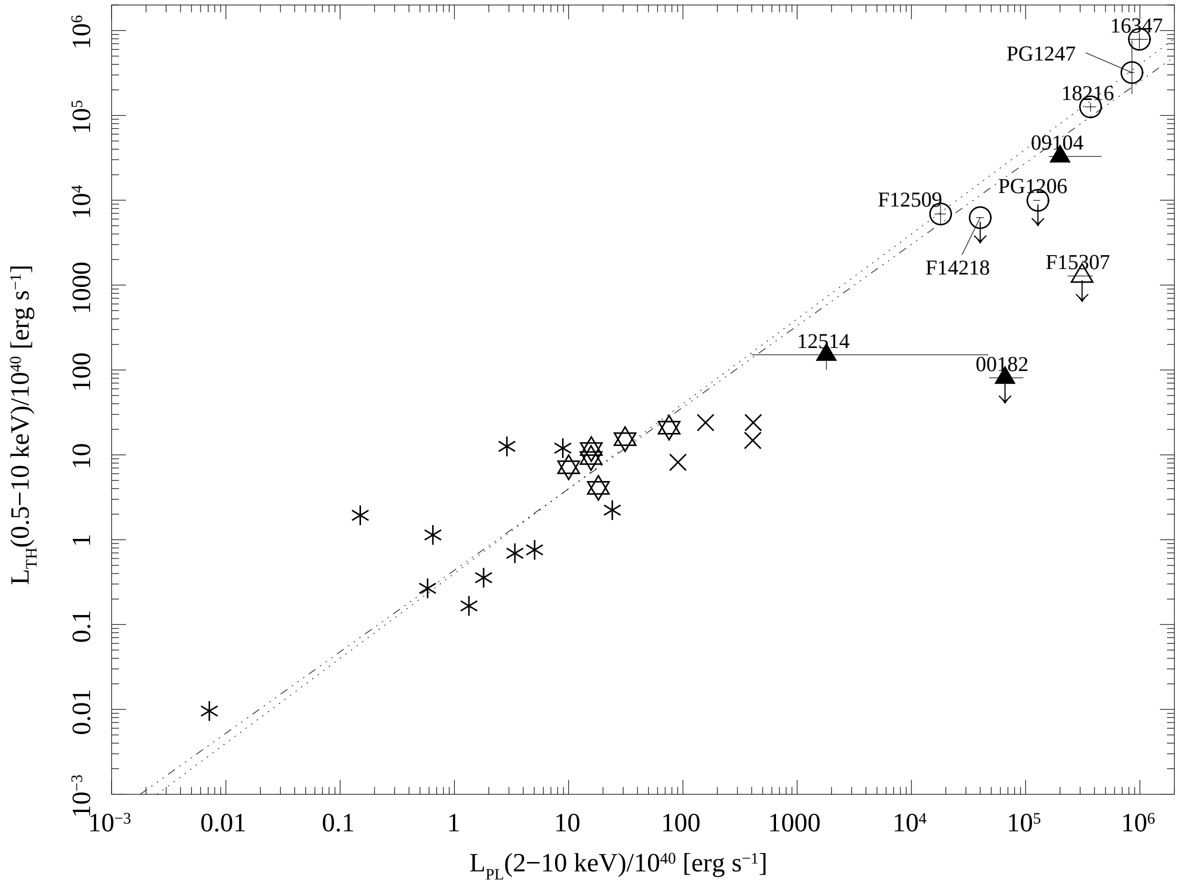

FIGURE 3.4: L_X (0.5-10 keV) of the soft excess component versus L_X (2-10 keV) of the power law component. Asterisks represent SB galaxies from Franceschini et al. (2003). The dotted line is a correlation obtained by Franceschini et al. (2003) for SB-dominated ULIRG. The dash-dotted line is a correlation for the SB-dominated ULIRG and the SB galaxies samples calculated by us. The soft excess in IRAS 09104+4109 is probably associated with cluster emission (see Sect. 3.3.5 for details). Symbols as in Fig.3.2.

with respect to the X-ray measurements.

The values of $L^{\rm AGN}_{\rm IR,(X)}/L_{\rm IR}$ plotted in Fig. 3.3 are independent of the SB luminosity, so this disagreement is probably due to the IR-to-X-ray ratio used to estimate the AGN IR luminosities through the X-ray luminosities. This favors the hypothesis of an intrinsic difference between the standard QSO SED and the AGN component of the HLIRG SED. This difference could be explained by the high luminosity of HLIRG compared to the local quasars used to estimate the Elvis et al. (1994) SED. It has been observed that $\alpha_{\rm OX}$ (i.e. the ratio between optical and X-ray luminosities) of QSO depends on the bolometric luminosity (Strateva et al. 2005; Steffen et al. 2006) and hence there is a dependence between the luminosity and SED shape of AGN (Hopkins et al. 2007). This topic is discussed in further detail in Chapter 5.

3.4.3 Soft X-ray excess

Fig. 3.4 is a luminosity-luminosity plot of the soft X-ray excess versus power law components. In IRAS 09104+4109, IRAS F12509+3122, PG 1247+267, IRAS 16347+7037 and IRAS 18216+6418 the soft excess component is too luminous to come solely from an SB (see Sect. 3.3.5 for a detailed description of each source). In the case of IRAS 09104+4109 the soft excess is probably due to an incomplete subtraction of the cluster emission, while in the remaining four sources is probably of the same origin as in luminous QSO (Piconcelli et al. 2005).

An X-ray thermal component associated with SB emission has been observed in all ULIRG from Franceschini et al. (2003). However, only in one out of thirteen HLIRG we have found a soft X-ray emission whose origin could be associated with SB activity. However this cannot lead to reject the existence of star formation processes in these sources. If SB and AGN contributions to the bolometric output are roughly equal, and the AGN X-ray emission is not absorbed, then the SB X-ray emission is around two orders of magnitude lower than the AGN emission in the soft X-ray band. Hence the XMM-*Newton* sensitivity could be insufficient to detect such a faint SB component. Only newer X-ray observatories, like the International X-rat Observatory (IXO, White and Hornschemeier 2009), could reach the sensitivity needed in such conditions.

The above HLIRG with AGN-like soft excess emission follow the correlation found for SB-dominated ULIRG by Franceschini et al. (2003) (dotted line in Fig. 3.4). To increase the statistics and to test if this correlation holds at lower IR luminosities, we included a sample of lower luminosity SB galaxies (Franceschini et al. 2003, and references therein).

The thermal emission of SB galaxies and SB-dominated ULIRG is originated in diffuse thermal plasma heated by supernova explosions and the power law is emitted by X-ray binaries. In AGN-dominated ULIRG the power law is a mixture of X-ray binaries and the AGN emission, and the thermal emission is associated with SB phenomena. Finally, for all but one of our sources both the thermal and the power law is emitted by the AGN. In spite of the different physical origins, somehow the ratio of both components manages to stay constant over eight orders of magnitude.

We calculated a non-parametric correlation coefficient (generalized Kendall's Tau[7]) for the SB galaxies and the SB-dominated ULIRG, finding a significance level[8] of 99.98% ($> 3\sigma$) for this correlation. The correlation slope is consistent with that obtained by Franceschini et al. (2003) for SB-dominated ULIRG only.

We also investigated the relationship between the X-ray soft excess component luminosity and the FIR luminosity (Fig. 3.5), both presumably related to star formation, finding no clear correlation. Using the generalized Kendall's Tau test, the significance level of the possible correlation is 96.66% ($< 3\sigma$).

[7] We employed the ASURV software for this test (Isobe et al. 1985, 1986).

[8] Note that even excluding the isolated source in the bottom left corner, this correlation remains almost unchanged.

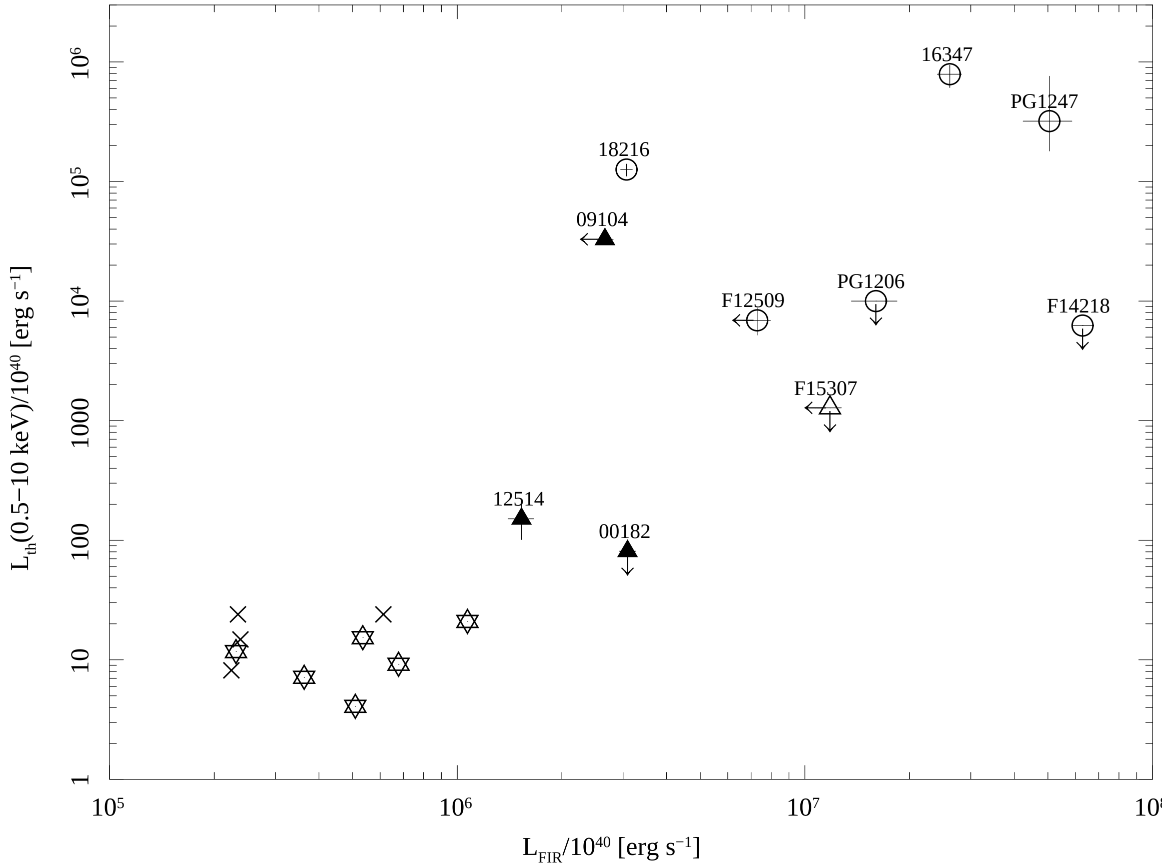

FIGURE 3.5: L_X (0.5-10 keV) of the soft excess component versus FIR luminosity. The soft excess in IRAS 09104+4109 is probably associated with cluster emission (see Sect. 3.3.5 for details). Symbols as in Fig.3.2.

3.4.4 Cosmic evolution

We also tested a possible cosmological evolution in the sample. We estimated the SFR for each source using its IR luminosity (Kennicutt 1998). Their SFR and 2-10 keV-to-IR-luminosity ratio versus redshift are plotted in Fig. 3.6. Cosmic star formation shows a large decline between $z \sim 2$ and the present day (Franceschini et al. 1999), so we expect an increment of the SFR of HLIRG up to $z \sim 2$. Higher SFR at higher redshift is observed in the upper panel of Fig. 3.6. However the sources follow the lower envelope, which is the *IRAS* FSC sensitivity limit (solid line in Fig. 3.6), clearly indicating a selection effect. Therefore, we cannot draw conclusions about the dependence of SFR with redshift.

As shown in the bottom panel of the Fig. 3.6, the ratio of hard X-ray-to-FIR luminosity remains roughly constant with z. This holds even if we subtract the FIR luminosity emitted by the AGN, calculated using the X-ray PL luminosity as in Fig. 3.3.

We have seen that the IR emission is consistent with an AGN origin, but if we assume that the IR excess shown in Fig. 3.2 is associated with the SB activity, Fig. 3.6 shows that its evolution must be similar to that of the X-ray emission. This, in turn, suggests that the presence of an SB and the occurrence of AGN activity through accretion onto a super-massive black hole are physically related. This result is in

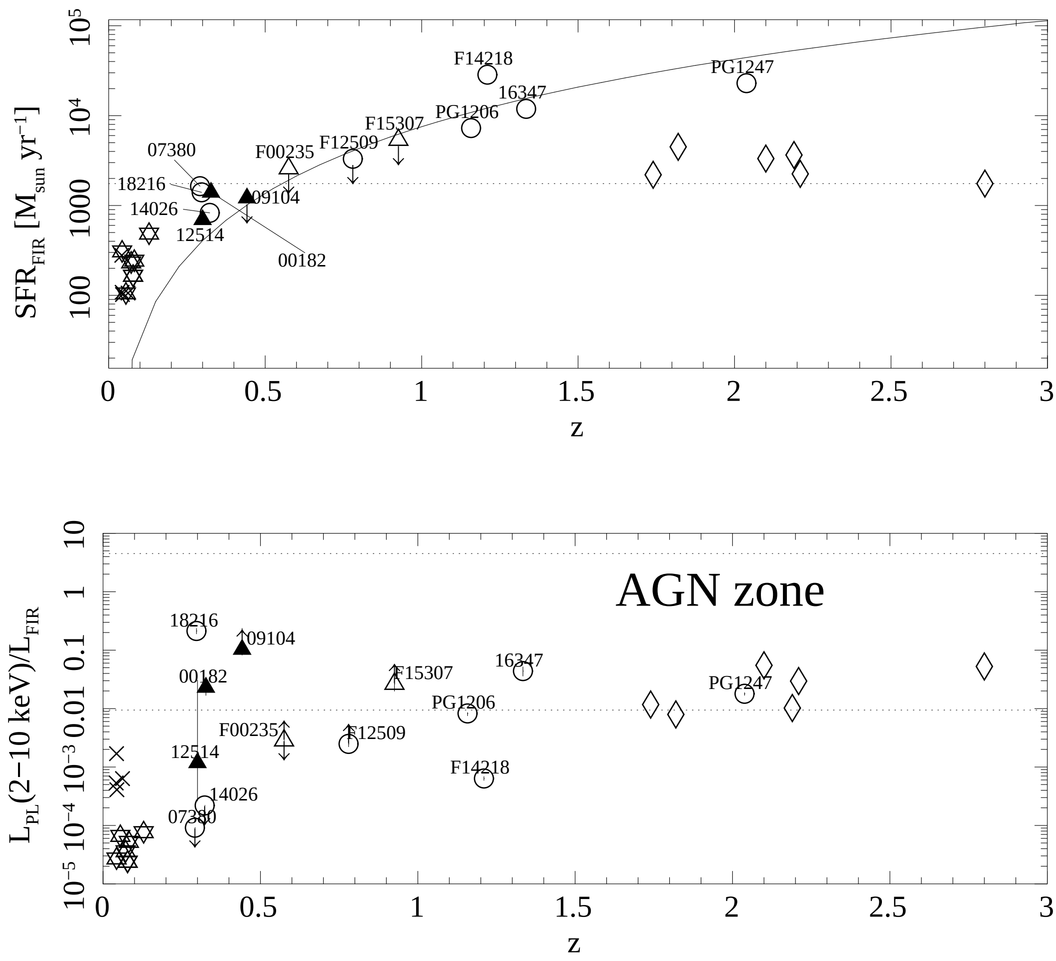

FIGURE 3.6: Symbols as in Fig.3.2. **Top:** SFR derived from FIR luminosity (Kennicutt 1998), versus redshift. The dotted line represents the SFR limit corresponding to the HLIRG definition. The solid line is the SFR for a source with *IRAS* fluxes equals to the *IRAS* FSC sensitivity limits (Moshir et al. 1990). **Bottom:** 2-10 keV power law-X-ray-to-FIR luminosities ratio versus redshift. The area between the dotted lines represent the expected ratio for a quasar (with 90% of dispersion) with a standard SED (Elvis et al. 1994; Risaliti and Elvis 2004).

agreement with the coeval black hole/stellar bulge formation hypothesis (Granato et al. 2004; Stevens et al. 2005; Di Matteo et al. 2005).

3.5 Conclusions

We performed a systematic X-ray study of a sample of thirteen HLIRG using XMM-*Newton* data from the public archive and our own private data. We modelled the X-ray spectra of each source, finding very heterogeneous spectral properties, with all X-ray detected HLIRG of the sample (ten sources) having AGN-dominated X-ray spectra.

The hard X-ray luminosity of most X-ray detected HLIRG (eight out of ten) is consistent with emission originated in an AGN. Only two HLIRG (IRAS 12514+1027 and IRAS F14218+3845) seem to show a composite AGN/SB nature: their X-ray luminosity is too high to be produced only by an SB, and their IR luminosity is too high to be produced by only an AGN. The remaining three HLIRG (IRAS F00235+1024, IRAS 07380-2342 and IRAS 14026+4341) are undetected in X-rays.

There are five Compton-thick candidate sources in our sample, including all the type 2 AGN (four) and one SB object still undetected in X-rays. We found evidence for X-ray absorption in three of the type 2 AGN and our analysis supports the Compton-thick nature of these sources. Through the study of their MIR spectra we were able to confirm the presence of highly obscured AGN in these sources (see Chapter 4).

We detected five HLIRG with soft excess emission. Four sources present luminosities consistent with type 1 AGN soft excess. While all ULIRG from Franceschini et al. (2003) present a soft X-ray thermal component associated with an SB, only in one HLIRG we did find a soft excess probably associated with SB emission. However we cannot reject the presence of an SB component which can be faint in X-rays but significantly important for the bolometric output. We need data in other spectral windows (e.g. MIR observations) and alternative techniques of analysis to detect the SB emission (see Chapters 4 and 5).

We have also seen that the hard X-ray luminosity associated with the AGN is systematically below that expected for a local QSO (Elvis et al. 1994; Risaliti and Elvis 2004) of the same IR luminosity. This could be explained by an intrinsic difference between the SED of the AGN component in HLIRG and the SED of local QSO. A different explanation could be that the IR luminosity of these objects have a strong IR contribution from SB, larger than in “normal” QSO. Our analysis seem to favour the former hypothesis, but more conclusive evidence is needed: in Chapter 5 we carry out a detailed study of the broadband (from radio to X-rays) SED of these HLIRG to obtain a better understanding of this issue.

We have also found that the hard-X-ray-to-FIR luminosity ratio remains constant with z, suggesting that the AGN and SB phenomena are physically connected in HLIRG.

Chapter 4

Analysis of *Spitzer*-IRS spectra of HLIRG

4.1 Motivation

In Chapter 3 we used X-ray spectroscopy to disentangle the AGN and SB emission of HLIRG. We found X-ray thermal emission associated with SB for just one source. If this component actually exists in the remaining sources, the much brighter AGN emission probably dilutes the X-rays originated in star-forming processes.

We also found strong evidence that a significant fraction of these objects is heavily obscured, reaching the Compton Thick level (hydrogen column, $N_H > 10^{24}$ cm^{-2}), as previous studies for some of them suggested (Wilman et al. 2003; Iwasawa et al. 2005), allowing, in the best case, only the detection of reflected X-ray emission. To avoid these problems and to obtain an independent and complementary view of these objects we need to move to another spectral window.

In this chapter we present a study of a sample of HLIRG in the Mid-Infrared (MIR), within the wavelength range 5-8 μm. This spectral range is very efficient in detecting AGN emission and less affected by absorption than the X-rays. The studied sample, the *Spitzer* HLIRG sample (see Chapter 2), is composed of thirteen HLIRG observed with the IRS instrument onboard *Spitzer*, nine of them also observed by XMM-*Newton*.

Several diagnostic methods are available to unravel the AGN and SB activity through the MIR spectra, e.g. the study of high-ionization emission lines and the polycyclic aromatic hydrocarbon (PAH) features (Laurent et al. 2000; Spoon et al. 2007), or the analysis of the continuum around 4 μm (Risaliti et al. 2006). The MIR continuum of pure AGN and pure SB show small dispersion shortward of 8 μm (Netzer et al. 2007; Brandl et al. 2006), allowing the use of universal templates to reproduce the AGN and SB emission in sources where both physical processes are present. Hence, we can decompose the AGN and SB components of composite sources modelling the continuum of their MIR spectra with these templates.

The SB/AGN continuum spectral decomposition has been used successfully on ULIRGs (Nardini et al. 2008; Risaliti et al. 2010; Nardini et al. 2009, 2010) to disentangle the emission of both components. A significant number of HLIRG has been observed with the Infrared Spectrograph (IRS, Houck et al. 2004) on board *Spitzer*, allowing good quality spectra to apply this diagnostic technique. The key reason for using the continuum emission at $\lambda \simeq 5-8\,\mu$m as a diagnostic is the difference of the 3 μm to bolometric ratios between AGN and SB (approximately two orders of magnitude larger in the former). This makes the detection of the AGN component possible even when the AGN is heavily obscured and/or bolometrically weak compared to the SB. However this difference of the bolometric ratios is lower than that showed in the X-ray range, which can reach three or four orders of magnitude (see Chapter 5, Fig. 5.7), allowing the detection of the SB emission even in AGN dominated sources.

This chapter is outlined as follow. Section 4.2 describes the *Spitzer* IR telescope. The IRS data reduction is explained in Sect. 4.3. In Sect. 4.4 we briefly explain the decomposition process and the results obtained. Section 4.5 present results obtained through the MIR spectral analysis and Sect. 4.6 summarizes our conclusions.

4.2 The *Spitzer* Space Telescope

The *Spitzer Space Telescope* (Werner et al. 2004) is the fourth and final element in NASA's family of Great Observatories. *Spitzer* was launched on the 25th of August of 2003 into an Earth-trailing heliocentric orbit.

The Observatory carries an 85-centimetre cryogenic telescope and three cryogenically cooled science instruments capable of performing IR imaging and spectroscopy in the 3.6 to 160 μm range. While the Spitzer cryogenic lifetime requirement was 2.5 years of normal operations, the actual cryogenic lifetime was 5 years and a half. The cryogen was depleted on May 15, 2009.

On the focal plane of the telescope there are three science instruments. Wide field, broadband imaging is the main purpose of the Infrared Array Camera (IRAC), working in the 3.6-8 μm range, and the Multiband Imaging Photometer for Spitzer (MIPS), working in the 24-160 μm. The spectroscopic functions of the observatory are carried out mainly by the Infrared Spectrograph (IRS) in the 5-40 μm range. In addition, MIPS has a low resolution spectroscopic mode between 55-95 μm.

4.2.1 Infrared Array Camera

IRAC (Fazio et al. 2004) is a four-channel camera able to perform IR imaging in four bands (3.6, 4.5, 5.8, and 8 μm) simultaneously over a 5.2×5.2 arcmin field of view (FOV). 3.6 and 5.8 μm channels view the same telescope field, and 4.5 and 8 μm channels view a different adjacent field simultaneously. IRAC provides diffraction-limited imaging internally; image quality is limited primarily by the Spitzer telescope. The angular resolution of the four detectors is ~ 1.5 arcsec. The median 1σ sensitivity for the four IRAC channels is 0.60 μJy, 1.2 μJy, 8.0 μJy and 9.8 μJy, respectively, for 100 seconds of integration with low background.

4.2.2 Infrared Spectrograph

The IRS (Houck et al. 2004) instrument provides *Spitzer* with low and moderate resolution spectroscopic capabilities from 5.2 to 38.0 microns. The IRS is composed of four separate modules, with two modules providing R~ 60 – 120 spectral resolution over 5.2-38.0 μm and two modules providing R~ 600 spectral resolution over 9.9-37.2 μm. The median 1σ continuum sensitivity for the IRS low-resolution modules is about 0.05 mJy and about 2mJy for the high-resolution modules, in 512 seconds of integration with low background.

IRS can operate in several different observation modes. The "staring mode" is the basic "point and shoot" operating mode of the IRS. In this configuration, science targets are placed on one or more of the IRS slits (corresponding to the diverse wavelength ranges and spectral resolutions) for a specified integration time. The total integration time is divided in "ramps" and "cycles". The ramp duration is the time between the first and last non-destructive reads of the detector, and the number of cycles is the number of times a given spectrum is repeated before moving on to the next slit or the next target. Standard staring mode successively places the target at two different slit locations for each requested slit and cycle to provide redundancy against cosmic rays and detector artifacts.

4.2.3 Multiband Imaging Photometer for Spitzer

MIPS (Rieke et al. 2004) is an instrument with capabilities for imaging and photometry in broad spectral bands centred nominally at 24, 70, and 160 μm, and for low-resolution spectroscopy between 55 and 95 μm. The instrument contains 3 separate detector arrays with an angular resolution of 6, 18, and 40 arcsec, at 24, 70 and 160 μm respectively. The sensitivity of MIPS is highly dependent of the IR sky background. For low background level the 1σ sensitivity is 16.1 MJy/ster, 5.15 MJy/ster, and 6.53 MJy/ster at 24, 70 and 160 μm respectively (for extended sources). All three arrays view the sky simultaneously. The 24 μm camera provides roughly a 5 arcmin square FOV. The 70 micron camera provides a FOV that is roughly 2.5 by 5 arcmin. The 160 μm array projects to the equivalent of a 0.5 by 5 arcmin FOV.

4.3 Data reduction

All sources from the *Spitzer* HLIRG sample has been observed by the IRS onboard *Spitzer* in low resolution mode (see Table 4.1). We have used public IRS spectra (data obtained in standard staring

TABLE 4.1: Description of the *Spitzer* observations.

Sources	Program ID	Exposure (s)	Date
IRAS 00182-7112	666	94.4	2003-11-14
IRAS F00235+1024	3746	94.4	2005-08-11
IRAS 07380-2342	3746	12.6	2005-03-23
IRAS 09104+4109	1018	73.4	2003-11-29
IRAS F10026+4949	82	14.7	2004-04-17
IRAS F12509+3122	3746	62.9	2005-06-06
IRAS 12514+1027	105	94.4	2005-02-06
IRAS 14026+4341	61	102.8	2005-05-22
IRAS F15307+3252	105	243.8	2004-03-04
IRAS F16124+3241	105	243.8	2005-03-19
EJ1640+41	3640	243.8	2005-08-13
IRAS 18216+6418	82	31.5	2004-04-17
IRAS F23569-0341	3746	243.8	2004-12-13

mode using the two low-resolution modules) from the *Spitzer* Archive. For our purpose the co-added images provided by the *Spitzer Science Centre* (SSC) are a good starting point. A co-added image is obtained as the average over multiple telescope pointings. Each snapshot of these images has been processed by the pipeline (version S15.3), that among other basic operations includes the linearisation and the fitting of the signal ramp, the dark subtraction and the flat-fielding (see IRS Pipeline Handbook, SSC 2005). Since each observation in staring mode consists of two exposures with different position of the source along the slit (see Sect. 4.2.2), the images have been background-subtracted by differencing the two observations in the nodding cycle.

The software `SPICE` was used for the extraction and the wavelength and flux calibration of the spectra, following the standard procedure for point-like sources (see IRS Data Handbook, SSC 2008). The spectra have been also de-redshifted to rest frame.

4.4 SB/AGN spectral decomposition

The MIR spectra of pure AGN and pure SB show little dispersion below the 9.7 μm silicate feature. This allow us the use of universal AGN/SB templates to parametrize the observed energy output of HLIRG in the wavelength range of the IRS shortward 8 μm.

Following the Nardini et al. 2008, hereafter N08, model for ULIRGs:

$$f_\nu^{\rm obs} = f_6^{\rm int} \left[\alpha_6 \, u_\nu^{\rm AGN} \, e^{-\tau(\lambda)} + (1 - \alpha_6) \, u_\nu^{\rm SB} \right], \tag{4.1}$$

where α_6 is the AGN relative contribution to the intrinsic flux density at 6 μm ($f_6^{\rm int}$) while $u_\nu^{\rm AGN}$ and $u_\nu^{\rm SB}$ are the AGN and SB templates normalized at 6 μm. This model has only three free parameters: α_6, the optical depth of the AGN at 6 μm ($\tau(6\ \mu$m)) and the flux normalization.

Additional high-ionization emission lines and molecular absorption features (due to ices and aliphatic hydrocarbons), whenever present, were fitted using Gaussian profiles.

The SB template used in our model was calculated by N08. This template is calculated from the mean MIR spectra of the five brightest sources among pure SB in their ULIRG sample. The SB emission present little spectral dispersion below 8 μm (see Fig. 4.1(a)).

The AGN emission is well reproduced using a power law with a fixed spectral index: $f_\lambda \propto \lambda^{0.8}$. The spectral index was calculated using the mean SED of the brightest PG QSO in the 3-8 μm band from Netzer et al. (2007) (see Fig. 4.1(b)).

The AGN component in this model was corrected with an exponential attenuation to take into account the reddening of the NIR radiation due to any compact absorber in the line of sight. The optical depth follows the conventional law $\tau(\lambda) \propto \lambda^{-1.75}$ (Draine 1989). The SB template does not need a similar correction because the possible effects of obscuration were already accounted in the observational template.

The modelling and fitting program Sherpa (Freeman et al. 2001), included in the software package CIAO 3.4 (Fruscione et al. 2006), was used to implement our model and analyse the spectra.

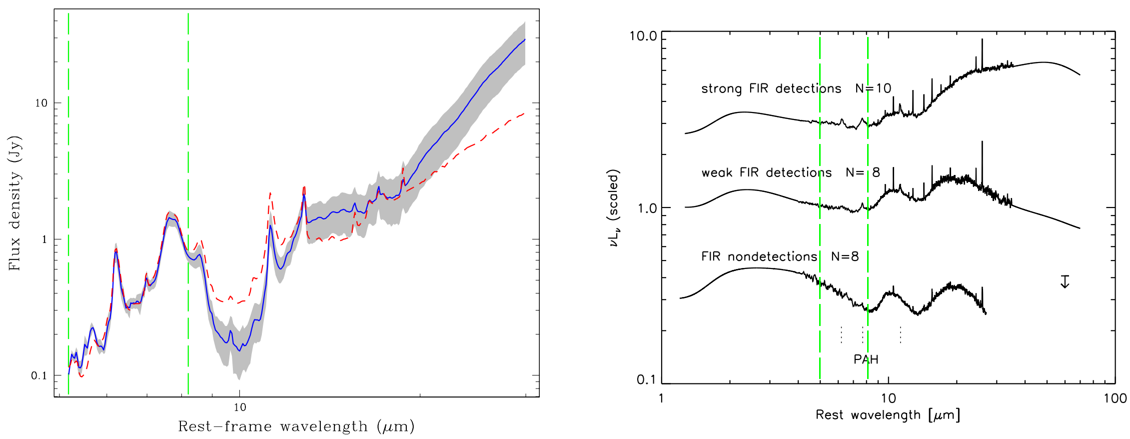

(a) SB MIR template.

(b) Mean AGN MIR spectra.

FIGURE 4.1: (a) Mean SB MIR spectra estimated by Brandl et al. (2006) (dashed red line) and N08 (solid blue line). The shaded grey area is the 1σ dispersion in the N08 spectra. Figure from N08. (b) Average MIR spectra of PG-QSO. Figure from Netzer et al. (2007). The vertical long-dashed green lines enclose the fitting region.

One of our HLIRG was barely detected by *Spitzer* and for three sources our model could not be properly applied (see below for a further discussion on these objects), but the rest of them (nine sources) were well fitted by our model (see Fig. 4.2 and Table 4.2).

The 6 μm emission of these HLIRG is largely dominated by the AGN component ($\alpha_6 > 0.9$), which also dominates along the 5-8 μm spectral range (see Fig. 4.2). IRAS F00235+1024 and particularly IRAS F16124+3241 are the only two sources where SB and AGN components are comparable, but even here the AGN emission is above that of the SB. Most sources optically classified as type I AGN show minor absorption, while all sources classified as NL or type II objects shows high absorption or broad absorption features (see Table 4.2).

4.4.1 Notes on particular sources

IRAS 00182-7112

This CT QSO2 shows a heavily absorbed spectrum and the continuum cannot be well estimated, so our model is not a good approximation in this case. The MIR spectrum shows no signs of SB activity within the 5-8 μm range, since the PAH features are totally suppressed, and it is very similar to the MIR spectra of deeply obscured AGN (e.g., NGC 4418, NGC 1068). This result, in addition to evidence from other wavelength regions (e.g., strong iron K_α emission line with equivalent width ~ 1 keV in the X-ray spectrum, see Chapter 3, Sect. 3.3.5), suggests that the power source hiding behind the optically thick material could be a buried AGN. The broadband SED of this source is also consistent with a CT source (see Chapter 5).

Spoon et al. (2004a) present a detailed study of these data: their analysis of the strong absorption and weak emission features in the 4-27 μm spectrum suggest the existence of a dense warm gas cloud close to the nucleus of the source. There is also evidence of star formation activity away from the absorbing region, being responsible for up to 30% of the IR luminosity of the system. As stated above, the high obscuration of this source suggest that the results obtained from our model are not reliable. Nevertheless, the SB contribution to the IR luminosity we obtained for this source ($\sim$ 20%, see Sect. 4.5.2 below) is consistent with the Spoon et al. (2004a) estimate.

IRAS 09104+4109

This is a radio-loud QSO 2 (Norman et al. 2002) and the MIR spectrum is probably dominated by synchrotron emission, modifying the shape of the AGN emission. Since our AGN template just models the reprocessed emission by dust, our model is inadequate for this object.

TABLE 4.2: Parameters of the best fit model.

Sources [a]	χ^2/d.o.f.	$f_6^{\mathrm{int}\ b}$ Jy	α_6 [b]	$\tau(6\ \mu\mathrm{m})$ [b]	Additional features
IRAS 00182-7112*	87 / 65	$0.104^{+0.006}_{-0.005}$	0.992 ± 0.003	0.73 ± 0.06	two broad bumps and two absorptions lines
IRAS F00235+1024	64 / 69	$0.090^{+0.018}_{-0.016}$	$0.983^{+0.006}_{-0.008}$	2.64 ± 0.19	-
IRAS 07380-2342	16 / 78	$0.217^{+0.019}_{-0.017}$	$0.992^{+0.007}_{-0.008}$	0.50 ± 0.08	-
IRAS 09104+4109*	30 / 71	$0.186^{+0.008}_{-0.007}$	0.997 ± 0.003	0.70 ± 0.04	one emission line
IRAS F10026+4949	26 / 141	$0.133^{+0.042}_{-0.009}$	> 0.993	$0.50^{+0.23}_{-0.06}$	-
IRAS F12509+3122	17 / 82	0.028 ± 0.002	$0.964^{+0.012}_{-0.014}$	0.10 ± 0.08	-
IRAS 12514+1027	26 / 66	$0.062^{+0.004}_{-0.025}$	$0.969^{+0.016}_{-0.010}$	$0.05^{+0.05}_{-0.04}$	one broad gaussian in absorption, one emission line, two absorption lines
IRAS 14026+4341	19 / 77	$0.075^{+0.004}_{-0.003}$	0.976 ± 0.006	0.06 ± 0.05	-
IRAS F15307+3252	72 / 86	0.034 ± 0.002	$0.967^{+0.009}_{-0.010}$	0.52 ± 0.06	-
IRAS F16124+3241	9 / 79	$0.008^{+0.005}_{-0.003}$	$0.90^{+0.05}_{-0.10}$	$1.4^{+0.5}_{-0.6}$	-
EJ1640+41	51 / 124	$0.018^{+0.003}_{-0.002}$	> 0.992	$0.17^{+0.13}_{-0.10}$	-
IRAS 18216+6418*	31 / 75	$0.149^{+0.007}_{-0.010}$	$0.991^{+0.006}_{-0.009}$	< 0.04	one broad gaussian in absorption

[a] Sources where our model is not reliable are marked with asterisk.
[b] All errors are quoted at 90% confidence level for one parameter of interest (i.e. $\Delta\chi^2 = 2.71$) throughout this chapter.

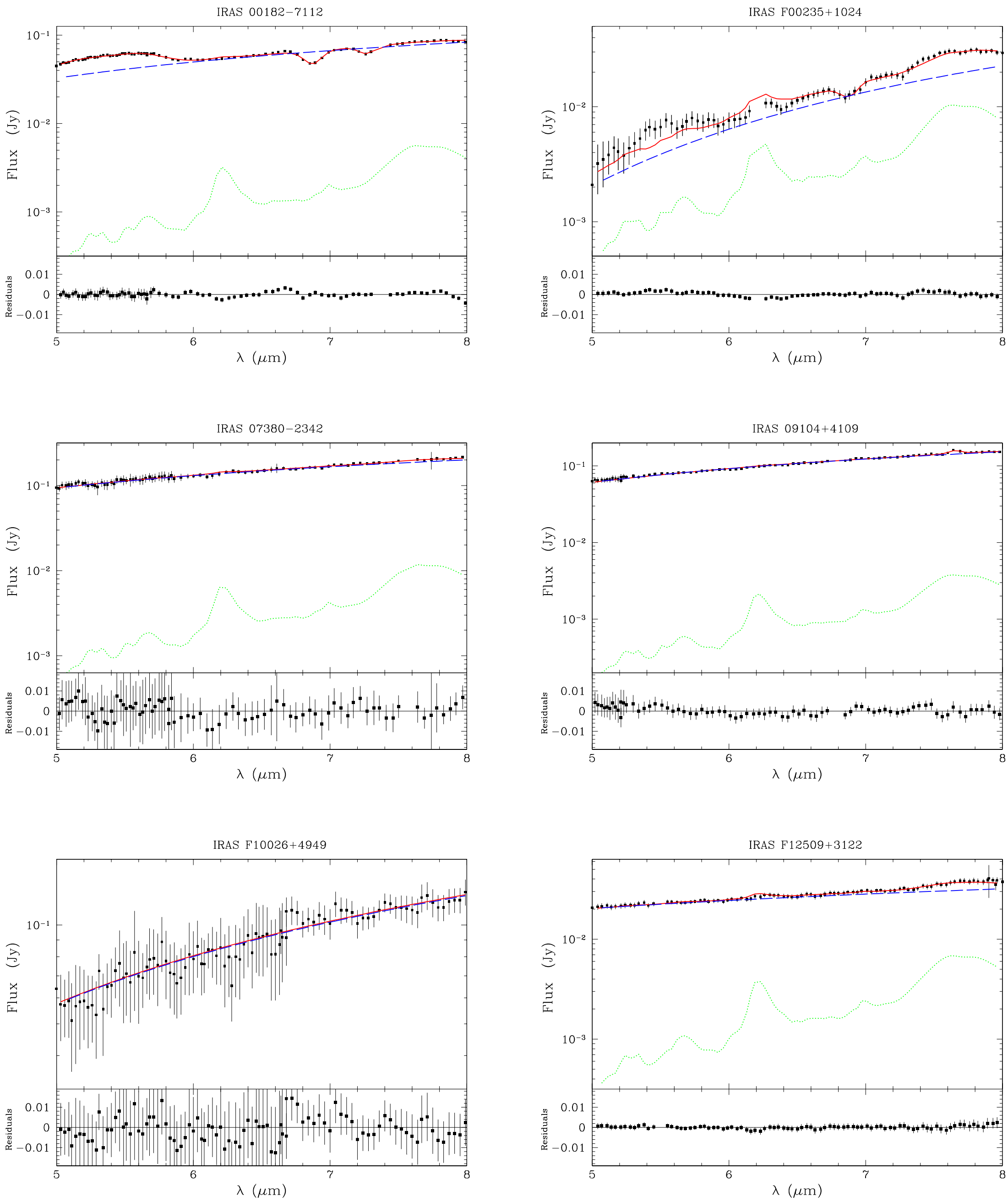

FIGURE 4.2: Rest-frame MIR spectra of HLIRG obtained with the IRS instrument onboard *Spitzer*. Solid red line is our best fit model, the blue dashed line is the AGN component and the green dotted line is the SB component.

IRAS 18216+6418

Our model did not fit well the spectrum of this QSO. The continuum seems to be flatter than the adopted power law. We could obtain a better fit by adding a broad Gaussian absorption feature, but nothing seems to justify this addition ($\tau(6\ \mu m) \sim 0$ and this object is a type I AGN). The flatter continuum

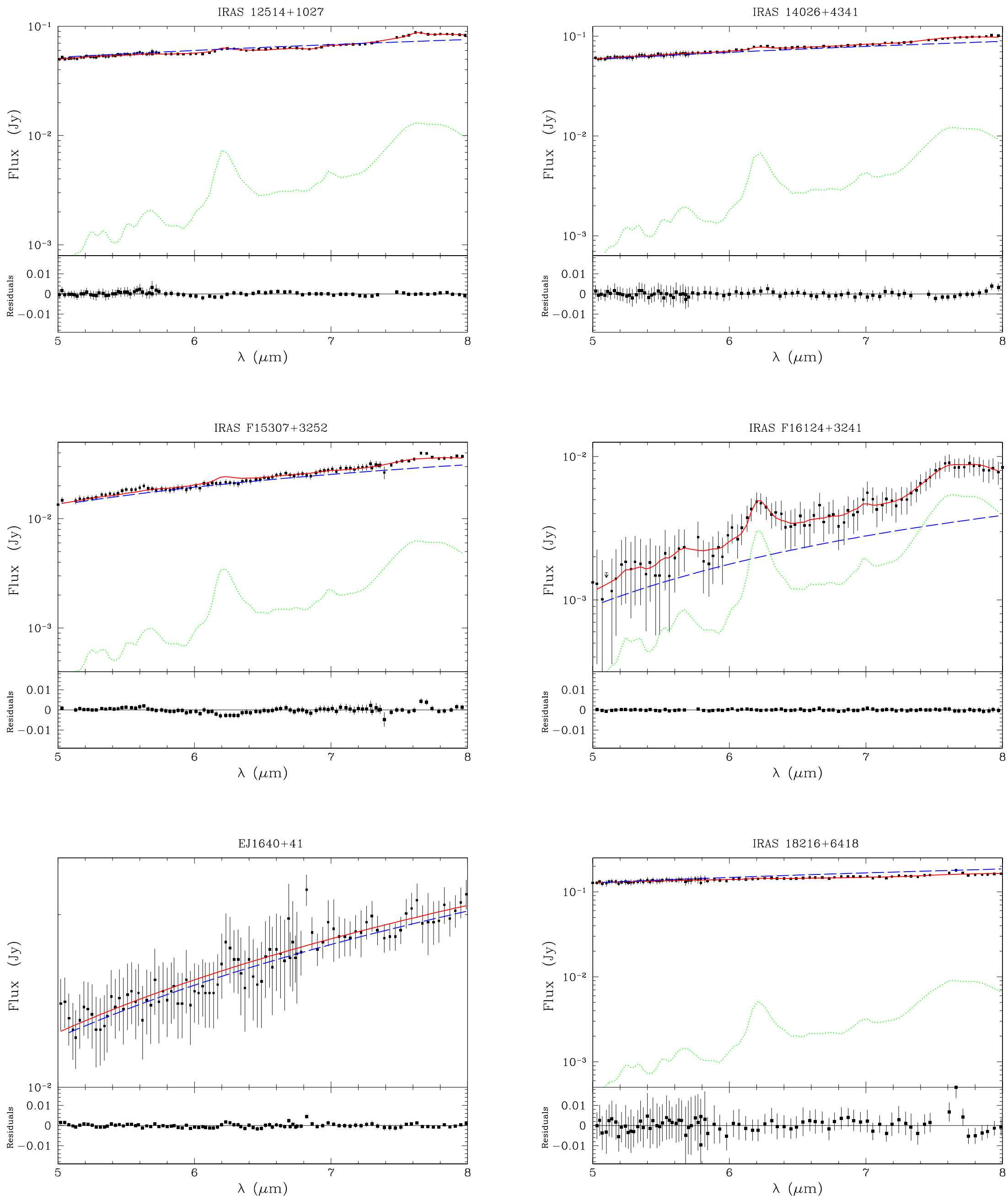

FIGURE 4.2: Continued.

could be caused by synchrotron contamination[1] or could simply be the natural dispersion around the template: a flatter AGN slope has been detected in ~ 10% of ULIRG (Nardini et al. 2010).

[1]This source is a radio quiet AGN but with many properties of radio loud sources (F02), e.g. its radio emission is significantly higher than that estimated by an standard AGN SED (see Fig. 5.7(c)).

IRAS F23569-0341

This source was barely detected by *Spitzer* and the extracted spectrum had a very poor S/N ratio, so we excluded it from the subsequent analysis. The submillimeter bolometer SCUBA was not able to detect this object either (Farrah et al. 2002a).

4.5 Results

The 5-8 μm spectra of most ULIRG show signatures of AGN activity, but the relative contribution of the AGN emission at 6 μm spans over a broad range, from complete SB-dominated to complete AGN-dominated output (N08, Nardini et al. 2009, 2010). Our spectral decomposition, on the other hand, clearly states that MIR spectra of HLIRG are dominated by the nuclear AGN emission reprocessed by the dusty torus. This is consistent with previous studies showing that the fraction of ULIRG harbouring an AGN and the relative contribution of this component increase with IR luminosity (Veilleux et al. 2002; Nardini et al. 2010).

This result is also in agreement with our conclusions obtained in other energy ranges (see Chapters 3 and 5). Moreover, based on the completeness and non AGN bias of the F02's sample (see Chapter 2), our analysis is a strong direct evidence that all HLIRG harbour an AGN.

4.5.1 Star formation rate from PAH emission

Many studies have shown the tight correlation between the presence of Polycyclic Aromatic Hydrocarbon (PAH) features in the MIR spectrum and the presence of SB activity (Genzel et al. 1998; Rigopoulou et al. 2000; Brandl et al. 2006). The PAH emission arises in the photo-dissociation region that lies between the HII region of an SB and the surrounding molecular cloud where the stars are formed. The PAH spectral features are, in addition, very uniform, especially below 8 μm (cf. Fig. 4.1(a) or Fig. 2 from Sargsyan and Weedman 2009).

The MIR spectra of our sources are strongly dominated by the AGN emission, so we cannot obtain a reliable direct measure of the PAH emission. Instead, we estimated this emission through the SB component obtained with the spectral fitting. We estimated the peak flux of the PAH emission at 7.7 μm using our SB template normalized with the best-fit parameters:[2]

$$f_\lambda^{\mathrm{SB}}(7.7\,\mu\mathrm{m}) = f_6^{\mathrm{int}}\,(1-\alpha_6)\,u_\nu^{\mathrm{SB}}(7.7\,\mu\mathrm{m}). \tag{4.2}$$

[2] $u_\nu^{\mathrm{SB}}(7.7\,\mu\mathrm{m})$ was estimated interpolating the SB template of N08 at 7.7 μm.

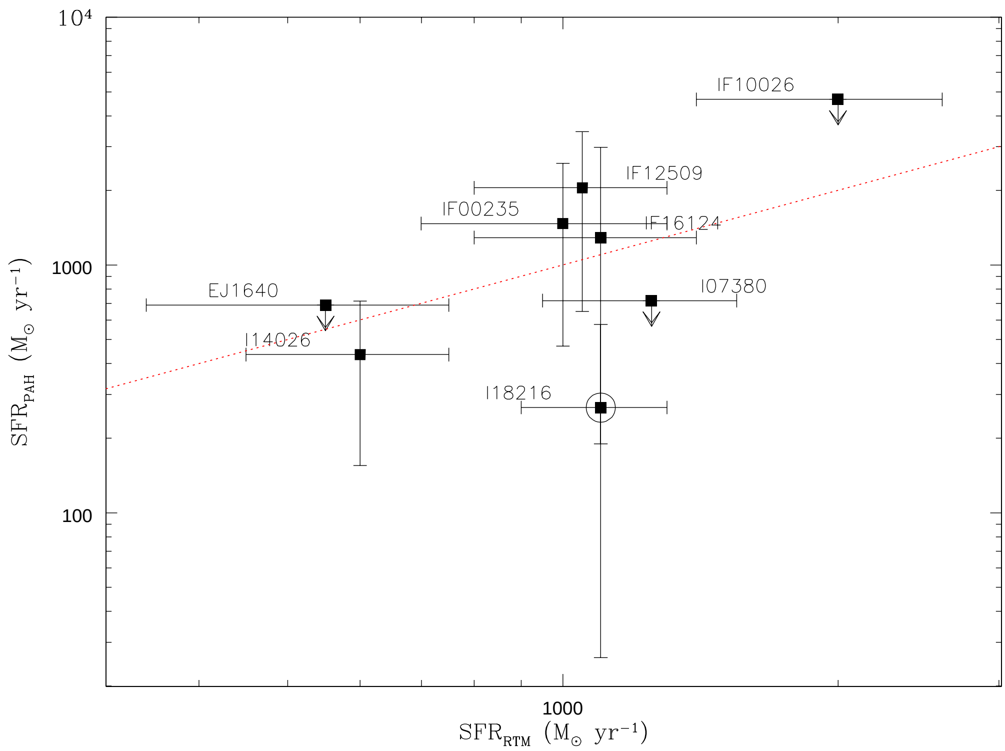

FIGURE 4.3: Comparison of the SFR estimated through PAH emission and through IR SED modelling using RTM (F02). Open circles mark those sources where our model is inaccurate.

After converting these fluxes into luminosities, we estimated the star formation rate (SFR) of these HLIRG using the relation obtained by Sargsyan and Weedman (2009):

$$\log \mathrm{SFR_{PAH}} = \log\left[\lambda L_\lambda^{\mathrm{SB}}(7.7\ \mu\mathrm{m})\right] - 42.57 \pm 0.2, \tag{4.3}$$

for SFR in solar masses per year and $\lambda L_\lambda(7.7\ \mu\mathrm{m})$ in ergs per s. Our estimates of 7.7 μm fluxes includes both the PAH emission and the underlying SB continuum due to dust emission, but Eq. 4.3 is calibrated respect to the total 7.7 μm flux, including both components too. In any case, the continuum contribution is typically just $\sim 10\%$ of the total (Sargsyan and Weedman 2009).

We compared our SFR estimates with those obtained by F02 using radiative transfer models (RTM) to reproduce the IR SED of these objects, and we found consistent results (see Fig. 4.3). Despite most being AGN dominated objects (see Sect. 4.5.2 below), we still found SFR between $\sim 500 - 1000\ M_\odot\ \mathrm{yr}^{-1}$.

Figure 4.4 shows the SFR we calculated versus the total (a) and SB (b) IR luminosity. We estimated the SB luminosity as:

$$L_{\mathrm{IR}}^{\mathrm{SB}} = (1 - \alpha_{\mathrm{IR}})\, L_{\mathrm{IR}}, \tag{4.4}$$

where L_{IR} is the total IR emission calculated through the *IRAS* fluxes (Sanders and Mirabel 1996) and α_{IR} is the fractional contribution of the AGN to the total IR luminosity (see Sect. 4.5.2 below).

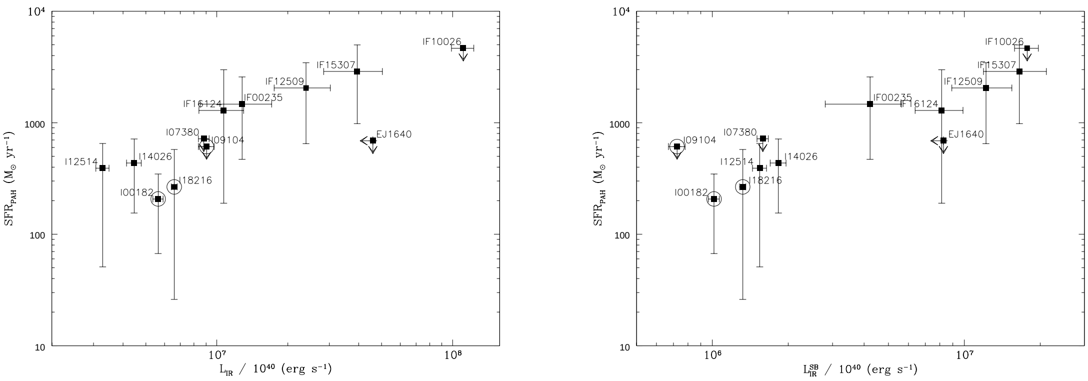

(a) (b)

FIGURE 4.4: SFR estimated using the 7.7 μm PAH emission versus the (a) total and (b) starburst IR luminosities.

We did a generalized Kendall's Tau test[3] to check any possible correlation between these quantities. There is a tight correlation between SFR and SB luminosity (the probability that both quantities are correlated is 99.9% $> 3\sigma$) as expected from several theoretical results (Kennicutt 1998; Draine and Li 2001, 2007, and references therein).

Total IR luminosity and SFR show a weaker, but slightly significant, correlation (the probability is 98.1% $> 2\sigma$). This slight correlation and the high SFR suggest that SB emission could be a significant contributor to the IR output (see Sect. 4.5.2).

4.5.2 AGN contribution to the IR luminosity

We defined the 6 μm to IR bolometric ratio as:

$$R = \frac{\nu_6 f_6^{\rm int}}{F_{\rm IR}}, \tag{4.5}$$

where $F_{\rm IR}$ is the total IR flux estimated through IRAS fluxes as in Sanders and Mirabel (1996). The hypothesis that the IR flux is almost coincident with the total bolometric one is typically a fair assumption in ULIRG, but in principle we cannot adopt this hypothesis for our sources. The study of the HLIRG' broad band SED performed in Chapter 5 reveals that an important number of sources classified as HLIRG emits a significant fraction of their bolometric luminosity outside the IR range. Therefore we limited our analysis to the IR luminosity only.

We can derive a connection between R and our parameter α_6:

$$R = \frac{R^{\rm AGN}\, R^{\rm SB}}{\alpha_6\, R^{\rm SB} + (1-\alpha_6)\, R^{\rm AGN}}, \tag{4.6}$$

[3]We used the ASURV software for this test (Isobe et al. 1986).

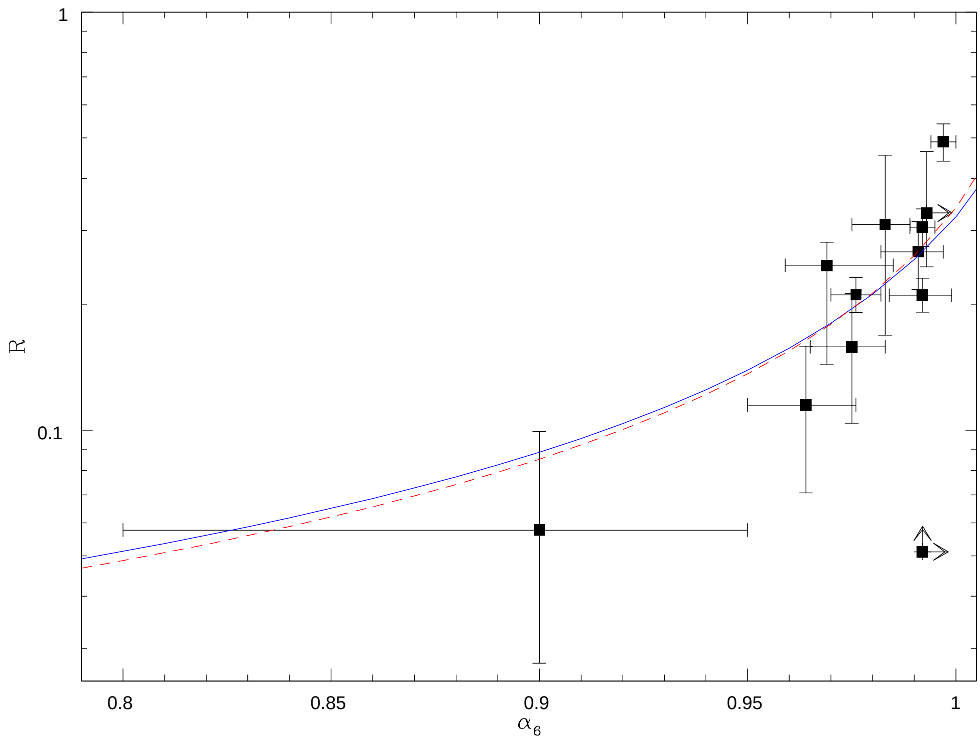

FIGURE 4.5: 6 μm-to-bolometric flux ratio (R) versus α_6. Red-slashed line is our best fit for the relation between R and α_6 given by Eq. 4.6. Blue-solid line is the best fit obtained by N08 for a sample of ULIRG.

where R^{AGN} and R^{SB} are the equivalents of R for pure (unobscured) AGN and pure SB, as defined in Eq. 4.5. We fitted the relation between R and α_6 for our sample of HLIRG considering R^{AGN} and R^{SB} as free parameters, and we found $R^{\mathrm{AGN}} = 0.34 \pm 0.04, R^{\mathrm{SB}} = (1.1 \pm 0.3) \times 10^{-2}$. In spite of our limited sample and the range of α_6, these results are in good agreement with those by N08 for a larger sample of ULIRG, who found $R^{\mathrm{AGN}} = 0.32^{+0.11}_{-0.08}, R^{\mathrm{SB}} = \left(1.17^{+0.09}_{-0.07}\right) \times 10^{-2}$. Fig. 4.5 shows R versus α_6 for our sample of HLIRG, including our fit and the one obtained by N08.

Using α_6 and the values of R^{AGN} and R^{SB} shown above,[4] we estimated the fractional AGN contribution (α_{IR}) to the IR output of each source:

$$\alpha_{\mathrm{IR}} = \frac{F_{\mathrm{IR}}^{\mathrm{AGN}}}{F_{\mathrm{IR}}} = \frac{\alpha_6}{\alpha_6 + (R^{\mathrm{AGN}}/R^{\mathrm{SB}})(1-\alpha_6)}. \tag{4.7}$$

Figure 4.6 compares the α_{IR} estimates obtained through our MIR decomposition with those calculated through the IR SED modelling using radiative transfer models (RTM) by Verma et al. 2002, RR00, F02. Our estimates seem to be consistent with those obtained through RTM for most sources. Apart from the three sources where our model is not suitable, we found that the IR luminosity of seven out of nine HLIRG is AGN dominated. Moreover, the SB contribution is significant for all sources, spanning

[4]Calculations were done with the N08 values. Their sample is significantly larger and α_6 spans over all the range of possible values, so we considered their fit results more accurate.

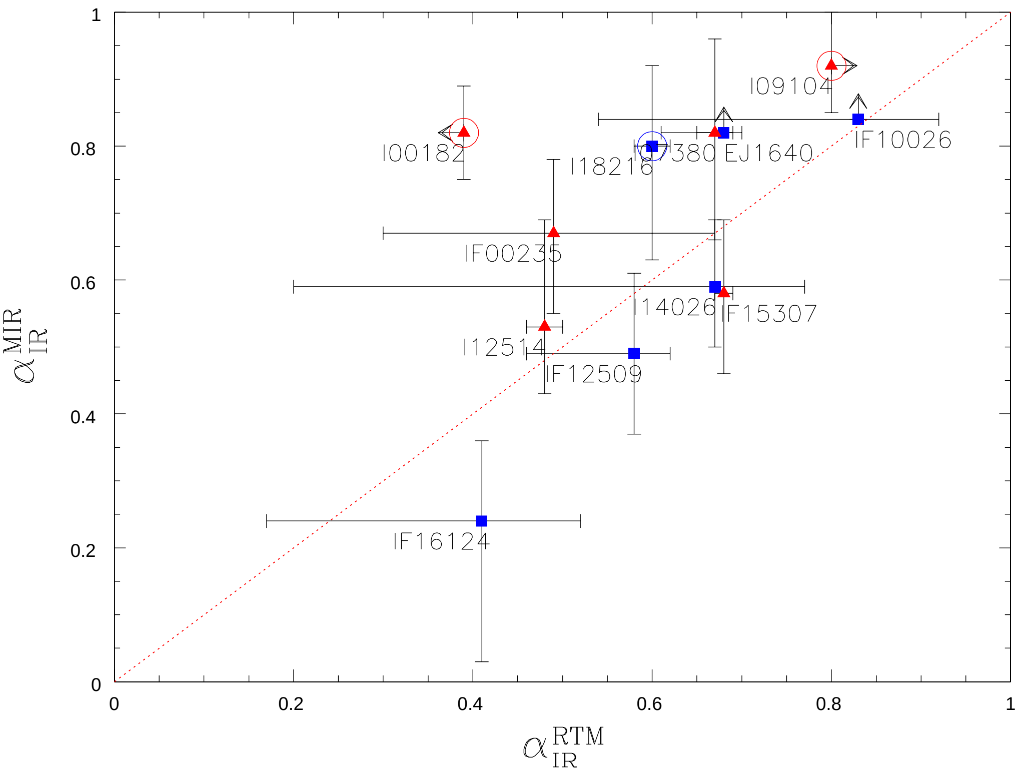

FIGURE 4.6: Comparison of the AGN contribution to the IR luminosity estimated through MIR spectral decomposition and through RTM. Blue squares are type I AGN and red triangles are type II AGN and SB. Open circles mark those sources where our model is inaccurate.

from $\sim 15\% - 60\%$ (considering the error interval). Using only the sources from F02's sample, the mean SB contribution is $\sim 30\%$, close to 35% obtained by F02. This significant SB contribution is consistent with the correlation found between SFR and IR luminosity and the high SFR estimated (see Sect. 4.5.1). Our analysis confirms the idea that star formation and accretion into SMBH are both crucial phenomena to understand the properties of these extreme objects.

4.5.3 Covering Factor

An important physical parameter to unveil the distribution of dust in the nuclear environment of an AGN is the covering factor (CF), i.e. the fraction of sky covered by dust viewed from the central engine of the AGN. The CF is also critical to understand the fraction of direct nuclear emission that is absorbed by dust and re-emitted in the IR range and hence has a significant role in the bolometric luminosity corrections of AGN.

We estimated the CF of HLIRG and compared it to the average CF of AGN in the samples employed to estimate average AGN SED and the standard bolometric corrections (Elvis et al. 1994; Risaliti and Elvis 2004; Richards et al. 2006; Hopkins et al. 2007).

TABLE 4.3: AGN luminosities used to calculate the CF and final estimates of this parameter.

Sources	$L_{\rm X}$ [a] erg s^{-1}	$L_{\rm AGN}^{\rm DIR}$ [b] erg s^{-1}	$\lambda L_{\lambda}(6\,\mu{\rm m})$ [c] erg s^{-1}	$L_{\rm AGN}^{\rm TH}$ [d] erg s^{-1}	CF [e]
IRAS 00182-7112	$(6.6^{+2.9}_{-1.8})\times 10^{44}$	$(4.2^{+2.2}_{-1.3})\times 10^{46}$	$(1.8 \pm 0.1)\times 10^{46}$	$(5.8^{+0.2}_{-0.1})\times 10^{46}$	$1.4^{+0.6}_{-0.8}$
IRAS F00235+1024†	$< 1.6\times 10^{44}$	$< 6.3\times 10^{45}$	$(6.1 \pm 1.2)\times 10^{46}$	$(1.9^{+0.8}_{-0.6})\times 10^{47}$	> 30
IRAS 07380-2342†	$< 2.0\times 10^{44}$	$< 8.4\times 10^{45}$	$(2.9 \pm 0.3)\times 10^{46}$	$(9.3^{+3.3}_{-2.5})\times 10^{46}$	> 11
IRAS 09104+4109	$(2.0^{+2.6}_{-4.0})\times 10^{45}$	$(1.9^{+3.1}_{-0.4})\times 10^{47}$	$(6.8 \pm 0.3)\times 10^{46}$	$(2.1^{+0.7}_{-0.5})\times 10^{47}$	< 1.6
IRAS F12509+3122	$(1.8 \pm 0.2)\times 10^{44}$	$(7.3 \pm 0.9)\times 10^{45}$	$(3.9 \pm 0.3)\times 10^{46}$	$(1.2^{+0.4}_{-0.3})\times 10^{47}$	$16.8^{+6.3}_{-4.9}$
IRAS 12514+1027	$(0.2^{+4.5}_{-0.1})\times 10^{44}$	$(0.04^{+1.41}_{-0.03})\times 10^{46}$	$(8.8 \pm 0.6)\times 10^{45}$	$(2.7^{+1.0}_{-0.7})\times 10^{46}$	< 141
IRAS 14026+4341†	$(3.0 \pm 1.8)\times 10^{44}$	$(1.4^{+1.0}_{-0.9})\times 10^{46}$	$(1.27 \pm 0.07)\times 10^{46}$	$(4.0^{+1.4}_{-1.0})\times 10^{47}$	$2.8^{+2.0}_{-2.1}$
IRAS F15307+3252	$(3.1^{+0.7}_{-0.8})\times 10^{45}$	$(3.4^{+0.9}_{-1.0})\times 10^{47}$	$(8.1 \pm 0.7)\times 10^{46}$	$(2.5^{+0.9}_{-0.7})\times 10^{47}$	0.7 ± 0.3
IRAS 18216+6418	$(3.7 \pm 0.4)\times 10^{44}$	$(4.3 \pm 0.5)\times 10^{47}$	$(2.1 \pm 0.1)\times 10^{46}$	$(6.6^{+2.3}_{-1.7})\times 10^{46}$	$0.15^{+0.06}_{-0.04}$

[a] Absorption corrected X-2-10 keV luminosity as estimated in Chapter 3. In sources marked with †a factor of 60 (Panessa et al. 2006) has been applied to transform its observed X-ray luminosity to intrinsic X-ray luminosity.

[b] Primary, unabsorbed AGN luminosity.

[c] Absorption corrected AGN luminosity at 6 μm.

[d] Reprocessed AGN luminosity.

[e] Covering factor.

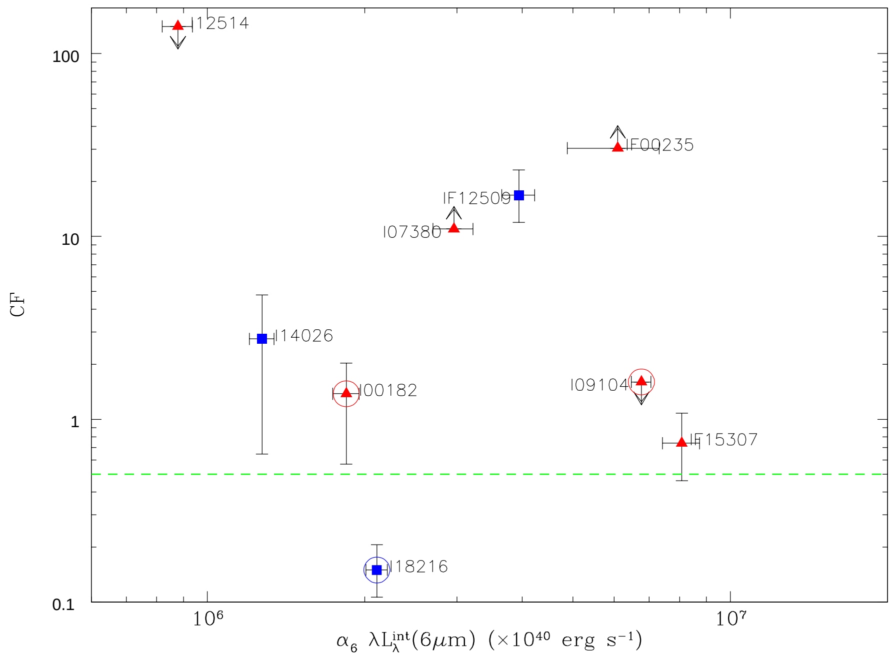

FIGURE 4.7: CF versus the AGN MIR luminosity ($\lambda L_\lambda(12.3\mu m)$). Green dashed line is the CF estimated for the average QSO SED from Hopkins et al. (2007).

The CF can therefore be obtained as the ratio between the thermal reprocessed luminosity of the AGN and the direct (above $\sim 1\ \mu$m), unobscured AGN luminosity (Maiolino et al. 2007; Rowan-Robinson et al. 2009). The thermal luminosity can be estimated through the continuum MIR emission of the sources. Assuming that the IR AGN luminosity is dominated by the reprocessed emission and using the best-fit parameters obtained in our MIR spectral decomposition, the thermal emission of the AGN can be estimated as:

$$L_{\rm AGN}^{\rm TH} \sim \frac{\alpha_6\ \lambda\ L_\lambda(6\ \mu{\rm m})}{R^{\rm AGN}}. \tag{4.8}$$

Since X-ray emission is a primary product of the central engine of AGN, X-ray luminosity is usually a good proxy to estimate the direct AGN emission (Maiolino et al. 2007; Rowan-Robinson et al. 2009). We have applied the X-ray-to-bolometric luminosity ratio estimated by Marconi et al. (2004):

$$\log \frac{L_{\rm AGN}^{\rm DIR}}{L_{\rm X}} = 1.54 + 0.24\mathcal{L} + 0.012\mathcal{L}^2 - 0.0015\mathcal{L}^3, \tag{4.9}$$

where $L_{\rm AGN}^{\rm DIR}$ is the direct intrinsic bolometric AGN luminosity (optical-UV and X-ray luminosities), $\mathcal{L} = \log\left(L_{\rm AGN}^{\rm DIR}/L_\odot\right) - 12$ and $L_{\rm X}$ is the intrinsic (i.e. absorption corrected) 2-10 keV luminosity.

Therefore we could estimate the CF of those HLIRG in our sample with both MIR and X-ray data (nine out of thirteen objects). We used the intrinsic X-ray luminosities estimated in Chapter 3. The sources IRAS F00235+1024 and IRAS 07380-2342 are affected by CT absorption (see Chapters 3 and 5) so the upper limits on their X-ray luminosities have been increased by a factor of 60, the average ratio between intrinsic and observed X-ray luminosities in CT sources (Panessa et al. 2006). The galaxy IRAS 14026+4341 was not detected in our X-ray analysis, but it has a counterpart in the 2XMMi catalogue (Watson et al. 2009). We estimated its 2-10 keV luminosity through the fluxes of the 2XMMi catalogue and since this object seems to be an X-ray absorbed QSO (see Chapter 5, Sect. 5.4.4) we applied the same correction described above to calculate its intrinsic X-ray luminosity.

Table 4.3 shows the derived AGN luminosities calculated to estimate the CF and final estimates of this parameter, and CF versus AGN luminosity at 6 μm is plotted in Fig. 4.7.

A significant fraction (five out of nine) of these sources show a CF consistent (within errors) with ~ 1 (including two upper limits), greater than the CF found in the average SED of local QSO[5] (CF~ 0.5). This result and the presence of heavy X-ray absorption showed by most of these sources (all but one source, IRAS 14026+4341, show signatures of CT absorption in their X-ray emission) point towards large amounts of gas and dust enshrouding their nuclear environment as it has been found in ULIRG (Spoon et al. 2004b; Verma et al. 2005; Yan et al. 2010).

We found one source with CF ~ 0.2. This source, IRAS 18216+6418, is a QSO with no sign of X-ray or MIR obscuration. The low CF is consistent with previous studies finding a decrease in the CF of QSO with increasing luminosity (Maiolino et al. 2007; Treister et al. 2008). The decrease could be explained by "torus receding" models (Lawrence 1991; Maiolino et al. 2007; Hasinger 2008): low-luminosity AGN are surrounded by a dust torus of obscuring material covering a large fraction of the central source. High-luminosity AGN would be able to clean out the environment ionizing the surrounding medium or blowing it away through outflowing winds. Hence the opening angle of the torus would be larger and the covered solid angle would be lower (assuming that the height of the torus is not luminosity dependent).

The remaining three sources show CF>> 1, values with no physical meaning. Two of them were not detected in X-rays (see Chapter 3) and their broadband SED suggest that this low X-ray emission is due to high obscuration (see Chapter 5). Hence their direct AGN emission is probably underestimated. Observational and theoretical results predict even larger correction factors between the observed and intrinsic X-ray luminosity of CT AGN, depending on the amount of absorption and on the viewing angle with respect to the obscuring torus (Haardt et al. 1994; Iwasawa et al. 1997). Applying the largest correction factors, of the order of ~ 1000, we obtain CF consistent with unity.

The remaining source, IRAS F12509+3122, is a QSO with no evidence of X-ray obscuration (see Chapter 3) but its X-ray emission is significantly below the predicted by the average QSO SED from Hopkins et al. (2007) given its IR luminosity (see Chapter 5, Fig. 5.7(c)). Hence the direct AGN emission of this source is also underestimated. As reported above, the low X-ray luminosity of IRAS F12509+3122 cannot be related to X-ray absorption. An increase has been observed in the

[5]The average CF was estimated through a direct integration of the Richards et al. (2006) and Hopkins et al. (2007) average AGN SED. The direct AGN emission was calculated integrating the SED at wavelengths shortward 1 μm, and the thermal emission integrating the SED at wavelengths longward 2 μm.

X-ray bolometric correction of AGN with Eddington ratio ($\lambda_{Edd} = L_{BOL}/L_{Edd}$), from $\kappa_X \sim 15 - 30$ for $\lambda_{Edd} \lesssim 0.1$ to $\kappa_X \sim 70 - 120$ for $\lambda_{Edd} \gtrsim 0.2$ (Vasudevan and Fabian 2009). Using the SDSS spectra of IRAS F12509+3122 and the McLure and Jarvis (2002) relation between black hole mass and MgII emission line's width we estimated $\lambda_{Edd} \sim 0.5$ for this object. This high Eddington ratio suggests that the X-ray bolometric correction for this source could be higher than that obtained in Eq. 4.9. Further studies are needed to check how the Eddington ratio influences the X-ray luminosity of HLIRG.

4.6 Conclusions

We have studied low resolution MIR spectra of thirteen HLIRG observed by *Spitzer*, nine of them also observed by XMM-*Newton*. Using the AGN/SB spectral decomposition technique developed by N08 we modelled their 5-8 μm spectrum and estimated the contribution of each component to the total IR luminosity.

We have also found that all HLIRG in the sample harbour an AGN that clearly dominates the MIR spectrum. Given the completeness of the F02 sample, this is a strong evidence suggesting that all HLIRG harbour an AGN. In terms of IR contribution our results suggest that most sources are dominated by the AGN output, but all of these AGN dominated HLIRG also show a significant SB activity, with a mean SB contribution of $\sim 30\%$. The SFR estimated through the PAH features in the spectra are also very high for all sources, i.e. within $\sim 200 - 2000\ M_{\odot}\mathrm{yr}^{-1}$. These results agree with previous results obtained by modelling the IR SED of HLIRG with radiative transfer models (RR00; F02; Verma et al. 2002), providing further support to the assumptions of these detailed models. The large mean AGN contribution we found ($\sim 70\%$) is consistent with previous studies of ULIRG pointing toward an increase of the AGN emission with increasing luminosity (Veilleux et al. 2002; Nardini et al. 2010). Our study confirms the crucial role of both AGN and SB to explain the properties of these extreme sources.

Using X-ray and MIR data we were able to estimate the CF of these HLIRG finding that a significant fraction (five out of nine) have CF~ 1. Most of these sources with large CF also show heavy absorption in X-rays and high optical depth or absorption features in their MIR spectrum. This strongly suggests that the nuclear environment of these sources is heavily enshrouded by large amounts of gas and dust, as has been observed in ULIRG.

Chapter 5

Spectral energy distributions of HLIRG

5.1 Motivation

In Chapter 3 we presented a systematic X-ray study of the XMM-*Newton* HLIRG Sample. We found that the X-ray emission of most sources is consistent with an AGN origin. However HLIRG showed a systematic IR excess over the IR luminosity usually expected for a local QSO (Elvis et al. 1994; Risaliti and Elvis 2004). We mentioned several hypotheses to explain this excess, like X-ray obscuration or SB IR emission, but we concluded that the most plausible explanation is an intrinsic difference between the SED of AGN in HLIRG and the SED of local QSO.

On the other hand, X-ray thermal emission associated with SB is found for just one source, while all ULIRG show a SB component in their X-ray spectra (Franceschini et al. 2003). If this component actually exists, the much brighter AGN emission probably dilutes the X-rays originated in star-forming processes. Studying the MIR spectra of HLIRG (see Chapter 4) we were able to detect the SB emission of these sources and estimate the relative contribution of the AGN and SB emission to the total IR output.

To complement the above studies, a proper study of the SED of these objects is desirable. Several studies of HLIRG SED have been published in the literature (RR00; F02; Verma et al. 2002), but they were always limited to the IR energy range only. These studies apply a two component model (AGN+SB) to model the IR emission, using radiative transfer models (RTM) for the AGN dust torus (Efstathiou and Rowan-Robinson 1995; Rowan-Robinson 1995) and the SB (Efstathiou et al. 2000) components. RR00 studied a sample of 45 HLIRG, finding a continuum distribution in the relative contribution of the AGN and SB components, from pure SB to pure AGN, with most objects showing a composite nature. On the other hand, F02 selected a complete sample of HLIRG in a manner independent of obscuration, inclination or AGN content and included sub-mm data,[1] finding that all HLIRG in the sample were composite objects.

We present here a study of HLIRG SED with two majors advances compared with the earlier studies commented above: (a) we have greatly enlarged the wavelength range, from radio to X-rays, and (b) we have significantly increased the number of photometric data. However, as a self consistent analytical model able to reproduce the whole SED in so broad frequency ranges would be very complex to compute (and beyond the scope of this thesis), we have compared our constructed SED with empirical AGN and SB templates.

The chapter is organized as follows. Section 5.2 explains how we built the SED and the data used to this end, and Sect. 5.3 the methods we have employed to model the SED. Results are presented in Sect. 5.4 and compared with previous studies of HLIRG in Sect. 5.5. Section 5.6 report these results and summarizes our conclusions. The work presented in this chapter has been published in an international journal as Ruiz et al. (2010b).

5.2 Data compilation

Our goal is to construct a well-sampled SED for each object in a broad frequency range, from radio to X-rays. For this purpose, we have carefully searched in the literature and in several astronomical databases. See Appendix A for a complete description of the origin of the photometry data for each HLIRG.

All the data included in the SED (presented in Tables A.1-A.13, see Appendix A) were converted to monochromatic flux density units, corrected for the Galactic absorption and blue-shifted to rest-frame. We corrected each SED for the line-of-sight Galactic absorption, using in the IR, optical and UV the Fitzpatrick (2004) extinction curves (A_V extinction and color excess E(B-V) for each source were obtained from NED), and in X-rays using the Galactic neutral hydrogen map from Dickey and Lockman (1990).

5.2.1 Radio

Most of the HLIRG in the sample have at least one observation in the radio range. These data come from different observations by the Very Large Array (VLA), the Australia Telescope Compact Array (ATCA), the 30 m telescope of the Institut de Radioastronomie Millimétrique (IRAM - Institute of Millimetric Radioastronomy) and other radio-telescopes.

[1]Starburst models predict larger sub-mm emission than AGN models, hence the addition of sub-mm data in the SED analysis introduce a tight constraint on the SB luminosities (F02).

5.2.2 Infrared

Our sources have been frequently observed in the IR band. There are photometric data from *IRAS* (Point Source Catalog, Joint IRAS Science Working Group 1988; Faint Source Catalog, Moshir et al. 1990) or *ISO* for all the objects. Most of them were also observed with the Submillimetre Common-User Bolometer Array (SCUBA) in the sub-mm band, and have NIR data from the 2 Micron All Sky Survey[2] (2MASS, Cutri et al. 2003).

In addition, there are public *Spitzer* MIR data available for several sources: IRAC photometric data and IRS spectra (see Chapt. 4, Sect. 4.2). We reduced and analysed the IRAC data[3] performing our own photometric measurements for the SED construction. We re-binned the IRS spectra in broad bands, avoiding known emission and absorption features (a further analysis of these MIR spectra was presented in Chapter 4).

5.2.3 Optical and UV

Most of the optical data were obtained from the Sloan Digital Sky Survey-Data Release 5[4] (SDSS-DR5, Adelman-McCarthy et al. 2007) and SuperCOSMOS Sky Survey[5] (SSS). A few data in the V and B bands were taken from the XMM-*Newton* Optical Monitor (OM).

We have only a few data in the UV range, most from the OM. The remaining data come from IUE and FUSE observations.

5.2.4 X-ray

In the X-ray band the XMM-*Newton* spectra studied in Chapter 3 are available. We re-binned each X-ray spectrum in just a few bands[6]. In addition, the X-ray and the OM data come from simultaneous observations, allowing us to check any variability effect.

5.2.5 Overall description of the SED

Figure 5.1 shows the SED we built for our sources. We divided the sources into two classes according to their optical spectral classification. On one hand we grouped the objects classified as type I AGN

[2]http://www.ipac.caltech.edu/2mass/

[3]The software `SPICE` was used for the reduction of IRAC data, following the standard procedure for point-like sources (see IRAC Data Handbook, SSC 2006).

[4]http://www.sdss.org/dr5

[5]http://www-wfau.roe.ac.uk/sss/

[6]Through our X-ray data reduction we did not detect the source IRAS 14026+4341. Even so, this source has a counterpart in the 2XMMi catalog (Watson et al. 2009). We have considered the five energy band fluxes as in the 2XMMi catalog.

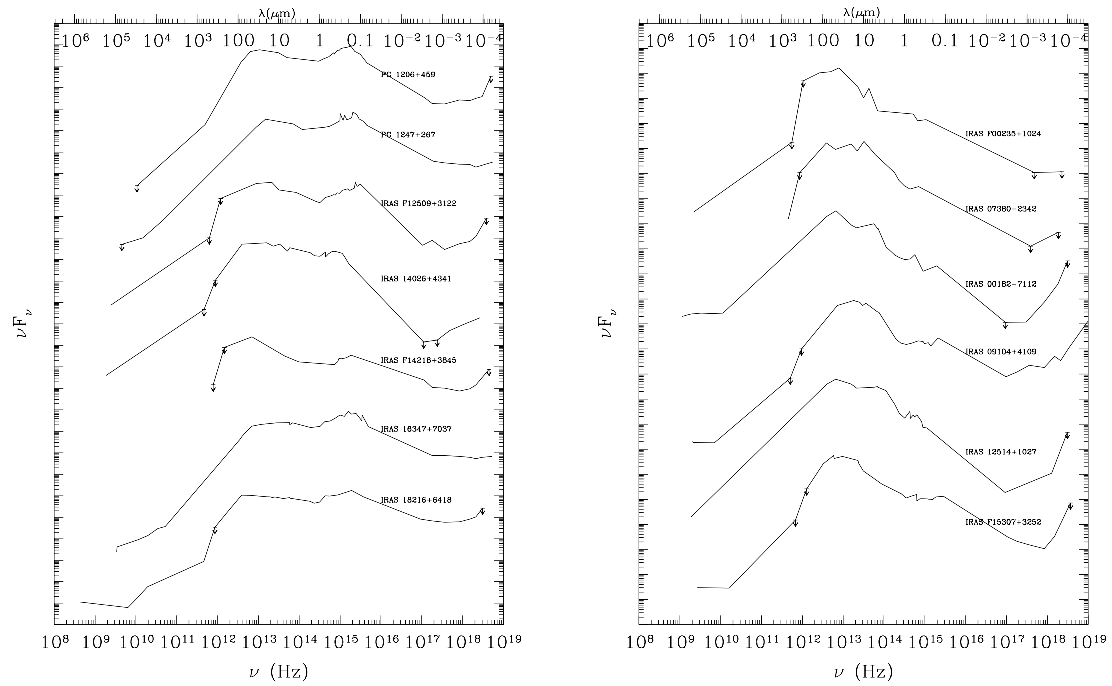

(a) Class A HLIRG. (b) class B HLIRG.

FIGURE 5.1: Rest-frame spectral energy distributions of the sample. Fluxes are shifted for clarity.

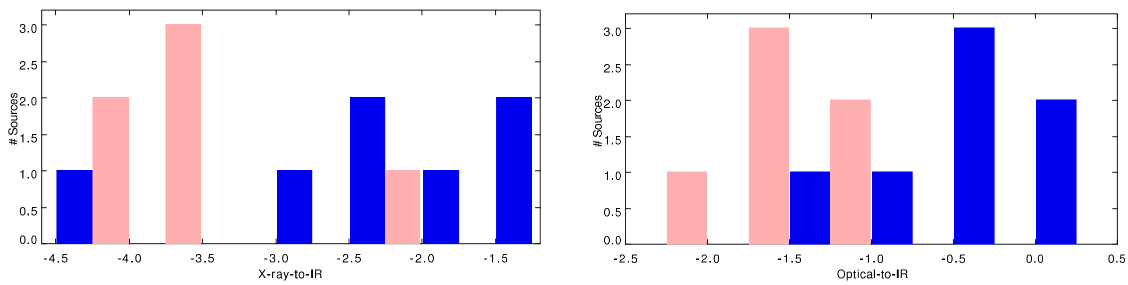

(a) $\log F_X/F_{IR}$ (b) $\log F_{opt}/F_{IR}$

FIGURE 5.2: Distribution of (a) X-ray-to-IR and (b) Optical-to-IR flux ratios for class A (blue) and class B (pink) HLIRG.

(named class A sources) and on the other hand the objects classified as type II AGN and SB (named class B sources).

From a purely phenomenological point of view, class A and B sources seem to show different SED shapes. Class A objects have an SED approximately flat from the FIR to the optical range (the typical shape of quasars' SED), while class B objects show a prominent broad IR bump dominating the emission over the rest of the spectrum.

To check if the above distinction holds quantitatively, we compared the distribution of X-ray-to-IR and optical-to-IR flux ratios for class A and class B sources. We estimated the monochromatic fluxes at three different rest-frame wavelengths, in the IR (30 μm), optical (4400 Å) and X-rays (2 keV) through a linear interpolation of the SED (these points lie in well-sampled regions of the SED, so these are reasonable estimates of the continua at those energies). Figure 5.2 show the distribution of the X-ray-to-IR ($F_{\mathrm{X}}/F_{\mathrm{IR}}$) and optical-to-IR ($F_{\mathrm{opt}}/F_{\mathrm{IR}}$) flux ratios for the class A (blue histogram) and class B (pink histogram) sources. The distributions seem to be different for both classes of HLIRG. By using a Kolmogorov-Smirnov test, the probability that class A and class B samples come from different parent populations is 92.6% ($< 2\sigma$) for the $F_{\mathrm{X}}/F_{\mathrm{IR}}$ distribution and $\sim$ 99.7% ($\lesssim 3\sigma$) for the $F_{\mathrm{opt}}/F_{\mathrm{IR}}$ distribution.

This rough analysis of the SED properties is clearly limited, but the results seem to support our classification of HLIRG in two classes. We suggest that since the SED classification is directly related to the optical spectra classification, the distinct SED shape of HLIRG could be explained by different levels of obscuration in the line of sight and/or the relative contribution of the SB emission to the total output.

5.3 SED fitting

Once all the SED were built, our aim was to check for AGN and/or SB emission in these sources and estimate the contribution of these components to the total output. We fitted all SED by using the χ^2 minimization technique with a simple model based on representative templates (see below, Sect. 5.3.1 for details). The fitting procedure and the SED templates were implemented with the modelling and fitting tool `Sherpa` (Freeman et al. 2001), included in the CIAO 3.4 software package (Fruscione et al. 2006).

Our fiducial model comprises two additive components, one associated to the AGN emission and the other associated to the SB emission. We can express this model as follows:

$$F_{\nu} = F_{\mathrm{BOL}} \left(\alpha \, u_{\nu}^{\mathrm{AGN}} + (1 - \alpha) \, u_{\nu}^{\mathrm{SB}} \right), \tag{5.1}$$

where F_{BOL} is the total bolometric flux, α is the relative contribution of the AGN to F_{BOL}, F_{ν} is the total flux at the frequency ν, while u_{ν}^{AGN} and u_{ν}^{SB} are the normalized AGN and SB templates (i.e., the value of the integral over the whole range of frequencies is unity for each SED template). This model contains only two free parameters, F_{BOL} (the normalization) and α. The bolometric luminosity can be therefore estimated as:

$$L_{\mathrm{BOL}} = 4\pi D_L^2 F_{\mathrm{BOL}}, \tag{5.2}$$

where D_L is the luminosity distance.

The model we adopted to fit the SED is somehow rough and does not provide a precise description of the SED features, so we expect a poor fit in terms of χ^2 value. However, the entire SED shape, from the radio to soft gamma rays, depends on a large number of physical parameters which produce different SED shapes even among the same class of sources (AGN, SB, etc.). Moreover, the impact of the different individual physical quantities on the overall SED and, perhaps most importantly, the effect of their interplay and interaction on the overall SED shape is far from being robustly settled from a theoretical point of view. The development of an analytical or semi-analytical model would be of great importance, but given that such models are difficult to build and likely not unique, they clearly are beyond the scope of this work. We propose instead the simpler template-fitting approach to distinguish, as a zeroth-order approximation, the relative component contribution (AGN and/or SB) to the overall bolometric luminosity of each source.

We chose the fit with the lowest reduced χ^2 as our "best fit" model. As stated above, the expected value of χ^2/d.o.f. >> 1 even for these best fits. Nevertheless, this quantity vary significantly for most sources between the different combination of templates we tested during the χ^2 minimization process. In those objects where different types of templates gave similar χ^2 values, we chose the template most consistent with previous results in the literature.

Our templates were chosen to minimize the contribution of the host galaxy's non-SB stellar emission (Sect.5.3.1), but there could still be a remnant of this emission in the templates. Therefore, by adding two different templates we could have summed twice this stellar emission. We checked this effect adding a stellar template to the model[7]. The normalization of this component was free and negative, in order to subtract the "second" stellar contribution. The addition of the new component did not change the final results of the SED fitting, so we can reject the possibility of any important stellar contamination in our templates.

5.3.1 Templates

The templates we employed to model the SED of our sources are empirical SED both from average samples and from individual "representative" SB and Seyfert (Sy) galaxies in the local universe (see Table 5.1).

To reproduce the AGN contribution we used six AGN templates:

1. Two mean SED of radio-quiet local unobscured QSO Fig. 5.3(a): a luminosity-independent SED (Elvis et al. 1994; Richards et al. 2006) and a luminosity-dependent one (Hopkins et al. 2007). The latter template is similar to the standard SED of QSO from Elvis et al. (1994), but the value of α_{OX} depends on the bolometric luminosity (Steffen et al. 2006), and the X-ray emission beyond 0.5 keV is modelled by a power law ($\Gamma = 1.8$) with a cut-off at 500 keV and a reflection

[7] The SED of the elliptical galaxy M87 was employed to model the stellar emission.

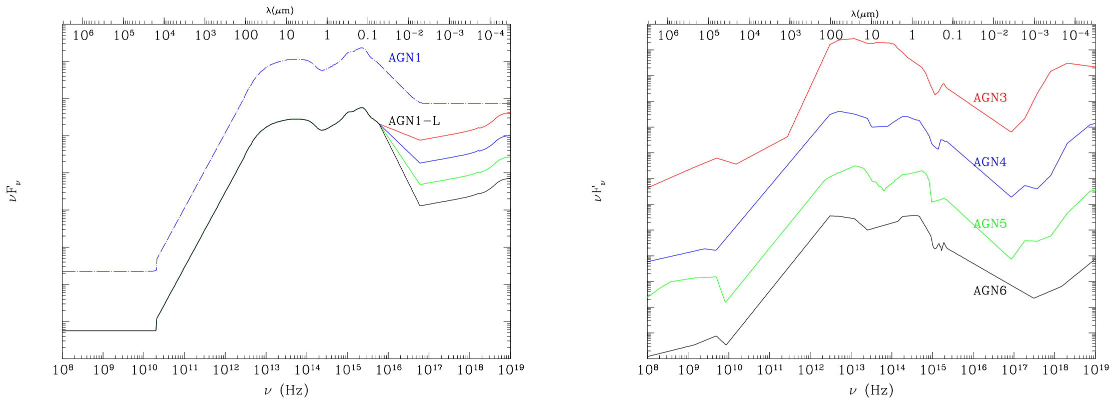

(a) AGN I templates. (b) AGN II templates.

FIGURE 5.3: AGN templates. (a) The top blue line is the standard SED for radio quiet quasar (AGN1, Richards et al. 2006). The group below is the luminosity dependent SED for quasar (AGN1-L, Hopkins et al. 2007), plotted for several bolometric luminosities (the top red line is for 10^{10} $L_\odot$ and the bottom black line is for 10^{16} $L_\odot$). (b) Listed downwards: NGC 5506 (AGN3, $N_{\rm H} = 3\times10^{22}$ cm^{-2}), NGC 4507 (AGN4, $N_{\rm H} = 4\times10^{23}$ cm^{-2}), Mnk 3 (AGN5, $N_{\rm H} = 1.4\times10^{24}$ cm^{-2}), NGC 3393 (AGN6, $N_{\rm H} > 1\times10^{25}$ cm^{-2}). The SED fluxes are shifted for clarity. See Sect. 5.3.1 for details.

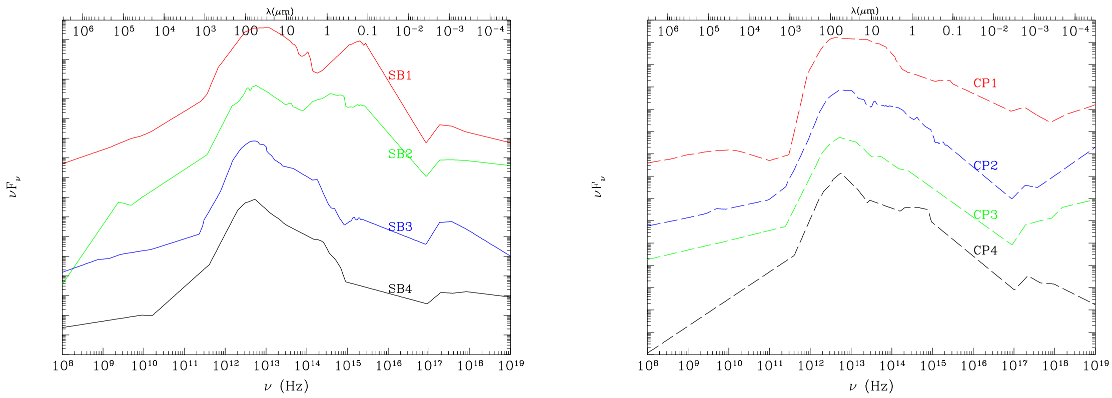

(a) SB templates. (b) Composite templates.

FIGURE 5.4: SB and composite templates. (a) Pure SB templates, listed downwards: NGC 5253, NGC 7714, M82, IRAS 12112+0305. (b) Composite templates (AGN + SB), listed downwards: NGC 1068, Mrk 231, IRAS 19254-7245, IRAS 22491-1808. The SED fluxes are shifted for clarity. See Sect. 5.3.1 for details.

component generated with the PEXRAV model (Magdziarz and Zdziarski 1995). Therefore this template has two parameters: normalization (the bolometric flux of the AGN) and redshift. For a given flux and redshift, the bolometric luminosity is calculated and, hence, the value of α_{OX}. The first parameter was left free to vary, while the second was fixed according to the redshifts obtained in the literature.

2. Four Seyfert 2 (obscured AGN) sources (Fig. 5.3). These objects have column densities varying from 10^{22} cm^{-2} (Compton thin objects) to greater than 10^{25} cm^{-2} (Compton thick objects). They

TABLE 5.1: SED templates.

Name	Source	Description
AGN1	...	Luminosity independent average SED[a] of QSO
AGN1-L	...	Luminosity-dependent average SED[b] of QSO
AGN3	NGC 5506	Sy2, $N_{\rm H} = 3 \times 10^{22}{\rm cm}^{-2}$
AGN4	NGC 4507	Sy2, $N_{\rm H} = 4 \times 10^{23}{\rm cm}^{-2}$
AGN5	Mnk 3	Sy2, $N_{\rm H} = 1.4 \times 10^{24}{\rm cm}^{-2}$
AGN6	NGC 3393	Sy2, $N_{\rm H} > 1 \times 10^{25}{\rm cm}^{-2}$
SB1	NGC 5253	Young and dusty SB
SB2	NGC 7714	Young and unobscured SB
SB3	M82	Old SB
SB4	IRAS 12112+0305	SB-dominated ULIRG
CP1	NGC1068	Composite template: AGN: ∼ 50%
CP2	Mnk 231	Composite template: AGN: ∼ 70%
CP3	IRAS 19254-7245	Composite template: AGN: ∼ 45%
CP4	IRAS 22491-1808	Composite template: AGN: ∼ 70%

[a] Richards et al. 2006.
[b] Hopkins et al. 2007.

were selected from a sample of Seyfert 2 galaxies with minimal SB contribution (Bianchi et al. 2006). The AGN templates show two bumps, in the FIR and in the NIR-optical, except the AGN3 template, which only presents a broad IR bump. The differences between them are the relative height of these bumps, the position of their peaks and the ratio between the optical and X-ray fluxes.

To represent the SB emission we chose a set of four SB galaxies well observed in the full spectral range (Fig. 5.4(a)). We tried to cover a broad range of burst ages, dust contents and SFR. These physical properties are reflected in the SED showing different levels of obscuration, width and wavelength peaks.

1. NGC 5253 is a low-metalicity star-forming dwarf galaxy. Its nucleus is the site of a highly obscured and extremely young ($<$ 10 Myr) burst of star formation (Beck et al. 1996), with a SFR$\sim 8\ M_\odot{\rm yr}^{-1}$.

2. NGC 7714 is a young unobscured SB (Brandl et al. 2004) with SFR=6 $M_\odot{\rm yr}^{-1}$ and a burst age between 3-5 Myr (Gonzalez-Delgado et al. 1995).

3. M82 is an evolved SB galaxy with SFR$\sim 10\ M_\odot{\rm yr}^{-1}$ (Strickland et al. 2004).

4. IRAS 12112+0305 is a bright ULIRG powered by SB and with severe limits to any AGN contribution (Imanishi et al. 2007; Nardini et al. 2008). The estimated SFR for this object is $\sim 600\ M_\odot{\rm yr}^{-1}$ (Franceschini et al. 2003).

All of them show two bumps, peaking in the FIR and in the NIR-optical. The main difference between the templates is the relative height between these bumps and their widths.

We included four “composite” SED templates built from sources which harbour both an AGN and a SB (Fig. 5.4(b)):

1. NGC 1068 is a type 2 Seyfert galaxy which harbours a heavily buried AGN ($N_{\rm H} > 10^{25}$ cm^{-2}, Matt et al. 1997) and also an intense SB (Telesco et al. 1984). The bolometric luminosity of this object is roughly evenly divided between the two component, the SB emission dominates longward of 30 μm and the AGN dominates shortward of 20-10 μm.

2. Mrk 231 is an ULIRG ($L_{\rm IR} = 3.2 \times 10^{12}$) optically classified as a broad absorption line QSO (Berta 2005) with a massive young nuclear SB, which is responsible for 25%-40% of the nuclear bolometric luminosity (Davies et al. 2004).

3. IRAS 19254-7245, the “superantennae”, is a double-nucleated ULIRG optically classified as a Sy2 galaxy with intense star formation. The AGN contribution to the total output is $\sim 40 - 50\%$ (Berta et al. 2003).

4. IRAS 22491-1808 is a Sy2 ULIRG (Berta 2005) where the AGN emission is $\sim$ 70% of the bolometric luminosity (Farrah et al. 2003).

We fitted these composite templates to those HLIRG where the initial AGN+SB model was insufficient to reproduce the data (see Sect. 5.4.2).

We obtained the photometric data for the templates with the VOSED[8] and VOSpec[9] software. These utilities use Virtual Observatory (Quinn et al. 2004) tools to extract photometric and spectral data from several astronomical archives and catalogues. The templates were completed with data from the NED database in wavelength ranges where VOSED and VOSpec provided no data. These objects have been repeatedly observed at all frequency ranges, particularly in the NIR and optical bands. We rejected some redundant data and tried to extract only the nuclear emission to avoid as much contamination from the host galaxy as possible. For this purpose we chose only those data with a roughly constant aperture within the nucleus of the galaxy.

5.4 Results

Figures 5.7 and 5.8 show the SED[10] and the best-fit model selected for each object, and Table 5.2 summarizes the results of our analysis. See Sect. 5.4.4 for comments on some particular sources.

[8]http://sdc.laeff.inta.es/vosed

[9]http://esavo.esa.int/vospec

[10]Several photometric points are upper limits. The most conservative approach was chosen for the fit. We set the point to zero and the upper error bar to the upper limit value.

5.4.1 Class A HLIRG

We found that our simple two-component SED model is a fair approximation for six out of seven of these HLIRG (see Fig. 5.7). They are well fitted with type I AGN templates, consistent with their optical classification, and an additional SB component in three objects. The AGN component dominates the bolometric output in four out of these six sources, while two objects present a powerful SB component ((IRAS F12509+3122 and IRAS F14218+3845) responsible for 60%-70% of the bolometric luminosity. The seventh object (IRAS 14026+4341), optically classified as a QSO, is the only source not well-fitted with a type I AGN template, probably because is an X-ray absorbed QSO (see Sect. 5.4.4 for further details).

Our analysis reveals three sources with an SB-dominated SED (IRAS F12509+3122, IRAS 14026+4341 and IRAS F14218+3845), one AGN-dominated (IRAS 18216+6418) source with a significant SB contribution and three sources which seem to be extremely luminous quasars with no particular differences from the local ones, judging from their SED and X-ray spectra (see Sect. 3.3.5).

A noticeable result for the class A HLIRG is that the AGN1 template over-predicts the X-ray flux of these sources, as found in our previous X-ray analysis. These discrepancies in the X-ray band cannot be related to variability effects, because the OM data, simultaneous to the X-ray observations, match well with other optical and UV data obtained at different epochs. When we modelled these objects with the luminosity dependent AGN1-L SED template, we found a significant improvement in the fit in terms of χ^2 for most sources (four out of six, an SB-dominated and three pure AGN sources) and the X-ray emission is better predicted. This result is consistent with the known α_{OX} luminosity relationship (Strateva et al. 2005; Steffen et al. 2006; Kelly et al. 2008).

We must also note that the IR-to-bolometric ratio of these sources is within $\sim 40-70\%$, which means that an important fraction of their bolometric output is not emitted in the IR range. Hence, strictly speaking, they should not be considered as HLIRG[11], particularly those with a completely AGN-dominated SED, where less than 50% of their bolometric luminosity is emitted in the IR. This "contamination" can be expected given the selection criteria of the RR00 parent sample (see Chapter 2), which simply selected those known sources with total observed $L_{\rm IR} > 10^{13}\ L_\odot$.

5.4.2 Class B HLIRG

We found that these sources are fitted with a dominant SB component and, in most cases, a minor AGN contribution (< 10%). But our model presents some problems for class B HLIRG that we did not find in class A objects (see Fig. 5.1(b)):

[11]As members of the LIRG family, bona fide HLIRG should present a bolometric luminosity dominated by the IR emission.

1. The level of obscuration in the observed X-ray spectra is higher than that expected from the AGN templates.

2. Most sources show an excess in the MIR-NIR band not modelled by these templates, i.e. the width of the IR bump seems to be broader than the bumps in the SB templates.

3. The peak of the template does not match the IR peak of the SED in several sources.

In order to improve the fit quality for the class B sources, we repeated the SED fitting with a set of templates from composite sources (see Sect. 5.3.1), where both AGN and SB emission are significant. By using these composite templates, we found that the statistical quality of our fits was significantly improved for all but one case (IRAS F15307+3252). For most objects, the χ^2 obtained with any of the composite templates is significantly lower than the χ^2 obtained with any combination of pure AGN and pure SB templates. CP1 is the best-fit for three out of six sources (IRAS 00182-7112, IRAS F00235+1024 and IRAS 07380-2342), consistent with their spectral classification (type II AGN) and X-ray obscuration level (Compton-Thick). Another two sources are best-fitted with the CP2 template (IRAS 09104+4109 and IRAS 12514+1027). We also selected the CP1 template as the best-fit model for the last source (IRAS F15307+3252) despite, in a purely statistical sense, no significant improvement was found (see Sect. 5.4.4 for further explanations).

The galaxy IRAS F00235+1024 is the only source that still shows a significant IR excess with respect to its best-fit template, which suggest that the SB contribution may be larger in this source than in the CP1 template ($\sim$ 50%).

5.4.3 Fitting without X-ray data

In order to check to what extent X-ray data influenced the SED fitting results, we excluded X-ray data from the SED fitting procedure. Class A sources were still well represented by the same models (see Table 5.2, columns labelled as “no X-rays”), while class B galaxies were preferentially fitted with an AGN3 template (Compton thin model) and an SB component. Moreover, the AGN contribution grows significantly in most sources, specially in the class B sources. When X-rays are included, a severe limit is imposed and the AGN contribution falls dramatically. This shows that X-rays are important to obtain an accurate model with our technique and, hence, a better estimation of the contribution of each component to the total output.

TABLE 5.2: Best fit models for the HLIRG's SED.

Source	z	Type	CT[a]	Best Fit model[b]							log L_{BOL}[c]	AGN / SB[d]
				all data[e]			no X-rays[f]			composite temp.[g]		
				Model		α	Model		α			
Class A HLIRG												
PG 1206+459	1.158	QSO	-	AGN1-L	-	1	AGN1	-	1	**AGN1-L**	48.4	1 / 0
PG 1247+267	2.038	QSO	-	AGN1-L	-	1	AGN1	-	1	**AGN1-L**	49.2	1 / 0
IRAS F12509+3122	0.780	QSO	-	AGN1-L	SB1	0.3	AGN1	SB4	0.5	**AGN1-L+SB1**	47.7	0.3 / 0.7
IRAS 14026+4341	0.323	QSO	-	-	SB2	0	**AGN1**	**SB2**	0.3	SB2	46.7	0.3 / 0.7
IRAS F14218+3845	1.21	QSO	-	AGN1	SB1	0.4	AGN1	SB1	0.3	**AGN1+SB1**	47.2	0.4 / 0.6
IRAS 16347+7037	1.334	QSO	-	AGN1-L	-	1	AGN1	-	1	**AGN1-L**	48.9	1 / 0
IRAS 18216+6418	0.297	QSO	-	AGN1	SB3	0.8	AGN1	SB3	0.8	**AGN1+SB3**	47.4	0.8 / 0.2
Class B HLIRG												
IRAS F00235+1024	0.575	NL-SB	✓	-	SB3	0	-	SB3	0	**CP1**	46.7	~0.5 / ~0.5
IRAS 07380-2342	0.292	SB	-	AGN4	SB1	0.06	AGN3	SB1	0.3	**CP1**	47.0	~0.5 / ~0.5
IRAS 00182-7112	0.327	QSO 2	✓	AGN3	SB4	0.06	AGN3	SB3	0.3	**CP1**	46.6	~0.5 / ~0.5
IRAS 09104+4109	0.442	QSO 2	✓	AGN4	SB4	0.09	AGN3	SB1	0.8	**CP2**	47.3	~0.7 / ~0.3
IRAS 12514+1027	0.32	Sy2	✓	AGN5	SB4	0.06	AGN3	SB2	0.9	**CP2**	46.7	~0.7 / ~0.3
IRAS F15307+3252	0.926	QSO 2	✓	AGN1	SB3	0.03	AGN3	SB1	0.8	**CP1**	47.9	~0.5 / ~0.5

[a] Compton Thick candidates.
[b] The best fit adopted to estimate the bolometric luminosity and the AGN and SB fraction is marked in bold fonts.
[c] Bolometric luminosity in CGS units.
[d] Fraction of the bolometric luminosity originated in AGN and SB. Calculated through the parameter α of the best fit model.
[e] Best fit using our original set of templates.
[f] Best fit not using X-ray data.
[g] Best fit including the templates of composite sources.

5.4.4 Notes on particular sources

IRAS 14026+4341

This source is optically classified as a type I AGN (Rowan-Robinson 2000), in agreement with the SDSS classification, and MIR *Spitzer* data also suggest an AGN in this object (see Chapt. 4), but our best-fit is obtained with the SB2 template. The X-ray data impose a severe constraint, rejecting the AGN templates which predict a higher emission in the X-ray band. If we fit again this SED without X-ray data (see Sect. 5.4.3) we find that the best fit is obtained with the combination of AGN1 and SB2 templates.

The X-ray emission of this source seems to be affected by absorption (see Fig. 5.7(d)): it is not detected in the soft X-ray band (0.5-2 keV) and its 2XMMi hardness ratio ($HR3 \sim -0.2$)[12] is consistent with an X-ray absorbed AGN (Della Ceca et al. 2004). This indicates IRAS 14026+4341 as an X-ray absorbed QSO. The X-ray absorption in these objects is caused by ionized gas, in which there is no dust, and hence its optical/UV emission is not obscured (Page et al. 2010, in preparation). These objects are often embedded in ultraluminous SB galaxies (Page et al. 2007), and they have been pointed out as a transitional phase in an evolutionary sequence relating the growth of massive black holes to the formation of galaxies (Stevens et al. 2005; Page et al. 2007).

Under these circumstances, we selected as our best fit the model resulting from fitting the SED without X-ray data. We must note, however, that both models (pure SB or AGN+SB) poorly fit the data between $\sim 1-100\ \mu m$. The observed IR excess, which is maybe related to the X-ray emission absorbed and reprocessed in the IR, cannot be reproduced by AGN1 template (an unabsorbed template).

IRAS F15307+3252

This object was optically classified as a QSO 2 (Rowan-Robinson 2000) and there is strong evidence in X-rays favouring a heavily obscured AGN (Iwasawa et al. 2005). However we found that its SED best-fit in terms of χ^2 is obtained with an SB template with minor AGN1 contribution. The CP1 template is also a fair fit, but with a slightly worse χ^2.

Previous analyses of the IR emission of this HLIRG (Deane and Trentham 2001; Verma et al. 2002) suggest that the SB contribution is considerably lower than we found with a pure SB template. Hence we selected the CP1 as “best fit”, which is also consistent with its optical classification, to estimate the AGN and SB contribution to the bolometric luminosity.

[12] $HR3 = \frac{CR(2.0-4.5\ \mathrm{keV}) - CR(1.0-2.0\ \mathrm{keV})}{CR(2.0-4.5\ \mathrm{keV}) + CR(1.0-2.0\ \mathrm{keV})}$, where CR is the count rate in the given 2XMMi energy band.

TABLE 5.3: IR and X-ray luminosities (CGS units).

Source	$\log L_{\rm IR}^{\rm tot}$ [a]	$\log L_{\rm IR}^{\rm AGN}$ [a]	$\log L_{\rm IR}^{\rm SB}$ [a]	$\log L_{\rm IR,RTM}^{\rm tot}$ [b]	$\log L_{\rm IR,RTM}^{\rm AGN}$ [b]	$\log L_{\rm IR,RTM}^{\rm SB}$ [b]	$\log L_{\rm X}^{\rm AGN}$ [c]	$N_{\rm H}$ [d] $[{\rm cm}^{-2}]$
Class A HLIRG								
PG 1206+459	48.0	48.0	0	47.8	47.8	< 46.7	$45.11^{+0.02}_{-0.04}$	-
PG 1247+267	48.8	48.8	0	47.9	47.9	< 46.8	$45.93^{+0.02}_{-0.03}$	-
IRAS F12509+3122	47.6	46.8	47.5	47.0	46.8	46.6	$42.26^{+0.05}_{-0.05}$	-
IRAS 14026+4341[e]	46.5	45.8	46.5	46.5	46.3	46.1	$42.7^{+0.2}_{-0.5}$	-
IRAS F14218+3845	47.1	46.5	46.9	46.9	46.1	46.8	$44.60^{+0.03}_{-0.03}$	-
IRAS 16347+7037	48.5	48.5	0	47.7	47.7	< 46.8	$46.00^{+0.07}_{-0.09}$	-
IRAS 18216+6418	47.1	46.9	46.6	46.8	46.6	46.4	$45.6^{+0.04}_{-0.05}$	-
Class B HLIRG								
IRAS F00235+1024	46.7	46.4	46.4	46.7	46.4	46.4	< 42.2	$> 10^{25}$
IRAS 07380-2342	47.0	46.7	46.7	47.0	46.8	46.5	< 41.7	-
IRAS 00182-7112	46.6	46.3	46.3	46.7	< 46.5	46.7	$44.82^{+0.16}_{-0.14}$	$> 10^{25}$
IRAS 09104+4109	47.3	47.1	46.8	46.8	46.8	< 46.2	$45.30^{+0.36}_{-0.09}$	$> 10^{25}$
IRAS 12514+1027	46.7	46.5	46.2	46.5	46.2	46.2	$43.3^{+1.4}_{-0.7}$	$(4^{+20}_{-3}) \times 10^{23}$
IRAS F15307+3252	47.9	47.6	47.6	46.9	46.6	46.7	$45.49^{+0.09}_{-0.11}$	$> 10^{25}$

[a] IR luminosities (1-1000 μm) estimated using our SED fitting.
[b] IR luminosities (1-1000 μm) estimated by the analysis of the IR SED using RTM (Rowan-Robinson 2000; Farrah et al. 2002a).
[c] Absorption corrected 2-10 keV luminosities.
[d] Intrinsic absorption estimated using X-ray spectra.
[e] The X-ray luminosity of this source has been calculated from 2XMMi fluxes (Watson et al. 2009), and it is not corrected from absorption.

5.5 Comparison with previous results

5.5.1 X-ray emission

We can estimate the expected X-ray luminosity of the AGN and SB components for each source in our sample with the parameters obtained in our SED analysis, and compare them with the X-ray luminosities calculated through XMM-*Newton* observations.

We have seen that the AGN SED of these sources is better modelled with a luminosity dependent template. Hence we employed the relation obtained by Sani et al. (private communication)[13] for ULIRG to estimate the intrinsic 2-10 keV luminosity for a given AGN bolometric luminosity:

$$\frac{L_{2-10}}{L_{Bol}} = 0.043\left(\frac{L_{Bol}}{10^{45}}\right)^{-0.357}. \tag{5.3}$$

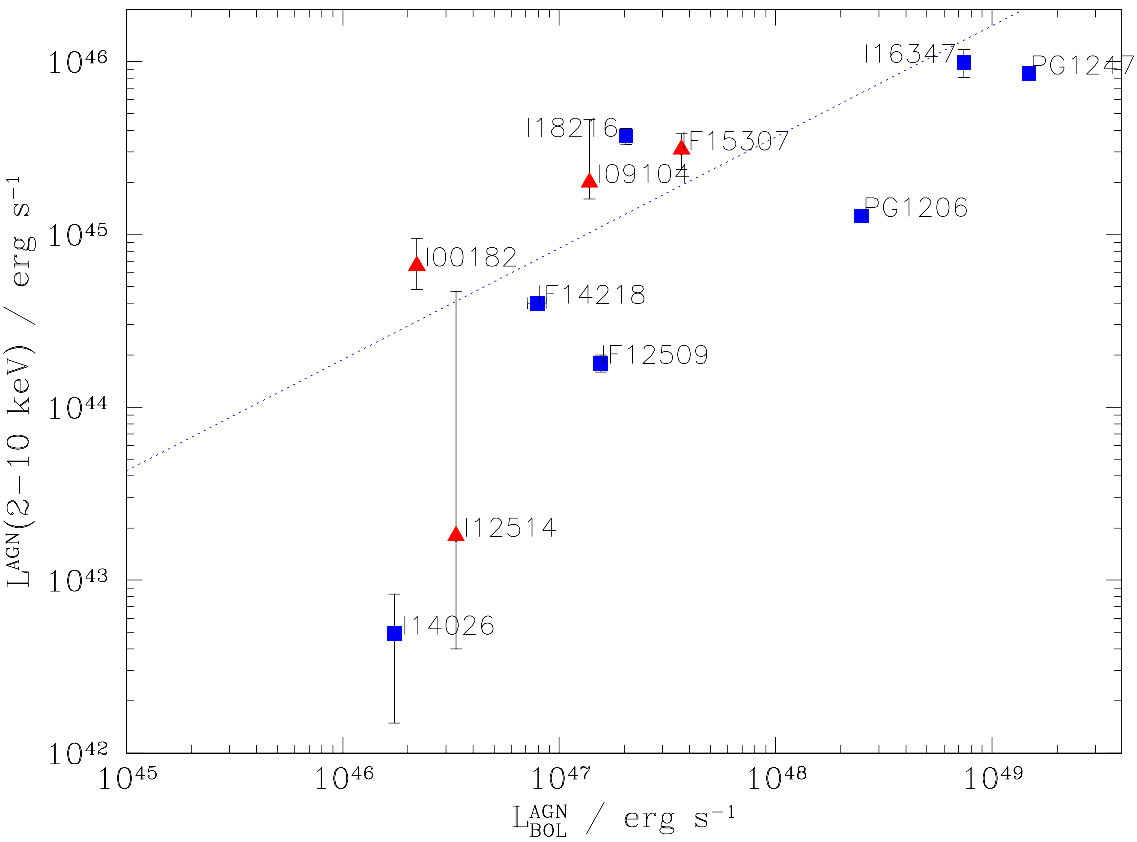

FIGURE 5.5: Bolometric versus observed, absorption-corrected 2-10 keV AGN luminosities. Blue squares are class A HLIRG, red triangles are class B HLIRG. The blue dotted line reflects the ratio between these luminosities as in Eq. 5.3.

[13]This ratio is obtained from the Steffen et al. (2006) relation between X-ray and 2500 Å luminosities and then linking the 2500 Å luminosity with the bolometric one through the Elvis et al. (1994) SED.

Figure 5.5 shows those sources detected in X-rays and with an AGN component in their SED model. We plotted the bolometric luminosity of the AGN component versus the intrinsic (absorption corrected) 2-10 keV luminosity, as calculated in Chapter 3.

Most sources are scattered along the Eq. 5.3 estimate. This scatter is probably related to the intrinsic dispersion in X-ray luminosities of AGN, i.e. for a given bolometric luminosity there is a broad range of possible X-ray luminosities (Steffen et al. 2006).

There are, however, three sources with X-ray luminosities much lower than that estimated by Eq. 5.3 (PG 1206+459, IRAS F12509+3122 and IRAS 14026+4341). We calculated the X-ray luminosity of IRAS 14026+4341 using the 2XMMi X-ray fluxes, so it is not corrected by intrinsic absorption. Hence this large discrepancy between the prediction and the observed luminosity is likely another sign of X-ray absorption (see Sect. 5.4.4).

For the other two sources we did not find any sign of X-ray absorption (see Chapter 3). This effect could in principle be due to an overestimate of the AGN contribution to the bolometric luminosity. If we assume that the difference between the bolometric luminosity calculated with the SED fitting and that estimated with Eq. 5.3 is completely caused by star formation, we find that the SB contribution to the total output should be larger than 90% in these two sources. Such a powerful SB must be clearly reflected in the SED shape, but we did not find this kind of deviation in the SED analysis of these sources. The X-ray weakness of these HLIRG therefore cannot be related to the underestimate of the SB contribution to the bolometric output or to X-ray absorption. They seem to be intrinsically weak X-ray sources (Leighly et al. 2001, 2007).

5.5.2 IR SED: comparison with previous works

The IR ($1 - 1000$ μm) SED of our sources has been previously studied: Rowan-Robinson (2000), Farrah et al. (2002a) and Verma et al. (2002) modelled it using radiative transfer models (RTM). We estimated the IR luminosities of our models, integrating the SED between $1 - 1000$ μm, and compared their results with ours.

The IR luminosities estimated through our SED fitting and the ones estimated using the radiative transfer models match fairly well (see Fig. 5.6(a)) for many sources. For three objects (PG 1247+259, IRAS F15307+3252 and IRAS 16347+7037), our luminosity estimation is almost an order of magnitude greater than the RTM estimation, probably because our best-fit models overestimate the FIR/sub-mm emission (see Figs. 5.7(b), 5.7(b) and 5.8(b)). This spectral emission is probably better recovered by using RTM. Nevertheless, in spite of this large disagreement in luminosities, our AGN contribution estimates are consistent with those obtained through RTM for these objects, as Fig. 5.6(b) shows.

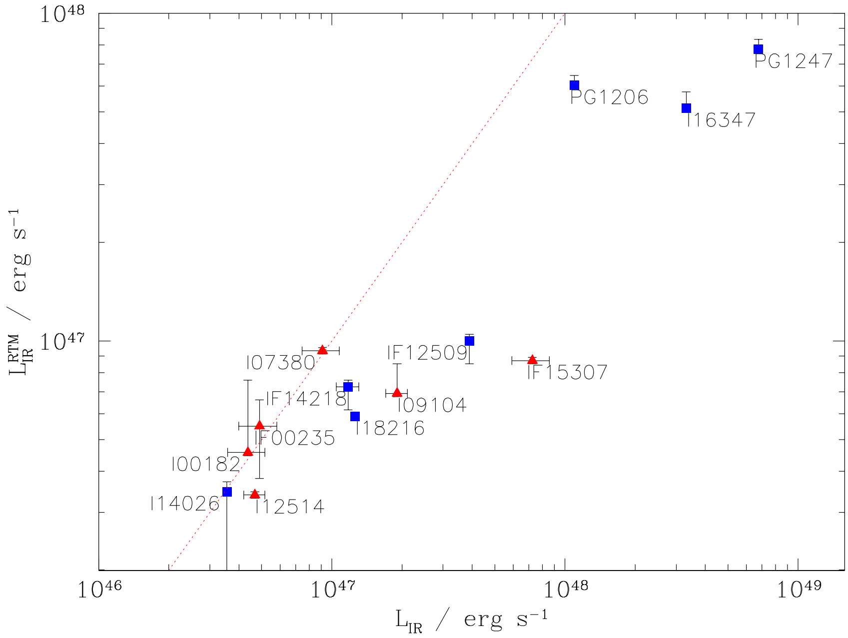

(a) Total IR luminosities.

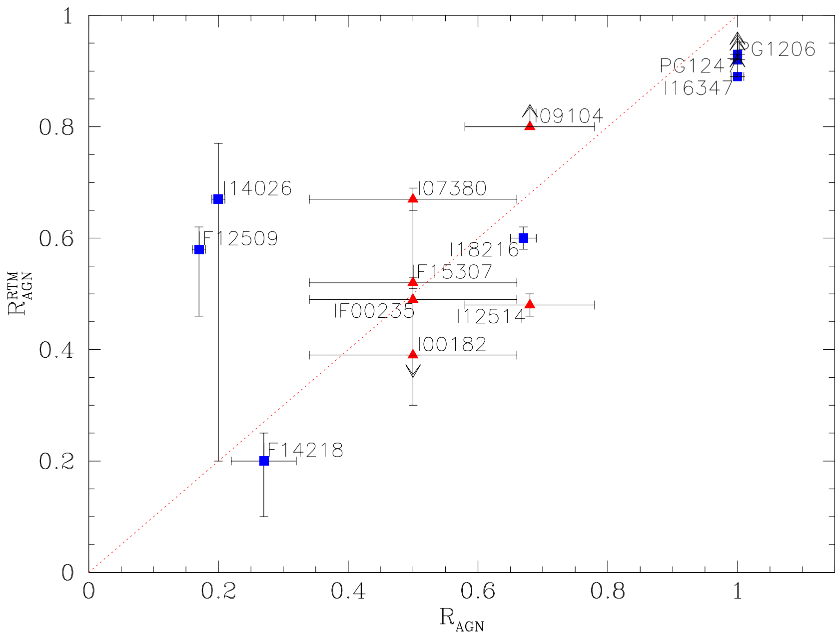

(b) AGN to total IR luminosity ratios.

FIGURE 5.6: (a) Total IR luminosity estimated using our templates (L_{IR}) and using radiative transfer models (L_{IR}^{RTM}). (b) AGN to total IR luminosity ratios estimated through our model (R^{AGN}) and using radiative transfer models (R_{AGN}^{RTM}). Blue squares are class A HLIRG, red triangles are class B HLIRG. The red dotted lines mean equal values.

The latter plot shows that our AGN contribution estimates for most sources are roughly consistent with those obtained through RTM. We can conclude that our simple model based on templates is a fair method to obtain an overall estimate of the AGN and SB relative contribution to the IR output.

5.6 Discussion and conclusions

In this chapter we built and analysed the multi-wavelength SED (from radio to X-rays) of a sample of 13 HLIRG, previously studied in detail in X-rays. We assembled the SED using public data in several astronomical databases and in the literature, and we modelled them through templates.

These broadband SED can be roughly well fitted by templates, and their best fits are consistent with the optical classification of most sources (9 out of 13). Among class A sources we found three objects fitted with pure type 1 luminosity-dependent AGN templates. They seem to be very luminous quasars and, since most of their bolometric output is not emitted in the IR band, should not be considered as “bona fide” HLIRG. The remaining four class A HLIRG require in addition to a type 1 AGN template (only one of these require a luminosity-dependent AGN template), an SB component which is in three cases dominant with respect to the AGN.

On the other hand we found that class B sources cannot be fitted with a simple combination of pure AGN and pure SB templates: a composite (i.e. AGN and SB activity are both significant) template is needed. This suggests that there should be some feedback between the accretion process and star formation that changes the shape of the SED in a way that cannot be imitated just by combining a pure SB and a pure AGN components. The main observational imprint of this feedback seems to be an excess in the SED around $\sim 10\ \mu$m with respect to the predicted emission of a pure AGN and a pure SB combined model.

Our division between class A and class B sources is based on the optical spectral classification, and since all objects show a significant AGN emission, the SED shape differences between the two groups could be an inclination effect as in the unified model of AGN (Antonucci and Miller 1985): those HLIRG where we have a direct view of the nucleus are luminous QSO and show a class A SED, while those HLIRG seen through the molecular torus and/or other obscuring material show a class B SED. The comparable mean SB contribution of class A (excluding the pure AGN sources) and class B sources is consistent with this hypothesis. Within this scenario, all types of “bona fide” HLIRG belong to the same class of sources, seen at different inclination angles.

Farrah et al. (2002a) proposed however that HLIRG population is comprised of (1) mergers between gas rich galaxies, as found in the ULIRG population, and (2) young active galaxies going through their maximal star formation periods whilst harbouring an AGN.

The $N_{\rm H}$ distribution we found in the X-ray study seems to favour the two-population hypothesis. In a pure inclination scenario we would expect a broad range of X-ray absorption, from not at all absorbed to heavily absorbed sources. Yet we found only objects with no significant intrinsic absorption (all but one class A sources) or CT-absorbed objects (all class B sources). Since AGN observed in ULIRG usually show heavy absorption in X-rays (Franceschini et al. 2003; Ptak et al. 2003; Teng et al. 2005), in principle class B sources could represent the high-luminosity tail of the ULIRG population distribution.

The study of the host galaxy morphology and environment of HLIRG also supports the two-population hypothesis. Farrah et al. (2002b) found in a sample of nine HLIRG observed by HST both strongly interactive systems and objects with no clear signs of ongoing interactions. Five sources of this sample are also included in ours: IRAS F00235+1024 and IRAS F15307+3252 (class B objects) show signs of strong interactions, while IRAS F12509+3122, IRAS F14218+3845 and IRAS 16347+7037 (class A objects) are isolated systems. This result favour our suggestion that class B HLIRG could be objects at the extreme bright end of the ULIRG population distribution.

Hence, while class B HLIRG share common properties with ULIRG (high levels of X-ray obscuration, strong star formation, signs of mergers and interactions), class A HLIRG seem to be a different class of objects. Excluding the three pure AGN sources, class A objects could be among the young active galaxies proposed by Farrah et al. (2002a). The powerful SB we found in these sources and the large amounts of gas available to fuel the star formation (as calculated by Farrah et al. 2002a), along with the non-detection of mergers or interactions in these systems support this idea. Moreover, the SB emission of the bona fide class A HLIRG is modelled with young SB templates (SB1 and SB2) in all but one object (IRAS 18216+ 6418), which is modelled with an old SB (SB3). This source could be a more evolved object.

Therefore, the "bona fide" HLIRG studied in this work likely belong to two different populations:

1. Young, isolated active galaxies undergoing their first episode of major star formation with little connection with a recent major merger.

2. Galaxies which have recently experienced a merger/disturbance that brought lots of gas and dust into the inner regions. This event triggered both the star formation and the AGN activity in a heavily obscured environment. These objects are well-suited as the high luminosity version of the ULIRG population.

Nevertheless, our sample of HLIRG is not complete in any sense and we cannot derive further conclusions about the global properties of the HLIRG population. Further studies based on larger and complete samples of HLIRG are needed to conclude if the division between class A and class B objects is just due to an inclination effect, or is based on intrinsic differences of their physical properties.

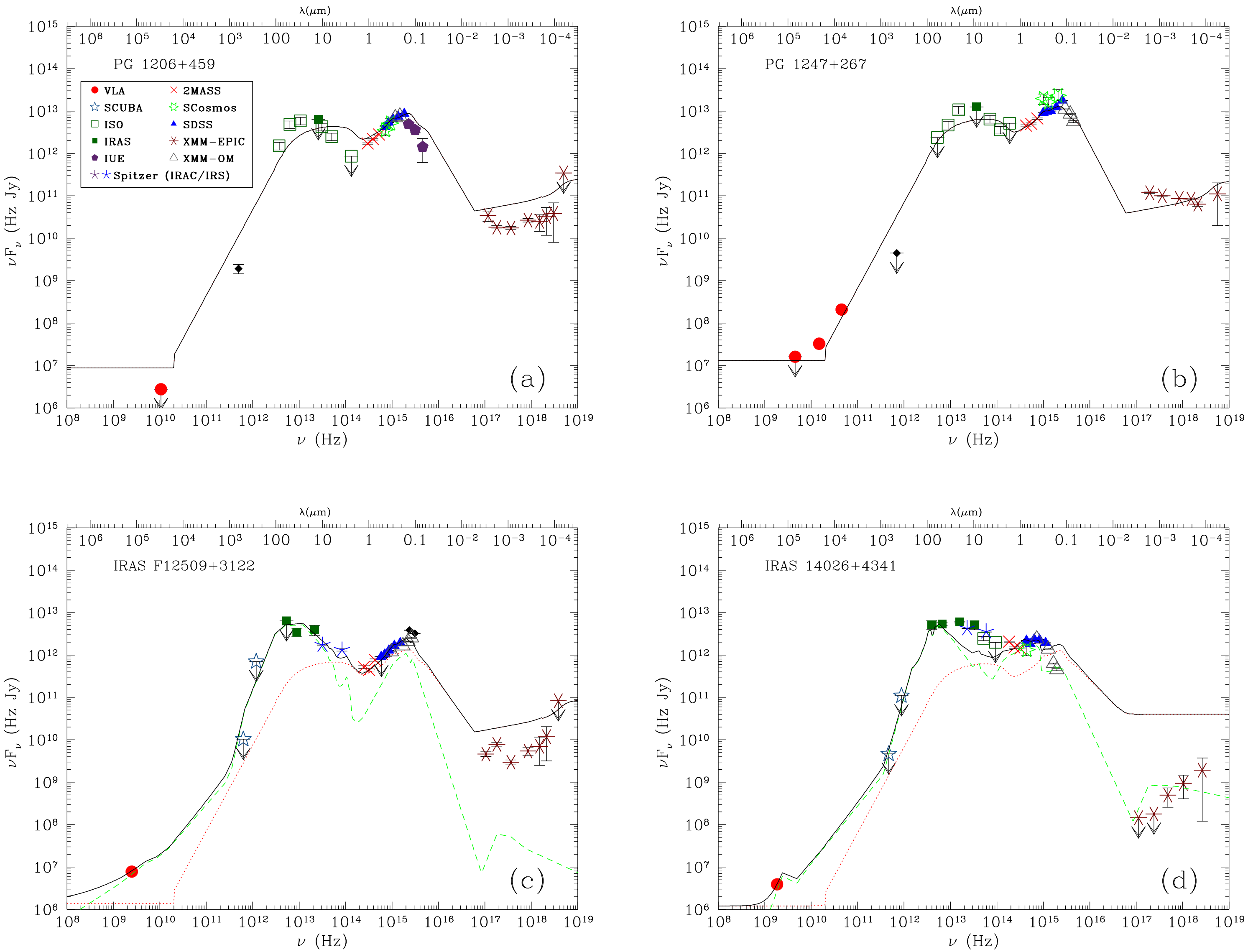

FIGURE 5.7: Rest-frame SED of class A HLIRG and their best fit models (solid lines). Red dotted lines are the AGN components and green dashed lines are the SB components.

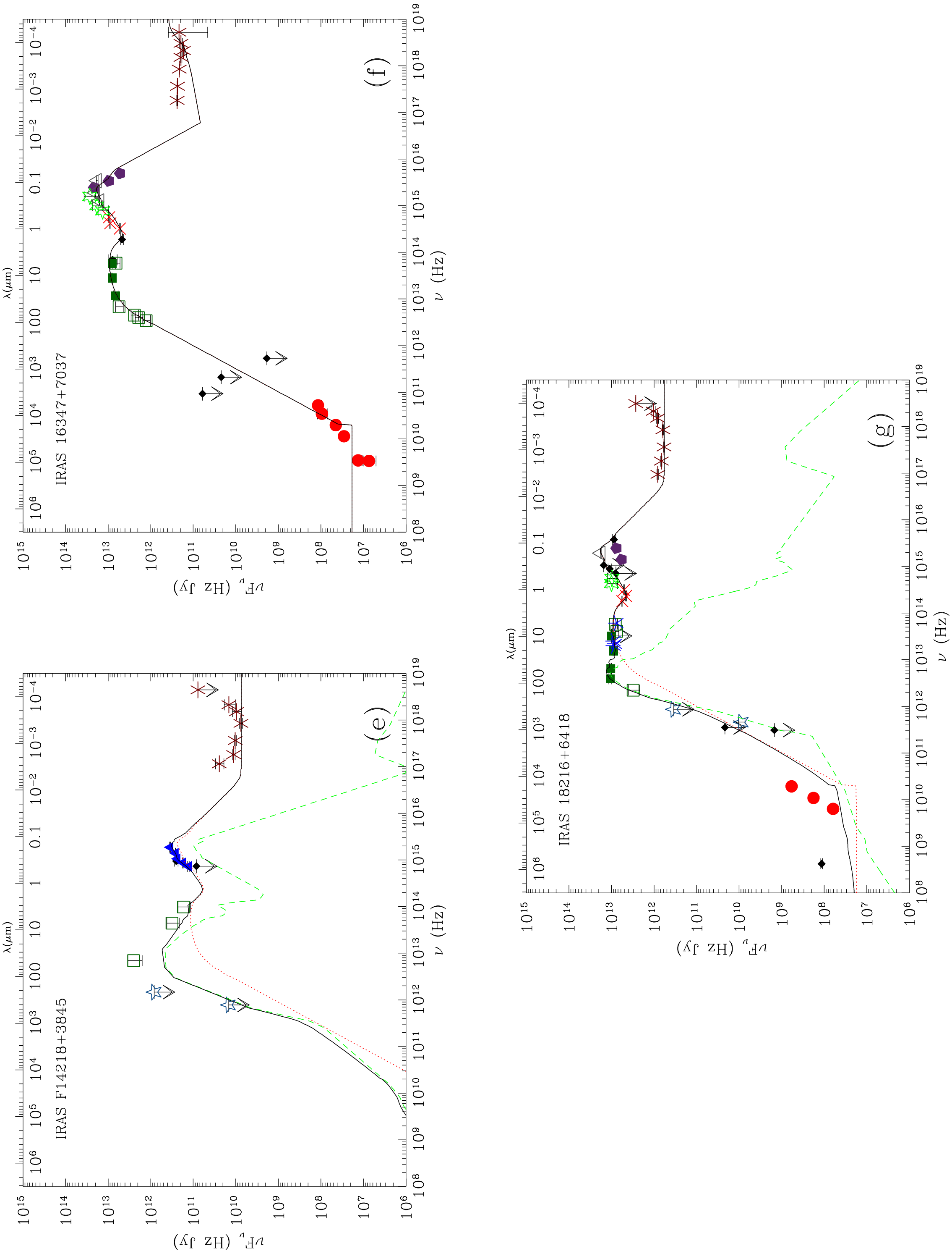

FIGURE 5.7: Continued.

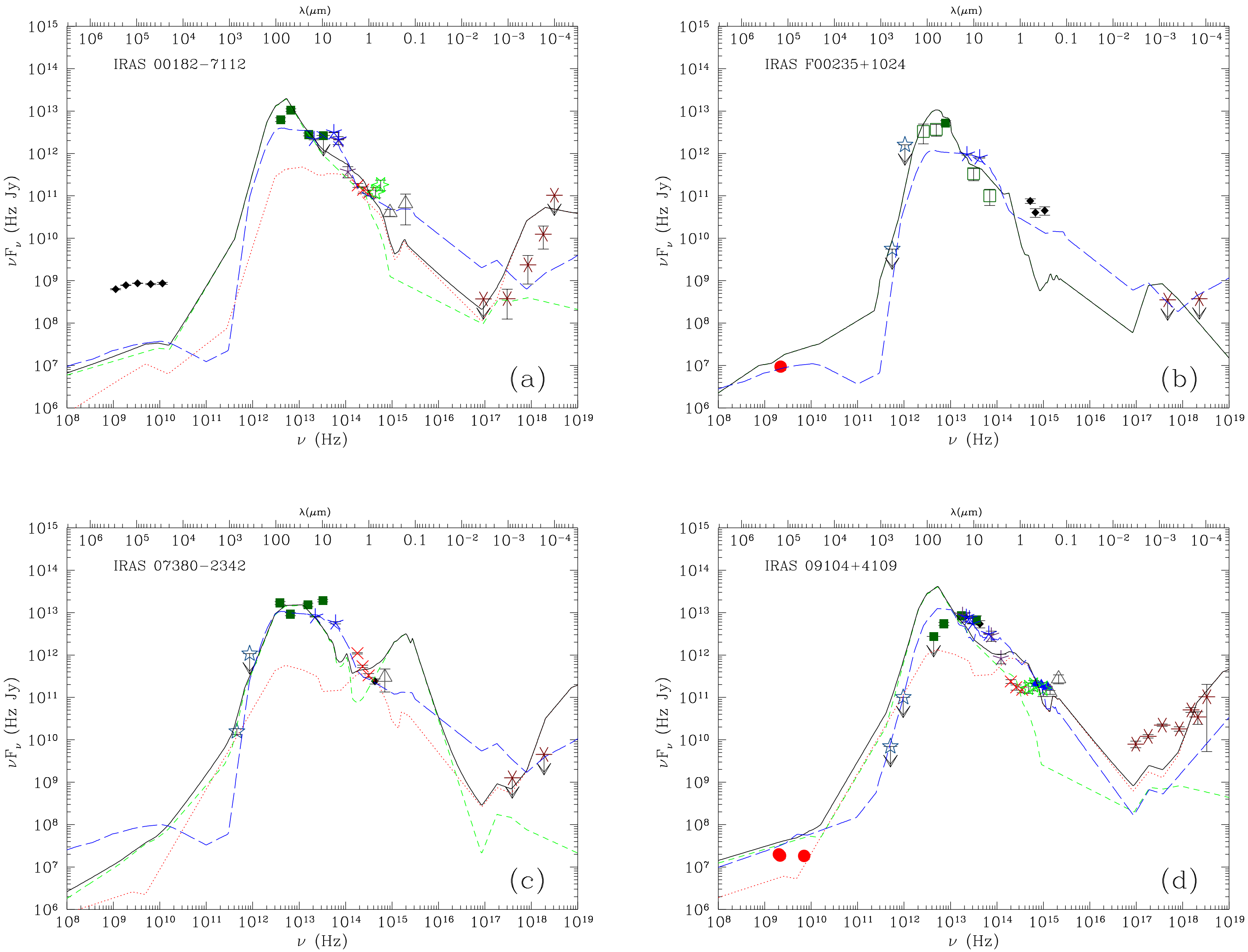

FIGURE 5.8: Rest-frame SED of class B HLIRG and their best fit models (black solid lines). We have also included the composite templates (long-dashed blue line).

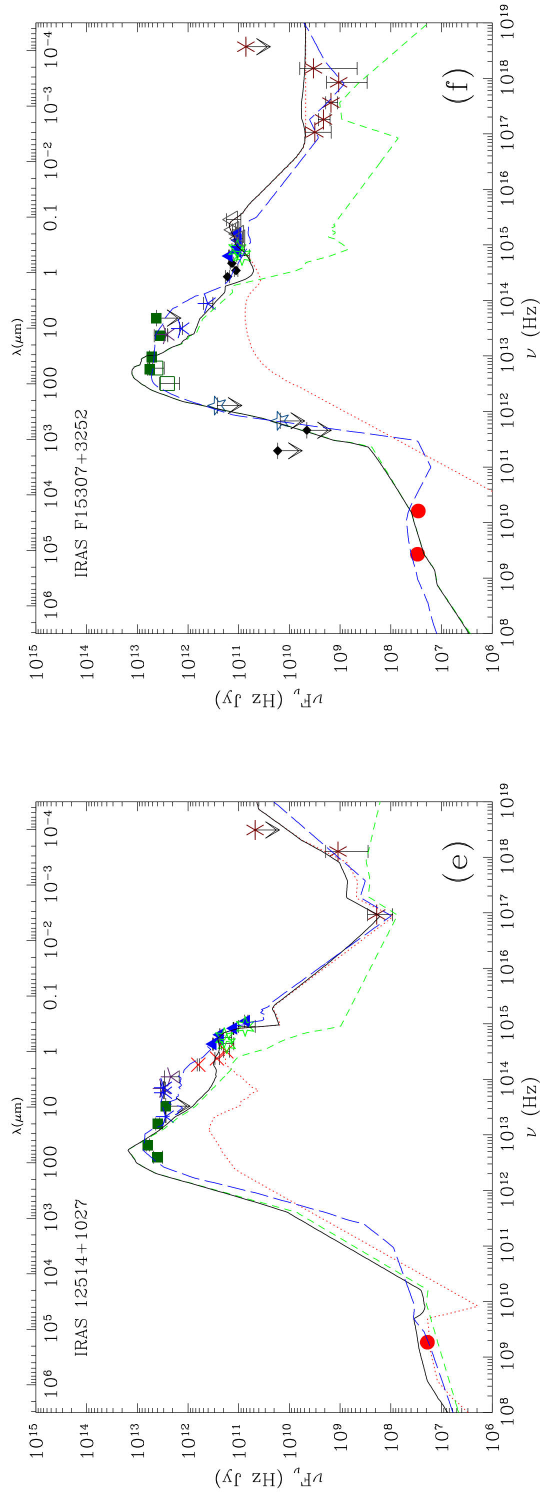

FIGURE 5.8: Continued.

Chapter 6

Conclusions and future work

6.1 Conclusions

The largest and most comprehensive study as of the date focussed on Hyperluminous Infrared Galaxies has been presented in this thesis. Through the study of an intermediate redshift ($z \lesssim 2$, with a mean redshift of ~ 0.8) sample of HLIRG of moderate size (extracted from a larger sample of HLIRG candidates assembled by RR00) we have characterized the properties of these objects in X-rays and MIR and we tried to unravel the origin of their extreme luminosity through several techniques. We have employed multi-wavelength data from state-of-the-art observatories (XMM-*Newton*, *Chandra*, *Spitzer*) for this study.

Table 6.1 summarizes the most relevant properties of each source studied throughout this work. It reflects the detection of AGN emission, SB emission and absorption/obscuration signatures in their X-ray spectra, MIR spectra and in their broadband SED through the methods explained in Chapters 3, 4 and 5. We also included the results of the study of the host galaxy morphology and environment of HLIRG performed by Farrah et al. (2002b), the AGN contribution to the total IR output, the CF and the SFR estimated in Chapter 4. For those sources with no MIR data we used the AGN contribution estimated through the SED analysis.

The broadband SED and MIR analyses revealed that all the studied sources harbour an AGN which dominates the IR luminosity in all but two sources. Through these spectral windows we also found SB emission in all but five sources. In Chapter 5 we concluded that three out of these five objects (PG 1206+459, PG 1247+267 and IRAS 1634+7037) are pure QSO and should not be considered "bona fide" HLIRG. This could be also the case of the remaining two sources (IRAS F10026+4949 and EJ1640+41) given their optical spectral classification and the lack of detection of SB emission in the MIR. However the study of their IR SED carried out by FO2 suggests that these sources have an SB contribution around $20-30\%$ of the total IR output. So these sources, instead of pure

TABLE 6.1:

Source	Type [a]	Class [b]	AGN [c]			SB [d]			Obscuration [e]			Merger [f]	α_{IR} [g]	CF [h]	SFR [i]	Family[j]
			X-ray	SED	MIR	X-ray	SED	MIR	X-ray	SED	MIR				$M_{\odot}$ yr^{-1}	
IRAS 00182-7112	QSO 2	B	✓	✓	✓	×	✓	✓	✓	✓	✓	...	0.8	~ 1	~ 200	ULIRG
IRAS F00235+1024	NL	B	×	✓	✓	×	✓	✓	×	✓	✓	✓	0.7	×	~ 1500	ULIRG
IRAS 07380-2342	NL	B	×	✓	✓	×	✓	✓	×	✓	✓	...	0.8	×	< 200	ULIRG
IRAS 09104+4109	QSO 2	B	✓	✓	✓	×	✓	✓	✓	✓	✓	...	0.9	~ 1	< 600	ULIRG
IRAS F10026+4949	Sy1	...	...	...	✓	...	...	×	...	...	✓	✓	> 0.8	...	< 4000	-
PG 1206+459	QSO	A	✓	✓	...	×	×	...	×	×	...	...	1.0	...	×	QSO
PG 1247+267	QSO	A	✓	✓	...	×	×	...	×	×	...	...	1.0	...	×	QSO
IRAS F12509+3122	QSO	A	✓	✓	✓	×	✓	✓	×	×	×	×	0.5	×	~ 2000	non-ULIRG
IRAS 12514+1027	Sy2	B	✓	✓	✓	✓	✓	✓	✓	✓	✓	...	0.5	~ 1	~ 400	ULIRG
IRAS 14026+4341	QSO	A	×	✓	✓	×	✓	✓	×	???	×	...	0.6	~ 1	~ 400	non-ULIRG
IRAS F14218+3845	QSO	A	✓	✓	...	×	✓	...	×	×	...	×	0.3	...		non-ULIRG
IRAS F15307+3252	QSO 2	B	✓	✓	✓	×	✓	✓	✓	✓	✓	✓	0.6	0.7	~ 3000	ULIRG
IRAS F16124+3241	NL	...	...	...	✓	...	...	✓	...	...	✓	...	0.2	...	~ 1200	ULIRG
IRAS 16347+7037	QSO	A	✓	✓	...	×	×	...	×	×	...	×	1.0	...	×	QSO
ELAISP90 J164010+41050	QSO	...	...	...	✓	...	...	×	...	...	×	...	> 0.8	...	< 700	non-ULIRG
IRAS 18216+6418	QSO	A	✓	✓	✓	×	✓	✓	×	×	×	...	0.6	0.2	~ 300	non-ULIRG

[a] Classification based on the optical spectrum.
[b] Classification based on the broadband SED shape (see Chapter 5).
[c] AGN emission detected in the referred energy range.
[d] SB emission detected in the referred energy range.
[e] Obscuration/absorption signatures detected in the referred energy range.
[f] HST images show signs of interactions or ongoing mergers (Farrah et al. 2002b).
[g] AGN contribution to the total IR luminosity, calculated through the spectral decomposition of their MIR emission (see Chapter 4). We included the AGN contribution estimated through its SED analysis for those sources with no MIR spectrum (see Chapter 5).
[h] CF estimated through the MIR and X-ray emission (see Chapter 4). Those sources in which meaningless CF were found are marked with ×.
[i] SFR estimated through the PAH emission (see Chapter 4).
[j] Final classification of each source based on its global properties.

QSO could be similar to other class A HLIRG (see Chapter 5) with significant SB contribution, like IRAS 18216+6418 or IRAS F14218+3845.

The emission of the AGN dominates the X-ray spectrum of those sources observed and detected by XMM-*Newton*. We detected SB emission in the X-ray spectra of just one source. The lack of X-ray emission associated with an SB in the remaining sources, even in those where the MIR and SED analyses suggested an important SB contribution to the total output is due to the difference of the X-ray-to-bolometric ratios between AGN and SB, e.g. the SED plots of IRAS F12509+3122, IRAS F14218+3845 or IRAS 18216+6418 (Figs. 5.7(c), 5.7(a), 5.7(c)) show that the SB emission in the X-ray band is within two to four orders of magnitude lower than the AGN emission. Such a faint component is impossible to be disentangled given the current sensitivity of XMM-*Newton*. We could expect in principle detecting the X-ray emission from the SB in, at least, the obscured sources (as we did in IRAS 12514+1027) where the observed AGN emission is fainter. However in those sources the low signal-to-noise ratio of their X-ray spectra (see Figs. 3.1(a), 3.1(h)) makes obtaining a significant detection of the SB component very hard.

Three sources were not detected in our X-ray analysis. The broadband SED and MIR spectra of two of them (IRAS 00182-7112 and IRAS F00235+1024) clearly suggest that they are strongly obscured by dust. On the other hand, although IRAS 14026+4341 was not detected in our analysis, it has a counterpart in the 2XMMi catalogue (see Chapter 5, Sect. 5.4.4). This object shows no signs of obscuration in its optical emission, but it seem to be absorbed in the EUV and soft X-rays (see Fig. 5.7(d)). These properties could be explained if this HLIRG is an absorbed X-ray QSO, as we proposed in Chapter 5. These objects are absorbed by ionized gas, in which there is no dust, and hence its optical emission is not obscured. This also explain the non detection of obscuration in its MIR spectrum.

We can conclude that the most efficient method to disentangle the AGN and SB emission of HLIRG is the MIR spectral decomposition. MIR emission of the AGN can be detected even in strongly obscured environments where X-rays are completely absorbed. Moreover, given the low dispersion of AGN and SB emission within the 5-8 μm range, we can characterize the SB emission even in those sources where the AGN component largely dominates the MIR spectrum.

Excluding from the subsequent discussion the three pure QSO, since they are a contamination due to the selection criteria of the RR00 parent sample (see Chapter 2), we found that AGN and SB phenomena are both needed to fully explain the multiwavelength properties of HLIRG. The AGN component dominates the total IR output, or at least is as important as the SB component, in most sources ($\sim 85\%$ of the sample). All of them show strong star formation, with SFR within $200 - 2000\ M_\odot\ \mathrm{yr}^{-1}$.

However these sources do not seem to be an homogeneous population. On one hand there are sources with large amounts of gas and dust enshrouding the nucleus as it is suggested by the strong absorption shown in X-rays (IRAS 00182-7112, IRAS 09104+4109, IRAS 12514+1027, IRAS F15307+3252) and MIR (IRAS 00182-7112, IRAS F00235+1024, IRAS 07380-2342, IRAS 09104+4109, IRAS 12514+1027, IRAS F15307+3252, IRAS F16124+3241) and by the shape of their SED (IRAS 00182-7112, IRAS F00235+1024, IRAS 07380-2342, IRAS 09104+4109, IRAS 12514+1027, IRAS F15307+3252). Their large ($\sim$ 1) dust covering factors are also consistent with a nucleus almost completely enshrouded by dust (IRAS 00182-7112, IRAS 09104+4109, IRAS 12514+1027, IRAS F15307+3252). The gas and dust fuel powerful AGN activity and strong star formation, that could be triggered by galaxy interactions and/or mergers, as some HST images suggest (IRAS F00235+1024, IRAS F15307+3252). The analysis of their SED also hints toward a strong feedback between both phenomena. These are common properties of ULIRG and hence we can consider these HLIRG as the objects occupying the high luminosity tail of the ULIRG population distribution. In Table 6.1 we labelled as “ULIRG” those sources which could possibly belong to this population.

On the other hand we found HLIRG with minor MIR/optical/X-ray obscuration, suggesting lower quantities of gas and dust than in the “ULIRG-like” population. We were able to estimate the dust CF of just one source of this kind (IRAS 18216+6418), but it is significantly lower than the CF of ULIRG or standard AGN (see Chapter 4), consistent with low quantities of dust in the nuclear environment. However the strong SB observed in these sources require large amounts of gas to fuel the star formation. They seem to be isolated galaxies, with no signs of interactions or ongoing mergers, as some HST observations suggest (IRAS F12509+3122, IRAS F14218+3845). As we proposed in Chapter 5, these HLIRG could be young active galaxies undergoing their first major episode of star formation. We labelled in Table 6.1 those sources which we believe belong to this population as “non-ULIRG”.

Summarizing, we proposed that the sources studied in this work come from three different populations:

1. Very luminous quasars with minor star formation activity.
2. HLIRG showing clear signs of major mergers and interactions, with heavily obscured nuclei and strong feedback between the star formation and AGN activity. These sources could be the higher luminosity version of ULIRG.
3. Isolated HLIRG with low X-ray absorption and powerful SB and large amounts of gas available to fuel the star formation. These sources could be young active galaxies going through their maximal star formation periods whilst harbouring an AGN.

he idea that bona fide HLIRG are composed of two populations should be verified by further observational studies based on larger and, most importantly, complete samples of HLIRG. Moreover our simple template-fitting approach should be complemented with theoretical models of AGN and SB emission (e.g. radiative transfer models), since the two approaches are complementary in many ways and their combination may shed further light onto the relative SB-AGN contribution and on the feedback processes which take place in HLIRG.

6.2 Future work

The results obtained in this work can be improved in the future through:

- **increasing the size of the HLIRG sample**. This thesis is based on the study of a moderate number of sources (~ 20). This number was a significant fraction of the total known HLIRG (~ 50) when our work has started. However, the wide area surveys carried out by new IR telescopes like *Spitzer* (FIDEL or SWIRE surveys, see Lonsdale et al. 2003; Dickinson and FIDEL team 2007) or AKARI (Murakami et al. 2007), or the forthcoming observations of *Herschel* (Pearson and Khan 2009), are dramatically increasing the number of known HLIRG. All these new data allow the construction of HLIRG samples with a much larger number of sources, selected in an homogeneous way, and hence aim at stronger conclusions about the properties of the global population of HLIRG.

- **a comparison with other populations of astronomical sources**. Our work is limited to moderate redshift HLIRG, but now the new IR observatories have discovered a growing number of high-z HLIRG (Lonsdale et al. 2006b). Comparing the properties of low-z and high-z ULIRG and HLIRG is crucial to understand the evolution of these objects trough cosmic time. Moreover, study the link between HLIRG and other composite luminous sources like sub-mm galaxies (Blain et al. 2002; Alexander et al. 2005) or absorbed QSO (Stevens et al. 2005; Page et al. 2007) is mandatory to obtain a global view of the co-evolution of AGN and galaxy formation.

- **the next generation of X-ray observatories (long term)**. The joint mission of NASA, ESA and JAXA to develop the International X-ray Observatory (IXO, White and Hornschemeier 2009) will provide an excellent tool for the study of HLIRG. The extension of the energy range and sensitivity beyond 10 keV will allow the direct observation of the nuclear emission of the highest absorbed sources. In addition, the increasing sensitivity in soft X-rays will probably allow the detection of the star forming processes in X-rays even in AGN dominated HLIRG.

Appendix A

Tables of SED data

Along this appendix a table is presented for each HLIRG with the fluxes employed to build their SED (see Chapt. 5) and the origin of each data. Frequencies and fluxes are in the observer's frame. The re-binned spectra from XMM-*Newton*-EPIC and *Spitzer*-IRS are not included in these tables. Those fluxes without errors are upper limits.

TABLE A.1: IRAS 00182-7112.

ν Hz	F_ν Jy	Error Jy	Ref.
8.43×10^{8}	4.23×10^{-1}	1.28×10^{-2}	SUMSS [a]
1.40×10^{9}	3.17×10^{-1}	3.00×10^{-3}	ATCA[b]
2.50×10^{9}	1.97×10^{-1}	3.00×10^{-3}	ATCA[b]
4.80×10^{9}	9.80×10^{-2}	3.00×10^{-3}	ATCA[b]
8.60×10^{9}	5.70×10^{-2}	3.00×10^{-3}	ATCA[b]
3.00×10^{12}	1.19×10^{0}	1.19×10^{-1}	IRAS [a]
5.00×10^{12}	1.20×10^{0}	8.37×10^{-2}	IRAS [a]
1.20×10^{13}	1.33×10^{-1}	1.02×10^{-2}	IRAS [a]
2.50×10^{13}	6.02×10^{-2}	...	IRAS [a]
5.23×10^{13}	2.23×10^{-2}	4.78×10^{-3}	*Spitzer*-IRAC
8.44×10^{13}	2.53×10^{-3}	7.47×10^{-4}	*Spitzer*-IRAC
1.39×10^{14}	7.22×10^{-4}	7.83×10^{-5}	2MASS
1.80×10^{14}	4.37×10^{-4}	7.34×10^{-5}	2MASS
2.43×10^{14}	2.68×10^{-4}	4.34×10^{-5}	2MASS
3.33×10^{14}	2.02×10^{-4}	5.57×10^{-5}	SSS
4.28×10^{14}	2.28×10^{-4}	6.30×10^{-5}	SSS
6.81×10^{14}	2.97×10^{-5}	5.40×10^{-6}	XMM-OM
1.48×10^{15}	1.90×10^{-5}	1.30×10^{-5}	XMM-OM

[a] Data from NED.
[b] Drake et al. 2004.

TABLE A.2: IRAS F00235+1024.

ν Hz	F_ν Jy	Error Jy	Ref.
1.40×10^{9}	2.70×10^{-3}	5.00×10^{-4}	VLA [a]
3.53×10^{11}	6.38×10^{-3}	...	SCUBA [c]
6.66×10^{11}	9.67×10^{-1}	...	SCUBA [c]
1.66×10^{12}	8.05×10^{-1}	3.93×10^{-1}	ISO [a]
3.15×10^{12}	4.78×10^{-1}	1.48×10^{-1}	ISO [a]
5.00×10^{12}	4.28×10^{-1}	5.56×10^{-2}	IRAS [a]
2.00×10^{13}	6.75×10^{-3}	2.14×10^{-3}	ISO [a]
4.44×10^{13}	9.20×10^{-4}	3.80×10^{-4}	ISO [a]
1.39×10^{14}	1.01×10^{-4}	5.00×10^{-6}	APM [c]
3.33×10^{14}	8.00×10^{-5}	1.00×10^{-5}	APM [c]
4.28×10^{14}	3.10×10^{-5}	7.00×10^{-6}	USNO-B1.0
6.81×10^{14}	1.80×10^{-5}	4.00×10^{-6}	USNO-B1.0
3.02×10^{17}	4.68×10^{-10}	...	XMM-EPIC
1.45×10^{18}	1.04×10^{-10}	...	XMM-EPIC

[a] Data from NED.
[c] Farrah et al. 2002a.

Table A.3: IRAS 07380-2342.

ν Hz	F_ν Jy	Error Jy	Ref.
3.53×10^{11}	2.68×10^{-2}	4.20×10^{-3}	SCUBA [c]
6.66×10^{11}	9.67×10^{-1}	...	SCUBA [c]
3.00×10^{12}	3.55×10^{0}	2.84×10^{-1}	IRAS [a]
5.00×10^{12}	1.17×10^{0}	9.36×10^{-2}	IRAS [a]
1.20×10^{13}	8.00×10^{-1}	8.00×10^{-2}	IRAS [a]
2.50×10^{13}	4.84×10^{-1}	3.39×10^{-2}	IRAS [a]
1.39×10^{14}	4.08×10^{-3}	1.49×10^{-4}	2MASS
1.80×10^{14}	1.35×10^{-3}	9.71×10^{-5}	2MASS
2.43×10^{14}	4.74×10^{-4}	4.79×10^{-5}	2MASS
3.33×10^{14}	1.62×10^{-4}	2.23×10^{-5}	DENIS
5.45×10^{14}	3.80×10^{-5}	2.10×10^{-5}	XMM-OM
3.02×10^{17}	2.51×10^{-9}	...	XMM-EPIC
1.45×10^{18}	1.87×10^{-9}	...	XMM-EPIC

[a] Data from NED.
[c] Farrah et al. 2002a.

Table A.4: IRAS 09104+4109.

ν Hz	F_ν Jy	Error Jy	Ref.
1.40×10^{9}	6.88×10^{-3}	1.31×10^{-4}	VLA [a]
1.49×10^{9}	6.00×10^{-3}	1.00×10^{-3}	VLA [a]
4.90×10^{9}	1.80×10^{-3}	3.00×10^{-4}	VLA [a]
3.53×10^{11}	9.54×10^{-3}	...	SCUBA [c]
6.66×10^{11}	7.28×10^{-2}	...	SCUBA [c]
3.00×10^{12}	4.38×10^{-1}	...	IRAS [a]
5.00×10^{12}	5.25×10^{-1}	4.20×10^{-2}	IRAS [a]
1.20×10^{13}	3.34×10^{-1}	1.30×10^{-2}	IRAS [a]
1.26×10^{13}	3.33×10^{-1}	1.70×10^{-2}	*Spitzer*-IRAC
1.43×10^{13}	2.70×10^{-1}	7.00×10^{-2}	IRTF [d]
2.50×10^{13}	1.30×10^{-1}	3.11×10^{-2}	IRAS [a]
2.97×10^{13}	8.80×10^{-2}	1.70×10^{-2}	IRTF [d]
5.23×10^{13}	2.64×10^{-2}	7.11×10^{-3}	*Spitzer*-IRAC
8.44×10^{13}	4.74×10^{-3}	1.21×10^{-3}	*Spitzer*-IRAC
1.39×10^{14}	8.21×10^{-4}	8.61×10^{-5}	2MASS
1.80×10^{14}	4.59×10^{-4}	6.24×10^{-5}	2MASS
2.43×10^{14}	2.97×10^{-4}	4.64×10^{-5}	2MASS
3.33×10^{14}	2.42×10^{-4}	6.69×10^{-5}	SSS
3.28×10^{14}	5.06×10^{-4}	7.45×10^{-6}	SDSS-dr5
3.93×10^{14}	7.04×10^{-4}	3.42×10^{-6}	SDSS-dr5
4.28×10^{14}	2.12×10^{-4}	5.85×10^{-5}	SSS
4.81×10^{14}	2.11×10^{-4}	1.69×10^{-6}	SDSS-dr5
6.28×10^{14}	1.51×10^{-4}	1.26×10^{-6}	SDSS-dr5
6.81×10^{14}	1.08×10^{-4}	3.97×10^{-5}	SSS
8.47×10^{14}	1.01×10^{-4}	3.16×10^{-6}	SDSS-dr5
9.67×10^{14}	5.90×10^{-5}	6.00×10^{-6}	XMM-OM
1.48×10^{15}	7.50×10^{-5}	1.80×10^{-5}	XMM-OM
7.86×10^{18}	1.06×10^{-7}	5.91×10^{-8}	BeppoSAX [a]

[a] Data from NED.
[c] Farrah et al. 2002a.
[d] Kleinmann et al. 1988.

Table A.5: PG 1206+459.

ν Hz	F_ν Jy	Error Jy	Ref.
4.90×10^{9}	1.20×10^{-4}	...	VLA [a]
2.30×10^{11}	1.80×10^{-3}	4.50×10^{-4}	IRAM [a]
1.72×10^{12}	1.89×10^{-1}	3.78×10^{-2}	ISO [a]
2.93×10^{12}	3.53×10^{-1}	7.06×10^{-2}	ISO [a]
4.93×10^{12}	2.57×10^{-1}	5.14×10^{-2}	ISO [a]
1.20×10^{13}	1.13×10^{-1}	...	IRAS [a]
1.43×10^{13}	6.40×10^{-2}	1.28×10^{-2}	ISO [a]
2.34×10^{13}	2.30×10^{-2}	4.60×10^{-3}	ISO [a]
2.50×10^{13}	2.07×10^{-1}	3.60×10^{-2}	IRAS [a]
6.17×10^{13}	3.00×10^{-3}	...	ISO [a]
1.39×10^{14}	2.64×10^{-3}	9.46×10^{-5}	2MASS
1.80×10^{14}	2.57×10^{-3}	1.22×10^{-4}	2MASS
2.43×10^{14}	2.43×10^{-3}	7.76×10^{-5}	2MASS
3.33×10^{14}	2.27×10^{-3}	6.26×10^{-4}	SSS
3.28×10^{14}	2.78×10^{-3}	1.26×10^{-5}	SDSS-dr5
3.93×10^{14}	2.94×10^{-3}	9.76×10^{-6}	SDSS-dr5
4.28×10^{14}	2.51×10^{-3}	6.93×10^{-4}	SSS
4.81×10^{14}	2.92×10^{-3}	9.45×10^{-6}	SDSS-dr5
5.45×10^{14}	2.62×10^{-3}	3.00×10^{-5}	XMM-OM
6.28×10^{14}	2.53×10^{-3}	7.01×10^{-6}	SDSS-dr5
6.81×10^{14}	2.25×10^{-3}	1.30×10^{-5}	XMM-OM
8.47×10^{14}	2.20×10^{-3}	9.06×10^{-6}	SDSS-dr5
1.05×10^{15}	1.00×10^{-3}	9.21×10^{-5}	IUE
1.46×10^{15}	5.25×10^{-4}	7.25×10^{-5}	IUE
2.11×10^{15}	1.45×10^{-4}	8.32×10^{-5}	IUE

[a] Data from NED.

Table A.6: PG 1247+267.

ν Hz	F_ν Jy	Error Jy	Ref.
1.49×10^{9}	1.17×10^{-3}	...	VLA [a]
4.90×10^{9}	7.20×10^{-4}	8.00×10^{-5}	VLA [a]
1.49×10^{10}	1.51×10^{-3}	2.20×10^{-4}	VLA [a]
2.30×10^{11}	2.10×10^{-3}	...	IRAM [a]
1.72×10^{12}	1.50×10^{-1}	...	ISO [a]
2.93×10^{12}	1.74×10^{-1}	3.48×10^{-2}	ISO [a]
4.93×10^{12}	2.36×10^{-1}	4.72×10^{-2}	ISO [a]
1.20×10^{13}	1.13×10^{-1}	...	IRAS [a]
2.34×10^{13}	3.00×10^{-2}	6.00×10^{-3}	ISO [a]
3.91×10^{13}	1.00×10^{-2}	2.00×10^{-3}	ISO [a]
6.17×10^{13}	9.00×10^{-3}	...	ISO [a]
1.39×10^{14}	3.55×10^{-3}	1.36×10^{-4}	2MASS
1.80×10^{14}	2.99×10^{-3}	1.45×10^{-4}	2MASS
2.43×10^{14}	2.93×10^{-3}	1.10×10^{-4}	2MASS
3.33×10^{14}	6.31×10^{-3}	1.74×10^{-3}	SSS
3.28×10^{14}	3.01×10^{-3}	1.37×10^{-5}	SDSS-dr5
3.93×10^{14}	2.66×10^{-3}	9.69×10^{-6}	SDSS-dr5
4.28×10^{14}	4.03×10^{-3}	1.11×10^{-3}	SSS
4.81×10^{14}	2.26×10^{-3}	8.02×10^{-6}	SDSS-dr5
6.28×10^{14}	2.13×10^{-3}	6.42×10^{-6}	SDSS-dr5
6.81×10^{14}	3.54×10^{-3}	1.30×10^{-3}	SSS
8.47×10^{14}	2.27×10^{-3}	9.92×10^{-6}	SDSS-dr5
9.67×10^{14}	1.17×10^{-3}	8.00×10^{-6}	XMM-OM
1.25×10^{15}	6.70×10^{-4}	2.00×10^{-5}	XMM-OM
1.48×10^{15}	3.70×10^{-4}	2.00×10^{-5}	XMM-OM

[a] Data from NED.

TABLE A.7: IRAS F12509+3122.

ν Hz	F_ν Jy	Error Jy	Ref.
1.40×10^{9}	1.76×10^{-3}	1.25×10^{-4}	VLA [a]
3.53×10^{11}	9.23×10^{-3}	...	SCUBA [c]
6.66×10^{11}	3.33×10^{-1}	...	SCUBA [c]
3.00×10^{12}	6.75×10^{-1}	...	IRAS [a]
5.00×10^{12}	2.18×10^{-1}	4.36×10^{-2}	IRAS [a]
1.20×10^{13}	1.03×10^{-1}	2.75×10^{-2}	IRAS [a]
1.39×10^{14}	1.18×10^{-3}	8.78×10^{-5}	2MASS
1.80×10^{14}	7.75×10^{-4}	8.07×10^{-5}	2MASS
2.43×10^{14}	9.77×10^{-4}	6.01×10^{-5}	2MASS
3.33×10^{14}	8.60×10^{-4}	...	APM [c]
3.28×10^{14}	8.73×10^{-4}	7.57×10^{-6}	SDSS-dr5
3.93×10^{14}	8.39×10^{-4}	3.56×10^{-6}	SDSS-dr5
4.28×10^{14}	7.20×10^{-4}	7.00×10^{-5}	APM
4.81×10^{14}	8.39×10^{-4}	3.12×10^{-6}	SDSS-dr5
5.45×10^{14}	6.60×10^{-4}	1.60×10^{-5}	XMM-OM
6.28×10^{14}	8.32×10^{-4}	2.89×10^{-6}	SDSS-dr5
8.47×10^{14}	7.22×10^{-4}	4.89×10^{-6}	SDSS-dr5
9.67×10^{14}	4.94×10^{-4}	6.00×10^{-6}	XMM-OM
1.25×10^{15}	4.68×10^{-4}	7.00×10^{-6}	XMM-OM
1.33×10^{15}	7.83×10^{-4}	9.94×10^{-7}	HST-FOS
1.48×10^{15}	4.69×10^{-4}	1.60×10^{-5}	XMM-OM
1.75×10^{15}	5.16×10^{-4}	1.38×10^{-6}	HST-FOS

[a] Data from NED.
[c] Farrah et al. 2002a.

TABLE A.8: IRAS 12514+1027.

ν Hz	F_ν Jy	Error Jy	Ref.
1.40×10^{9}	7.78×10^{-3}	1.46×10^{-4}	VLA [a]
3.00×10^{12}	7.55×10^{-1}	1.51×10^{-1}	IRAS [a]
5.00×10^{12}	7.12×10^{-1}	5.70×10^{-2}	IRAS [a]
1.20×10^{13}	1.90×10^{-1}	1.58×10^{-2}	IRAS [a]
2.50×10^{13}	6.32×10^{-2}	...	IRAS [a]
5.23×10^{13}	3.46×10^{-2}	4.03×10^{-3}	*Spitzer*-IRAC
8.44×10^{13}	1.49×10^{-2}	4.82×10^{-3}	*Spitzer*-IRAC
1.39×10^{14}	2.57×10^{-3}	1.26×10^{-4}	2MASS
1.80×10^{14}	8.45×10^{-4}	8.57×10^{-5}	2MASS
2.43×10^{14}	4.07×10^{-4}	5.40×10^{-5}	2MASS
3.33×10^{14}	2.88×10^{-4}	7.96×10^{-5}	SSS
3.28×10^{14}	5.66×10^{-4}	1.15×10^{-5}	SDSS-dr5
3.93×10^{14}	3.39×10^{-4}	2.96×10^{-6}	SDSS-dr5
4.28×10^{14}	2.46×10^{-4}	6.81×10^{-5}	SSS
4.81×10^{14}	2.82×10^{-4}	2.30×10^{-6}	SDSS-dr5
6.28×10^{14}	1.16×10^{-4}	1.50×10^{-6}	SDSS-dr5
6.81×10^{14}	5.78×10^{-5}	2.13×10^{-5}	SSS
8.47×10^{14}	4.79×10^{-5}	3.53×10^{-6}	SDSS-dr5

[a] Data from NED.

Table A.9: IRAS 14026+4341.

ν Hz	F_ν Jy	Error Jy	Ref.
1.40×10^{9}	1.59×10^{-3}	1.39×10^{-4}	VLA [a]
3.53×10^{11}	7.53×10^{-3}	...	SCUBA [c]
6.66×10^{11}	9.40×10^{-2}	...	SCUBA [c]
3.00×10^{12}	9.94×10^{-1}	2.39×10^{-1}	IRAS [a]
5.00×10^{12}	6.22×10^{-1}	5.60×10^{-2}	IRAS [a]
1.20×10^{13}	2.85×10^{-1}	1.41×10^{-2}	IRAS [a]
2.50×10^{13}	1.18×10^{-1}	2.71×10^{-2}	IRAS [a]
3.91×10^{13}	3.60×10^{-2}	4.00×10^{-3}	ISO [a]
7.05×10^{13}	1.60×10^{-2}	...	ISO [a]
1.39×10^{14}	8.47×10^{-3}	2.29×10^{-4}	2MASS
1.80×10^{14}	4.75×10^{-3}	1.57×10^{-4}	2MASS
2.43×10^{14}	3.33×10^{-3}	1.01×10^{-4}	2MASS
3.33×10^{14}	2.26×10^{-3}	6.25×10^{-4}	SSS
3.28×10^{14}	3.83×10^{-3}	2.05×10^{-5}	SDSS-dr5
3.93×10^{14}	2.70×10^{-3}	1.23×10^{-5}	SDSS-dr5
4.81×10^{14}	2.82×10^{-3}	1.17×10^{-5}	SDSS-dr5
5.45×10^{14}	2.44×10^{-3}	1.90×10^{-5}	XMM-OM
6.28×10^{14}	2.09×10^{-3}	9.05×10^{-6}	SDSS-dr5
8.47×10^{14}	1.30×10^{-3}	7.19×10^{-6}	SDSS-dr5
9.67×10^{14}	7.70×10^{-4}	4.00×10^{-6}	XMM-OM
1.25×10^{15}	2.65×10^{-4}	7.00×10^{-6}	XMM-OM
1.48×10^{15}	1.59×10^{-4}	9.00×10^{-6}	XMM-OM
8.46×10^{16}	1.42×10^{-10}	8.39×10^{-10}	2XMMi
1.81×10^{17}	2.14×10^{-10}	3.50×10^{-10}	2XMMi
3.63×10^{17}	7.82×10^{-10}	3.76×10^{-10}	2XMMi
7.86×10^{17}	6.81×10^{-10}	3.85×10^{-10}	2XMMi
1.99×10^{18}	5.49×10^{-10}	5.17×10^{-10}	2XMMi

[a] Data from NED.
[c] Farrah et al. 2002a.

Table A.10: IRAS F14218+3845.

ν Hz	F_ν Jy	Error Jy	Ref.
3.53×10^{11}	8.55×10^{-3}	...	SCUBA [c]
6.66×10^{11}	2.53×10^{-1}	...	SCUBA [c]
3.15×10^{12}	1.64×10^{-1}	6.10×10^{-2}	ISO [a]
2.00×10^{13}	3.23×10^{-3}	1.04×10^{-3}	ISO [a]
4.44×10^{13}	7.90×10^{-4}	2.60×10^{-4}	ISO [a]
3.33×10^{14}	5.00×10^{-5}	...	APM [c]
3.28×10^{14}	7.97×10^{-5}	4.34×10^{-6}	SDSS-dr5
3.93×10^{14}	9.09×10^{-5}	1.26×10^{-6}	SDSS-dr5
4.28×10^{14}	1.14×10^{-4}	1.05×10^{-5}	APM
4.81×10^{14}	1.01×10^{-4}	1.02×10^{-6}	SDSS-dr5
6.28×10^{14}	8.52×10^{-5}	7.85×10^{-7}	SDSS-dr5
8.47×10^{14}	8.47×10^{-5}	2.26×10^{-6}	SDSS-dr5

[a] Data from NED.
[c] Farrah et al. 2002a.

TABLE A.11: IRAS F15307+3252.

ν Hz	F_ν Jy	Error Jy	Ref.
1.40×10^{9}	5.71×10^{-3}	1.09×10^{-4}	VLA [a]
8.42×10^{9}	9.20×10^{-4}	4.00×10^{-5}	VLA [a]
1.02×10^{11}	4.50×10^{-2}	...	OVMA [a]
2.39×10^{11}	5.10×10^{-3}	...	OVMA [a]
3.53×10^{11}	1.15×10^{-2}	...	SCUBA [c]
6.66×10^{11}	1.06×10^{-1}	...	SCUBA [c]
1.66×10^{12}	4.14×10^{-1}	1.76×10^{-1}	ISO [a]
3.00×10^{12}	5.10×10^{-1}	6.20×10^{-2}	IRAS [a]
3.15×10^{12}	3.68×10^{-1}	1.16×10^{-1}	ISO [a]
5.00×10^{12}	2.80×10^{-1}	2.70×10^{-2}	IRAS [a]
1.20×10^{13}	8.00×10^{-2}	2.40×10^{-2}	IRAS [a]
1.26×10^{13}	5.70×10^{-2}	3.00×10^{-3}	*Spitzer*-IRAC
2.50×10^{13}	4.50×10^{-2}	...	IRAS [a]
1.39×10^{14}	3.20×10^{-4}	3.00×10^{-5}	MMT [a]
1.80×10^{14}	1.68×10^{-4}	1.40×10^{-5}	MMT [a]
2.43×10^{14}	1.48×10^{-4}	1.20×10^{-5}	MMT [a]
3.33×10^{14}	6.70×10^{-5}	1.85×10^{-5}	SSS
3.28×10^{14}	1.28×10^{-4}	3.91×10^{-6}	SDSS-dr5
3.93×10^{14}	7.17×10^{-5}	1.06×10^{-6}	SDSS-dr5
4.28×10^{14}	6.32×10^{-5}	1.75×10^{-5}	SSS
4.81×10^{14}	5.90×10^{-5}	8.70×10^{-7}	SDSS-dr5
6.28×10^{14}	4.40×10^{-5}	6.89×10^{-7}	SDSS-dr5
6.81×10^{14}	3.40×10^{-5}	4.00×10^{-6}	XMM-OM
8.21×10^{14}	2.90×10^{-5}	2.00×10^{-6}	XMM-OM
8.47×10^{14}	3.34×10^{-5}	1.69×10^{-6}	SDSS-dr5
9.67×10^{14}	3.00×10^{-5}	2.00×10^{-6}	XMM-OM
1.48×10^{15}	1.90×10^{-5}	6.00×10^{-6}	XMM-OM

[a] Data from NED.
[c] Farrah et al. 2002a.

TABLE A.12: IRAS 16347+7037.

ν Hz	F_ν Jy	Error Jy	Ref.
1.45×10^{9}	9.40×10^{-4}	3.00×10^{-4}	VLA [a]
1.49×10^{9}	1.65×10^{-3}	3.10×10^{-4}	VLA [a]
4.90×10^{9}	1.08×10^{-3}	1.10×10^{-4}	VLA [a]
8.48×10^{9}	9.70×10^{-4}	1.50×10^{-4}	VLA [a]
1.49×10^{10}	1.17×10^{-3}	3.20×10^{-4}	VLA [a]
2.25×10^{10}	9.60×10^{-4}	1.70×10^{-4}	VLA [a]
4.00×10^{10}	2.78×10^{-1}	...	FCRAO [a]
9.00×10^{10}	4.50×10^{-2}	...	NRAO-12m [a]
2.30×10^{11}	1.50×10^{-3}	...	IRAM [a]
1.48×10^{12}	1.58×10^{-1}	3.16×10^{-2}	ISO [a]
1.72×10^{12}	2.06×10^{-1}	4.12×10^{-2}	ISO [a]
1.93×10^{12}	2.30×10^{-1}	4.60×10^{-2}	ISO [a]
2.93×10^{12}	3.49×10^{-1}	6.98×10^{-2}	ISO [a]
5.00×10^{12}	2.46×10^{-1}	3.20×10^{-2}	IRAS [a]
1.20×10^{13}	1.22×10^{-1}	4.15×10^{-3}	IRAS [a]
2.50×10^{13}	5.93×10^{-2}	1.01×10^{-2}	IRAS [a]
2.52×10^{13}	4.80×10^{-2}	9.60×10^{-3}	ISO [a]
2.97×10^{13}	4.90×10^{-2}	1.10×10^{-2}	Hale-5m [e]
8.10×10^{13}	1.07×10^{-2}	9.48×10^{-4}	Hale-5m [e]
1.39×10^{14}	6.99×10^{-3}	2.13×10^{-4}	2MASS
1.80×10^{14}	8.91×10^{-3}	2.75×10^{-4}	2MASS
2.43×10^{14}	6.96×10^{-3}	2.06×10^{-4}	2MASS
3.33×10^{14}	7.07×10^{-3}	1.95×10^{-3}	SSS
4.28×10^{14}	7.27×10^{-3}	2.01×10^{-3}	SSS
5.45×10^{14}	4.76×10^{-3}	4.00×10^{-5}	XMM-OM
6.81×10^{14}	6.20×10^{-3}	2.28×10^{-3}	SSS
8.21×10^{14}	3.71×10^{-3}	1.60×10^{-5}	XMM-OM
1.05×10^{15}	3.77×10^{-3}	4.97×10^{-6}	IUE
1.46×10^{15}	1.22×10^{-3}	4.71×10^{-6}	IUE
1.48×10^{15}	1.59×10^{-3}	6.00×10^{-5}	XMM-OM
2.11×10^{15}	4.60×10^{-4}	8.92×10^{-6}	IUE

[a] Data from NED.
[e] Neugebauer et al. 1987.

TABLE A.13: IRAS 18216+6418.

ν Hz	F_ν Jy	Error Jy	Ref.
3.25×10^{8}	2.11×10^{-1}	9.65×10^{-3}	WENSS [a]
4.90×10^{9}	7.50×10^{-3}	4.00×10^{-4}	VLA [a]
8.42×10^{9}	1.26×10^{-2}	6.00×10^{-4}	VLA [a]
1.49×10^{10}	2.33×10^{-2}	1.10×10^{-3}	VLA [a]
2.39×10^{11}	3.70×10^{-3}	...	APM [c]
2.73×10^{11}	4.70×10^{-2}	...	APM [c]
3.53×10^{11}	1.48×10^{-2}	2.60×10^{-3}	SCUBA [c]
6.66×10^{11}	3.08×10^{-1}	...	SCUBA [c]
1.72×10^{12}	1.07×10^{0}	3.21×10^{-1}	ISO [a]
3.00×10^{12}	2.13×10^{0}	1.70×10^{-1}	IRAS [a]
5.00×10^{12}	1.24×10^{0}	4.96×10^{-2}	IRAS [a]
1.20×10^{13}	4.45×10^{-1}	1.19×10^{-2}	IRAS [a]
2.50×10^{13}	2.38×10^{-1}	...	IRAS [a]
3.12×10^{13}	1.43×10^{-1}	1.43×10^{-2}	ISO [a]
4.44×10^{13}	1.09×10^{-1}	1.10×10^{-2}	ISO [a]
1.39×10^{14}	2.35×10^{-2}	6.04×10^{-4}	2MASS
1.80×10^{14}	1.47×10^{-2}	4.25×10^{-4}	2MASS
2.43×10^{14}	1.19×10^{-2}	3.18×10^{-4}	2MASS
3.33×10^{14}	1.69×10^{-2}	4.68×10^{-3}	SSS
4.28×10^{14}	1.24×10^{-2}	3.42×10^{-3}	SSS
5.45×10^{14}	7.55×10^{-3}	...	APM [c]
6.81×10^{14}	8.10×10^{-3}	7.00×10^{-4}	APM
8.21×10^{14}	9.04×10^{-3}	...	APM [c]
1.48×10^{15}	4.94×10^{-3}	6.00×10^{-5}	XMM-OM

[a] Data from NED.
[c] Farrah et al. 2002a.

References

Adelman-McCarthy, J. K., Agüeros, M. A., Allam, S. S., Anderson, K. S. J., Anderson, S. F., Annis, J., Bahcall, N. A., Bailer-Jones, C. A. L., Baldry, I. K., Barentine, J. C., Beers, T. C., Belokurov, V., Berlind, A., Bernardi, M., Blanton, M. R., Bochanski, J. J., Boroski, W. N., Bramich, D. M., Brewington, H. J., Brinchmann, J., Brinkmann, J., Brunner, R. J., Budavári, T., Carey, L. N., Carliles, S., Carr, M. A., Castander, F. J., Connolly, A. J., Cool, R. J., Cunha, C. E., Csabai, I., Dalcanton, J. J., Doi, M., Eisenstein, D. J., Evans, M. L., Evans, N. W., Fan, X., Finkbeiner, D. P., Friedman, S. D., Frieman, J. A., Fukugita, M., Gillespie, B., Gilmore, G., Glazebrook, K., Gray, J., Grebel, E. K., Gunn, J. E., de Haas, E., Hall, P. B., Harvanek, M., Hawley, S. L., Hayes, J., Heckman, T. M., Hendry, J. S., Hennessy, G. S., Hindsley, R. B., Hirata, C. M., Hogan, C. J., Hogg, D. W., Holtzman, J. A., Ichikawa, S., Ichikawa, T., Ivezić, Ž., Jester, S., Johnston, D. E., Jorgensen, A. M., Jurić, M., Kauffmann, G., Kent, S. M., Kleinman, S. J., Knapp, G. R., Kniazev, A. Y., Kron, R. G., Krzesinski, J., Kuropatkin, N., Lamb, D. Q., Lampeitl, H., Lee, B. C., Leger, R. F., Lima, M., Lin, H., Long, D. C., Loveday, J., Lupton, R. H., Mandelbaum, R., Margon, B., Martínez-Delgado, D., Matsubara, T., McGehee, P. M., McKay, T. A., Meiksin, A., Munn, J. A., Nakajima, R., Nash, T., Neilsen, Jr., E. H., Newberg, H. J., Nichol, R. C., Nieto-Santisteban, M., Nitta, A., Oyaizu, H., Okamura, S., Ostriker, J. P., Padmanabhan, N., Park, C., Peoples, Jr., J., Pier, J. R., Pope, A. C., Pourbaix, D., Quinn, T. R., Raddick, M. J., Re Fiorentin, P., Richards, G. T., Richmond, M. W., Rix, H., Rockosi, C. M., Schlegel, D. J., Schneider, D. P., Scranton, R., Seljak, U., Sheldon, E., Shimasaku, K., Silvestri, N. M., Smith, J. A., Smolčić, V., Snedden, S. A., Stebbins, A., Stoughton, C., Strauss, M. A., SubbaRao, M., Suto, Y., Szalay, A. S., Szapudi, I., Szkody, P., Tegmark, M., Thakar, A. R., Tremonti, C. A., Tucker, D. L., Uomoto, A., Vanden Berk, D. E., Vandenberg, J., Vidrih, S., Vogeley, M. S., Voges, W., Vogt, N. P., Weinberg, D. H., West, A. A., White, S. D. M., Wilhite, B., Yanny, B., Yocum, D. R., York, D. G., Zehavi, I., Zibetti, S., and Zucker, D. B.: 2007, *ApJS* **172**, 634

Alexander, D. M., Bauer, F. E., Chapman, S. C., Smail, I., Blain, A. W., Brandt, W. N., and Ivison, R. J.: 2005, *ApJ* **632**, 736

Allen, S. W. and Fabian, A. C.: 1998, *MNRAS* **297**, L57

Antonucci, R. R. J. and Miller, J. S.: 1985, *ApJ* **297**, 621

Armus, L., Heckman, T., and Miley, G.: 1987, *AJ* **94**, 831

Armus, L., Heckman, T. M., and Miley, G. K.: 1989, *ApJ* **347**, 727

Asari, N. V., Cid Fernandes, R., Stasińska, G., Torres-Papaqui, J. P., Mateus, A., Sodré, L., Schoenell, W., and Gomes, J. M.: 2007, *MNRAS* **381**, 263

Aussel, H., Gerin, M., Boulanger, F., Desert, F. X., Casoli, F., Cutri, R. M., and Signore, M.: 1998, *A&A* **334**, L73

Baan, W. A., Haschick, A. D., and Henkel, C.: 1989, *ApJ* **346**, 680

Barnes, J. E.: 2002, *MNRAS* **333**, 481

Barnes, J. E. and Hernquist, L. E.: 1991, *ApJ* **370**, L65

Baumgartner, W., Horner, D., and Mushotzky, R.: 2001, *Bulletin of the American Astronomical Society* **33**, 1337

Beck, S. C., Turner, J. L., Ho, P. T. P., Lacy, J. H., and Kelly, D. M.: 1996, *ApJ* **457**, 610

Berta, S.: 2005, *Ph.D. thesis*, Dipartimento di Astronomia, Univ. di Padova, Vicolo dell'Osservatorio 2, I-35122, Padova, Italy

Berta, S., Fritz, J., Franceschini, A., Bressan, A., and Pernechele, C.: 2003, *A&A* **403**, 119

Bianchi, S., Guainazzi, M., and Chiaberge, M.: 2006, *A&A* **448**, 499

Binggeli, B. and Cameron, L. M.: 1991, *A&A* **252**, 27

Blain, A. W., Smail, I., Ivison, R. J., Kneib, J., and Frayer, D. T.: 2002, *Phys. Rep.* **369**, 111

Boller, T., Bertoldi, F., Dennefeld, M., and Voges, W.: 1998, *A&AS* **129**, 87

Brandl, B. R., Bernard-Salas, J., Spoon, H. W. W., Devost, D., Sloan, G. C., Guilles, S., Wu, Y., Houck, J. R., Weedman, D. W., Armus, L., Appleton, P. N., Soifer, B. T., Charmandaris, V., Hao, L., Higdon, J. A. M. S. J., and Herter, T. L.: 2006, *ApJ* **653**, 1129

Brandl, B. R., Devost, D., Higdon, S. J. U., Charmandaris, V., Weedman, D., Spoon, H. W. W., Herter, T. L., Hao, L., Bernard-Salas, J., Houck, J. R., Armus, L., Soifer, B. T., Grillmair, C. J., and Appleton, P. N.: 2004, *ApJS* **154**, 188

Bryant, P. M. and Scoville, N. Z.: 1999, *AJ* **117**, 2632

Bushouse, H. A., Borne, K. D., Colina, L., Lucas, R. A., Rowan-Robinson, M., Baker, A. C., Clements, D. L., Lawrence, A., and Oliver, S.: 2002, *ApJS* **138**, 1

Calzetti, D.: 1997, *AJ* **113**, 162

Canalizo, G. and Stockton, A.: 2001, *ApJ* **555**, 719

Capetti, A., Verdoes Kleijn, G., and Chiaberge, M.: 2005, *A&A* **439**, 935

Chary, R. and Elbaz, D.: 2001, *ApJ* **556**, 562

Clements, D. L., Saunders, W. J., and McMahon, R. G.: 1999, *MNRAS* **302**, 391

Clements, D. L., Sutherland, W. J., McMahon, R. G., and Saunders, W.: 1996, *MNRAS* **279**, 477

Condon, J. J., Huang, Z., Yin, Q. F., and Thuan, T. X.: 1991, *ApJ* **378**, 65

Connolly, A. J., Szalay, A. S., Dickinson, M., Subbarao, M. U., and Brunner, R. J.: 1997, *ApJ* **486**, L11

Conti, P. S.: 1991, *ApJ* **377**, 115

Crummy, J., Fabian, A. C., Gallo, L., and Ross, R. R.: 2006, *MNRAS* **365**, 1067

Cutri, R. M., Huchra, J. P., Low, F. J., Brown, R. L., and vanden Bout, P. A.: 1994, *ApJ* **424**, L65

Cutri, R. M., Skrutskie, M. F., van Dyk, S., Beichman, C. A., Carpenter, J. M., Chester, T., Cambresy, L., Evans, T., Fowler, J., Gizis, J., Howard, E., Huchra, J., Jarrett, T., Kopan, E. L., Kirkpatrick, J. D., Light, R. M., Marsh, K. A., McCallon, H., Schneider, S., Stiening, R., Sykes, M., Weinberg, M., Wheaton, W. A., Wheelock, S., and Zacarias, N.: 2003, *2MASS All Sky Catalog of point sources.*, The IRSA 2MASS All-Sky Point Source Catalog, NASA/IPAC Infrared Science Archive.

Daddi, E., Dannerbauer, H., Elbaz, D., Dickinson, M., Morrison, G., Stern, D., and Ravindranath, S.: 2008, *ApJ* **673**, L21

Daddi, E., Dickinson, M., Morrison, G., Chary, R., Cimatti, A., Elbaz, D., Frayer, D., Renzini, A., Pope, A., Alexander, D. M., Bauer, F. E., Giavalisco, M., Huynh, M., Kurk, J., and Mignoli, M.: 2007, *ApJ* **670**, 156

Dahlem, M., Weaver, K. A., and Heckman, T. M.: 1998, *ApJS* **118**, 401

Dale, D. A. and Helou, G.: 2002, *ApJ* **576**, 159

Darling, J. and Giovanelli, R.: 2002, *AJ* **124**, 100

Dasyra, K. M., Ho, L. C., Armus, L., Ogle, P., Helou, G., Peterson, B. M., Lutz, D., Netzer, H., and Sturm, E.: 2008, *ApJ* **674**, L9

Davies, R. I., Tacconi, L. J., and Genzel, R.: 2004, *ApJ* **613**, 781

Davis, M., Guhathakurta, P., Konidaris, N. P., Newman, J. A., Ashby, M. L. N., Biggs, A. D., Barmby, P., Bundy, K., Chapman, S. C., Coil, A. L., Conselice, C. J., Cooper, M. C., Croton, D. J., Eisenhardt, P. R. M., Ellis, R. S., Faber, S. M., Fang, T., Fazio, G. G., Georgakakis, A., Gerke, B. F., Goss, W. M., Gwyn, S., Harker, J., Hopkins, A. M., Huang, J.-S., Ivison, R. J., Kassin, S. A., Kirby, E. N., Koekemoer, A. M., Koo, D. C., Laird, E. S., Le Floc'h, E., Lin, L., Lotz, J. M., Marshall, P. J., Martin, D. C., Metevier, A. J., Moustakas, L. A., Nandra, K., Noeske, K. G., Papovich, C., Phillips, A. C., Rich, R. M., Rieke, G. H., Rigopoulou, D., Salim, S., Schiminovich, D., Simard, L., Smail, I., Small, T. A., Weiner, B. J., Willmer, C. N. A., Willner, S. P., Wilson, G., Wright, E. L., and Yan, R.: 2007, *ApJ* **660**, L1

Deane, J. R. and Trentham, N.: 2001, *MNRAS* **326**, 1467

Della Ceca, R., Maccacaro, T., Caccianiga, A., Severgnini, P., Braito, V., Barcons, X., Carrera, F. J., Watson, M. G., Tedds, J. A., Brunner, H., Lehmann, I., Page, M. J., Lamer, G., and Schwope, A.: 2004, *A&A* **428**, 383

den Herder, J. W., Brinkman, A. C., Kahn, S. M., Branduardi-Raymont, G., Thomsen, K., Aarts, H., Audard, M., Bixler, J. V., den Boggende, A. J., Cottam, J., Decker, T., Dubbeldam, L., Erd, C., Goulooze, H., Güdel, M., Guttridge, P., Hailey, C. J., Janabi, K. A., Kaastra, J. S., de Korte, P. A. J., van Leeuwen, B. J., Mauche, C., McCalden, A. J., Mewe, R., Naber, A., Paerels, F. B., Peterson, J. R., Rasmussen, A. P., Rees, K., Sakelliou, I., Sako, M., Spodek, J., Stern, M., Tamura, T., Tandy, J., de Vries, C. P., Welch, S., and Zehnder, A.: 2001, *A&A* **365**, L7

Devriendt, J. E. G., Guiderdoni, B., and Sadat, R.: 1999, *A&A* **350**, 381

Dey, A. and van Breugel, W.: 1995, in I. Shlosman (NY:CUP) (ed.), *Mass-Transfer Induced Activity in Galaxies*, p. 263

Di Matteo, P., Bournaud, F., Martig, M., Combes, F., Melchior, A., and Semelin, B.: 2008, *A&A* **492**, 31

Di Matteo, T., Springel, V., and Hernquist, L.: 2005, *Nature* **433**, 604

Dickey, J. M. and Lockman, F. J.: 1990, *ARA&A* **28**, 215

Dickinson, M. and FIDEL team: 2007, in *Bulletin of the American Astronomical Society*, Vol. 38 of *Bulletin of the American Astronomical Society*, p. 822

Dickinson, M., Giavalisco, M., and The Goods Team: 2003a, in R. Bender and A. Renzini (eds.), *The Mass of Galaxies at Low and High Redshift*, p. 324

Dickinson, M., Papovich, C., Ferguson, H. C., and Budavári, T.: 2003b, *ApJ* **587**, 25

Downes, D. and Solomon, P. M.: 1998, *ApJ* **507**, 615

Draine, B. T.: 1989, in E. Böhm-Vitense (ed.), *Infrared Spectroscopy in Astronomy*, Vol. 290 of *ESA Special Publication*, pp 93–98

Draine, B. T. and Li, A.: 2001, *ApJ* **551**, 807

Draine, B. T. and Li, A.: 2007, *ApJ* **657**, 810

Drake, C. L., Bicknell, G. V., McGregor, P. J., and Dopita, M. A.: 2004, *AJ* **128**, 969

Dudik, R. P., Weingartner, J. C., Satyapal, S., Fischer, J., Dudley, C. C., and O'Halloran, B.: 2007, *ApJ* **664**, 71

Ebrero, J., Carrera, F. J., Page, M. J., Silverman, J. D., Barcons, X., Ceballos, M. T., Corral, A., Della Ceca, R., and Watson, M. G.: 2009, *A&A* **493**, 55

Efstathiou, A. and Rowan-Robinson, M.: 1995, *MNRAS* **273**, 649

Efstathiou, A., Rowan-Robinson, M., and Siebenmorgen, R.: 2000, *MNRAS* **313**, 734

Ehle, M., Breitfellner, M., González Riestra, R., Guainazzi, M., Loiseau, N., P. Rodríguez, P., Santos-Lleó, M., Schartel, N., Tomás, L., Verdugo, E., and Dahlem, M.: 2005, *XMM-Newton Users' Handbook*, XMM-Newton SOC Team, 2.3 edition

Elitzur, M., Nenkova, M., and Ivezić, Z.: 2004, in S. Aalto, S. Huttemeister, and A. Pedlar (eds.), *The Neutral ISM in Starburst Galaxies*, Vol. 320 of *Astronomical Society of the Pacific Conference Series*, p. 242

Elitzur, M. and Shlosman, I.: 2006, *ApJ* **648**, L101

Elmegreen, B. G.: 1994, *ApJ* **433**, 39

Elmegreen, B. G.: 2004, *ArXiv Astrophysics e-prints*

Elvis, M.: 2000, *ApJ* **545**, 63

Elvis, M., Wilkes, B. J., McDowell, J. C., Green, R. F., Bechtold, J., Willner, S. P., Oey, M. S., Polomski, E., and Cutri, R.: 1994, *ApJS* **95**, 1

Engelbracht, C. W., Rieke, G. H., Gordon, K. D., Smith, J., Werner, M. W., Moustakas, J., Willmer, C. N. A., and Vanzi, L.: 2008, *ApJ* **678**, 804

Engelbracht, C. W., Rieke, M. J., Rieke, G. H., Kelly, D. M., and Achtermann, J. M.: 1998, *ApJ* **505**, 639

Ettori, S. and Fabian, A. C.: 1999, *MNRAS* **305**, 834

Evans, A. S., Sanders, D. B., Cutri, R. M., Radford, S. J. E., Surace, J. A., Solomon, P. M., Downes, D., and Kramer, C.: 1998, *ApJ* **506**, 205

Fabian, A. C. and Crawford, C. S.: 1995, *MNRAS* **274**, L63

Fabian, A. C., Cutri, R. M., Smith, H. E., Crawford, C. S., and Brandt, W. N.: 1996, *MNRAS* **283**, L95

Fabian, A. C. and Iwasawa, K.: 1999, *MNRAS* **303**, L34

Fabian, A. C., Iwasawa, K., Reynolds, C. S., and Young, A. J.: 2000, *PASP* **112**, 1145

Fang, T., Davis, D. S., Lee, J. C., Marshall, H. L., Bryan, G. L., and Canizares, C. R.: 2002, *ApJ* **565**, 86

Farrah, D., Afonso, J., Efstathiou, A., Rowan-Robinson, M., Fox, M., and Clements, D.: 2003, *MNRAS* **343**, 585

Farrah, D., Bernard-Salas, J., Spoon, H. W. W., Soifer, B. T., Armus, L., Brandl, B., Charmandaris, V., Desai, V., Higdon, S., Devost, D., and Houck, J.: 2007, *ApJ* **667**, 149

Farrah, D., Rowan-Robinson, M., Oliver, S., Serjeant, S., Borne, K., Lawrence, A., Lucas, R. A., Bushouse, H., and Colina, L.: 2001, *MNRAS* **326**, 1333

Farrah, D., Serjeant, S., Efstathiou, A., Rowan-Robinson, M., and Verma, A.: 2002a, *MNRAS* **335**, 1163

Farrah, D., Verma, A., Oliver, S., Rowan-Robinson, M., and McMahon, R.: 2002b, *MNRAS* **329**, 605

Fazio, G. G., Hora, J. L., Allen, L. E., Ashby, M. L. N., Barmby, P., Deutsch, L. K., Huang, J., Kleiner, S., Marengo, M., Megeath, S. T., Melnick, G. J., Pahre, M. A., Patten, B. M., Polizotti, J., Smith, H. A., Taylor, R. S., Wang, Z., Willner, S. P., Hoffmann, W. F., Pipher, J. L., Forrest, W. J., McMurty, C. W., McCreight, C. R., McKelvey, M. E., McMurray, R. E., Koch, D. G., Moseley, S. H., Arendt, R. G., Mentzell, J. E., Marx, C. T., Losch, P., Mayman, P., Eichhorn, W., Krebs, D., Jhabvala, M., Gezari, D. Y., Fixsen, D. J., Flores, J., Shakoorzadeh, K., Jungo, R., Hakun, C., Workman, L., Karpati, G., Kichak, R., Whitley, R., Mann, S., Tollestrup, E. V., Eisenhardt, P., Stern, D., Gorjian, V., Bhattacharya, B., Carey, S., Nelson, B. O., Glaccum, W. J., Lacy, M., Lowrance, P. J., Laine, S., Reach, W. T., Stauffer, J. A., Surace, J. A., Wilson, G., Wright, E. L., Hoffman, A., Domingo, G., and Cohen, M.: 2004, *ApJS* **154**, 10

Ferrarese, L. and Ford, H.: 2005, *Space Science Reviews* **116**, 523

Fitzpatrick, E. L.: 2004, in A. N. Witt, G. C. Clayton, & B. T. Draine (ed.), *Astrophysics of Dust*, Vol. 309 of *Astronomical Society of the Pacific Conference Series*, p. 33

Fontanot, F., De Lucia, G., Monaco, P., Somerville, R. S., and Santini, P.: 2009, *MNRAS* **397**, 1776

Franceschini, A., Aussel, H., Cesarsky, C. J., Elbaz, D., and Fadda, D.: 2001, *A&A* **378**, 1

Franceschini, A., Bassani, L., Cappi, M., Granato, G. L., Malaguti, G., Palazzi, E., and Persic, M.: 2000, *A&A* **353**, 910

Franceschini, A., Braito, V., Persic, M., Della Ceca, R., Bassani, L., Cappi, M., Malaguti, P., Palumbo, G. G. C., Risaliti, G., Salvati, M., and Severgnini, P.: 2003, *MNRAS* **343**, 1181

Franceschini, A., Hasinger, G., Miyaji, T., and Malquori, D.: 1999, *MNRAS* **310**, L5

Franceschini, A., Mazzei, P., de Zotti, G., and Danese, L.: 1994, *ApJ* **427**, 140

Frayer, D. T., Ivison, R. J., Scoville, N. Z., Evans, A. S., Yun, M. S., Smail, I., Barger, A. J., Blain, A. W., and Kneib, J.-P.: 1999, *ApJ* **514**, L13

Frayer, D. T., Ivison, R. J., Scoville, N. Z., Yun, M., Evans, A. S., Smail, I., Blain, A. W., and Kneib, J.-P.: 1998, *ApJ* **506**, L7

Freeman, P., Doe, S., and Siemiginowska, A.: 2001, in J. L. Starck & F. D. Murtagh (ed.), *Society of Photo-Optical Instrumentation Engineers (SPIE) Conference Series*, Vol. 4477 of *Presented at the Society of Photo-Optical Instrumentation Engineers (SPIE) Conference*, pp 76–87

Fruscione, A., McDowell, J. C., Allen, G. E., Brickhouse, N. S., Burke, D. J., Davis, J. E., Durham, N., Elvis, M., Galle, E. C., Harris, D. E., Huenemoerder, D. P., Houck, J. C., Ishibashi, B., Karovska, M., Nicastro, F., Noble, M. S., Nowak, M. A., Primini, F. A., Siemiginowska, A., Smith, R. K., and Wise, M.: 2006, in *Society of Photo-Optical Instrumentation Engineers (SPIE) Conference Series*, Vol. 6270 of *Presented at the Society of Photo-Optical Instrumentation Engineers (SPIE) Conference*

Fukazawa, Y., Makishima, K., and Ohashi, T.: 2004, *PASJ* **56**, 965

Gallimore, J. F., Baum, S. A., and O'Dea, C. P.: 1997, *Nature* **388**, 852

Gao, Y. and Solomon, P. M.: 2004, *ApJS* **152**, 63

Gebhardt, K., Bender, R., Bower, G., Dressler, A., Faber, S. M., Filippenko, A. V., Green, R., Grillmair, C., Ho, L. C., Kormendy, J., Lauer, T. R., Magorrian, J., Pinkney, J., Richstone, D., and Tremaine, S.: 2000, *ApJ* **539**, L13

Genzel, R. and Cesarsky, C. J.: 2000, *ARA&A* **38**, 761

Genzel, R., Lutz, D., Sturm, E., Egami, E., Kunze, D., Moorwood, A. F. M., Rigopoulou, D., Spoon, H. W. W., Sternberg, A., Tacconi-Garman, L. E., Tacconi, L., and Thatte, N.: 1998, *ApJ* **498**, 579

George, I. M. and Fabian, A. C.: 1991, *MNRAS* **249**, 352

Ghisellini, G., Haardt, F., and Matt, G.: 1994, *MNRAS* **267**, 743

Gierliński, M. and Done, C.: 2004, *MNRAS* **349**, L7

Gierliński, M. and Done, C.: 2006, *MNRAS* **371**, L16

Gilli, R.: 2004, *Advances in Space Research* **34**, 2470

Gilli, R., Comastri, A., and Hasinger, G.: 2007, *A&A* **463**, 79

Gonzalez-Delgado, R. M., Perez, E., Diaz, A. I., Garcia-Vargas, M. L., Terlevich, E., and Vilchez, J. M.: 1995, *ApJ* **439**, 604

Goodrich, R. W., Veilleux, S., and Hill, G. J.: 1994, *ApJ* **422**, 521

Granato, G. L., Danese, L., and Franceschini, A.: 1996, *ApJ* **460**, L11

Granato, G. L., De Zotti, G., Silva, L., Bressan, A., and Danese, L.: 2004, *ApJ* **600**, 580

Haardt, F., Maraschi, L., and Ghisellini, G.: 1994, *ApJ* **432**, L95

Haas, M., Chini, R., Meisenheimer, K., Stickel, M., Lemke, D., Klaas, U., and Kreysa, E.: 1998, *ApJ* **503**, L109

Haas, M., Müller, S. A. H., Chini, R., Meisenheimer, K., Klaas, U., Lemke, D., Kreysa, E., and Camenzind, M.: 2000, *A&A* **354**, 453

Hall, P. B., Ellingson, E., and Green, R. F.: 1997, *AJ* **113**, 1179

Häring, N. and Rix, H.: 2004, *ApJ* **604**, L89

Harwit, M. and Pacini, F.: 1975, *ApJ* **200**, L127

Hasinger, G.: 2008, *A&A* **490**, 905

Hasinger, G., Miyaji, T., and Schmidt, M.: 2005, *A&A* **441**, 417

Heavens, A., Panter, B., Jimenez, R., and Dunlop, J.: 2004, *Nature* **428**, 625

Hines, D. C., Schmidt, G. D., Gordon, K. D., Wills, B. J., Smith, P. S., Allen, R. G., and Sitko, M. L.: 2001, *Bulletin of the American Astronomical Society* **33**, 899

Hines, D. C., Schmidt, G. D., Smith, P. S., Cutri, R. M., and Low, F. J.: 1995, *ApJ* **450**, L1

Hines, D. C., Schmidt, G. D., Wills, B. J., Smith, P. S., and Sowinski, L. G.: 1999, *ApJ* **512**, 145

Ho, L. C.: 1999, *ApJ* **516**, 672

Hopkins, P. F., Hernquist, L., Cox, T. J., Di Matteo, T., Martini, P., Robertson, B., and Springel, V.: 2005, *ApJ* **630**, 705

Hopkins, P. F., Richards, G. T., and Hernquist, L.: 2007, *ApJ* **654**, 731

Houck, J. R., Roellig, T. L., van Cleve, J., Forrest, W. J., Herter, T., Lawrence, C. R., Matthews, K., Reitsema, H. J., Soifer, B. T., Watson, D. M., Weedman, D., Huisjen, M., Troeltzsch, J., Barry, D. J., Bernard-Salas, J., Blacken, C. E., Brandl, B. R., Charmandaris, V., Devost, D., Gull, G. E., Hall, P., Henderson, C. P., Higdon, S. J. U., Pirger, B. E., Schoenwald, J., Sloan, G. C., Uchida, K. I., Appleton, P. N., Armus, L., Burgdorf, M. J., Fajardo-Acosta, S. B., Grillmair, C. J., Ingalls, J. G., Morris, P. W., and Teplitz, H. I.: 2004, *ApJS* **154**, 18

Houck, J. R., Schneider, D. P., Danielson, G. E., Neugebauer, G., Soifer, B. T., Beichman, C. A., and Lonsdale, C. J.: 1985, *ApJ* **290**, L5

Hughes, D. H., Dunlop, J. S., and Rawlings, S.: 1997, *MNRAS* **289**, 766

Hunter, D. A., Elmegreen, B. G., and Ludka, B. C.: 2010, *AJ* **139**, 447

Imanishi, M., Dudley, C. C., Maiolino, R., Maloney, P. R., Nakagawa, T., and Risaliti, G.: 2007, *ApJS* **171**, 72

Immeli, A., Samland, M., Gerhard, O., and Westera, P.: 2004, *A&A* **413**, 547

Irwin, M. J., Ibata, R. A., Lewis, G. F., and Totten, E. J.: 1998, *ApJ* **505**, 529

Isobe, T., Feigelson, E. D., and Nelson, P. I.: 1985, *BAAS* **17**, 573

Isobe, T., Feigelson, E. D., and Nelson, P. I.: 1986, *ApJ* **306**, 490

Iwasawa, K.: 1999, *MNRAS* **302**, 96

Iwasawa, K., Crawford, C. S., Fabian, A. C., and Wilman, R. J.: 2005, *MNRAS* **362**, L20

Iwasawa, K., Fabian, A. C., and Ettori, S.: 2001, *MNRAS* **321**, L15

Iwasawa, K., Fabian, A. C., and Matt, G.: 1997, *MNRAS* **289**, 443

Jaffe, W., Meisenheimer, K., Röttgering, H. J. A., Leinert, C., Richichi, A., Chesneau, O., Fraix-Burnet, D., Glazenborg-Kluttig, A., Granato, G., Graser, U., Heijligers, B., Köhler, R., Malbet, F., Miley, G. K., Paresce, F., Pel, J., Perrin, G., Przygodda, F., Schoeller, M., Sol, H., Waters, L. B. F. M., Weigelt, G., Woillez, J., and de Zeeuw, P. T.: 2004, *Nature* **429**, 47

Jiménez-Bailón, E., Santos-Lleó, M., Piconcelli, E., Matt, G., Guainazzi, M., and Rodríguez-Pascual, P.: 2007, *A&A* **461**, 917

Joint IRAS Science Working Group: 1988, in *IRAS Point Source Catalog (1988)*

Joseph, R. D.: 1999, *Ap&SS* **266**, 321

Kaastra, J. S. and Mewe, R.: 1993, *A&AS* **97**, 443

Kellogg, E., Baldwin, J. R., and Koch, D.: 1975, *ApJ* **199**, 299

Kelly, B. C., Bechtold, J., Trump, J. R., Vestergaard, M., and Siemiginowska, A.: 2008, *ApJS* **176**, 355

Kendziorra, E., Bihler, E., Grubmiller, W., Kretschmar, B., Kuster, M., Pflueger, B., Staubert, R., Braeuninger, H. W., Briel, U. G., Meidinger, N., Pfeffermann, E., Reppin, C., Stoetter, D., Strueder, L., Holl, P., Kemmer, J., Soltau, H., and von Zanthier, C.: 1997, in O. H. Siegmund and M. A. Gummin (eds.), *Society of Photo-Optical Instrumentation Engineers (SPIE) Conference Series*, Vol. 3114 of *Society of Photo-Optical Instrumentation Engineers (SPIE) Conference Series*, pp 155–165

Kendziorra, E., Colli, M., Kuster, M., Staubert, R., Meidinger, N., and Pfeffermann, E.: 1999, in O. H. Siegmund and K. A. Flanagan (eds.), *Society of Photo-Optical Instrumentation Engineers (SPIE) Conference Series*, Vol. 3765 of *Society of Photo-Optical Instrumentation Engineers (SPIE) Conference Series*, pp 204–214

Kennicutt, R. C.: 1998, *ApJ* **498**, 541

Kewley, L. J., Dopita, M. A., Sutherland, R. S., Heisler, C. A., and Trevena, J.: 2001, *ApJ* **556**, 121

Kii, T., Williams, O. R., Ohashi, T., Awaki, H., Hayashida, K., Inoue, H., Kondo, H., Koyama, K., Makino, F., Makishima, K., Saxton, R. D., Stewart, G. C., Takano, S., Tanaka, Y., and Turner, M. J. L.: 1991, *ApJ* **367**, 455

Kim, C., Kim, W., and Ostriker, E. C.: 2008, *ApJ* **681**, 1148

Kim, D. and Sanders, D. B.: 1998, *ApJS* **119**, 41

Kleinmann, D. E. and Low, F. J.: 1970, *ApJ* **159**, L165

Kleinmann, S. G., Hamilton, D., Keel, W. C., Wynn-Williams, C. G., Eales, S. A., Becklin, E. E., and Kuntz, K. D.: 1988, *ApJ* **328**, 161

Komatsu, E., Dunkley, J., Nolta, M. R., Bennett, C. L., Gold, B., Hinshaw, G., Jarosik, N., Larson, D., Limon, M., Page, L., Spergel, D. N., Halpern, M., Hill, R. S., Kogut, A., Meyer, S. S., Tucker, G. S., Weiland, J. L., Wollack, E., and Wright, E. L.: 2009, *ApJS* **180**, 330

Kormendy, J. and Gebhardt, K.: 2001, in J. C. Wheeler and H. Martel (eds.), *20th Texas Symposium on relativistic astrophysics*, Vol. 586 of *American Institute of Physics Conference Series*, p. 363

Kormendy, J. and Sanders, D. B.: 1992, *ApJ* **390**, L53

Krumholz, M. R., Matzner, C. D., and McKee, C. F.: 2006, *ApJ* **653**, 361

Kuster, M., Benlloch, S., Kendziorra, E., and Briel, U. G.: 1999, in O. H. Siegmund and K. A. Flanagan (eds.), *Society of Photo-Optical Instrumentation Engineers (SPIE) Conference Series*, Vol. 3765 of *Society of Photo-Optical Instrumentation Engineers (SPIE) Conference Series*, pp 673–682

Lambas, D. G., Tissera, P. B., Alonso, M. S., and Coldwell, G.: 2003, *MNRAS* **346**, 1189

Larson, R. B.: 1987, in S. M. Faber (ed.), *Nearly Normal Galaxies. From the Planck Time to the Present*, pp 26–35

Laurent, O., Mirabel, I. F., Charmandaris, V., Gallais, P., Madden, S. C., Sauvage, M., Vigroux, L., and Cesarsky, C.: 2000, *A&A* **359**, 887

Lawrence, A.: 1991, *MNRAS* **252**, 586

Leech, K. J., Rowan-Robinson, M., Lawrence, A., and Hughes, J. D.: 1994, *MNRAS* **267**, 253

Leighly, K. M., Halpern, J. P., Helfand, D. J., Becker, R. H., and Impey, C. D.: 2001, *AJ* **121**, 2889

Leighly, K. M., Halpern, J. P., Jenkins, E. B., Grupe, D., Choi, J., and Prescott, K. B.: 2007, *ApJ* **663**, 103

Lilly, S. J., Eales, S. A., Gear, W. K. P., Hammer, F., Le Fèvre, O., Crampton, D., Bond, J. R., and Dunne, L.: 1999, *ApJ* **518**, 641

Lípari, S., Terlevich, R., Díaz, R. J., Taniguchi, Y., Zheng, W., Tsvetanov, Z., Carranza, G., and Dottori, H.: 2003, *MNRAS* **340**, 289

Lonsdale, C. J., Farrah, D., and Smith, H. E.: 2006a, *Ultraluminous Infrared Galaxies*, p. 285, Springer Verlag

Lonsdale, C. J., Omont, A., Polletta, M. d. C., Zylka, R., Shupe, D., Smith, Jr., H. E., Berta, S., Bavouzet, N., Lagache, G., Farrah, D., Bertoldi, F., Cox, P., de Breuck, C., Dole, H., Lutz, D., Tacconi, L., Perez-Fournon, I., Aussel, H., McCracken, H., Clements, D., Rowan-Robinson, M., Franceschini, A., Frayer, D., Surace, J., and Siana, B.: 2006b, in *Bulletin of the American Astronomical Society*, Vol. 38 of *Bulletin of the American Astronomical Society*, p. 1171

Lonsdale, C. J., Smith, H. E., Rowan-Robinson, M., Surace, J., Shupe, D., Xu, C., Oliver, S., Padgett, D., Fang, F., Conrow, T., Franceschini, A., Gautier, N., Griffin, M., Hacking, P., Masci, F., Morrison, G., O'Linger, J., Owen, F., Pérez-Fournon, I., Pierre, M., Puetter, R., Stacey, G., Castro, S., Polletta, M. d. C., Farrah, D., Jarrett, T., Frayer, D., Siana, B., Babbedge, T., Dye, S., Fox, M., Gonzalez-Solares, E., Salaman, M., Berta, S., Condon, J. J., Dole, H., and Serjeant, S.: 2003, *PASP* **115**, 897

Loose, H. H., Kruegel, E., and Tutukov, A.: 1982, *A&A* **105**, 342

López-Sánchez, Á. R. and Esteban, C.: 2008, *A&A* **491**, 131

López-Sánchez, A. R. and Esteban, C.: 2009, *A&A* **508**, 615

Low, F. J., Cutri, R. M., Kleinmann, S. G., and Huchra, J. P.: 1989, *ApJ* **340**, L1

Low, J. and Kleinmann, D. E.: 1968, *AJ* **73**, 868

Lutz, D., Maiolino, R., Spoon, H. W. W., and Moorwood, A. F. M.: 2004, *A&A* **418**, 465

Magdziarz, P. and Zdziarski, A. A.: 1995, *MNRAS* **273**, 837

Magorrian, J., Tremaine, S., Richstone, D., Bender, R., Bower, G., Dressler, A., Faber, S. M., Gebhardt, K., Green, R., Grillmair, C., Kormendy, J., and Lauer, T.: 1998, *AJ* **115**, 2285

Maiolino, R., Shemmer, O., Imanishi, M., Netzer, H., Oliva, E., Lutz, D., and Sturm, E.: 2007, *A&A* **468**, 979

Marconi, A., Comastri, A., Gilli, R., Hasinger, G., Hunt, L. K., Maiolino, R., Risaliti, G., and Salvati, M.: 2006, *Memorie della Societa Astronomica Italiana* **77**, 742

Marconi, A., Risaliti, G., Gilli, R., Hunt, L. K., Maiolino, R., and Salvati, M.: 2004, *MNRAS* **351**, 169

Masegosa, J. and Márquez, I.: 2003, *Ap&SS* **284**, 483

Mason, K. O., Breeveld, A., Much, R., Carter, M., Cordova, F. A., Cropper, M. S., Fordham, J., Huckle, H., Ho, C., Kawakami, H., Kennea, J., Kennedy, T., Mittaz, J., Pandel, D., Priedhorsky, W. C., Sasseen, T., Shirey, R., Smith, P., and Vreux, J.-M.: 2001, *A&A* **365**, L36

Mateos, S., Barcons, X., Carrera, F. J., Ceballos, M. T., Caccianiga, A., Lamer, G., Maccacaro, T., Page, M. J., Schwope, A., and Watson, M. G.: 2005a, *A&A* **433**, 855

Mateos, S., Barcons, X., Carrera, F. J., Ceballos, M. T., Hasinger, G., Lehmann, I., Fabian, A. C., and Streblyanska, A.: 2005b, *A&A* **444**, 79

Mateos, S., Carrera, F. J., Page, M. J., Watson, M. G., Corral, A., Tedds, J. A., Ebrero, J., Krumpe, M., Schwope, A., and Ceballos, M. T.: 2010, *A&A* **510**, A35+

Matsuhara, H., Wada, T., Matsuura, S., Nakagawa, T., Kawada, M., Ohyama, Y., Pearson, C. P., Oyabu, S., Takagi, T., Serjeant, S., White, G. J., Hanami, H., Watarai, H., Takeuchi, T. T., Kodama, T., Arimoto, N., Okamura, S., Lee, H. M., Pak, S., Im, M. S., Lee, M. G., Kim, W., Jeong, W., Imai, K., Fujishiro, N., Shirahata, M., Suzuki, T., Ihara, C., and Sakon, I.: 2006, *PASJ* **58**, 673

Matt, G., Fabian, A. C., Guainazzi, M., Iwasawa, K., Bassani, L., and Malaguti, G.: 2000, *MNRAS* **318**, 173

Matt, G., Guainazzi, M., Frontera, F., Bassani, L., Brandt, W. N., Fabian, A. C., Fiore, F., Haardt, F., Iwasawa, K., Maiolino, R., Malaguti, G., Marconi, A., Matteuzzi, A., Molendi, S., Perola, G. C., Piraino, S., and Piro, L.: 1997, *A&A* **325**, L13

Matt, G., Guainazzi, M., and Maiolino, R.: 2003, *MNRAS* **342**, 422

McKee, C. F. and Ostriker, E. C.: 2007, *ARA&A* **45**, 565

McLure, R. J. and Dunlop, J. S.: 2002, *MNRAS* **331**, 795

McLure, R. J. and Jarvis, M. J.: 2002, *MNRAS* **337**, 109

McMahon, R. G., Priddey, R. S., Omont, A., Snellen, I., and Withington, S.: 1999, *MNRAS* **309**, L1

Mewe, R., Gronenschild, E. H. B. M., and van den Oord, G. H. J.: 1985, *A&AS* **62**, 197

Mihos, J. C. and Hernquist, L.: 1996, *ApJ* **464**, 641

Miller, M. C.: 2006, *MNRAS* **367**, L32

Moorwood, A. F. M.: 1996, *Space Science Reviews* **77**, 303

Morel, T., Efstathiou, A., Serjeant, S., Márquez, I., Masegosa, J., Héraudeau, P., Surace, C., Verma, A., Oliver, S., Rowan-Robinson, M., Georgantopoulos, I., Farrah, D., Alexander, D. M., Pérez-Fournon, I., Willott, C. J., Cabrera-Guerra, F., Gonzalez-Solares, E. A., Cabrera-Lavers, A., Gonzalez-Serrano, J. I., Ciliegi, P., Pozzi, F., Matute, I., and Flores, H.: 2001, *MNRAS* **327**, 1187

Moshir, M., Kopan, G., Conrow, T., McCallon, H., Hacking, P., Gregorich, D., Rohrback, G., Melnyk, M., Rice, W., Fullmer, M., White, J., and Chester, T.: 1990, in *IRAS Faint Source Catalogue, version 2.0 (1990)*

Murakami, H., Baba, H., Barthel, P., Clements, D. L., Cohen, M., Doi, Y., Enya, K., Figueredo, E., Fujishiro, N., Fujiwara, H., Fujiwara, M., Garcia-Lario, P., Goto, T., Hasegawa, S., Hibi, Y., Hirao, T., Hiromoto, N., Hong, S. S., Imai, K., Ishigaki, M., Ishiguro, M., Ishihara, D., Ita, Y., Jeong, W., Jeong, K. S., Kaneda, H., Kataza, H., Kawada, M., Kawai, T., Kawamura, A., Kessler, M. F., Kester, D., Kii, T., Kim, D. C., Kim, W., Kobayashi, H., Koo, B. C., Kwon, S. M., Lee, H. M., Lorente, R., Makiuti, S., Matsuhara, H., Matsumoto, T., Matsuo, H., Matsuura, S., Müller, T. G., Murakami, N., Nagata, H., Nakagawa, T., Naoi, T., Narita, M., Noda, M., Oh, S. H., Ohnishi, A., Ohyama, Y., Okada, Y., Okuda, H., Oliver, S., Onaka, T., Ootsubo, T., Oyabu, S., Pak, S., Park, Y., Pearson, C. P., Rowan-Robinson, M., Saito, T., Sakon, I., Salama, A., Sato, S., Savage, R. S., Serjeant, S., Shibai, H., Shirahata, M., Sohn, J., Suzuki, T., Takagi, T., Takahashi, H., Tanabé, T., Takeuchi, T. T., Takita, S., Thomson, M., Uemizu, K., Ueno, M., Usui, F., Verdugo, E., Wada, T., Wang, L., Watabe, T., Watarai, H., White, G. J., Yamamura, I., Yamauchi, C., and Yasuda, A.: 2007, *PASJ* **59**, 369

Murphy, Jr., T. W., Armus, L., Matthews, K., Soifer, B. T., Mazzarella, J. M., Shupe, D. L., Strauss, M. A., and Neugebauer, G.: 1996, *AJ* **111**, 1025

Mushotzky, R. F.: 2004, in J. S. Mulchaey, A. Dressler, and A. Oemler (eds.), *Clusters of Galaxies: Probes of Cosmological Structure and Galaxy Evolution*, p. 123

Mushotzky, R. F., Fabian, A. C., Iwasawa, K., Kunieda, H., Matsuoka, M., Nandra, K., and Tanaka, Y.: 1995, *MNRAS* **272**, L9

Nandra, K., Fabian, A. C., Brandt, W. N., Kunieda, H., Matsuoka, M., Mihara, T., Ogasaka, Y., and Terashima, Y.: 1995, *MNRAS* **276**, 1

Nandra, K. and Iwasawa, K.: 2007, *MNRAS* **382**, L1

Nandra, K., O'Neill, P. M., George, I. M., and Reeves, J. N.: 2007, *MNRAS* **382**, 194

Nandra, K. and Pounds, K. A.: 1994, *MNRAS* **268**, 405

Narayan, R., Tchekhovskoy, A., and McKinney, J. C.: 2010, *ArXiv e-prints*

Nardini, E., Risaliti, G., Salvati, M., Sani, E., Imanishi, M., Marconi, A., and Maiolino, R.: 2008, *MNRAS* **385**, L130

Nardini, E., Risaliti, G., Salvati, M., Sani, E., Watabe, Y., Marconi, A., and Maiolino, R.: 2009, *MNRAS* **399**, 1373

Nardini, E., Risaliti, G., Watabe, Y., Salvati, M., and Sani, E.: 2010, *MNRAS* p. 584

Netzer, H., Lutz, D., Schweitzer, M., Contursi, A., Sturm, E., Tacconi, L. J., Veilleux, S., Kim, D.-C., Rupke, D., Baker, A. J., Dasyra, K., Mazzarella, J., and Lord, S.: 2007, *ApJ* **666**, 806

Neugebauer, G., Green, R. F., Matthews, K., Schmidt, M., Soifer, B. T., and Bennett, J.: 1987, *ApJS* **63**, 615

Norman, C., Hasinger, G., Giacconi, R., Gilli, R., Kewley, L., Nonino, M., Rosati, P., Szokoly, G., Tozzi, P., Wang, J., Zheng, W., Zirm, A., Bergeron, J., Gilmozzi, R., Grogin, N., Koekemoer, A., and Schreier, E.: 2002, *ApJ* **571**, 218

Ogasaka, Y., Inoue, H., Brandt, W. N., Fabian, A. C., Kii, T., Nakagawa, T., Fujimoto, R., and Otani, C.: 1997, *PASJ* **49**, 179

Oliver, S., Rowan-Robinson, M., Alexander, D. M., Almaini, O., Balcells, M., Baker, A. C., Barcons, X., Barden, M., Bellas-Velidis, I., Cabrera-Guerra, F., Carballo, R., Cesarsky, C. J., Ciliegi, P., Clements, D. L., Crockett, H., Danese, L., Dapergolas, A., Drolias, B., Eaton, N., Efstathiou, A., Egami, E., Elbaz, D., Fadda, D., Fox, M., Franceschini, A., Genzel, R., Goldschmidt, P., Graham, M., Gonzalez-Serrano, J. I., Gonzalez-Solares, E. A., Granato, G. L., Gruppioni, C., Herbstmeier, U., Héraudeau, P., Joshi, M., Kontizas, E., Kontizas, M., Kotilainen, J. K., Kunze, D., La Franca, F., Lari, C., Lawrence, A., Lemke, D., Linden-Vørnle, M. J. D., Mann, R. G., Márquez, I., Masegosa, J., Mattila, K., McMahon, R. G., Miley, G., Missoulis, V., Mobasher, B., Morel, T., Nørgaard-Nielsen, H., Omont, A., Papadopoulos, P., Perez-Fournon, I., Puget, J., Rigopoulou, D., Rocca-Volmerange, B., Serjeant, S., Silva, L., Sumner, T., Surace, C., Vaisanen, P., van der Werf, P. P., Verma, A., Vigroux, L., Villar-Martin, M., and Willott, C. J.: 2000, *MNRAS* **316**, 749

Omont, A., McMahon, R. G., Bergeron, J., Cox, P., Guilloteau, S., Kreysa, E., Pajot, F., Pécontal, E., Petitjean, P., Solomon, P. M., and Storrie-Lombardi, L. J.: 1997, in J. Bergeron (ed.), *The Early Universe with the VLT.*, p. 357

Osterbrock, D. E.: 1989, *Astrophysics of gaseous nebulae and active galactic nuclei*, Mill Valley, CA, University Science Books

Overzier, R. A., Heckman, T. M., Kauffmann, G., Seibert, M., Rich, R. M., Basu-Zych, A., Lotz, J., Aloisi, A., Charlot, S., Hoopes, C., Martin, D. C., Schiminovich, D., and Madore, B.: 2008, *ApJ* **677**, 37

Page, M. J., Carrera, F. J., Ebrero, J., Stevens, J. A., and Ivison, R. J.: 2007, in V. Charmandaris, D. Rigopoulou, and N. Kylafis (eds.), *Studying Galaxy Evolution with Spitzer and Herschel*

Page, M. J., Davis, S. W., and Salvi, N. J.: 2003, *MNRAS* **343**, 1241

Page, M. J., Mittaz, J. P. D., and Carrera, F. J.: 2001, *MNRAS* **325**, 575

Panessa, F., Barcons, X., Bassani, L., Cappi, M., Carrera, F. J., Dadina, M., Ho, L. C., Iwasawa, K., and Pellegrini, S.: 2007, in T. di Salvo, G. L. Israel, L. Piersant, L. Burderi, G. Matt, A. Tornambe, & M. T. Menna (ed.), *The Multicolored Landscape of Compact Objects and Their Explosive Origins*, Vol. 924 of *American Institute of Physics Conference Series*, pp 830–835

Panessa, F., Bassani, L., Cappi, M., Dadina, M., Barcons, X., Carrera, F. J., Ho, L. C., and Iwasawa, K.: 2006, *A&A* **455**, 173

Pearson, C. and Khan, S. A.: 2009, *MNRAS* **399**, L11

Peeters, E., Spoon, H. W. W., and Tielens, A. G. G. M.: 2004, *ApJ* **613**, 986

Persic, M. and Rephaeli, Y.: 2002, *A&A* **382**, 843

Persic, M., Rephaeli, Y., Braito, V., Cappi, M., Della Ceca, R., Franceschini, A., and Gruber, D. E.: 2004, *A&A* **419**, 849

Peterson, B. M.: 1997, *An Introduction to Active Galactic Nuclei*, Cambridge University Press

Piconcelli, E., Fiore, F., Nicastro, F., Mathur, S., Brusa, M., Comastri, A., and Puccetti, S.: 2007, *A&A* **473**, 85

Piconcelli, E., Jimenez-Bailón, E., Guainazzi, M., Schartel, N., Rodríguez-Pascual, P. M., and Santos-Lleó, M.: 2005, *A&A* **432**, 15

Price, D. J. and Bate, M. R.: 2009, *MNRAS* **398**, 33

Prieto, M. A., Reunanen, J., Tristram, K. R. W., Neumayer, N., Fernandez-Ontiveros, J. A., Orienti, M., and Meisenheimer, K.: 2010, *MNRAS* **402**, 724

Ptak, A., Heckman, T., Levenson, N. A., Weaver, K., and Strickland, D.: 2003, *ApJ* **592**, 782

Quinn, P. J., Barnes, D. G., Csabai, I., Cui, C., Genova, F., Hanisch, B., Kembhavi, A., Kim, S. C., Lawrence, A., Malkov, O., Ohishi, M., Pasian, F., Schade, D., and Voges, W.: 2004, in P. J. Quinn & A. Bridger (ed.), *Society of Photo-Optical Instrumentation Engineers (SPIE) Conference Series*, Vol. 5493 of *Presented at the Society of Photo-Optical Instrumentation Engineers (SPIE) Conference*, pp 137–145

Read, A. M. and Ponman, T. J.: 2003, *A&A* **409**, 395

Reeves, J. N. and Turner, M. J. L.: 2000, *MNRAS* **316**, 234

Rephaeli, Y., Gruber, D., and Persic, M.: 1995, *A&A* **300**, 91

Richards, G. T., Lacy, M., Storrie-Lombardi, L. J., Hall, P. B., Gallagher, S. C., Hines, D. C., Fan, X., Papovich, C., Vanden Berk, D. E., Trammell, G. B., Schneider, D. P., Vestergaard, M., York, D. G., Jester, S., Anderson, S. F., Budavári, T., and Szalay, A. S.: 2006, *ApJS* **166**, 470

Rieke, G. H.: 1988, *ApJ* **331**, L5

Rieke, G. H. and Lebofsky, M. J.: 1979, *ARA&A* **17**, 477

Rieke, G. H. and Low, F. J.: 1972, *ApJ* **176**, L95

Rieke, G. H. and Low, F. J.: 1975, *ApJ* **197**, 17

Rieke, G. H., Young, E. T., Engelbracht, C. W., Kelly, D. M., Low, F. J., Haller, E. E., Beeman, J. W., Gordon, K. D., Stansberry, J. A., Misselt, K. A., Cadien, J., Morrison, J. E., Rivlis, G., Latter, W. B., Noriega-Crespo, A., Padgett, D. L., Stapelfeldt, K. R., Hines, D. C., Egami, E., Muzerolle, J., Alonso-Herrero, A., Blaylock, M., Dole, H., Hinz, J. L., Le Floc'h, E., Papovich, C., Pérez-González, P. G., Smith, P. S., Su, K. Y. L., Bennett, L., Frayer, D. T., Henderson, D., Lu, N., Masci, F., Pesenson, M., Rebull, L., Rho, J., Keene, J., Stolovy, S., Wachter, S., Wheaton, W., Werner, M. W., and Richards, P. L.: 2004, *ApJS* **154**, 25

Rigopoulou, D., Franceschini, A., Aussel, H., Genzel, R., van der Werf, P., Cesarsky, C. J., Dennefeld, M., Oliver, S., Rowan-Robinson, M., Mann, R. G., Perez-Fournon, I., and Rocca-Volmerange, B.: 2000, *ApJ* **537**, L85

Risaliti, G. and Elvis, M.: 2004, *A Panchromatic View of AGN*, p. 187, ASSL Vol. 308: Supermassive Black Holes in the Distant Universe

Risaliti, G., Imanishi, M., and Sani, E.: 2010, *MNRAS* **401**, 197

Risaliti, G., Maiolino, R., Marconi, A., Sani, E., Berta, S., Braito, V., Ceca, R. D., Franceschini, A., and Salvati, M.: 2006, *MNRAS* **365**, 303

Rix, H., Rieke, G., Rieke, M., and Carleton, N. P.: 1990, *ApJ* **363**, 480

Ross, R. R. and Fabian, A. C.: 1993, *MNRAS* **261**, 74

Rowan-Robinson, M.: 1995, *MNRAS* **272**, 737

Rowan-Robinson, M.: 2000, *MNRAS* **316**, 885

Rowan-Robinson, M., Saunders, W., Lawrence, A., and Leech, K.: 1991, *MNRAS* **253**, 485

Rowan-Robinson, M., Valtchanov, I., and Nandra, K.: 2009, *MNRAS* **397**, 1326

Ruiz, A., Carrera, F. J., and Panessa, F.: 2006, in A. Wilson (ed.), *The X-ray Universe 2005*, Vol. 604 of *ESA Special Publication*, p. 659

Ruiz, A., Carrera, F. J., and Panessa, F.: 2007, *A&A* **471**, 775

Ruiz, A., Carrera, F. J., Panessa, F., and Miniutti, G.: 2010a, in J. M. Diego, L. J. Goicoechea, J. I. González-Serrano, & J. Gorgas (ed.), *Highlights of Spanish Astrophysics V*, p. 347

Ruiz, A., Miniutti, G., Panessa, F., and Carrera, F. J.: 2010b, *A&A, in press (astro-ph/1003.0800)*

Ruiz, A., Risaliti, G., Nardini, E., Panessa, F., and Carrera, F. J.: 2010c, *in preparation*

Ruiz, M., Rieke, G. H., and Sheilds, J. D.: 1994, in *Bulletin of the American Astronomical Society*, Vol. 26 of *Bulletin of the American Astronomical Society*, p. 1356

Sanders, D. B., Mazzarella, J. M., Kim, D., Surace, J. A., and Soifer, B. T.: 2003, *AJ* **126**, 1607

Sanders, D. B. and Mirabel, I. F.: 1996, *ARA&A* **34**, 749

Sanders, D. B., Phinney, E. S., Neugebauer, G., Soifer, B. T., and Matthews, K.: 1989, *ApJ* **347**, 29

Sanders, D. B., Soifer, B. T., Elias, J. H., Madore, B. F., Matthews, K., Neugebauer, G., and Scoville, N. Z.: 1988, *ApJ* **325**, 74

Sarazin, C. L.: 1986, *Reviews of Modern Physics* **58**, 1

Sargsyan, L. A. and Weedman, D. W.: 2009, *ApJ* **701**, 1398

Saunders, W., Sutherland, W., Efstathiou, G., Tadros, H., Maddox, S., White, S., Oliver, S., Keeble, O., Rowan-Robinson, M., and Frenk, C.: 1995, in S. J. Maddox and A. Aragon-Salamanca (eds.), *Wide Field Spectroscopy and the Distant Universe*, p. 88

Saxton, R. D., Barstow, M. A., Turner, M. J. L., Williams, O. R., Stewart, G. C., and Kii, T.: 1997, *MNRAS* **289**, 196

Schmitt, H. R., Kinney, A. L., Calzetti, D., and Storchi Bergmann, T.: 1997, *AJ* **114**, 592

Schweitzer, M., Lutz, D., Sturm, E., Contursi, A., Tacconi, L. J., Lehnert, M. D., Dasyra, K. M., Genzel, R., Veilleux, S., Rupke, D., Kim, D.-C., Baker, A. J., Netzer, H., Sternberg, A., Mazzarella, J., and Lord, S.: 2006, *ApJ* **649**, 79

Scoville, N., Aussel, H., Brusa, M., Capak, P., Carollo, C. M., Elvis, M., Giavalisco, M., Guzzo, L., Hasinger, G., Impey, C., Kneib, J.-P., LeFevre, O., Lilly, S. J., Mobasher, B., Renzini, A., Rich, R. M., Sanders, D. B., Schinnerer, E., Schminovich, D., Shopbell, P., Taniguchi, Y., and Tyson, N. D.: 2007, *ApJS* **172**, 1

Serjeant, S., Mortier, A. M. J., Ivison, R. J., Egami, E., Rieke, G. H., Willner, S. P., Rigopoulou, D., Alonso-Herrero, A., Barmby, P., Bei, L., Dole, H., Engelbracht, C. W., Fazio, G. G., Le Floc'h, E., Gordon, K. D., Greve, T. R., Hines, D. C., Huang, J., Misselt, K. A., Miyazaki, S., Morrison, J. E., Papovich, C., Pérez-González, P. G., Rieke, M. J., Rigby, J., and Wilson, G.: 2004, *ApJS* **154**, 118

Shakura, N. I. and Sunyaev, R. A.: 1973, *A&A* **24**, 337

Shankar, F., Salucci, P., Granato, G. L., De Zotti, G., and Danese, L.: 2004, *MNRAS* **354**, 1020

Shapiro, K. L., Genzel, R., Förster Schreiber, N. M., Tacconi, L. J., Bouché, N., Cresci, G., Davies, R., Eisenhauer, F., Johansson, P. H., Krajnović, D., Lutz, D., Naab, T., Arimoto, N., Arribas, S., Cimatti, A., Colina, L., Daddi, E., Daigle, O., Erb, D., Hernandez, O., Kong, X., Mignoli, M., Onodera, M., Renzini, A., Shapley, A., and Steidel, C.: 2008, *ApJ* **682**, 231

Shlosman, I., Begelman, M. C., and Frank, J.: 1990, *Nature* **345**, 679

Smail, I., Ivison, R. J., and Blain, A. W.: 1997, *ApJ* **490**, L5

Soifer, B. T. and Neugebauer, G.: 1991, *AJ* **101**, 354

Soifer, B. T., Rowan-Robinson, M., Houck, J. R., de Jong, T., Neugebauer, G., Aumann, H. H., Beichman, C. A., Boggess, N., Clegg, P. E., Emerson, J. P., Gillett, F. C., Habing, H. J., Hauser, M. G., Low, F. J., Miley, G., and Young, E.: 1984, *ApJ* **278**, L71

Soifer, B. T., Sanders, D. B., Madore, B. F., Neugebauer, G., Danielson, G. E., Elias, J. H., Lonsdale, C. J., and Rice, W. L.: 1987, *ApJ* **320**, 238

Spergel, D. N., Verde, L., Peiris, H. V., Komatsu, E., Nolta, M. R., Bennett, C. L., Halpern, M., Hinshaw, G., Jarosik, N., Kogut, A., Limon, M., Meyer, S. S., Page, L., Tucker, G. S., Weiland, J. L., Wollack, E., and Wright, E. L.: 2003, *ApJS* **148**, 175

Spoon, H. W. W., Armus, L., Cami, J., Tielens, A. G. G. M., Chiar, J. E., Peeters, E., Keane, J. V., Charmandaris, V., Appleton, P. N., Teplitz, H. I., and Burgdorf, M. J.: 2004a, *ApJS* **154**, 184

Spoon, H. W. W., Marshall, J. A., Houck, J. R., Elitzur, M., Hao, L., Armus, L., Brandl, B. R., and Charmandaris, V.: 2007, *ApJ* **654**, L49

Spoon, H. W. W., Moorwood, A. F. M., Lutz, D., Tielens, A. G. G. M., Siebenmorgen, R., and Keane, J. V.: 2004b, *A&A* **414**, 873

Springel, V. and Hernquist, L.: 2005, *ApJ* **622**, L9

Springel, V., White, S. D. M., Jenkins, A., Frenk, C. S., Yoshida, N., Gao, L., Navarro, J., Thacker, R., Croton, D., Helly, J., Peacock, J. A., Cole, S., Thomas, P., Couchman, H., Evrard, A., Colberg, J., and Pearce, F.: 2005, *Nature* **435**, 629

SSC: 2005, *IRS S11 Pipeline Handbook*, Spitzer Science Center, 1.0 edition

SSC: 2006, *Infrared Array Camera Data Handbook*, Spitzer Science Center, 3.0 edition

SSC: 2008, *Infrared Spectrograp Data Handbook*, Spitzer Science Center, 3.2 edition

Steffen, A. T., Strateva, I., Brandt, W. N., Alexander, D. M., Koekemoer, A. M., Lehmer, B. D., Schneider, D. P., and Vignali, C.: 2006, *AJ* **131**, 2826

Stevens, J. A., Jarvis, M. J., Coppin, K. E. K., Page, M. J., Greve, T. R., Carrera, F. J., and Ivison, R. J.: 2010, *MNRAS* p. 627

Stevens, J. A., Page, M. J., Ivison, R. J., Carrera, F. J., Mittaz, J. P. D., Smail, I., and McHardy, I. M.: 2005, *MNRAS* **360**, 610

Strateva, I. V., Brandt, W. N., Schneider, D. P., Vanden Berk, D. G., and Vignali, C.: 2005, *AJ* **130**, 387

Strickland, D. K., Heckman, T. M., Colbert, E. J. M., Hoopes, C. G., and Weaver, K. A.: 2004, *ApJS* **151**, 193

Strüder, L., Briel, U., Dennerl, K., Hartmann, R., Kendziorra, E., Meidinger, N., Pfeffermann, E., Reppin, C., Aschenbach, B., Bornemann, W., Bräuninger, H., Burkert, W., Elender, M., Freyberg, M., Haberl, F., Hartner, G., Heuschmann, F., Hippmann, H., Kastelic, E., Kemmer, S., Kettenring, G., Kink, W., Krause, N., Müller, S., Oppitz, A., Pietsch, W., Popp, M., Predehl, P., Read, A., Stephan, K. H., Stötter, D., Trümper, J., Holl, P., Kemmer, J., Soltau, H., Stötter, R., Weber, U., Weichert, U., von Zanthier, C., Carathanassis, D., Lutz, G., Richter, R. H., Solc, P., Böttcher, H., Kuster, M., Staubert, R., Abbey, A., Holland, A., Turner, M., Balasini, M., Bignami, G. F., La Palombara, N., Villa, G., Buttler, W., Gianini, F., Lainé, R., Lumb, D., and Dhez, P.: 2001, *A&A* **365**, L18

Sturm, E., Lutz, D., Verma, A., Netzer, H., Sternberg, A., Moorwood, A. F. M., Oliva, E., and Genzel, R.: 2002, *A&A* **393**, 821

Surace, J. A., Sanders, D. B., Vacca, W. D., Veilleux, S., and Mazzarella, J. M.: 1998, *ApJ* **492**, 116

Telesco, C. M., Becklin, E. E., Wynn-Williams, C. G., and Harper, D. A.: 1984, *ApJ* **282**, 427

Teng, S. H., Veilleux, S., Anabuki, N., Dermer, C. D., Gallo, L. C., Nakagawa, T., Reynolds, C. S., Sanders, D. B., Terashima, Y., and Wilson, A. S.: 2009, *ApJ* **691**, 261

Teng, S. H., Wilson, A. S., Veilleux, S., Young, A. J., Sanders, D. B., and Nagar, N. M.: 2005, *ApJ* **633**, 664

Tran, H. D.: 2001, *ApJ* **554**, L19

Tran, H. D., Brotherton, M. S., Stanford, S. A., van Breugel, W., Dey, A., Stern, D., and Antonucci, R.: 1999, *ApJ* **516**, 85

Tran, H. D., Cohen, M. H., and Villar-Martin, M.: 2000, *AJ* **120**, 562

Tran, Q. D., Lutz, D., Genzel, R., Rigopoulou, D., Spoon, H. W. W., Sturm, E., Gerin, M., Hines, D. C., Moorwood, A. F. M., Sanders, D. B., Scoville, N., Taniguchi, Y., and Ward, M.: 2001, *ApJ* **552**, 527

Treister, E., Krolik, J. H., and Dullemond, C.: 2008, *ApJ* **679**, 140

Turner, M. J. L., Abbey, A., Arnaud, M., Balasini, M., Barbera, M., Belsole, E., Bennie, P. J., Bernard, J. P., Bignami, G. F., Boer, M., Briel, U., Butler, I., Cara, C., Chabaud, C., Cole, R., Collura, A., Conte, M., Cros, A., Denby, M., Dhez, P., Di Coco, G., Dowson, J., Ferrando, P., Ghizzardi, S., Gianotti, F., Goodall, C. V., Gretton, L., Griffiths, R. G., Hainaut, O., Hochedez, J. F., Holland, A. D., Jourdain, E., Kendziorra, E., Lagostina, A., Laine, R., La Palombara, N., Lortholary, M., Lumb, D., Marty, P., Molendi, S., Pigot, C., Poindron, E., Pounds, K. A., Reeves, J. N., Reppin, C., Rothenflug, R., Salvetat, P., Sauvageot, J. L., Schmitt, D., Sembay, S., Short, A. D. T., Spragg, J., Stephen, J., Strüder, L., Tiengo, A., Trifoglio, M., Trümper, J., Vercellone, S., Vigroux, L., Villa, G., Ward, M. J., Whitehead, S., and Zonca, E.: 2001, *A&A* **365**, L27

Turner, T. J. and Miller, L.: 2009, *A&A Rev.* **17**, 47

Ueda, Y., Akiyama, M., Ohta, K., and Miyaji, T.: 2003, *ApJ* **598**, 886

Ueda, Y., Eguchi, S., Terashima, Y., Mushotzky, R., Tueller, J., Markwardt, C., Gehrels, N., Hashimoto, Y., and Potter, S.: 2007, *ApJ* **664**, L79

Urry, C. M. and Padovani, P.: 1995, *PASP* **107**, 803

Vasudevan, R. V. and Fabian, A. C.: 2009, *MNRAS* **392**, 1124

Veilleux, S., Kim, D.-C., and Sanders, D. B.: 1999, *ApJ* **522**, 113

Veilleux, S., Kim, D.-C., and Sanders, D. B.: 2002, *ApJS* **143**, 315

Verma, A., Charmandaris, V., Klaas, U., Lutz, D., and Haas, M.: 2005, *Space Science Reviews* **119**, 355

Verma, A., Rowan-Robinson, M., McMahon, R., and Andreas Efstathiou, A. E.: 2002, *MNRAS* **335**, 574

Véron-Cetty, M.-P. and Véron, P.: 2006, *A&A* **455**, 773

Vogel, S. N., Kulkarni, S. R., and Scoville, N. Z.: 1988, *Nature* **334**, 402

Wang, J., Wei, J. Y., and He, X. T.: 2006, *ApJ* **638**, 106

Watson, M. G., Schröder, A. C., Fyfe, D., Page, C. G., Lamer, G., Mateos, S., Pye, J., Sakano, M., Rosen, S., Ballet, J., Barcons, X., Barret, D., Boller, T., Brunner, H., Brusa, M., Caccianiga, A., Carrera, F. J., Ceballos, M., Della Ceca, R., Denby, M., Denkinson, G., Dupuy, S., Farrell, S., Fraschetti, F., Freyberg, M. J., Guillout, P., Hambaryan, V., Maccacaro, T., Mathiesen, B., McMahon, R., Michel, L., Motch, C., Osborne, J. P., Page, M., Pakull, M. W., Pietsch, W., Saxton, R., Schwope, A., Severgnini, P., Simpson, M., Sironi, G., Stewart, G., Stewart, I. M., Stobbart, A., Tedds, J., Warwick, R., Webb, N., West, R., Worrall, D., and Yuan, W.: 2009, *A&A* **493**, 339

Werner, M. W., Roellig, T. L., Low, F. J., Rieke, G. H., Rieke, M., Hoffmann, W. F., Young, E., Houck, J. R., Brandl, B., Fazio, G. G., Hora, J. L., Gehrz, R. D., Helou, G., Soifer, B. T., Stauffer, J., Keene, J., Eisenhardt, P., Gallagher, D., Gautier, T. N., Irace, W., Lawrence, C. R., Simmons, L., Van Cleve, J. E., Jura, M., Wright, E. L., and Cruikshank, D. P.: 2004, *ApJS* **154**, 1

White, N. E. and Hornschemeier, A. E.: 2009, in *American Astronomical Society Meeting Abstracts*, Vol. 213 of *American Astronomical Society Meeting Abstracts*, p. 217.02

White, N. E., Swank, J. H., and Holt, S. S.: 1983, *ApJ* **270**, 711

Whitmore, B. C., Zhang, Q., Leitherer, C., Fall, S. M., Schweizer, F., and Miller, B. W.: 1999, *AJ* **118**, 1551

Williams, J. P. and McKee, C. F.: 1997, *ApJ* **476**, 166

Wilman, R. J., Fabian, A. C., Crawford, C. S., and Cutri, R. M.: 2003, *MNRAS* **338**, L19

Wilman, R. J., Fabian, A. C., Cutri, R. M., Crawford, C. S., and Brandt, W. N.: 1998, *MNRAS* **300**, L7

Woods, D. F., Geller, M. J., and Barton, E. J.: 2006, *AJ* **132**, 197

Yamashita, A., Matsumoto, C., Ishida, M., Inoue, H., Kii, T., Makishima, K., Takahashi, T., and Tashiro, M.: 1997, *ApJ* **486**, 763

Yan, L., Tacconi, L. J., Fiolet, N., Sajina, A., Omont, A., Lutz, D., Zamojski, M., Neri, R., Cox, P., and Dasyra, K. M.: 2010, *ApJ* **714**, 100

Yaqoob, T. and Serlemitsos, P.: 2005, *ApJ* **623**, 112

Yu, Q. and Tremaine, S.: 2002, *MNRAS* **335**, 965

Yun, M. S. and Scoville, N. Z.: 1998, *ApJ* **507**, 774

Zwicky, F.: 1965, *ApJ* **142**, 1293